Thomas Kluge

ENHANCED LASER ION ACCELERATION FROM SOLIDS

HZDR

HELMHOLTZ
ZENTRUM DRESDEN
ROSSENDORF

TECHNISCHE
UNIVERSITÄT
DRESDEN

Enhanced Laser Ion Acceleration from Solids

DISSERTATION

zur Erlangung des akademischen Grades

Doctor rerum naturalium
(Dr. rer. nat.)

vorgelegt der
Fakultät Mathematik und Naturwissenschaften
der Technischen Universität Dresden

von

Dipl. Phys. Thomas KLUGE
geboren am 21.05.1982 in Dresden

eingereicht am 05. April 2012

Die Dissertation wurde in der Zeit von 05/2007 bis 03/2012
am Helmholtz-Zentrum Dresden-Rossendorf
im Institut für Strahlenphysik angefertigt

Erster Gutachter	Prof. Dr. Roland Sauerbrey
Zweiter Gutachter	Prof. Dr. Yasuhiko Sentoku
Eingereicht am	5. April 2012
Tag der Verteidigung	6. November 2012

For my wife.

Die Naturwissenschaft braucht der Mensch zum Erkennen,
den Glauben zum Handeln.

Max Planck

Abstract

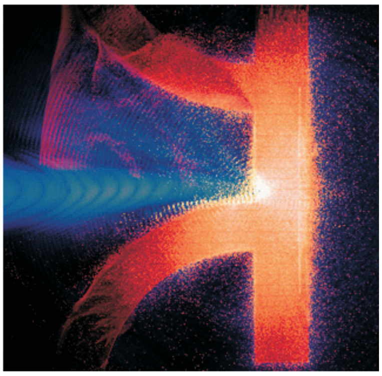

This thesis presents results on the theoretical description of ion acceleration using ultra-short ultra-intense laser pulses. It consists of two parts. One deals with the very general and underlying description and theoretic modeling of the laser interaction with the plasma, the other part presents three approaches of optimizing the ion acceleration by target geometry improvements using the results of the first part.

In the first part, a novel approach of modeling the electron average energy of an over-critical plasma that is irradiated by a few tens of femtoseconds laser pulse with relativistic intensity is introduced. The first step is the derivation of a general expression of the distribution of accelerated electrons in the laboratory time frame. As is shown, the distribution is homogeneous in the proper time of the accelerated electrons, provided they are at rest and distributed uniformly initially. The average hot electron energy can then be derived in a second step from a weighted average of the single electron energy evolution.

This result is applied exemplary for the two important cases of infinite laser contrast and square laser temporal profile, and the case of an experimentally more realistic case of a laser pulse with a temporal profile sufficient to produce a preplasma profile with a scale length of a few hundred nanometers prior to the laser pulse peak. The thus derived electron temperatures are in excellent agreement with recent measurements and simulations, and in particular provide an analytic explanation for the reduced temperatures seen both in experiments and simulations compared to the widely used ponderomotive energy scaling.

The implications of this new electron temperature scaling on the ion acceleration, i.e. the maximum proton energy, are then briefly studied in the frame of an isothermal 1D expansion model. Based on this model, two distinct regions of laser pulse duration are identified with respect to the maximum energy scaling. For short laser pulses, compared to a reference time, the maximum ion energy is found to scale linearly with the laser intensity for a simple flat foil, and the most important other parameter is the laser absorption efficiency. In particular the electron temperature is of minor importance. For long laser pulse durations the maximum ion energy scales only proportional to the square root of the laser peak intensity and the electron temperature has a large impact. Consequently, improvements of the ion acceleration beyond the simple flat foil target maximum energies should focus on the increase of the laser absorption in the first case and the increase of the hot electron temperature in the latter case.

In the second part, exemplary geometric designs are studied by means of simulations and analytic discussions with respect to their capability for an improvement of the laser absorption efficiency and temperature increase.

First, a stack of several foils spaced by a few hundred nanometers is proposed and it is shown that the laser energy absorption for short pulses and therefore the maximum proton energy can be significantly increased. Secondly, mass limited targets, i.e. thin foils with a finite lateral extension, are studied with respect to the increase of the hot electron temperature. An analytical model is provided predicting this temperature based on the lateral foil width. Finally, the important case of bent foils with attached flat top is analyzed. This target geometry resembles hollow cone targets with flat top attached to the tip, as were used in a recent experiment producing world record proton energies. The presented analysis explains the observed increase in proton energy with a new electron acceleration mechanism, the direct acceleration of surface confined electrons by the laser light. This mechanism occurs when the laser is aligned tangentially to the curved cone wall and the laser phase co-moves with the energetic electrons. The resulting electron average energy can exceed the energies from normal or oblique laser incidence by several times. Proton energies are therefore also greatly increased and show a theoretical scaling proportional to the laser intensity, even for long laser pulses.

Zusammenfassung

Diese Doktorarbeit präsentiert Ergebnisse zur theoretischen Beschreibung der Ionenbeschleunigung mittels ultrakurzer hochintensiver Laserpulse. Sie besteht aus zwei Teilen. Der erste Teil behandelt die grundlegende theoretische Modellierung der Laserwechselwirkung mit dem Plasma, der zweite Teil präsentiert beispielhaft drei Ansätze wie die Ionenbeschleunigung durch Verbesserungen der Targetgeometrie optimiert werden kann.

Im ersten Teil wird ein neuer Ansatz zur Modellierung der Durchschnittsenergie von Elektronen eines Plasmas beschrieben, welches von einem Laserpuls mit einer Dauer von einigen 10 Femtosekunden und relativistischer Intensität beschienen wird. In einem ersten Schritt wird ein allgemeiner Ausdruck für die Verteilung der beschleunigten Elektronen in der Laborzeit hergeleitet. Die Verteilung der Elektronen in ihrer Eigenzeit ist homogen, vorausgesetzt, dass sie vor der Bestrahlung ruhten und gleichmäßig verteilt waren. Die Durschnittsenergie der heißen Elektronen kann dann in einem zweiten Schritt durch eine gewichtete Mittelung des Energieverlaufs eines einzelnen Elektrons gewonnen werden.
Dieses Verfahren wird beispielhaft auf die zwei wichtigen Fälle eines idealen Rechteckpulses und eines realistischeren Laserpulses mit einem zeitlichen Verlauf, welcher ein Vorplasma mit einer Skalenlänge im Bereich einiger hundert Mirkometer vor Ankunft des Pulsmaximums erzeugt, angewandt. Die somit berechneten Durchschnittsenergien sind in hervorragender Übereinstimmung mit Experimenten und Simulationen und können im Besonderen die regelmäßig beobachteten Abweichungen zur ponderomotiven Energieskalierung erklären. Die Auswirkungen dieser Elektronenenergieskalierung auf die Ionenbeschleunigung, insbesondere auf die maximal zu erwartende Protonenenergie, werden kurz anhand eines eindimensionalen isothermalen Modells beleuchtet. Es ergeben sich zwei unterschiedliche Regime für die Skalierung der Maximalenergie mit der Laserintensität in Abhängigkeit der Laserpulsdauer. Bei kurzen Pulsen sagt das Modell eine Skalierung der Maximalenergie der Ionen proportional zur Laserintensität und Unabhängig von der Elektronentemperatur voraus. Die einzige wichtige weitere Größe in diesem Fall ist der Laserabsorptionskoeffizient. Bei langen Pulsen hingegen skaliert die Ionenenergie nur proportional zur Wurzel der Intensität und die Elektronenenergie hat einen gewichtigen Einfluss. Daher sollten sich Anstrengungen zur Erhöhung der Ionenenergieen über die einfachen flachen Folien hinaus im ersten Fall auf Verbesserungen der Laserabsorption konzentrieren und im letzteren Fall auf die Erhöhung der durchschnittlichen Energie heißer Elektronen.

Im zweiten Teil dieser Dissertation werden drei verschiedene Foliengeometrien mittels

Simulationen und analytischer Betrachtungen auf ihr Potenzial zur Erhöhung der Absorption und Elektronentemperatur hin untersucht.

Der erste Vorschlag ist ein Stapel mehrerer Folien mit einem Abstand einiger hundert Nanometer untereinander. Mittels eines solchen Targets lassen sich die Laserabsorption und damit die maximale Ionenenergie erheblich steigern. Eine weitere Möglichkeit zur Energieerhöhung stellen massereduzierte dünne Folien dar. Durch ihre endliche laterale Ausdehnung werden die heißen Elektronen räumlich begrenzt die daurch mehrfach vom Laser beschleunigt werden können. Ein analytisches Model wird hergeleitet, durch welches die resultierende Erhöhung der durchschnittlichen Elektronenenergie in Abhängigkeit der Folienbreite ermittelt werden kann. Abschließend wird eine gekrümmte Folie mit flachem Endstück betrachtet. Diese Geometrie reflektiert die Geometrie eines hohlen Zylinders mit flacher Folie an der Spitze. Mit solchen Targets konnte erst jüngst einer neuer Weltrekord für die höchste Protonenenergie durch Laserbeschleunigung aufgestellt werden. Die Analyse der Wechselwirkung eines tangential auf die Zylinderwand treffenden Lasers mit dem Plasma ergibt, dass Elektronen durch einen neuen Mechanismus kontinuierlich entlang der Oberfläche beschleunigt werden können und dabei ein Vielfaches der Energie erlangen können, welche erreicht werden können wenn der Laser senkrecht oder schräg auf eine Folie trifft. Folglich sind auch die Protonenenergien deutlich höher und skalieren sogar im Falle langer Pulse linear mit der Laserintensität.

Contents

List of Abbreviations

ASE	Amplified Spontaneous Emission
BSI	Barrier Suppression Ionization
CP	Circular Polarization
CPA	Chirped Pulse Amplification
DLLPA	Direct Laser Light Pressure Acceleration
DS	Directional Splitting
EOM	Equation of Motion
FDTD	Finite Difference Time Domain
FTC	Flat Top Cone
HZDR	Helmholtzzentrum Dresden-Rossendorf
LANL	Los Alamos National Laboratory
LET	Linear Energy Transfer
LLNL	Lawrence Livermore National Laboratory
LP	Linear Polarization
MLT	Mass Limited Target
PEM	Plasma Expansion Model
PIC	Particle-In-Cell
RIT	Relativistically Induced Transparency
RPA	Radiation Pressure Acceleration
SM-LWFA	Self Modulated Laser Wakefield Acceleration
TNSA	Target Normal Sheath Acceleration

TUD	Technische Universität Dresden
ZIK	Zentrum für Innovationskompetenz

List of Figures

Chapter 1

Introduction

1.1 History and Motivation

According to the World Health Organization, 2010 has most likely been the year where cancer related deaths have, for the first time in history, outnumbered deaths related to cardio-vascular diseases [1]. Each year there are about 12.4 million new incidences of cancer worldwide (reference year: 2008), excluding non-melanoma skin cancer. This compares to more than 7.5 million fatalities caused by cancer, which represents about one eighth of all deaths. Moreover there are yet more deaths related to cancer where cancer has not been the direct cause of death, which demonstrates the non-satisfying situation of cancer therapies. Those data are backed by the EUROCARE 4 survey [2]. For cancer diagnosed between 2000 and 2002 in Europe, the 10 year relative survival was about 43%. The most successfully employed therapy still is surgery which is responsible for about 50% of cured cases. Radiation therapy alone or in combination with surgery is responsible for 40%, while chemotherapy is responsible only for 10% of cured cases. Hence, radiation therapy is a very promising approach and has developed to be the second most successful therapy after surgical intervention. It can also significantly increase the median survival time and decrease side effects, since in many cases organs can be rescued that otherwise would have to be removed. If

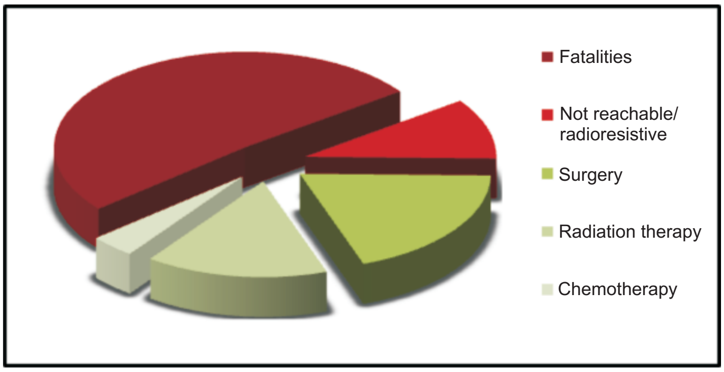

Figure 1.1: Relative number of cured cancers (10 year survival) with respect to the treatment methods, compared to fatalities (red).

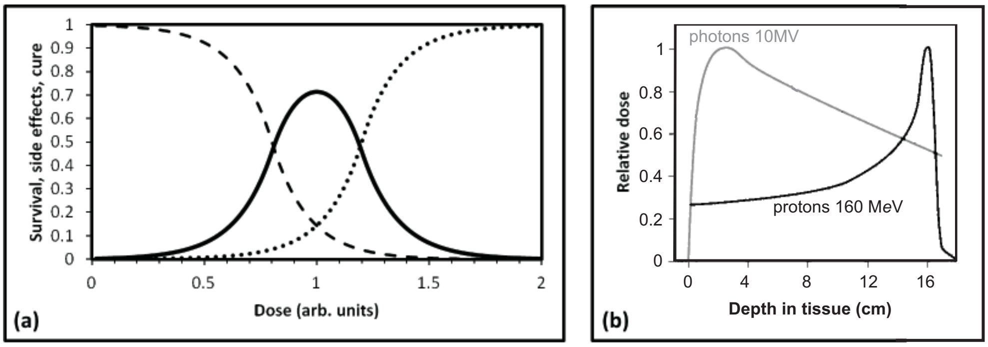

Figure 1.2: (a) Qualitative dose effect on tumor cell survival (dashed) and side effects on healthy tissue (dotted). With increasing dose, less tumor cells survive, but also more side effects are induced. Hence, there exists an optimum dose for successful treatment (solid). (b) Depth dose curve for photons (10 MV, gray) and protons (160 MeV, black).

diagnosed early and the cancer is consisting of a single, well distinguishable tumor, the radiotherapeutic prospects are generally good. However, in 20% of the cases, due to a complicated location or radio-resistivity of the tumor, an adequate treatment is not possible. Hence, an improvement of high volume conformity together with a higher biological effectiveness in the tumor volume, without increasing damage done to healthy surrounding tissue, is needed. Nowadays, radiotherapy is mostly given by means of intensity modulated photon irradiation or electron irradiation, since the required photon or electron generators have a small footprint compared to ion accelerators, and therefore fit well into the clinical environment, and have moderate investment costs.

An increase in radiation dose raises the probability of inducing radiation damage in cells, especially in the DNA. This may increase the local tumor damage but will also escalate the side effects induced in healthy tissue. Consequently, there exists an optimal dose below which the tumor is not effectively damaged and above which the danger of side effects reduces the chance of a successful treatment (Fig. 1.2a). In fact, in [3] it was shown that an improvement of treatment prospects cannot be achieved simply by increasing the dose.
A promising solution is the use of energetic protons or heavier ions instead of photons or electrons. Those particles combine two advantages. First, their energy deposition mechanism is characterized by a sharp dose maximum at the end of their passage (Bragg-peak, Fig. 1.2b) [4]. Second, ions show a very low lateral scattering of dose compared to photons or electrons, due to their large mass. This allows for a more conformal irradiation of the tumor volume and additionally the peaked dose deposition characteristics permits an increase of dose delivered to the tumor while at the same time sparing surrounding healthy tissue. Further advantages arise from beneficial properties of ion beams with respect to the

biological effectiveness. Heavy ions can have a high linear energy transfer (LET) along their trajectories [5]. Compared to light particles (electrons) or photons, the high LET, especially within the Bragg-peak, can have several beneficial properties [6]. Those include a higher relative biological effectiveness, a reduced sensitivity to the degree of oxygenation, a reduction of cell repair mechanisms and a reduction of the dependence of radio sensitivity upon the phase of cell division. However, the downside of ion radiation treatment with current technology are the large accelerator and beam transport facilities necessary to produce and deliver ions with sufficiently high energy. In order to reach a deep-seated tumor, ions with up to 250 A MeV may be necessary. Such facilities, especially when a gantry for variable beam orientation is required, turn out to be both very large and expensive with costs exceeding EUR 100 Mill [7].

To bring the advantages of ion therapy to a large number of patients, and to avoid the drawbacks and reduce costs and space requirements, in Dresden (Germany) a strong collaborative effort has been founded between the Technical University (TUD), the University Hospital Carl Gustav Carus, the Medical Faculty Carl Gustav Carus, and the Helmholtz-Zentrum Dresden-Rossendorf (HZDR). Those institutes work together under the roof of OncoRay in cooperation with the ZIK UltraOptics in Jena on the project OncoOptics, dedicated to bring high power lasers into particle therapy.

Laser accelerated ion beams are potentially very suitable for medical applications since they are extremely intense and have a very low emittance [8, 9, 10]. They are very short pulsed (femtoseconds to few picoseconds), enabling the use of novel, compact pulsed gantries [11]. Furthermore, the actual acceleration distance of the ions is extremely short with only a few microns. Another advantage is the fact, that the laser light can be steered very easily by optical components, hence a gantry may be envisioned that does not need enormous bending magnets making it heavy, mechanically challenging and expensive. Put together, a laser accelerator has many potential benefits compared to conventional ion accelerators. Laser acceleration of ions could make ion tumor therapy cheaper and fit into a clinical setting more easily [12, 13, 14, 10, 15]. Additionally, many other applications may profit from the beneficial properties of laser generated ion beams, such as fast ignition fusion [16], nuclear reactions and isotope production [17, 18].

However, one of the biggest challenges remains the issue of laser accelerated ion energies still falling short of therapeutically necessary values. High power lasers have been known to be able to produce energetic ions since the 1970's. Yet, for two decades, the energy of ions did not exceed a few hundred keV. The interest in this technology has jumped up with the advent of the chirped pulse amplification (CPA) in the 1990s [19], which allows higher pulse power and laser intensity (nowadays up to $\approx 10^{22}\,\mathrm{W/cm^2}$) at short pulse durations in the order of some ten to hundred femtoseconds. The pursuit of high ion energies has culminated in the year 2000 when protons with an energy close to 60 MeV were produced at the Lawrence Livermore National Laboratory (LLNL, USA) [20]. Nevertheless, even though this early success has triggered a significant amount of research worldwide, this energy was not exceeded until 2009 when experiments with novel flat top cone targets (FTC) were carried out at the Trident laser at the Los Alamos National Laboratory (LANL, USA) [21]. Those experiments, which are analyzed in Sec. 4.3.2 of this work, produced protons with an energy exceeding the old threshold of 60 MeV by more than 10% and now mark with 67.5 MeV the record of the highest published laser accelerated proton energy.

While up to now the highest ion energies have been achieved by the so called Target Normal Sheath Acceleration process (TNSA, Sec. 2.3.1), novel and potentially more efficient regimes have been predicted theoretically (Sec. 2.3.2). Yet, none of these could be demonstrated experimentally up until now and they would be technically extremely challenging. The silver bullet would be an enhancement of the conventional, reliable and robust TNSA mechanism. It is the focus of this thesis to introduce and study possible novel regimes within TNSA that have the potential of boosting the ion energies to therapeutically relevant energies of > 200 MeV. The studies were performed both analytically by analyzing the fundamental laser-matter interaction and by simulations that allow a detailed insight into the processes at shortest time scales that would be experimentally not accessible.

1.2 Thesis Outline

This thesis is concerned with the maximum ion energy from laser ion acceleration. There are various different mechanisms that can transfer energy from the laser to ions, which will be discussed in Chapter 2. Still, up to now experimentally the most efficient mechanism with respect to maximum ion energy and density is the TNSA mechanism (Sec. 2.3.1), where the laser first accelerates electrons on the front surface of a foil which in turn propagate through the target and set up an ion accelerating electrostatic field at the foil rear side. The final maximum ion energy in the TNSA regime depends only on the parameters of the plasma created at the foil rear side, namely the average *hot electron energy* T_e (commonly referred to as "temperature" for reasons explained later in Sec. 2.2.3), *hot electron density* n_e, and duration of the existence of the field which is governed by the *laser pulse duration* τ.

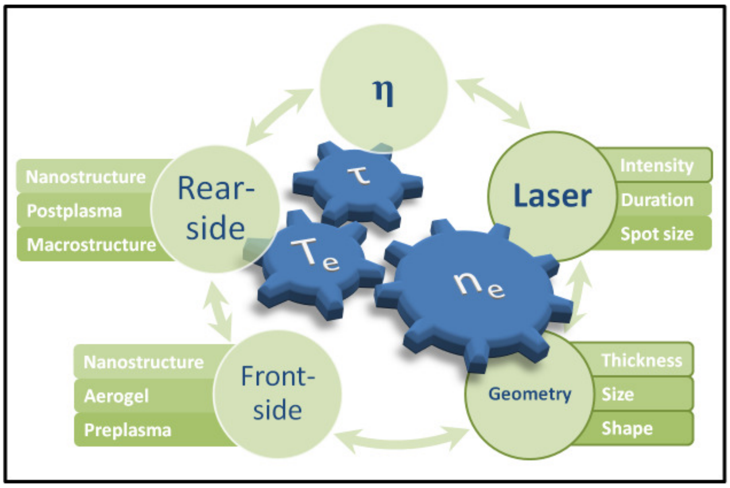

Figure 1.3: The acceleration of ions by intense short laser pulses is most commonly dominated by the TNSA process. The maximum ion energy is then determined by the plasma properties at the rear foil surface (hot electron temperature T_e, density n_e and the time the field can be sustained which is determined by the pulse duration τ. Those plasma parameters are in turn influenced by external parameters such as parameters of the laser, the structure of the front or rear surface of the target foil, the absorption efficiency and the target geometry, which also influence each other.

These plasma properties are in turn determined by a large variety of external parameters, which include all of the laser parameters – such as spot size, wave length, and intensity, the laser absorption efficiency η, the target foil front and rear surface structure, and other geometric parameters – such as the foil thickness, lateral size and shape (Fig. 1.3). To make things even more complicated, all of these quantities have complex dependencies on each other. Consequently one ends up with a multi-parameter space to optimize for the maximum possible ion energy at a given laser system. The only reasonable path is to study the parameters individually, since there is no unified theory on the complex interplay of the individual parameters and their effect on the maximum ion energy, and computer power for performing complex multi-parameter studies is presently insufficient. Consequently, it is necessary to first determine the most relevant parameters and subsequently reduce the complexity e.g. by only considering binary mutual interactions between the parameters.

A typical experimental setup as it is installed at the DRACO laser facility at the HZDR is shown in Fig. 1.4. As a minimum, such an experiment consists of the laser focusing parabola, the target (which in the most simple case is a flat foil), and an ion spectrometer. In the standard experiments this typically is a stack of radio-chromatic film to measure the ion dose as a function of penetration depth that in turn is dependent on the ion energy [22]. At DRACO, the experimental routine has progressed to a status where routinely and reproducibly ion beams with a maximum of ≈ 20 MeV can be produced [23, 24]. Each target

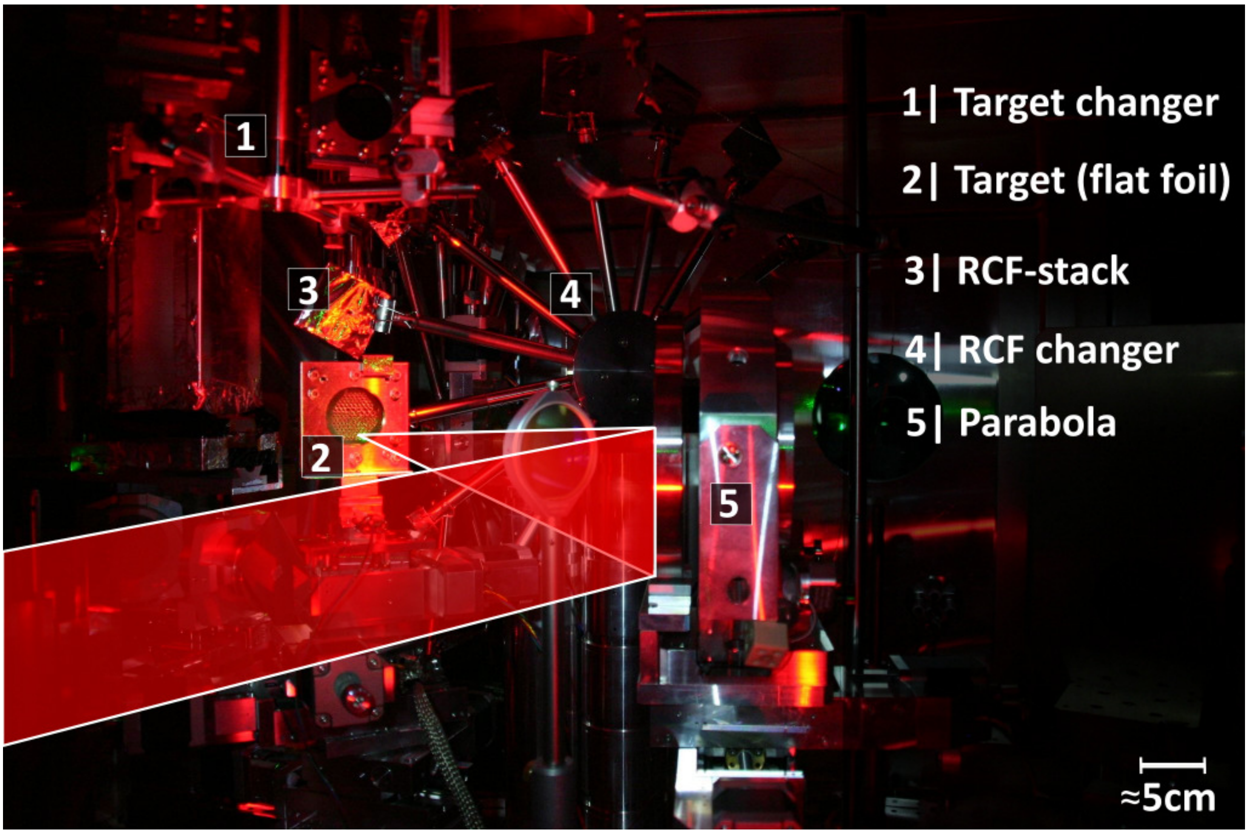

Figure 1.4: Typical setup of a laser ion acceleration experiment (DRACO, HZDR).

foil can be shot at more than 200 times and the target and RCF changing procedure can be automated.

The typical laser parameters discussed in this thesis are guided by the state-of-the-art laser systems used in the past years to efficiently accelerate ions. Their pulse duration is in the order of few 10 fs up to few 100 fs, reaching a peak intensity of up to $10^{18}\,\mathrm{W/cm^2} - 10^{21}\,\mathrm{W/cm^2}$ inside the focal spot which usually is in the order of a few µm. The typical total energy contained in a pulse thus ranges from approximately 1 J to 100 J. This sets limitations on the available pulse repetition rate, since optical elements need to cool between shots to prevent thermal effects.

This thesis will focus on two of the experimentally most important parameters determining the ion maximum energy, namely the laser intensity and target foil geometry. Since the focus will be put on the fundamental laser matter interaction, all options of intervention on the foil rear surface are neglected, as they are secondary effects within this scope. Thus with “geometry” here and in the following it is referred to fundamental properties such as the foil thickness, size and shape. The effects of naturally occurring preplasma due to laser prepulses and amplified spontaneous emission (ASE) are not explicitly in the focus of this thesis. Rather, its effects and its interplay with the geometric parameters will be discussed at the relevant locations. In this respect, also nano-structures [25] as well as the addition of low density aerogel on the front and rear surfaces are not considered explicitly.

The structure of the thesis follows the above considerations:

- In the next chapter the theory of laser matter interaction in the relevant regimes is briefly introduced, focusing on the interaction with solids (Sec. 2.2.3) and the acceleration of ions (Sec. 2.3), specifically in the TNSA regime (Sec. 2.3.1). The relevance of the plasma parameters and their impact on the maximum ion energy is explained and possible paths to the increase of ion energies that have been proposed in the past are briefly stated. For a comprehensive view on the theory of laser matter interaction the reader is pointed to the available literature, e.g. [26, 27, 28].

- The simulation methods used in this thesis are introduced in chapter 3. The laser-plasma interaction is simulated employing the Partice-in-Cell (PIC) method, that can solve Maxwell's equations on a grid, reducing the computational demands significantly compared to other methods, for example direct particle-particle methods.

- In chapter 4, the results of the studies in the frame of this work will be presented.
  - In Sec. 4.1, the scaling of the hot electron temperature with the laser intensity will be revisited, developing a novel ansatz based on a Lorentz invariant electron distribution. Furthermore, the impact of this refined scaling on ion acceleration is demonstrated.
  - In Sec. 4.2, the effect of ultra-thin foils and the possibility of independently optimizing electron density and temperature at a given pulse duration with respect to ion maximum energy is discussed. In other words, the optima of the relevant plasma parameters at unstructured flat foils are studied.
  - In Sec. 4.3.1, the effects of limiting the transverse foil extension are studied. These include electron refluxing, electron reacceleration and Coulomb explosion, as well as a spatial smoothening and reduction of beam divergence of the emitted ions in certain parameter ranges. The important concept of electron reacceleration of transversely refluxing electrons, first proposed by the author in [29], is described in detail.

- In Sec. 4.3.2, the influence of the target shape on the laser matter interaction is studied in the important exemplary case of hollow FTC targets. It is known that with these targets the laser field may be geometrically focused [30] and electrons at the inner cone wall surface may be resonantly driven [31] at certain parameters. In experimental situations a third mechanism – the continuous acceleration of electrons – may become important. This effect was first proposed by S. Gaillard, the author of this thesis and others [21] and is described in detail in [32]. A thorough analysis suggests that the achievable ion energies can exceed those of flat foils by several times, depending on the specific laser parameters. The use of FTC has already produced record breaking energetic protons of more than 67 MeV.

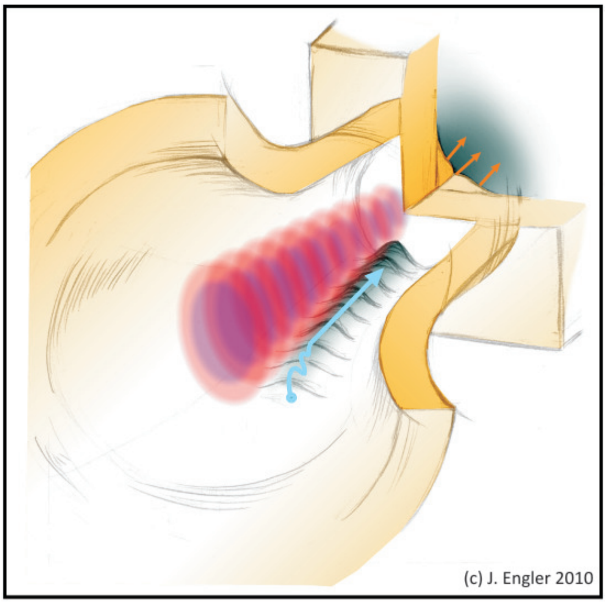

Figure 1.5: Artist's impression of laser-cone interaction (by J. Engler). Details in Sec. 4.3.2.

Chapter 2

Theoretical Background

This chapter is intended to give a short introduction to the most important aspects of high intensity short pulse laser interactions with matter and present basic concepts of laser-driven ion acceleration. More details on those topics can be found in the existing literature, e.g. in the books written by P. Gibbon [26], P. Mulser [27] or W. L. Kruer [33].

2.1 Units

Throughout this thesis, dimensionless units will be used. It is convenient to set the electron mass m_e, vacuum speed of light c the laser light angular frequency ω_0 and the elementary charge e to unity, $m_e = c = \omega_0 = e = 1$. Normalized quantities for the electric field $\boldsymbol{a}$, magnetic field $\boldsymbol{b}$, force $\boldsymbol{f}$, time t, length x and density n then follow from their counterparts $\boldsymbol{E}$, $\boldsymbol{B}$, $\boldsymbol{F}$, $\tilde{t}$, $\tilde{x}$ and $\tilde{n}$ in Si units

$$\boxed{\begin{array}{lll} \boldsymbol{a} = \dfrac{e\boldsymbol{E}}{m_\mathrm{e} c \omega_0} & \boldsymbol{b} = \dfrac{e\boldsymbol{B}}{m_\mathrm{e} \omega_0} & \boldsymbol{f} = \dfrac{\boldsymbol{F}}{m_\mathrm{e} c \omega_0} \\ t = \omega_0 \tilde{t} & x = \dfrac{\omega_0}{c} \tilde{x} & n = \dfrac{\tilde{n}}{n_c}. \end{array}}$$

The critical density n_c is defined by $n_c \equiv m_e \varepsilon_0 \omega_0^2 e^{-2}$ and equals one in the unit system defined above. When the plasma electron density equals the critical density, the plasma frequency $\omega_p = (e n_e / m_e \varepsilon_0)^{1/2}$ equals the laser light frequency ω_0, i.e. the laser light cannot propagate in the plasma for electron densities $n_e > 1$. For the sake of completeness, it follows from the above that the field strength amplitude a_0 of an electromagnetic wave with intensity I (given in Si units) can be calculated to be

$$\mathrm{a}_0 = \frac{e}{2\pi \mathrm{m}_e \mathrm{c}^2} \sqrt{\frac{2\mathrm{I}\lambda^2}{P \varepsilon_0 \mathrm{c}}} = \sqrt{\frac{2\mathrm{I}}{P \mathrm{n_c} \mathrm{m_e} c^3}} \tag{2.1}$$

where $P = 1$ for a linear polarized wave (LP) and $P = 2$ for a circular polarized wave (CP). $\mathrm{a}_0 = 1$ then corresponds to the intensity at which a free electron would acquire a kinetic energy of up to half its rest mass during one laser cycle (see Sec. 2.2.2), i.e. where the plasma electrons start to move relativistically.

2.2 Relativistic Electron Dynamics

2.2.1 Ionization

The interaction of intense laser fields with matter primarily deals with the interaction with ionized matter. The high electromagnetic fields cause any material to quickly ionize, so one primarily has to deal with plasmas while the material properties, besides density and atomic mass, are of minor importance.

From Bohr's model [34] a crude estimate of the laser strength at which ionization occurs can be derived. In the case of classical above barrier ionization (or barrier suppression ionization, BSI), for hydrogen-like atoms the ionization potential for the resulting charge state Z is given in dimensionless units by

$$\varepsilon_{Z,\kappa} = -\frac{1}{2}\left(\frac{\xi}{\hbar}\frac{Z}{\kappa}\right)^2 \tag{2.2}$$

where $\xi = e^2/(2\varepsilon_0\lambda m_e c^2)$ (for $\lambda = 1\,\mu\mathrm{m}$ it is $\xi \cong 1.771 \cdot 10^{-8}$), $\hbar$ is the reduced Plank's constant (for $\lambda = 1\,\mu\mathrm{m}$ it is $\hbar = 2.426 \cdot 10^{-6}$and κ is the effective main quantum number corresponding to the outermost electron in the charge state $Z + 1$. Assuming rotational symmetry[1], the total potential of the atom and the external field (that here is assumed to be static, which is possible when the individual ionization process happens fast compared to half a laser period (or $\varepsilon_{Z,\kappa} \gg \hbar\omega_0$), as it is usually for optical frequencies) reads

$$V = -\xi\frac{Z}{r} + a_0 r \tag{2.3}$$

which has a maximum at $r = -\sqrt{Z\xi/a_0}$ of $V_{max} = -2\sqrt{Z\xi a_0}$. Above barrier ionization then occurs when $\varepsilon_{Z,\kappa} \leq V_{max}$ so that ionization occurs for $a_0 \geq a_{Z,\kappa}$ where

$$a_{Z,\kappa} = \frac{1}{4\xi}\frac{\varepsilon^2_{z,\kappa}}{Z} = \frac{\xi^3}{16\hbar^4}\frac{Z^3}{\kappa^4} \tag{2.4}$$

---

[1] While this is a good approximation for many heavy ions, it is not true for a Hydrogen atom.

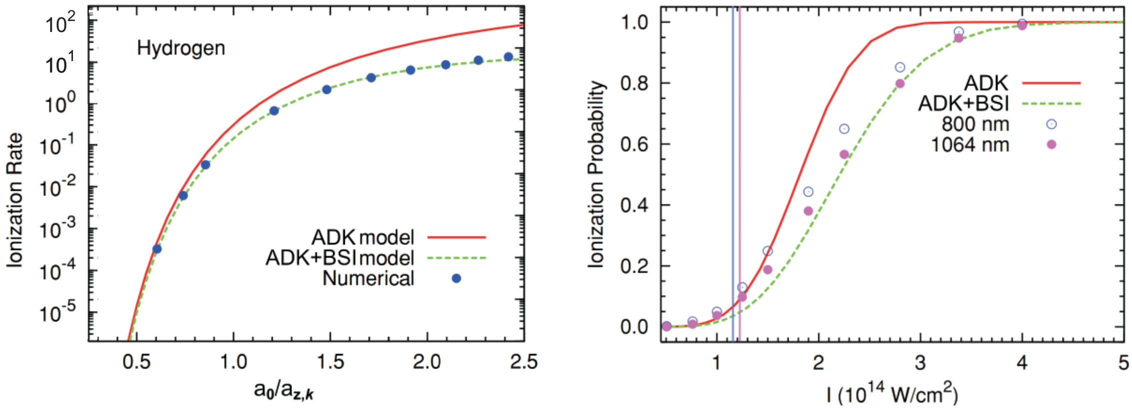

Figure 2.1: (a) Ionization rate for hydrogen-like atoms and (b) the resulting ionization degree after a laser pulse with $\tau = 47$, from [38]. Vertical lines mark intensity where $a_0 = a_{Z,k}$.

and for $\lambda = 1\,\mu\text{m}$

$$\boxed{a_{Z,\kappa} \approx 0.01\frac{Z^3}{\kappa^2}} \tag{2.5}$$

For hydrogen this equation underestimates the critical field by a factor of approximately 2 due to the violation of rotational symmetry. For hydrogen in the ground state the field strength for which over the barrier ionization starts to occur is $\mathrm{a}_{1,1} \approx 0.024$. In atoms possessing many electrons this asymmetry is broken and the respective critical field approaches that given by Eqn. (2.5). Clearly, relativistic laser strengths $\mathrm{a}_0 > 1$ as used in laser-ion acceleration experiments and as dealt with in the framework of this thesis by far exceed the critical field value for hydrogen ionization and for ultra-relativistic intensities with $\mathrm{a}_0 > 5$ even oxygen can be fully ionized.

The above simple estimate neglects effects such as multi-photon ionization or tunneling ionization [35, 36, 37] (TI), so one can expect ionization to occur at even lower intensities. Since the laser pulse peak is usually preceded by a comparably long low intensity tail (Gaussian tail, amplified spontaneous emission or prepulses), the ionization dynamics is consequently rather determined by the tunneling rate (ADK theory by Ammosov, Delone and Krainov [39]). An empiric formula for the ionization rate valid from TI to BSI was given by [38] (see Fig. 2.1). For example, assuming during the phase of amplified spontaneous emission (ASE) an intensity in the order of $5 \cdot 10^{17}\,\text{W/cm}^2$ ($a_0 \cong 0.64$ at $\lambda = 1\,\mu\text{m}$), the ionization rate of the often used aluminum to Al^{4+} (ionization potential 117.9 eV, $a_{4,1} = 0.64$) is approximately $0.04\,\text{fs}^{-1}$, hence after $2\,\text{ps}$ about 90% of Al will be 4-fold ionized.

For all the following it can therefore be assumed that the main laser pulse interacts with a pre-ionized plasma and the ionization process occurs before the main pulse, e.g. due to prepulses or ASE, or early during the rising edge.

2.2.2 Single electron dynamics in vacuum

The dynamics of a single electron in vacuum, neglecting laser absorption and radiation effects caused by the moving electron, are described by the Lorentz equation [40]

$$\frac{d\boldsymbol{p}(t)}{dt} = -\boldsymbol{a}(t) - \boldsymbol{\beta}(t) \times \boldsymbol{b}(t). \tag{2.6}$$

For a plane wave propagating in z-direction and linearly polarized in x-direction, $\boldsymbol{a}(z(t), t) = a_0 \cos \varphi(z(t), t)\boldsymbol{e}_x$ and $\boldsymbol{b}(z(t), t) = a(z(t), t)\boldsymbol{e}_y$ with the laser phase $\varphi(z(t), t) = t - z(t)$, the electron motion is given by a constant drift in longitudinal direction and a quiver motion in the laser polarization direction, superimposed with a longitudinal quiver motion. It can simply be derived from the Lagrange density [41]

$$\mathfrak{L} = -\gamma^{-1}(\beta(t)) - \boldsymbol{\beta}(t)\boldsymbol{A}(z(t), t) + \Phi(z(t), t) \tag{2.7}$$

(where, imposing the Coulomb gauge, $\boldsymbol{A} = -\boldsymbol{e}_x a_0 \sin \varphi(z(t), t)$ is the magnetic vector potential and $\Phi = 0$ is the scalar potential) and Hamilton's principle

$$\frac{d}{dt}\frac{\partial \mathfrak{L}}{\partial \beta_i} - \frac{\partial \mathfrak{L}}{\partial x_i} = 0. \tag{2.8}$$

Here,

$$\gamma = \sqrt{1 + \boldsymbol{p}^2} = \left(1 - \beta^2\right)^{-1/2} \tag{2.9}$$

is the relativistic Lorentz factor. The temporal evolution of the transverse momentum of an electron initially at rest at $t = t_0$, $z(t_0) = 0$ then reads

$$p_x\left(t\right) = -a_0\left[\sin \varphi(z(t), t) - \sin \varphi_0\right], \tag{2.10}$$

reflecting the conservation of the transverse canonical momentum $p_x^{kan}(t) = p_x(t) - A_x(t)$,

$$\boxed{p_x^{kan}(t) = const.} \tag{2.11}$$

Another constant of motion can be found from the temporal derivation of (2.9)

$$\begin{aligned}\frac{d\gamma}{dt} &= \frac{1}{\gamma}\left(p_x\dot{p_x} + p_z\dot{p_z}\right)\\ &= -\beta_x a\\ &= \frac{dp_z}{dt}\end{aligned} \tag{2.12}$$

where it was used $dp_x/dt = a\,(\beta_z - 1)$ and $dp_z/dt = -\beta_x a$ from Eqn. (2.6). For the longitudinal momentum one then finds the invariant

$$\boxed{\gamma - p_z = const.} \tag{2.13}$$

For an electron initially at rest, this leads with (2.9) to

$$\boxed{p_z = p_x^2/2} \tag{2.14}$$

and with (2.10) one obtains the explicit result

$$p_z = p_x^2/2 = \frac{a_0^2}{2}\left(\sin^2\varphi - 2a_0^2\sin\varphi\sin\varphi_0 + \sin^2\varphi_0\right) \tag{2.15}$$

which exhibits an oscillatory and a non-oscillatory component. For $\boldsymbol{A}(\varphi_0) = 0$, which is true for example in the important case of a laser pulse and an electron initially at rest at t_0 before the pulse is ramping up, Eqn. (2.10), (2.13) and (2.15) simplify to

$$\boxed{\begin{aligned}p_x &= -a_0\sin\varphi\\ p_z &= \frac{a_0^2}{2}\sin^2\varphi\\ \gamma &= 1 + p_z = 1 + \frac{p_x^2}{2}.\end{aligned}} \tag{2.16}$$

It is now straight forward to integrate the equations of motion (EOM) to obtain the electron trajectory. Figure 2.2 shows the momenta, velocities and trajectories for $\varphi_0 = 0$. In that case, the electron motion is the superposition of the famous figure-eight motion of the

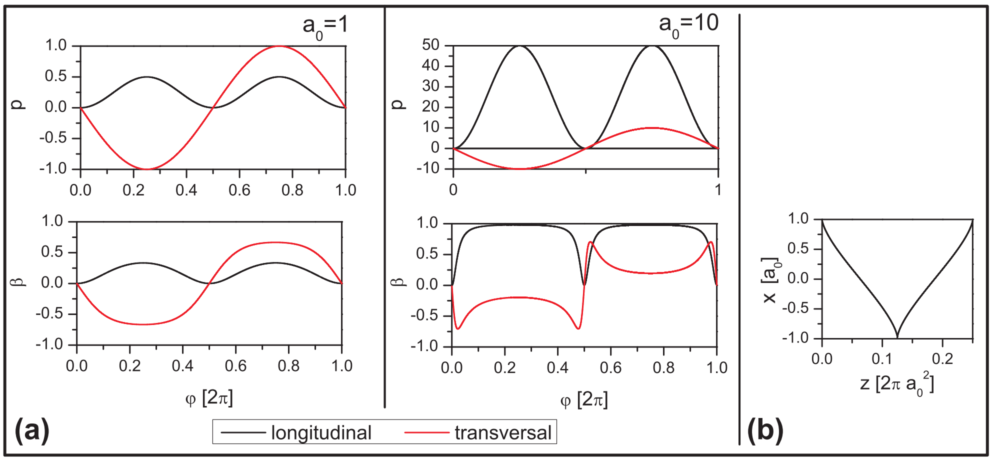

Figure 2.2: Trajectories of a free electron in a plane electromagnetic wave (a) in momentum-phase space (top) and velocity-phase space (bottom) for the longitudinal (transverse) components p_z, β_z (p_x, β_x) given by the black (red) lines, and (b) in real space. The electron is assumed to be at rest at $\varphi_0 = 0$ and the absolute value of the vector potential to be $A(\varphi_0) = 0$. This corresponds to the situation of an electron in a laser pulse ramped up adiabatically.

electron [42] and a longitudinal drift with constant velocity of

$$\boxed{\beta_{\text{drift}} = \frac{a_0^2}{4 + a_0^2},} \tag{2.17}$$

in the small field limit $a_0 \ll 1$ [43]. This expression is also exact relativistically as can be seen from $\beta_z = p_z/\gamma = (\gamma - 1)/\gamma = 1 - 1/\gamma$ where Eqn. (2.13) was used. From the definition of φ and (2.13) it also follows $d\varphi/dt = \gamma^{-1}$ and therefore

$$\left\langle \frac{1}{\gamma} \right\rangle_t = \frac{1}{\langle \gamma \rangle_\varphi}.$$

It then readily follows with (2.16)

$$\boxed{\begin{aligned} \beta_{\text{drift}} &= \langle \beta_z \rangle_t = 1 - \left\langle \frac{1}{\gamma} \right\rangle_t = 1 - \frac{1}{\langle \gamma \rangle_\varphi} \\ &= \frac{a_0^2}{4 + a_0^2}. \end{aligned}} \tag{2.18}$$

which is the same as Eqn. (2.17).

The resultant trajectory is a zig-zag motion in the laboratory frame with an amplitude of [42]

$$\boxed{\begin{aligned}\hat{x} =& a_0 \qquad (2.19)\\ \hat{z} =& \pi a_0^2/2 \qquad (2.20)\end{aligned}}$$

and a total energy of

$$\gamma = 1 + \frac{a_0^2 \sin^2 \varphi(t)}{2}. \tag{2.21}$$

For sub-relativistic laser intensities, i.e. $\mathrm{a}_0 \ll 1$ and $\beta \ll 1$, the electron motion can be approximately described solely by its motion in a plane transversal to the direction of propagation since the magnetic forces are weak. In this case the total energy is given simply by $\gamma \cong \sqrt{1+p_x^2} = \sqrt{1+a_0^2 \sin^2 t}$.

An important quantity in the field of laser particle acceleration physics is the *ponderomotive potential*, γ_p, which is often used as a measure of the electron temperature of the laser heated plasma. In the non-relativistic case the force

$$\boldsymbol{F}_p^N = -\boldsymbol{\nabla}\gamma_p \tag{2.22}$$

is called the *ponderomotive force* and is defined as the cycle averaged force on an electron in a laser pulse with a spatially and temporally slowly varying envelope $a_0 = a_0(t,z)$. The ponderomotive potential γ_p is the cycle averaged quiver energy of an electron initially at rest [44]. In the non-relativistic case the ponderomotive force is given by

$$\boldsymbol{F}_p^N(t,z) = -\frac{1}{4}\boldsymbol{\nabla}\left(a_0(t,z)^2\right), \tag{2.23}$$

and hence the non-relativistic ponderomotive potential reads

$$\gamma_p^N(t,z) = \frac{a_0(t,z)^2}{4}. \tag{2.24}$$

For a relativistically moving electron in a plane wave, the quiver energy can be derived simply by separating the average of the total energy (Eqn. (2.21)) into the energy of the constant drift $\gamma_{drift} = \left(1-\beta_{drift}^2\right)^{-1/2}$ and the average quiver energy in the center-of-mass frame (figure-eight). The phase averaged quiver energy, often referred to as the effective mass $m_{eff}(t,z) \equiv \left\langle \gamma_{oc}(t,z) \right\rangle_\varphi$ [27], then is

$$\boxed{\begin{aligned} m_{eff}(t,z) &= \frac{\left\langle \gamma(t,z) \right\rangle_\varphi}{\gamma_{drift}} \\ m_{eff}(t,z) &= \left(1 + \frac{a_0(t,z)^2}{2}\right)^{1/2} . \end{aligned}} \tag{2.25}$$

For small a_0 one recovers the non-relativistic expression (2.24). This justifies to call $m_{eff}(t,z) = \gamma_p$ the *relativistic ponderomotive potential*[2] so that analogous to the definition (2.22) the relativistic ponderomotive force in the co-moving frame can be defined as $\boldsymbol{F}_p = -\boldsymbol{\nabla} m_{eff}$. A transformation of this force into the laboratory frame can be found for example in [27, 41], in the non-relativistic case the ponderomotive force acts simply along the gradient of the envelope of the intensity of the laser pulse. While a passing pulse can deflect the electron trajectory, it does not change its energy, since the energy change during the rising pulse is exactly compensated by the falling intensity gradient behind the pulse maximum. Only when the electron is created in (e.g ionization) or extracted from (e.g. escape into an overdense plasma) the pulse during the irradiation, a net energy transfer can occur.

Because in the community of laser-ion acceleration some confusion is present about the question of applicability of Eqn. (2.25), it is worth noting that the ponderomotive potential γ_p gives the total kinetic energy only in the case of a *free single electron* in an electromagnetic wave, initially at rest, as it was introduced here. Even though in the case of an electron at the *surface of a solid* an expression for the electron energy with a structure similar to the explicit form (2.25) of the ponderomotive energy of a free electron can be derived (see Sec. 2.2.4), it there may not be confused with the expression given here.

2.2.3 Single electron dynamics at the surface of a solid

So far, only single free electrons have been considered in the interaction with the laser field. In the presence of a plasma additional forces arise through the interaction with other electrons and ions. Since the ion mass m_i is more than three orders of magnitude greater than the electron mass, the most significant interactions will be primarily between the laser fields and the electrons up to laser strengths of $a_0 \gg m_i/m_e$, while in many cases the ions may be assumed to be immobile or extremely sub-relativistic during the ultra-short laser

---

[2] Note that usually the term *ponderomotive energy* refers to the kinetic energy $m_{eff} - 1$ only.

pulse duration.

For a laser beam propagating in a cold, collisionless plasma with electron density $n_{e,0}$ the dispersion relation for electromagnetic waves reads [45]

$$\omega_p^2 = 1 - k^2 \tag{2.26}$$

where the electron plasma frequency ω_p is defined by

$$\omega_p = \sqrt{n_{e,0}}. \tag{2.27}$$

If the electrons under consideration have relativistic kinetic energy, the plasma frequency changes due to the relativistic mass increase,

$$\omega_p = \sqrt{\frac{n_e^{hot}}{\bar{\gamma}}}. \tag{2.28}$$

Here $\bar{\gamma}$ is the average energy of the hot electrons. The kinetic energy distribution in most practical situations of an LP laser interacting with matter is given by an exponentially decreasing function with increasing energy as seen both in experiments and PIC simulations [46, 47, 48, 49, 50, 29] and hence the *average* kinetic energy of hot electrons is commonly identified with the scale length of the distribution and referred to as the hot electron temperature $T_e^{hot} \equiv \bar{\gamma} - 1$.

The exact theoretical determination of the correct electron average kinetic energy accelerated by the intense fields of the laser is one of the most important and yet controversial physics issues in short-pulse laser-solid interaction [49, 51, 52, 53, 26]. Phenomenologically, even though the experimentally available data is biased by large scatter, for $a_0 \ll 1$ the experimentally observed electron temperatures suggest that they follow the ponderomotive scaling (2.25) [54, 55, 56, 57, 47], while for $a_0 \gg 1$ experimental results suggest a significantly weaker scaling [55, 57] (see Fig. 2.3). There the data fits better to the empirical scaling law of Beg et al. [56]

$$T_e \cong 0.47 a_0^{2/3}. \tag{2.29}$$

The exact description of the hot electron temperature in a laser heated plasma is of crucial importance for laser ion acceleration, since together with the number of accelerated electrons it determines the final ion maximum energy and hence represents a very valuable parameter

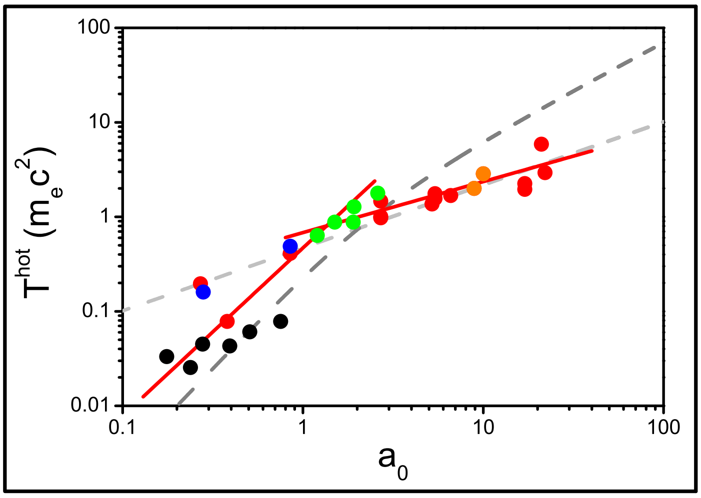

Figure 2.3: Measurements of the hot electron temperature (selected data; extracted from [47] (green), [54] (black), [55] (red), [56] (blue), [57] (orange)). The red lines show the best fit with a power law for data with $a_0 < 1$ and $a_0 > 1$, respectively. For comparison, model predictions are shown for the ponderomotive scaling (2.25) (dark gray dashed line) and Beg's empirical scaling law (2.29) (light gray dashed line). Though experimental data scatters significantly, for small a_0 the data apparently fits the ponderomotive scaling well, while for $a_0 > 1$ measurements fall short of ponderomotively predicted temperatures and fit better the $a_0^{2/3}$ scaling.

to optimize the ion acceleration, as will be explained later in Sec. 2.3.1. Furthermore, the experimental measurement of the absolute temperature, the temperature temporal evolution, the temperature scaling with intensity or the spatial distribution of hot electrons offers valuable insight in the interaction physics and comparison to theoretic predictions. It is one main topic of this thesis to study possibilities to increase and optimize the electron temperature and to optimize the temporal temperature evolution during the laser pulse interaction in order to increase the achievable ion energy.

The laser light cannot penetrate the plasma when $\omega_p > 1 - \sin^2\alpha$, where α is the laser incidence angle with respect to the target normal, as can be seen from Maxwell's equations [58]. In the following the derivation [59] of this result will be shown, including the possibility to treat the general case of a finite preplasma with decreasing electron density and assuming the ions remain at rest due to their large rest mass. This allows later in Sec. 2.2.4.1 to analyze the plasma response in such a case around the critical density surface. In the following the fields will be written in complex notation for simplicity, e.g. $\boldsymbol{a} = \boldsymbol{a}_0 \{\exp[i(t-z)]\}$. The real fields as defined before are then simply recovered by taking the respective real part. The two Maxwell equations including time derivatives of the fields are then written as

$$\boldsymbol{\nabla} \times \boldsymbol{a} = -\partial_t \boldsymbol{b} = -i\boldsymbol{b} \tag{2.30}$$

$$\boldsymbol{\nabla} \times \boldsymbol{b} = \partial_t \boldsymbol{a} + \boldsymbol{j} \equiv i\boldsymbol{a} - n_e \boldsymbol{v} \equiv i\mathrm{n}^2 \boldsymbol{a} \tag{2.31}$$

where the RHS of Eqn. (2.31) defines the refractive index n. Combining the two equations one obtains

$$\boldsymbol{\nabla}\left(\boldsymbol{\nabla a}\right) - \nabla^2 \boldsymbol{a} = \mathrm{n}^2 \boldsymbol{a}. \tag{2.32}$$

The electron velocity $\boldsymbol{v}$ is given by the Lorentz equation and in the non-relativistic limit is simply $i\boldsymbol{a}$ (see Eqn. (2.16)) and relativistically in the first approximation $\boldsymbol{v} \approx i\boldsymbol{a}/\bar{\gamma}$. Consequently, the refractive index n as it was introduced in the RHS of Eqn. (2.31) reads

$$\mathrm{n} = \sqrt{1 - \frac{n_e}{T_e + 1}} = \sqrt{1 - \omega_p^2}. \tag{2.33}$$

For a laser polarized in the plane defined by the direction of laser propagation and the direction of the density gradient, the z-component of Eqn. (2.32) can be rewritten as

$$\left[k_x^2 - \left(1 - \omega_p^2\right)\right] a_z + ik_x \partial_z a_x = 0. \tag{2.34}$$

The term $ik_x\partial_z a_x$ can be evaluated taking the divergence of (2.31). It follows

$$\mathrm{n}^2 \boldsymbol{\nabla a} + \boldsymbol{a\nabla}\left(\mathrm{n}^2\right) = 0 \tag{2.35}$$

and thus

$$\boldsymbol{\nabla a} = -\boldsymbol{a\nabla}\left(\ln \mathrm{n}^2\right). \tag{2.36}$$

Taking the gradient of this equation, one obtains for the z-component

$$ik_x \partial_z a_x = -\partial_z\left[a_z \partial_z\left(\ln \mathrm{n}^2\right)\right] - \partial_z^2 a_z \tag{2.37}$$

so that (2.34) can be rewritten with $k_x = \sin\alpha$ and the definition (2.33) of the refractive index n

$$\partial_z^2 a_z + \left(\mathrm{n}^2 - \sin^2\alpha\right) a_z + \partial_z\left[a_z \partial_z\left(\ln \mathrm{n}^2\right)\right] = 0. \tag{2.38}$$

Following the path described in [59] and substituting $a_z = g \sin\alpha/\mathrm{n}$, Eqn. (2.38) can be written in the form

$$\partial_z^2 g + \mathrm{n}_{eff}^2 g = 0 \tag{2.39}$$

with

$$\boxed{\mathrm{n}_{eff} = \sqrt{1 - \omega_p^2 - \sin^2\alpha + \frac{\partial_z^2\left(\mathrm{n}^2\right)}{2\mathrm{n}^2} - \frac{3}{4}\left[\frac{\partial_z\left(\mathrm{n}^2\right)}{\mathrm{n}^4}\right]^2}.} \tag{2.40}$$

If the density gradient is small, so that it is close to a step function $n_e(z) = \Theta(z) n_{e,0}$, the first three terms dominate, $\mathrm{n}_{eff}^2 \cong 1 - \left(\omega_p^2 + \sin^2\alpha\right)\Theta(z)$. Then for $z > 0$ and $\omega_p^2 + \sin^2\alpha > 1$ it readily follows that the refractive index becomes imaginary and with Eqn. (2.39) one obtains for the electric field inside the plasma an evanescent wave, $a_z \propto \exp\left(-z\sqrt{\omega_p^2 + \sin^2\alpha - 1}\right)$ with an amplitude of $a_z(z = 0) = 2a_0 \frac{\sin\alpha}{\omega_p}$ [26]. In that case, there exists no solution for a traveling wave inside the plasma but rather the field penetrates the plasma surface as an evanescent, exponentially decreasing wave up to a scale length

$$\boxed{\delta = \frac{1}{i\mathrm{n}_{eff}} = \frac{1}{\sqrt{\omega_p^2 + \sin^2\alpha - 1}}} \tag{2.41}$$

which is called *collisionless skin depth* and when using the relativistic plasma frequency Eqn. (2.28) it is also referred to as the *relativistic collisionless skin depth*.

The electron density at which the plasma frequency equals the laser frequency is called the critical density which, including relativistic effects, is given by $n_c^R = T_e + 1$ or in SI units by

$$n_c^R \approx \left(T_e\left[m_e c^2\right] + 1\right)\left(\lambda_0\left[\mu\right]\right)^{-2} \cdot 1.1 \cdot 10^{21}\,\mathrm{cm}^{-3}. \tag{2.42}$$

This density marks the point at which the refractive index becomes zero and the transition from transparent to opaque occurs. Plasmas with density $n_e < n_c^R$ are referred to as *underdense plasmas* while when the density is overcritical, $n_e > n_c^R$, they are called *overdense plasma*.

2.2.4 Collisionless laser absorption mechanisms at solids

In the following section, a brief overview will be given over the most relevant collisionless laser absorption mechanisms for linearly polarized light. As will turn out, the $\boldsymbol{v} \times \boldsymbol{B}$ heating mechanism together with anharmonic resonance represents the most important mechanism in the parameter range under discussion in this thesis. Other models, such as anomalous skin layer absorption [60], stochastic heating [61] and Landau damping [62], have been elaborated but yield approximately an order of magnitude lower absorption efficiencies than the $\boldsymbol{v} \times \boldsymbol{B}$ heating mechanism [27].

2.2.4.1 Resonance absorption

For p-polarized light incident on a plasma slab with a density gradient of scale length L the incoming light is reflected at the critical surface ($n_e = n_c^R$). This density gradient can be due to an expansion of the plasma prior to the main pulse caused by ASE or prepulses. As described above, the laser can tunnel through this critical density surface up to a skin depth in an evanescent wave (Eqn. 2.41). There, normally acting forces[3] can resonantly drive a Langmuir plasma wave [63] which grows over a number of periods until it is damped [64]. The excited plasma wave travels down the density gradient and thus its energy is not converted back into electromagnetic field energy and consequently is absorbed by the plasma. For relativistic intensities the $\boldsymbol{v} \times \boldsymbol{B}$ force becomes important and the eigenfrequency of a volume element becomes a function of the oscillation amplitude. The resulting anharmonic resonance for sufficiently intense laser pulses is described in Sec. 2.2.4.4.

Resonance absorption for a sub-relativistic electromagnetic wave must be treated in two steps. First, the occurrence of a resonance of the electric field component along the density gradient can be derived from the solution of Maxwell's equations. Denisov [65] gave an approximate solution for the case of small gradient scale lengths. White and Chen have then shown the existence of a singularity of the electric field at the critical density for the example of a linear density gradient but without loss of generality [59]. The discussion extends the considerations of the last section following Eqn. (2.40). In realistic cases the plasma boundary cannot simply be described by a step-function, but rather an expansion due to ASE or prepulses prior to the main pulse has to be considered. Assuming a linear density gradient $n_e = 1 + L \cdot z$ with scale length L around the critical density surface at

---

[3] In the non-relativistic limit, which is usually assumed in the derivation of resonance absorption, such a normal force component is naturally present by normal components of the electric field for an oblique laser incidence only, while for relativistic intensities the $\boldsymbol{v} \times \boldsymbol{B}$ force adds a normal force also for normal incidence.

$z = 0$, it is $\mathrm{n}^2 = -L \cdot z$. Then for small values of z, $z \ll L$ – corresponding to the condition $a_0 \ll L$–, the last two terms in (2.40) dominate. In this region one readily obtains

$$\mathrm{n}_{eff} \cong i\sqrt{\frac{3}{4z^2}} \tag{2.43}$$

so that with (2.39) it is

$$\partial_z^2 g \propto z^{-2} g. \tag{2.44}$$

The solution of this differential equation is $g \propto z^{-1/2}$ and therefore $a_z \propto \sin\alpha/z$. This demonstrates the resonant behavior of the longitudinal electric field around the critical density surface at $z = 0$. Fig. 2.5(a) shows schematically the longitudinal field structure. The physical reason for the resonance is that the laser field at the critical density surface has the same frequency as the plasma oscillations, so the laser can excite resonantly a Langmuir wave.

The second aspect when treating resonance absorption is the question of how the energy is actually absorbed into the plasma. In the neighborhood of the critical density the effective refractive index is imaginary and diverging for $z \to 0$, suggesting a strong absorption of the laser power. Though the singularity is avoided by non-linear effects, at low temperatures and flat density gradients the conversion efficiency can reach up to 50% for an optimum laser incidence angle α (Fig. 2.5(b)) and at steep plasma gradients and relativistic temperatures the conversion rate can even reach up to 100% [67]. Electron heating can happen through various mechanisms, e.g. oscillation down the field gradient, collisions or Landau damping. While the mechanism does not affect the total absorbed energy, it may strongly determine the distribution of electrons in the energy and phase space. At relativistic laser intensities as is dealt with in this thesis, the Langmuir wave becomes aperiodic and wave-breaking

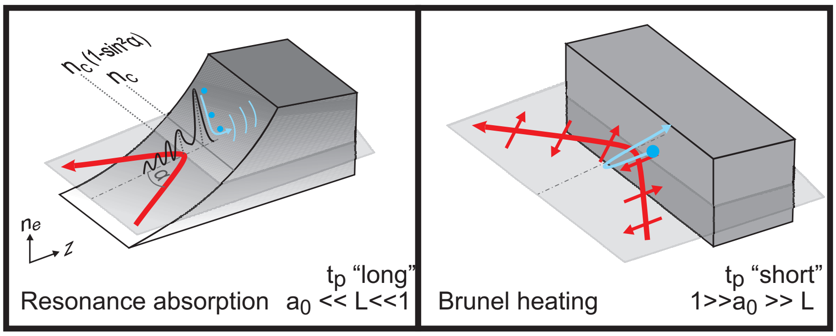

Figure 2.4: Schematic drawings of selected electron acceleration and plasma heating processes in laser interaction with solids. blue: electrons, gray: plasma (in second panel from right: magnetic field strength), red: laser (small arrows indicating polarization). Details see main text.

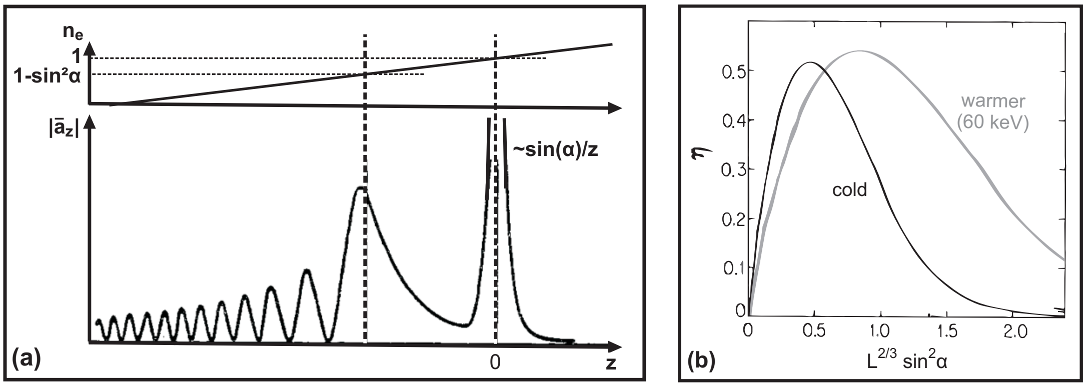

Figure 2.5: (a) Resonant increase of electric field strength at the critical density surface $n_e = 1$ for a linear density gradient. Behind $n_e = 1 - sin^2\alpha$ the electromagnetic wave decays in an evanescent wave that sharply increases at $n_e = 1$. (b) Laser absorption η for resonance absorption of non-relativistic laser pulses. Data extracted from [66] (black line) and [27] (gray line).

occurs. Electrons can be trapped and accelerated to high energies with a Maxwellian energy distribution [68]. For the resultant average energy T_e^{hot} in the long pulse regime (several ps to ns), most authors agree on a a_0^{ς} dependence with values for ς around $1/3$ [27]. According to [69] T_e^{hot} scales as

$$T_e^{hot} \cong 72 T_e^c a_0^{2/3} \tag{2.45}$$

where T_e^c is the temperature of the background electrons at the critical density. Eqn. (2.45) predicts the same scaling as was given by Beg et al. 1997 empirically (see Eqn. (2.29)) and quantitatively agrees with it for $T_e^c = 6.5 \times 10^{-3}$, strongly suggesting that the dominant absorption process there could have been resonance absorption. However, one has to be cautious in interpreting and extrapolating those experimental results since they are a based only on a fit in a relatively narrow range of barely relativistic laser intensities around $a_0 = 1$;

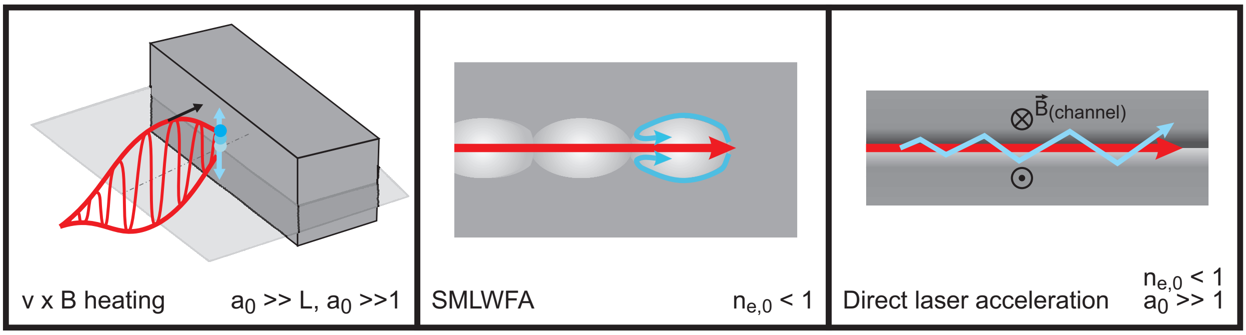

and the pulse duration was in the ps range[4]. Moreover, as will be derived in Sec. 4.1, a similar scaling can be derived for $\boldsymbol{v} \times \boldsymbol{B}$ heating when taking into account a non-ergodic behavior of the electrons. The resonance absorption mechanism is expected to cease to be functional as soon as the electron oscillation amplitude (2.20) exceeds the density scale length [70]. Hence, for $a_0 \geq L$ other absorption mechanisms become important, which usually is assumed to be the case in all high-power short-pulse laser-ion acceleration experiments with solids. Still the occurrence of resonant behavior still is important as will be explained in Sec. 2.2.4.4

2.2.4.2 Brunel heating or vacuum heating

Brunel heating was first mentioned by Brunel in 1988 [70], recognizing the role of collective electrostatic effects. When the plasma boundary is steep enough ($L \leq a_0$), the electric field

---

[4] It has been suggested, that a scaling

$$T_e^{hot} = \sqrt{1 + 2^{1/2} a_0} - 1 \tag{2.46}$$

similar to (2.29) arises simply assuming energy and momentum flux conservation over one laser period

$$\begin{aligned} a_0^2/2 &= n_e^{hot}(\gamma - 1)\beta_z \\ a_0^2/2 &= n_e^{hot} p_z \beta_z \\ \Rightarrow \gamma - 1 &= p_z \end{aligned} \tag{2.47}$$

i.e. without any further assumption on the specific electron absorption mechanism [53]. Then, the observed scaling could not be used as a proof of resonance absorption. However, the reasoning presented in [53] lacks justification in two crucial aspects. First, it has to be assumed that $n_e^{hot} = \gamma n_c$ in order to connect p_z and a_0 with the help of the conservation laws to give

$$p_z = \frac{a_0}{\sqrt{2}}. \tag{2.48}$$

This choice can not be justified with basic arguments and the result contradicts (2.16).
Secondly, and even more importantly, all quantities in (2.47) are cycle averaged quantities, $\langle n_e^{hot} \rangle_t$, $\langle p_z \rangle_t$, $\langle \beta_z \rangle_t$, $\langle \gamma \rangle_t$. When in Eqn. 8 in [53] it is used $\gamma_0^2 = \gamma^2 - p_z^2$ for the transverse quiver energy γ_0 in the frame co-moving with the electron beam (later, $\gamma_0 - 1$ is identified with the temperature T_e^{hot}), one has to take great care of averaging. For one, since all quantities are averaged quantities and the longitudinal quiver motion has been averaged, consequently γ_0 would contain only energy due to transverse motion. It is not clear however, why the longitudinal (quiver) motion should be disregarded. Moreover, writing Eqn. 8 more carefully, it should read $\langle \gamma_0^2 \rangle_t = \langle \gamma^2 \rangle_t - \langle p_z^2 \rangle_t$. However, neither can $\langle \gamma^2 \rangle_t$ be identified with $\langle \gamma \rangle_t^2 = (1 + \langle p_z \rangle_t)^2$, nor is $\langle \gamma_0 \rangle_t = \sqrt{\langle \gamma_0^2 \rangle_t}$ as was used in (2.47).
The physical argument given in [53] for the reduced temperature scaling is the fact that for an electron to obtain the full ponderomotive (=quiver) energy it would take a distance much longer than the skin length in a solid. While this is certainly true considering the free electron motion, it is not true for electrons confined to the surface of a solid, since the transverse canonical momentum is invariant (see Sec. 2.2.4.3 and 4.1.2).
For the reasons given, the applicability of (2.46) remains questionable and an alternative approach of explaining the experimental observations will be given in this thesis.

component of p-polarized light incident obliquely can extract electrons from the solid surface into vacuum. As the electric field changes its direction, it pushes the electrons back into the overcritical surface, where they can travel virtually as free electrons since the laser cannot penetrate the overcritical region beyond the skin length.

The theoretical description of the vacuum heating mechanism is based on a simple capacitor model in which the normal electric field component drives the charge separation and the longitudinal forces ($\boldsymbol{v} \times \boldsymbol{B}$ forces, see next paragraph) are neglected [70, 71, 26]. For infinitely sharp gradients, a maximum laser absorption is expected at an incident angle of 90°, decreasing to approximately 73° for $a_0 \gg 1$. For finite density scale lengths, a complex transition between Resonance absorption and Brunel heating is observed in simulations [26]. A more precise description must take into account the DC currents along the target surface created by the parallel electric field component of the oblique incoming light, which give rise to additional magnetic fields [72, 73, 74, 75]. Independently, at high intensities the longitudinal $\boldsymbol{v} \times \boldsymbol{B}$ forces may not be neglected any more.

2.2.4.3 $\boldsymbol{v} \times \boldsymbol{B}$ heating or ponderomotive acceleration in a skin layer

This mechanism was originally pointed out by [76]. It is very similar to the before mentioned Brunel-heating in that the laser directly accelerates electrons at a steep density gradient. Here, however, the $\boldsymbol{v} \times \boldsymbol{B}$ forces are not neglected – the Brunel-heating could be treated as the non-relativistic limit of $\boldsymbol{v} \times \boldsymbol{B}$ heating. While in the case of Brunel heating the electrons are pushed into the solid parallel to the polarization of the electric field and in resonance absorption electrons are ejected into the target normal direction, in the case of relativistic laser intensity or large preplasma scale lengths the electrons are primarily pushed into the solid in the direction of the laser axis [77]. Another clear indication for $\boldsymbol{v} \times \boldsymbol{B}$ heating is the appearance of electron bunches at $2\omega_0$ while for Brunel heating or resonance absorption one expects bunches separated by $1\omega_0$ [78].

At a steep density gradient at the interface between vacuum and solid ($n_{e,0} \gg \gamma$, $L \ll a_0$), the situation remains to be simple since the plasma can build up a bipolar electric field $\boldsymbol{a}_b$, balancing the longitudinal $\boldsymbol{v} \times \boldsymbol{B}$ forces (see Sec. 2.2.3), so that $\boldsymbol{a}_b \cong -\boldsymbol{\nabla}\gamma$ at all times. The EOM of the plasma then reads [79]

$$\frac{\partial}{\partial t}(\boldsymbol{p} - \boldsymbol{A}) - \boldsymbol{\beta} \times [\boldsymbol{\nabla} \times (\boldsymbol{p} - \boldsymbol{A})] = \boldsymbol{\nabla}(\Phi - \gamma)\,. \tag{2.49}$$

One trivial solution is hence given by $\boldsymbol{p} = p_x \boldsymbol{e}_x = A_x \boldsymbol{e}_x$ if $\boldsymbol{\nabla}(\Phi - \gamma) = 0$, reflecting again the conservation of transverse canonical momentum. For relativistic intensities, the $\boldsymbol{v} \times \boldsymbol{B}$ force, acting at twice the laser frequency, translates this transverse motion into longitudinal energy which then is absorbed by the plasma. This absorption mechanism therefore is efficient also for normally incident laser light, in contrast to the Brunel-heating. The time averaged total electron energy in this case is given by

$$\boxed{\langle\gamma\rangle_t = \left\langle\sqrt{1+p_x^2}\right\rangle_t .} \tag{2.50}$$

For $a_0 \ll 1$, this can be approximated by

$$\langle\gamma\rangle_t \cong \sqrt{1+\langle p_x^2\rangle_t} = \sqrt{1+a_0^2/2} \tag{2.51}$$

which is the same expression as the ponderomotive energy[5] (2.25): For non-relativistic intensities, the ponderomotive energy and the average quiver energy are equal.

This has been the cause of some confusion in the community of laser-electron acceleration. While Eqn. (2.25) is valid only for a single *free* electron in the EM wave, Eqn. (2.50) is the correct expression for a single electron at an infinitely steep solid density gradient. It is relativistically correct for arbitrary a_0 as long as the plasma frequency remains much larger than the laser frequency. Consequently, (2.50) should be used in the case of laser-solid interaction rather than the ponderomotive energy. The derivation of the important explicit result for $a_0 \geq 1$ will be one subject of this thesis in Sec. 4.1.2. There, necessary modifications for finite density scale lengths, as for example in the presence of prepulses or ASE, will be also discussed.

2.2.4.4 Anharmonic resonance

Only recently it was discovered that the process of energy transfer must be a resonant process. This can be found from very basic principles, namely that the process should act prompt, i.e. energy transfer to a single electron must happen within a few laser cycles, and must be capable of producing fast electrons in the Maxwellian tail of the electron

---

[5] On the right hand side of Eqn. 2.51 any possible reflected wave was neglected. This simplification is valid e.g. for high absorption and/or transmission. Otherwise a_0 must be replaced by the superposition of incoming and reflected light at the surface which for full reflection reads $a_0' = 2\frac{a_0}{\sqrt{\omega_p^2+1}}$

energy distribution, exceeding many times the average energy that was described in the last paragraph. Under the assumption that in collisionless laser absorption one single physical effect dominates it follows that this can only be resonance in the collective plasma potential, for no other physical effect than resonance is known capable of exciting electrons well beyond the quiver energy during few field oscillations [80].

When the laser impinges on the target, electrons at the target front surface start to oscillate transversely in the laser electric field and longitudinal by the magnetic field, as described in the previous section. In the longitudinal direction, in a simple nonrelativistic plane capacitor model the resting ions give rise to a restoring force

$$F_R = -\omega_p^2 \frac{d}{2} \frac{z}{|z|} \tag{2.52}$$

on the electrons, independent of the elongation. The resulting EOM reads

$$\ddot{z} - F_R = F_L \tag{2.53}$$

where F_L is the harmonic laser force with frequency $2\omega_0$. This resembles an anharmonic oscillator with an eigenfrequency depending on the excitation level,

$$\omega_{osc} = \frac{\pi}{4} \left(\omega_p^2 d\right)^{1/2} / z_0 \tag{2.54}$$

where z_0 is the oscillation amplitude [27]. For small excitations, the elongation from the critical density interface is small and hence $\omega_{osc} \gg 2\omega_0$, hence the electrons follow the laser field slowly gaining energy adiabatically. When the elongation becomes larger, the eigenfrequency reduces $\omega_{osc} \rightarrow 0$. When $\omega_{osc} \approx 2\omega_0$, resonance will occur accompanied by a high energy gain and a phase shift. This was first described by Mulser et al. [80] and it was shown numerically that each electron that gains significant energy during the laser interaction has gone through resonance before. The resonance causes a disruption of the electron trajectory which then leaves the laser interaction region and is injected into the plasma bulk. Therefore the electron does not transfer the energy back to the electromagnetic field after the resonance and disruption, breaking the adiabaticity. The resonant excitation of electrons caused by the anharmonic nature of the restoring force hence is the underlying cause of net energy transfer from the laser to electrons.

2.2.4.5 Laser wakefield acceleration

In the above electron acceleration scenarios it has been assumed that the target foil remains undestroyed by the laser pulse. This means that the foil remained solid and the electron density stayed overcritical, so that the laser is reflected at the critical density surface and cannot penetrate the target. In cases where the foil is thin and the laser is long or preceded by significant prepulses or ASE, the situation may change and the target can expand and turn transparent. A rough estimation neglecting relativistic effects[6] shows that this indeed is possible for a thin foil. Assuming for example an ultra-thin foil of thickness of $d = 0.05 \cdot 2\pi$, density $n_{e,0} = 700 n_c$ and an ASE intensity of 10^{-8} of the laser maximum intensity with $a_0 = 12$, the electron temperature during the ASE phase can be approximated by $T_e^{ASE} \approx \left(1 + 0.5 a_0^2 \times 10^{-8}\right)^{1/2} - 1 \approx 3.5 \times 10^{-7}$. As will be described in detail in Sec. 2.3.1.1, this temperature leads to a pressure on the target surfaces and subsequent expansion of the foil. With the ion sound speed

$$\boxed{c_s = \sqrt{\frac{Z T_e}{m_i}}} \tag{2.55}$$

the expansion of the ion front can be calculated. The distance of the ion front from the initial target surface is approximately given by $x_f = c_s t \left[2 \ln(\omega_{pi} t) + \ln 2 - 3\right]$ [81] where $\omega_{pi} = \left(n_{e,0} Z / m_i\right)^{1/2}$ is the ion plasma frequency. At the same time, the electron density reduces as $\bar{n}_e(t) \cong n_{e,0} d / (2 x_f + d)$. In the above example it is $c_s \approx 5.2 \times 10^{-6}$, and ω_{pi} falls from 0.6 to 0.02 when n_e reduces from 700 to 1. This means that the average density will have dropped below 1 after $t \approx 0.5\,\mathrm{ns}$, a typical time duration for ASE.

Once the electron density has dropped below 1, the laser can penetrate the target. The electron acceleration can now be described applying the discussions known from gases. For example, the laser now can excite a plasma wave that can accelerate electrons when they are injected by an additional mechanism [82, 83]. In gases, in the specific case of long laser pulses compared to a plasma period an electron plasma wave is excited by stimulated Raman forward scattering [84, 85, 86] (self modulated laser wakefield acceleration, SM-LWFA). The injection can be achieved by trapping hot background electrons which are preheated by other processes such as Raman backscattering and side scattering instabilities [87, 88, 89] or by self-injection [90]. A short laser pulse may even directly drive a non-linear plasma wave and accelerate self-injected electrons into the GeV range [91, 92].

An example where electrons in an initially thin solid foil were accelerated to more than

---

[6] The relativistic mass increase of hot electrons would lead to yet earlier transparency.

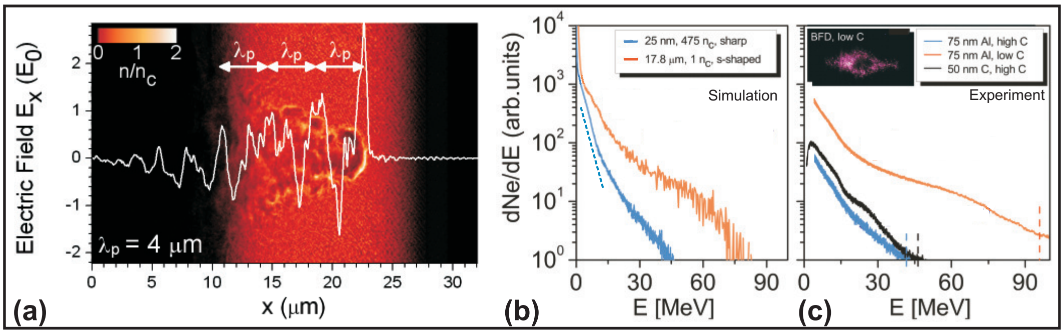

Figure 2.6: SM-LWFA at a solid foil. (a) shows the electron density distribution from a simulation of a 12.5λ thick plasma slab at critical density and s-shaped boundaries (2.5λ FWHM each), equivalent to a solid foil expanded prior to the main pulse due to ASE and prepulses. The overlay graph displays the electric field lineout along the laser axis, clearly showing a periodicity at the plasma wavelength λ_p. (b) The excited plasma wave accelerates electrons to a maximum energy of more than $\gamma = 160 m_e c^2 \approx a_x d$ (80 MeV) creating a hot electron tail in the electron energy spectrum (orange line). The blue line shows the spectrum of a solid foil with $n_{e,0} = 475$ and the same total number of electrons for comparison (resembling a situation unperturbed by ASE/prepulses). (c) shows experimental results obtained from various foils (consisting of aluminum (AL) and carbon (C)) at different contrast (C) combinations. For low contrast, the foil is heated and expands prior to the main pulse, as confirmed by the lack of reflection in the center seen in the back focus diagnostic (inset). At the same time, the measured electron spectrum exhibits a high energy tail as seen in the simulation. Laser: $a_0 = 12$, $w_0 = 14\pi$, Gaussian, pulse duration $t_p = 1200$.

90 MeV for low laser contrast compared to 45 MeV in the case of high laser contrast is shown in Fig. 2.6. This increase in energy was attributed to an expansion of the thin foil prior to the main pulse so that the density dropped below the critical density and the laser could penetrate the target and excite a plasma wave inside [50].

2.2.4.6 Direct laser acceleration

There exists one other mechanism to accelerate electrons in an underdense plasma [93, 94]. This is the direct laser acceleration of electrons in a self-generated plasma channel along the laser propagation first pointed out by [95, 96]. When the laser penetrates an underdense plasma, it expels electrons from the laser axis in transverse direction by the transverse ponderomotive force. This creates a gradient in the electron density and therefore a gradient in the refractive index as seen from Eqn. (2.33). This results in a self-focusing of the laser when the power exceeds the critical power for self-focusing and a long plasma channel is formed. As electrons are ponderomotively accelerated primarily in the forward direction, a net forward current is established with a surrounding magnetic field. Electrons pushed transversely undergo betatron oscillations in this field. When the betatron frequency equals the laser frequency as seen by the forward-moving electron, $\omega_\beta = 1 - \beta_z/\beta_{ph}$ (where $\beta_{ph} =$

$(1-\omega_p^2)^{-0.5}$ is the laser phase velocity), the electrons can come into resonance with the laser electric field and gain net energy. The effective electron temperature is expected to scale proportional to a_0 [96].

2.2.4.7 Ensemble averaging

As it is the objective of this section to give a prediction of the correct electron average kinetic energy $\bar{\gamma}_e$ of the electrons accelerated by the intense fields, it is important to point out a crucial fact which has not been considered before. All theoretical descriptions outlined above are valid only for single free electrons, even though the electrons were considered to be embedded in a plasma background. Still, even the average (2.50) is giving only the *temporal average of a single electron*, $\langle\gamma\rangle_t$, in which case the laser field damping can be neglected. In Sec. 4.1.2 a model for the correct average $\bar{\gamma}$ of the whole electron ensemble will be developed, showing a significantly different scaling than $\langle\gamma\rangle_t$, which means that it is crucial – especially in the relativistic case – to take into account $\bar{\gamma}_e \neq \langle\gamma\rangle_t$.

2.3 Ion acceleration

2.3.1 Target Normal Sheath Acceleration

As long as the laser intensity is moderate, so that the target foil remains intact during the laser pulse and subsequent ion acceleration, the acceleration of ions can be described by the Target-Normal-Sheath-Acceleration process [97, 98]. Here, staying "intact" means that the foil's electron density remains high enough and the electrons' relativistic mass remains low enough so that the plasma frequency stays large compared to the laser frequency (and hence the laser cannot penetrate the plasma more than a skin depth) and the charge deficiency in the foil and the expanding sheath is negligibly small. TNSA is widely accepted to be the dominant mechanism responsible for ion acceleration in most experiments up to now. The achievable ion energies with current laser systems are in the order of tens of AMeV, with a maximum at or below 60 AMeV [20, 97], a record that was set as early as 2000 and has never been exceeded until 2009. Experiments that are analyzed within the framework of this thesis were then able to increase that mark by more than 15% by optimizing the laser-target interaction process [21] (see Sec. 4.3.2) and still mark the record of published laser accelerated proton energies.

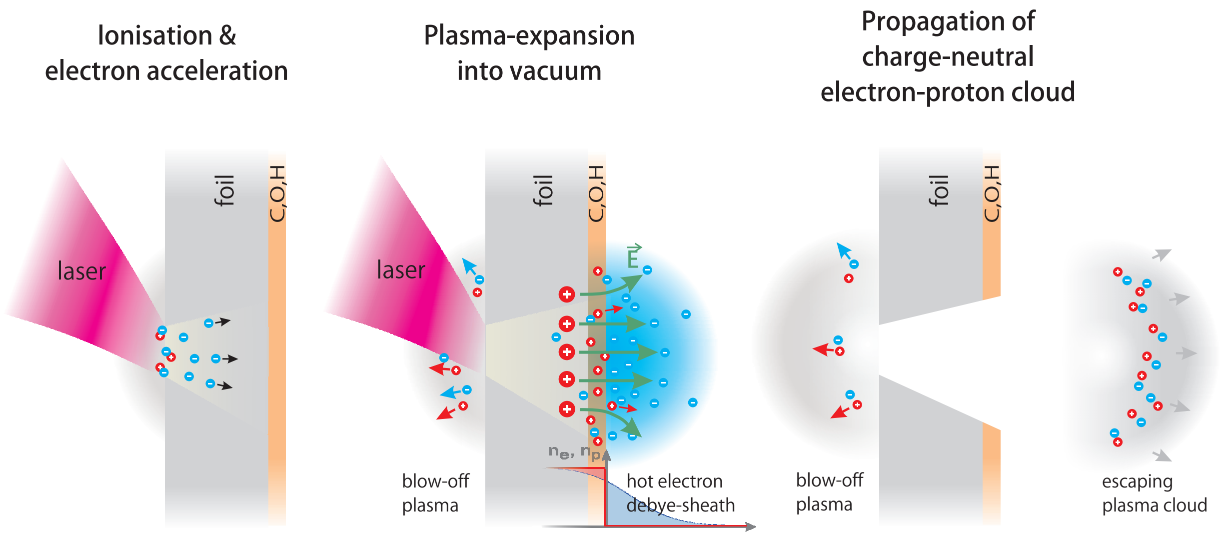

Figure 2.7: The TNSA process from left to right: The laser accelerates electrons at the target front side. Those electrons travel through the foil and exit at the rear, setting up a quasi-static electric field. Ions are accelerated in this field, reaching energies of up to $60 - 70\ MeV$.

Inspired by the early success of laser ion acceleration in the year 2000, there has been vivid research both experimentally (see e.g. [99, 8, 100, 101, 102, 103, 104, 105, 106, 107, 108, 109, 110, 111]) and theoretically (see e.g. [81, 112, 113, 52, 114, 29, 115, 116, 30]). Typically, hydro-carbon contaminants from (sub)micrometer thick foils are accelerated in a quasi static field set up by the hot laser accelerated electrons at the target surface. Experiments have shown excellent beam properties compared to conventional accelerators such as small source size, ultra-low emittance, high charge density and ultra-short bunch duration.

The TNSA process was introduced first by Hatchett et al. [97] in 2000 and by Wilks et al. [98] in 2001 and is based on the expansion of a hot plasma into a vacuum, which has been discussed in the pioneering work of Gurevich in 1965 [117] and others [118, 119, 120, 121]. Mora then later gave a detailed 1D description of the dynamics of an isothermal [81] and adiabatically cooling [112] plasma (see Sec. 2.3.1.1).

In the general picture of TNSA of ions (see Fig. 2.7) one assumes a reservoir of energetic electrons which is created by the laser pulse interaction with the front surface of the foil (see last Section). The energetic electrons exit the foil at the front and rear surface up to an average distance of the Debye length

$$\lambda_D = \sqrt{T_e^{hot}/n_e^{hot}}, \tag{2.56}$$

ionizing atoms at the surface. The electrons are pulled back into the target if their energy does not exceed the potential set up by the ions. Consequently, a quasi-static situation is present at the surfaces giving rise to quasi-static fields that accelerate the ions in the target normal direction. The maximum energy the ions can gain is determined by their charge-to-mass ratio, the field strength and the time duration in which the fields are maintained. The charge-to-mass ratio is largest for hydrogen ions (1:1), hence protons will be the most energetic ions whenever present at the surface (in the majority of experimental situations one will always find hydrogen together with carbon and oxygen as contaminants from accretion from air). The duration of the ion acceleration in the quasi-static field can be assumed to be in the order of the pulse duration in the two most accepted theories (Mora, Sec. 2.3.1.1 and Schreiber, Sec. 2.3.1.2). The field strength is determined by the density and average energy of the electrons accelerated by the laser. Consequently, those three parameters – pulse duration, hot electron density and hot electron temperature – are the experimental knobs where one can play with in order to increase the maximum ion energy. Schreiber et al. [113] established a relation between the maximum ion energy and the laser pulse duration (at constant laser pulse energy) using energy conservation between the amount of energy absorbed from the laser and the kinetic energy gained by the electrons, clearly indicating the existence of an optimum laser pulse duration. Using the same energy conservation argument, it is clear that the electron density and temperature in this simple picture (neglecting electron reflux, repeated heating, limited foil size etc.) cannot be changed independently from each other.

In the following two important TNSA models are briefly presented, representing the two classes of currently available models. First, the 1D Mora model of a plasma expanding into a vacuum will be introduced as a prominent representative of fluid based models. Then, Schreiber's model of ion acceleration will be given as a representative for a quasi static model where the electron population is assumed to be in a quasi static equilibrium state, setting up a quasi static electric field acting on the ions.

2.3.1.1 Plasma expansion into vacuum

The theoretical description of the expansion of a hot plasma into a vacuum dates back to the work of Gurevich in 1965 [117], followed by several other studies [118, 119, 120, 121]. Mora then later gave a detailed 1D description of the dynamics of an isothermal [81] and adiabatically cooling [112] plasma. In the 1D isothermal semi-infinite plasma expansion model (PEM) the expansion can be described by a self-similar temporal evolution of the system. The initial state is defined by cold ions of density $n_{i,0}$ occupying the half-space

$z < 0$ and hot electrons with Boltzmann distribution with temperature T_e^{hot} and density $n_{e,0}^{hot} = Zn_{i,0}$. Solving the Poisson equation for the initial state a simple expression for the electric field at $z = 0$ can be found

$$E_{front,0} = \sqrt{\frac{2}{e} n_{e,0}^{hot} T_e^{hot}} = \sqrt{\frac{2m_i^2}{Z^2 e}} c_s \omega_{pi} \tag{2.57}$$

where

$$\omega_{pi} = \sqrt{\frac{Zn_{e,0}^{hot}}{m_i}} \tag{2.58}$$

is the ion plasma frequency and e is Euler's number. Using the equations of continuity and motion, assuming quasi-neutrality in the expanding plasma, the electron density at position $z(t)$ with $z > c_s t$ can be described by

$$\boxed{n_e^{hot}(z,t) = Zn_i(z,t) = n_{e,0}^{hot} e^{-\frac{z}{c_s t} - 1}.} \tag{2.59}$$

In the limit $t \to \infty$ the self-similar solution becomes invalid when the local Debye-length

$$\lambda_D(z,t) = \sqrt{T_e^{hot} / n_e^{hot}(z,t)} \tag{2.60}$$

$$= \lambda_{D,0} \sqrt{n_{e,0}^{hot} / n_e^{hot}(z,t)} = \lambda_{D,0} e^{\left(1 + \frac{z}{c_s t}\right)/2} \tag{2.61}$$

becomes larger than the self-similar density scale length $c_s t$. This is happening at $x/t = 2c_s \ln \omega_{pi} t - c_s$ where Eqn. (2.59) predicts a front velocity of $v_{i,front} = 2c_s \ln \omega_{pi} t$. This implies a field of

$$E_{front} = 2c_s m_i / (Zt)\,. \tag{2.62}$$

With the simple interpolation formula between (2.57) and (2.62), $E_{front} \cong 2c_s \omega_{pi} m_i / \left(Z\sqrt{2e + \omega_{pi}^2 t^2}\right)$, the ion front velocity $v_{front}(t) = \int_0^t ZE_{front}(t')/m_i dt'$ and ion front position $x_{front}(t) = \int_0^t v_{front}(t')dt'$ can be calculated for all times . The ion energy at the front, which is the maximum energy, is then found to be

$$\boxed{\varepsilon_{max} \cong \frac{1}{2} m_i v_{front}^2 = 2ZT_e^{hot}\left[\ln\left(\tau + \sqrt{\tau^2 + 1}\right)\right]^2} \tag{2.63}$$

where $\tau = \omega_{pi} t / \sqrt{2e}$.

Since the laser pulse has a finite duration t_p, the hot electron bunch has a length in the order of $L \cong ct_p$ and hence it is intuitively clear that the accelerating fields can only be sustained for and the ion acceleration stops after that duration.

To evaluate (2.63) explicitly, the ion plasma frequency and therefore the hot electron temperature and density need to be known. As a first good approximation one may use the temperature scaling (2.51) and hot electron density (2.66). The final maximum ion energy is then given by (2.63) with $t \cong t_p$. As will be shown, the simple estimate for the temperature Eqn. (2.51) leads to an overestimation of the maximum ion energy especially in the relativistic intensity domain (see Fig. 4.10). In Sec. 4.1 the discussion of the maximum ion energy scaling will therefore be extended based on a more precise modeling of the electron temperature and density.

In the more realistic case of a foil of finite thickness d the electron bunch can fill the whole volume if $t_p > d$ and an adiabatic expansion phase is superimposed on the isothermal expansion since electrons can interact with the ions more than once [112]. This is one reason why ultra-thin foils have attracted interest for their potentially higher ion energies. In a 2D or 3D geometry, electrons can also spread in transverse direction, both reducing the electric field in the center, where the highest energy ions are accelerated, and keeping the electrons from a repeated interaction with the ions. Therefore, for a significant adiabatic expansion phase it must also be $t_p > w$ (where w is the transverse foil size) and consequently foils with a limited lateral extension can be useful since they can confine electrons in the center region. These and other effects in ultra-thin and mass limited targets will be analyzed and described in more detail in Sec. 4.2 and 4.3.1.

2.3.1.2 Schreiber model

Schreiber et al. formulated a different theoretical approach in 2006 [113]. This model assumes the same initial conditions as described in the last section, but proposes that the protons are accelerated in a potential defined by the initial, quasi static solution of the Poisson equation with the electrons being in a quasi static equilibrium state,

$$-\Phi = \frac{\varepsilon_\infty s(z/W)}{Z} \tag{2.64}$$

where

$$\varepsilon_\infty = \frac{Q}{2\pi W} \tag{2.65}$$

is the energy an ion with charge Z can gain at maximum at infinitely long laser pulse duration, $s(z/W) = 1 + z/W - \sqrt{1 + z^2/W^2}$ and $W = w_0 + d\tan(\theta)$ is the radius of the electron spot at the target rear side. Q denotes the number of electrons behind the foil.

Assuming that the laser accelerates N_e^{hot} electrons within a beam of length $L \approx t_p$ and considering that electrons with the average energy T_e^{hot} will exit the foil at the rear surface up to a distance of $\bar{z} = \sqrt{2T_e^{hot}/n_e^{hot}}$, it is

$$Q = 2N_e^{hot}\frac{\bar{z}}{t_p}.$$

Next, the number N_e^{hot} of hot electrons is approximated using the energy conservation between the absorbed laser energy, $\eta t_p \mathrm{a}_0^2 w_0^2 \pi/2$ (η being the laser absorption coefficient), and the total kinetic energy of the accelerated electrons, $N_e^{\mathrm{hot}} T_e$ [113]. Then it follows $N_e^{hot} = \pi\eta a_0^2 w_0^2 t_p/2T_e$. The density of hot electrons behind the foil is thus given by

$$\boxed{n_e^{hot} \cong \frac{Q}{\bar{z}W^2\pi} = \eta\frac{w_0^2 a_0^2}{W^2 T_e^{hot}}} \tag{2.66}$$

which correlates the hot electron density, temperature and laser intensity with each other. Now putting everything together, the maximum energy (2.65) which a proton can gain in an infinitely long laser pulse can be rewritten as

$$\varepsilon_\infty = \sqrt{\eta w_0^2 a_0^2/2}. \tag{2.67}$$

Solving the EOM of ions in the potential (2.64), the resulting maximum proton energy is found to be a function of the pulse duration with an intensity-dependent optimum value. The exact solution is an implicit function, which can be approximated by

$$\boxed{\varepsilon_{max} \cong \varepsilon_\infty \tanh^2\left(t_p/2t_{ref}^{Schreiber}\right)} \tag{2.68}$$

with the reference time $t_{ref}^{Schreiber} = W/(2\varepsilon_\infty/m_p)^{1/2}$ [24]. The limits for short and long pulse durations are then given by

$$\varepsilon_{max} \cong \varepsilon_\infty \eta a_0^2 \qquad t_p \ll t_{ref}^{Schreiber} \tag{2.69}$$

$$\varepsilon_{max} \cong \varepsilon_\infty \sqrt{\eta} a_0 \qquad t_p \gg t_{ref}^{Schreiber}. \tag{2.70}$$

2.3.2 Enhanced Ion Acceleration Concepts

2.3.2.1 In the TNSA regime

In the frame of this work, methods will be discussed that can increase the temperature and/or the density of hot electrons with the goal of increasing the maximum achievable energy, going beyond the ideas proposed over the last 10 years. Based on the TNSA at a flat foil, the optimizations concentrate on the foil front side laser absorption processes and the spatial electron confinement in order to increase the temperature and number of hot electrons. They include:

- Increase of laser intensity (Sec. 4.1)
- Ultra-thin and stacked foils (UTT, Sec. 4.2)
- Mass limited targets (MLT, Sec. 4.3.1)
- Flat top cone targets (FTC, Sec. 4.3.2)

All methods have in common that within the frame of this work the subsequent acceleration of ions still is governed by the well established TNSA mechanism, still exhibiting the beneficial properties ascribed to it, including small source size, low emittance and high bunch density.

All methods influence more than one plasma parameter at once, such as hot electron energy, density or total laser absorption and duration of the sheath field existence. It therefore is no simple task to find a global optimum for the laser target, optimizing intensity, thickness, shape, width and microstructure at the same time. Rather, in this work the individual fundamental mechanisms are studied with respect to their influence on electron density and temperature.

For a simple flat foil target the laser intensity, together with the pulse duration, are the decisive parameters defining the final maximum proton energy. As will be shown in Sec. 4.1.3, these two parameters are crucial to decide whether the optimization of the temperature or the density of hot electrons is more beneficial. While for short laser pulse durations the proton energy turns out to be influenced only by the pulse duration and the total absorbed energy $T_e^{hot} N_e^{hot} \propto \eta a_0^2 t_p$ with equal relative importance, for long pulses the most important parameter is the hot electron temperature while the relevance of the electron density and pulse duration is much less. Correspondingly one needs to choose the best optimization method matching the specific laser parameters. In the following the most prominent methods are briefly introduced.

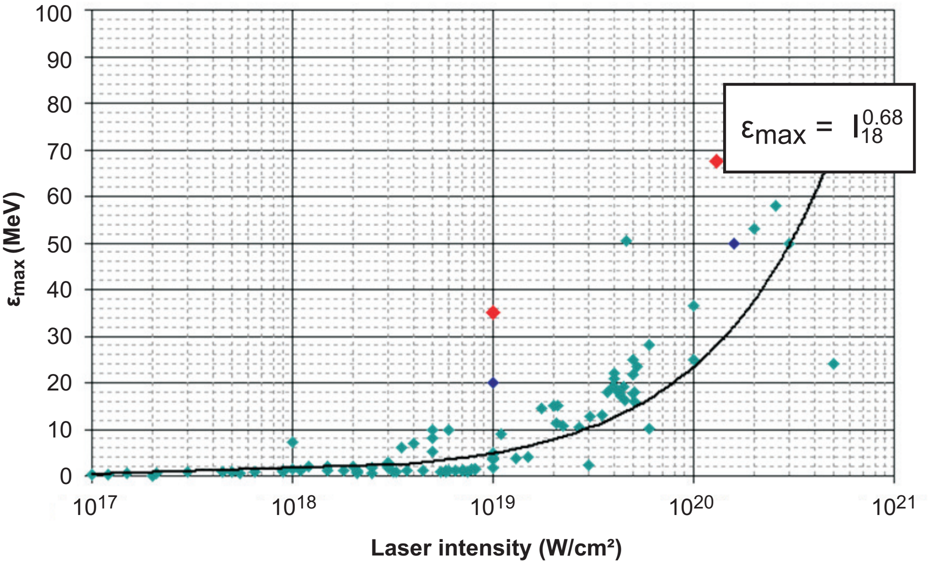

Figure 2.8: Collection of published experimental results for the maximum proton energy accelerated by short pulse laser systems up to the year 2009. Only the best shots are shown. Red dots mark shots on FTC at Trident, LANL. The best power law fit of all data follows the simple scaling law $\varepsilon_{max} = \left(I[\mathrm{W/cm}^2]/10^{18}\right)^{0.68}$. Courtesy K.A. Flippo/ S.G. Gaillard.

Laser intensity The increase of the laser intensity is perhaps one of the most prominent and straight forward methods to increase the maximum ion energy. A collection of available experimental data (Fig. 2.8) shows the empirical scaling

$$\boxed{\varepsilon_{max} = \left(\frac{I[\mathrm{W/cm}^2]}{10^{18}}\right)^{0.68}} \tag{2.71}$$

With increasing intensity, the electron temperature and density increase which leads to higher ion energies as can be readily seen in Eqn. 2.63. Even though the correct scaling of the electron temperature with laser intensity is crucial in predicting the final ion energies, a fully self-consistent theory which is in accordance with experiments was not available before this thesis. It was therefore one of the main tasks to develop such a model (Sec. 4.1).
Since current technologies and monetary issues set limitations on the available and feasible laser pulse intensity, other methods need to be explored to increase the maximum energies from a laser system.

Ultra-thin foils The thickness of foils as a possible means to increase the electron density has been mentioned before in Sec. 2.3.1.1. An increase of the hot electron density at the

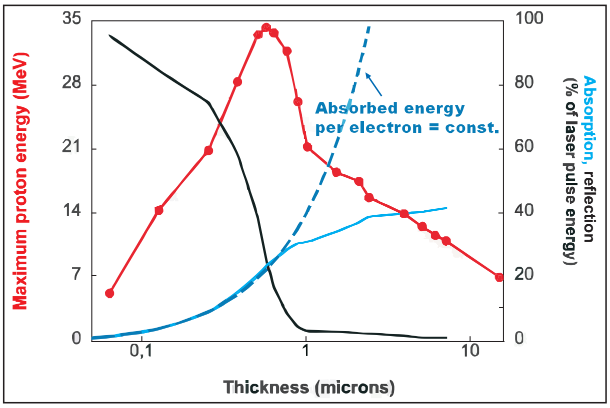

Figure 2.9: Simulated maximum proton energy (red), laser absorption (light blue) and reflection (black) as a function of foil thickness, extracted from [116]. At the optimum foil thickness (maximum proton energy) laser absorption and reflection are equal. As was suggested by the author of this thesis, the optimum foil thickness is given by the point when the laser can accelerate just all electrons to the same average energy, which is the case when the foil turns transparent. The blue dashed line shows the extrapolation of laser absorption if the absorbed energy per electron would remain constant for thicker foils than optimum. The observed laser absorption is less, since electrons inside the foil experience a reduced laser field strength screened by the front electrons. For thinner foils, the absorbed energy follows the line of constant energy per electron, yet the proton energies are reduced due to a reduced total number and density of hot electrons.

target rear surface is achieved by a simple geometrically smaller lateral spreading when the foil thickness is reduced as a consequence from a finite divergence of the electron beam [24]. Additionally, when the foil is very thin, it becomes transparent to the laser. The laser then can penetrate the target and instead of only interacting with the electrons at the surface it can transfer energy to all electrons within the focal volume [116], maximizing the number and energy of the hot electrons. At this optimum foil thickness, the laser absorption and transmission are equal (see Fig. 2.9).

As was suggested by [50], if the plasma expansion extends over a sufficiently broad length along the laser axis, the laser then may excite plasma waves inside the foil, accelerating the electrons and subsequently the ions to higher energies than they could gain at the surface of a solid. During the electron energy transfer to ions by TNSA at the foil rear surface, this energy loss can be balanced by continuous laser energy transfer to the electrons, maintaining an effective ion accelerating Debye sheath at the foil rear surface (Fig. 2.10).

Although the skin depth (2.41) in solids is in the order of a few nanometers only (e.g. for a density of $600n_c$ and $\lambda = 1\,\mu\text{m}$ it is $\delta = 6.5\,\text{nm}$), the transparency can set in at considerably larger thicknesses. This discrepancy can be attributed to the relativistic mass increase of hot electrons, and thus the decrease of the plasma frequency, when the laser intensity is relativistic [122].

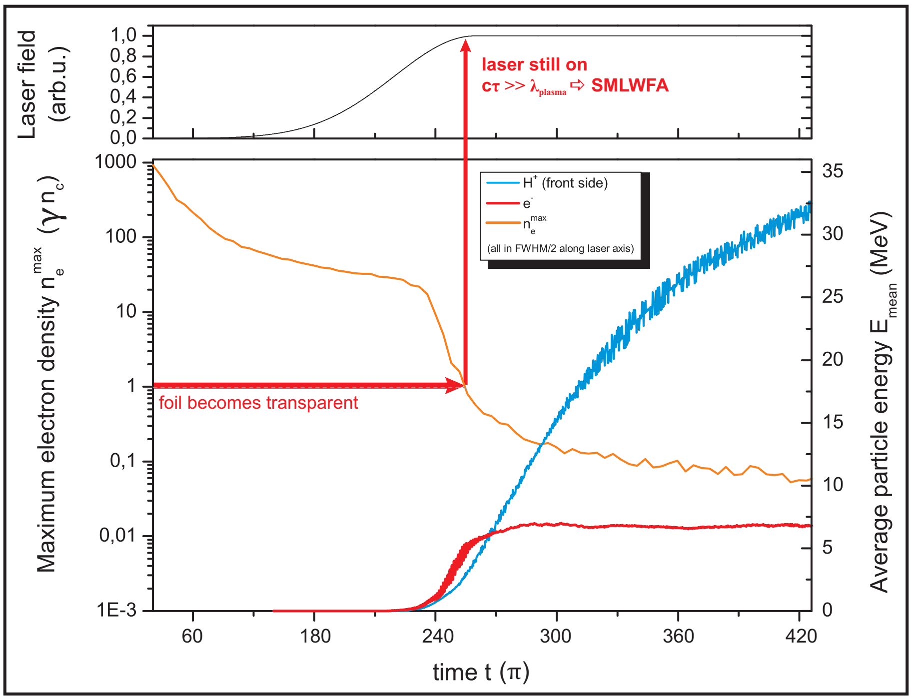

Figure 2.10: Continuous ion acceleration at a thin solid foil. While the laser intensity ramps up at the target front surface (upper panel), the electron density along the laser axis decreases due to thermal expansion and relativistic mass increase (orange line, lower panel). At $t \approx 650$ the foil becomes transparent. At this point the average energy of electrons along the laser axis (red line) remains approximately constant, while the energy of the ions is increasing constantly (blue line), verifying a constant energy transfer from the laser to electrons and from electrons to ions. Foil: thickness 0.01π preionized carbon at $n_{e,0} = 660$ with 0.004π thick proton contaminant on both surfaces. Laser: $a_0 = 12$, $w_0 = 14\pi$, gaussian.

This naturally results in the existence of a lower limit for the target thickness. When the foil is thicker than optimum, the laser cannot penetrate the target and the deeper laying electrons only see a reduced laser field strength, shielded by the electrons in front of them. This reduces the temperature of hot electrons while the density at the foil rear surface is decreased due to the divergence of the hot electron beam. When the foil becomes too thin the laser is mainly transmitted [110]. In this case, while the energy per electron (temperature) remains almost constant the hot electron density decreases, reducing the rear surface quasi static electric field and ion maximum energy. It will be shown in this thesis, that with a novel design concept the hot electron density can be optimized together with the electron temperature with respect to the pulse intensity and duration in order to circumvent this problem (Sec. 4.2).

Mass limited foils The ion source size at the foil rear surface is usually more than 100 µm, much larger than the typical laser spot size of 5 – 10 µm [8, 9, 105]. The difference can be explained with a transverse spreading of the hot electrons. A reduction of the target lateral dimension using so-called mass-limited targets (MLT) causes a lateral electron confinement and recirculation of hot electrons. Both confinement [106] and recirculation [20] are discussed to considerably enhance the density and kinetic energy of hot electrons as well they can change the shape of the hot Debye sheath and thus the emission characteristics of the ions [29, 109]. Theoretical studies have mostly concentrated on short laser pulses of a few tens of femtoseconds. In this case simulations showed that a reduction of the lateral foil size can lead to an increase of proton cutoff energy with an optimum of the laser absorption at the focal spot size. In a recent experiment [109], an increase of maximum proton energy with decreasing lateral target diameter has been observed for lasers with medium pulse durations of 400 fs. In Sec. 4.3.1, an analytical model will be developed to describe the electron temperature increase in MLT and to predict the ion maximum energies. Additionally a numerical study is performed extending to longer laser pulse durations. Four discrete regimes of MLTs as a function of the lateral dimension and with respect to the dominant physical effect are identified and described (see Tab. 4.6), starting from a regular infinitely large foil with regular TNSA going over confinement dominated MLTs down to reacceleration dominated foils and Coulomb exploding foils of sub-focal sized foils.

Flat top cone targets (FTC) Since the intensity is a crucial factor determining the electron energy (see Sec. 2.2.3), microfocusing in a hollow cone geometry could lead to an increase of the electron temperature. This was first pointed out by [30] for cones with straight side walls at modest laser intensity, and using micro-cone targets with a flat top at the tip indeed were shown to lead to significantly increased proton energies in [21, 107]. As the laser beam waist is reduced when the laser enters the cone, its intensity increases accordingly. Electrons are accelerated at the side walls and move due to self-generated quasi-static electric and magnetic fields directed along the walls towards the tip [30, 123, 31, 108, 124] (see Fig. 2.11). Nakamura et al. pointed out that electrons bound to the wall surface by those fields can be accelerated resonantly [31].

Another important electron acceleration mechanism was identified in the scope of the work of this thesis, namely the direct acceleration of surface confined electrons by the laser light pressure (DLLPA) [21, 32, 125]. Numerically it can be shown that in certain cases the resonant acceleration is very much suppressed and micro focusing alone is not sufficient to explain the numeric results. Then, the DLLPA mechanism is responsible for the majority of the electron temperature increase. The full analysis can be found in Sec. 4.3.2.

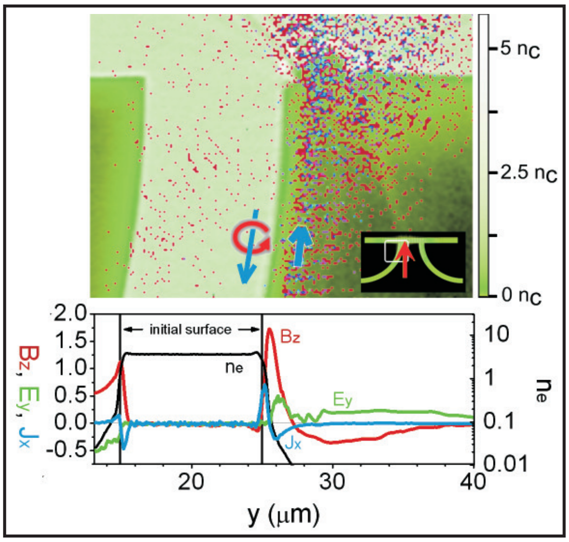

Figure 2.11: Top: Electron density for a laser incident tangentially at a cone wall at the time the laser maximum reaches the flat top front surface. Bottom: Currents and fields at a cone wall surface, averaged over one laser cycle. (Extracted from [125])

When a flat foil section is attached to the tip of the cone, the energetic electrons can set up a quasi-static field at its rear and accelerate ions as in the case of a regular flat foil. The increased electron energies then give rise to increased ion energies. An additional effect of curved-wall FTC is the confinement of electrons in the region of the tip due to self-generated resistive magnetic fields inside the cone walls. In that case, the electron confinement is comparable to MLT [126, 108].

Front side structure Another possible method to increase the ion maximum energy is a microscopic structuring of the foil front side. Such structures for example can be a monolayer of polystyrene microspheres, micro gratings or ripples of a size similar to the laser wavelength. It has been shown by simulations [25, 127], that such structures can significantly increase the laser absorption efficiency compared to an unstructured flat foil by increasing both the density and temperature of hot electrons, leading to an increase in ion energies. However, it appears that the same effect can be produced much simpler by a controlled preplasmas. Such preplasmas are created for example by prepulses and ASE prior to the main pulse and can also lead to an increase in laser absorption. For example, experimentally clear trends are seen for an increase in ion energies with increasing fs-prepulse levels [128], which can most probably be linked to an increased laser absorption in the preformed plasmas [129].

2.3.2.2 Radiation pressure acceleration (RPA)

So far, it has been assumed that the electron motion is governed by its quiver motion and that longitudinal forces are weak or can be balanced by the plasma without causing a significant dynamic effect. However, for intense laser pulses the non-oscillating part of the longitudinal force (2.15) may exert a significant pressure on the electrons at the front side strong enough for the density profile to steepen and to recess into the foil. The electrostatic field building up at the foil front surface can be estimated to be $a_{es} \approx a_0^2/2\sqrt{1+a_0^2/2}$ which is strong enough to accelerate ions into the target. The recession speed of the surface in the non-relativistic case then is $v_f \approx (\sqrt{2}a_0 Z/M)^{1/2}$ where Z is the ion charge and M the ion mass in units of the electron mass [130, 131]. This process is called hole boring mode of radiation pressure acceleration (RPA) and the maximum velocity ions can gain in that process is limited to just twice the recession speed, which typically is significantly less than ions could acquire at the foil rear surface TNSA [132, 133].

When the target foil is chosen thin enough for the laser to punch through and accelerate it as a single object, this scenario changes and ions can potentially gain high energy in a phase-stable way, as has been proposed analytically and numerically [134, 135, 136, 137, 138]. This regime is called the light sail (LS) mode of RPA as it shows similarities to the LS concept of space-flight [139]. While in space-flight usually time periods are long and radiation pressure is small, in laser ion acceleration it is vice versa. Here, the optimum condition for ion acceleration is defined by the possibility for the laser pressure to be just strong enough to extract all electrons from the target and set up a strong charge separation field [135]. This imposes the existence of an optimum thickness for the foil, which is derived quantitatively below. To sustain the lightsail (electron mirror) throughout the laser pulse duration, it is necessary to suppress electron heating and successive thermal explosion, which most easily could be done using CP light.

The optimum foil thickness for LS-RPA most often is derived from balancing the laser light pressure with the electrostatic areal force[7]. The laser light pressure reads

$$P_L = (1+\eta)\frac{I}{c} = (1+\eta)\frac{a_0^2}{2}Pn_c m_e c^2 \tag{2.72}$$

where $\eta = R - T$ (R: reflection, T: transmission). The electrostatic areal force set up by the charge separation induced by the light pressure amounts in a 1D model to $P_{es} = E_0 e n_{e,0} d$

---

[7] There are other arguments, for example the transition to transparency [137, 140], which lead to structural and quantitatively similar results.

where E_0 is the restoring field of the remanent ions which can be approximated with the field inside a plane capacitor, $E_0 = \frac{en_{e,0}d}{\varepsilon_0}$. Thus, the electrostatic pressure is given by

$$P_{es} = \frac{\left(en_{e,0}d\right)^2}{\varepsilon_0}. \tag{2.73}$$

In the optimum case, the laser pressure equals the electrostatic pressure at a certain threshold areal charge density, so that one gets

$$\begin{aligned} \frac{P}{2}\left(1+\eta\right)a_0^2 &= n_{e,0}^2 \frac{e^2\lambda^2}{4\pi^2\varepsilon_0 c^2 m_e n_c}\left(d_{opt}\right)^2 \frac{4\pi^2}{\lambda^2} \\ \sqrt{\frac{P}{2}\left(1+\eta\right)}a_0 &= \frac{n_{e,0}}{n_c}\frac{2\pi d^{opt}}{\lambda} \end{aligned} \tag{2.74}$$

which in dimensionless units used in this thesis simply reads

$$\boxed{\sqrt{\frac{P}{2}\left(1+\eta\right)}a_0 = n_{e,0}d^{opt}.} \tag{2.75}$$

From this, it follows that for a given intensity the optimum thickness should be the same for LP and CP lasers while for a given field strength the optimum thickness for a CP laser is a factor $\sqrt{2}$ greater than for a LP laser, simply proportional to the areal charge density if η is assumed to be constant.

Following that, the maximum energy ions can acquire during the radiation pressure push intuitively should be proportional both to the radiation pressure as well as the duration of the pulse. However, a detailed analysis solving the EOM of the foil ions yields for $R = 1$ the analytical expression [137]

$$\boxed{\varepsilon_{max}^{LS-RPA} = m_i\left(\frac{1}{\sqrt{1-\left[\frac{(1+\Lambda)^2-1}{(1+\Lambda)^2+1}\right]^2}}-1\right),\ \Lambda = 2\frac{Z}{m_i}\frac{a_0^2 t_p}{nd}} \tag{2.76}$$

At the optimum target thickness for a CP laser it becomes $\Lambda = \sqrt{2}Z/m_i \cdot a_0\tau$. While for small pulse durations and laser strengths $a_0 t_p/m_i \ll 1$ the maximum energy is indeed proportional the laser light pressure and pulse duration, $\varepsilon_{max} \propto a_0^2\tau$, for many realistic cases where $a_0 t_p/m_i \gg 1$ it is expected to scale proportional to $a_0\tau$ only, which is even worse than in TNSA (cp. Eqn. (2.71) and (4.30) in Sec. 4.1.3). Yet, the absolute predicted energies in

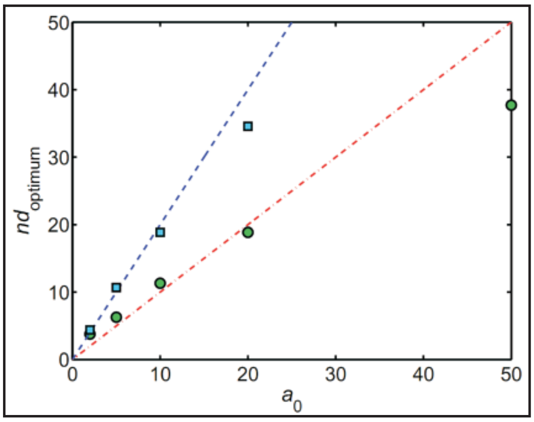

Figure 2.12: Optimum thickness as a function of laser strength a_0 at $n_{e,0} = 100$, extracted from [135]. The circles (squares) are the numerical values for the maximum proton energy for pulses with a temporal shape of a gaussian (flat top) and dash-dotted (dashed) lines are the RPA expectations $n_{e,0}d^{opt} = Fa_0$ with $F = 1$ ($F = 2$).

LS-RPA are still significantly larger than for TNSA for realistic laser parameters. However, it was suggested recently in [135] by simulations that the optimum thickness may actually not follow the simple linear law (2.75). For quick reference, Fig. 2.12 shows a replication of Fig. 3b from [135]. The most prominent observation are the different proportionality-factors between a_0 and the areal charge density for different pulse shapes. For example, for a gaussian (flat top) pulse it is $n_{e,0}d^{opt} = Fa_0$ with $F = 1$ ($F = 2$). Note that Eqn. (2.75) predicts with $F = \sqrt{\frac{P}{2}(1+\eta)}$ a value for F between 0 (full transmission) and $\sqrt{2}$ (full reflection) for a CP pulse, so $F = 2$ as empirically found for flat top pulses would be impossible. Moreover, for high laser intensities, deviations occur from the simple proportionality between a_0 and $d^{opt}n_{e,0}$. The numeric data from [135] follow much better the empiric formula

$$d^{opt} \propto a_0^{2/3}. \tag{2.77}$$

The deviation of the exponent of a_0 from unity remained unclear so far. It was speculated that the response of the ions, which was neglected in the derivation of Eqn. (2.75), contributes to modifications that become significant for large values of a_0. However, in Sec. 4.2.3 it will be shown that the deviation can be explained by an alternative approach taking into account the laser attenuation inside the foil.

Despite the promising high ion energy in LS-RPA, there has been no experimental confirmation of the LS-RPA mechanism so far. First hints towards the realization of this acceleration mode were published in [141], but an independent verification of the results has not yet succeeded. For realistic parameters, e.g. an intensity of $5 \times 10^{19}\,\mathrm{W/cm^2}$ ($a_0 \approx 5/\sqrt{2}$ for CP and $\lambda = 0.8\,\mu\mathrm{m}$) electron density $n_{e,0} = 660 n_c$ and $R \approx 1$, the optimum thickness is expected from (2.75) to be about $d^{opt} = 7.5 \times 10^{-3}$ (1.2 nm), which is well below the skin length of 6 nm (Eqn. (2.41)). Such thin foils are hard to manufacture, handle and characterize with respect to their homogeneity in thickness, presence of contaminants and corrugation. Other difficulties include the quick disintegration of the foil during the prepulse and ASE phase, development of transverse instabilities in the flying electron mirror [134, 142, 143] as well as bending of the foil in a 2D or 3D geometry, both leading to heating and a quick explosion of the sheath, even though there are advanced concepts to suppress the development of such instabilities e.g. by employing sophisticated target foil geometries and compositions or spatially and temporally tailored laser pulses, the experimental realization has not yet been achieved [138, 142, 143, 144, 145, 146].

Chapter 3

Methods

In the present work the code `iPICLS` by Y. Sentoku et al. [147] was used. It is a particle-in-cell (PIC) code, solving Maxwell's equations and integrating the equation of motion on a grid. The code can run on massively parallelized high-performance computers, typically spreading the computation over several 10 to 1000 CPUs. In the following the PIC method is briefly introduced and the necessary numerical simplifications are discussed.

3.1 The PIC method

The computer simulation of large systems of many particles is a demanding task. The naive approach of calculating the binary interactions of all N particles with each other would demand a computation time proportional to $N(N-1)$. Moreover, the temporal field evolution would have to be stored to correctly treat the field retardation. To simulate realistic systems within a feasible time period, the complexity has to be decreased even when using high power parallel computers. The probably most natural approach is to discretize the simulation volume L and time t by introducing a mesh with node distances Δx and finite time steps Δt. The plasma evolution can then be calculated by iteratively calculating the forces on the plasma with the Maxwell equations (Eulerian step) and the plasma reaction with the Lorentz equation (Lagrangian step). For the latter, particles can be introduced by defining the current $\boldsymbol{j}$ as

$$\boldsymbol{j} = \sum_{j=1}^{N_M} q_j R(\boldsymbol{r} - \boldsymbol{r}_t(t)) \boldsymbol{u}_j(t) \delta(\boldsymbol{u} - \boldsymbol{u}_j(t)). \tag{3.1}$$

Here $N_M = \alpha N$ is the number of model particles which usually must be chosen much smaller than the number of real particles, $\alpha \ll 1$. Then R is a distribution function defining the shape of a model particle. This scheme is called the Particle-in-Cell method and can be implemented numerically surprisingly easy by looping through the following steps:

1. Solve the Maxwell equations to obtain the fields in the next timestep at each mesh node.
2. Interpolate the fields at each particle position to obtain the force on each particle.
3. For each particle, integrate the EOM and move the particle accordingly.
4. Calculate the currents associated with the particle motion and assign them to the mesh nodes.
5. Calculate additional physics (ionization, collisions...)

For each step, various methods exist to optimize the calculations while at the same time keeping the result accurate. One popular method to solve the Maxwell equations is the finite difference in the time domain (FDTD) approach. The most intuitive solution then probably is to express also the spatial derivations in the Maxwell equations by finite differences (Yee-scheme) [148, 149]. With some care (e.g. providing a spatially ("Yee latice") and temporally ("Leapfrog") centered system of equations), this approach can be quite satisfying. Another method, which is employed in `iPICLS`, is the directional splitting (DS) of the fields, which in some circumstances can reduce numerical derivations, such as artificial heating of the system or artificial dispersion of waves. The DS method will be explained in more detail later in this section.

For the numeric simulations to be accurate and stable, one has to adopt certain requirements for the PIC parameters Δx, Δt, N_M and α:

1. $\Delta x_i \ll \lambda_D$ (to spatially resolve the Debye length which is the smallest relevant scale length in plasmas)
2. $\Delta t << \omega_p/2$ and $\Delta t \ll 1$ (to temporally resolve the laser wave and the plasma oscillations which are the highest relevant frequencies in plasmas)
3. $L \gg \lambda_D$ (the problem size must be large to reduce boundary effects)
4. $\alpha \ll 1$ (so that the smooth function R resembles the distribution of particles inside a model particle statistically well)
5. $N_M \gg L/\lambda_D$ (there must be many particles per Debye length to adequately resemble the real particle density)
6. $\Delta t \ll \Delta x_i/\sqrt{2}$ (to reduce numeric conductivity, "Courant condition").

The last condition (6) is a specialty for the Yee-scheme and can be dropped for the DS. If the above requirements are not fulfilled to a satisfactory level, the simulation will become inaccurate or unstable. The level at which this happens is greatly determined by the methods used for Maxwell solving and EOM integration. Three numerical effects are important to be able to estimate the necessary levels of smallness of the parameters: discretization errors, numerical dispersion and numerical heating.

Discretization errors The particle shape $R(\boldsymbol{r}-\boldsymbol{r}_j)$ of a particle j at postion $\boldsymbol{r}_j$ leads to an average force $\boldsymbol{F}_j$ on the particle of

$$\boldsymbol{F}_j = q_j \int R(\boldsymbol{r}-\boldsymbol{r}_j) \cdot [\boldsymbol{a}(\boldsymbol{r},t) + \boldsymbol{u}_j \times \boldsymbol{b}(\boldsymbol{r},t)] \, d\boldsymbol{r}. \tag{3.2}$$

Since the field values are only known at the mesh nodes, one has to identify $\boldsymbol{a}(\boldsymbol{r},t)$ and $\boldsymbol{b}(\boldsymbol{r},t)$ with their values at the nearest grid point. Let the force at grid point β be $\boldsymbol{F}_\beta$. The above equation can then be written as

$$\begin{aligned} \boldsymbol{F}_j &= \int \sum \boldsymbol{F}_\alpha S(x-x_\beta) R(x-x_j) d\boldsymbol{r} \\ S(x-x_\beta) &= \begin{cases} 1 & |x-x_\beta| \leq \Delta x/2 \\ 0 & |x-x_\beta| > \Delta x/2 \end{cases} \end{aligned} \tag{3.3}$$

It can then be demonstrated how the particle shape function can be used to reduce the fluctuation caused by the spatial discretization. In the lowest order one can define the model particles as dimensionless points, $R(\boldsymbol{r}-\boldsymbol{r}_j) = \delta(\boldsymbol{r}-\boldsymbol{r}_j)$. It then follows readily from (3.3) that the force on such a dimensionless particle is simply $\boldsymbol{F}_j = \boldsymbol{F}_{\beta'}$ where β' is the the nearest mesh node. This would cause a step-like change in the force when passing the center of a cell and would therefore introduce unphysically large frequencies into the simulation. The effect would be an artificial increase in energy (see paragraph about numerical heating). Alternatively, the function R can be defined for $|x-x_j| \leq (\Delta x)/2$ as

$$R(x-x_j) = (\Delta x)^{-1}. \tag{3.4}$$

This leads to a force on the particle given by a linear interpolation of the two mesh nodes nearest to the particle. Now, there are no jumps in the force anymore, but unphysically sharp edges now appear in the force at the cell borders. Therefore more complicated definitions of

R (and S) including higher orders of x^n and spatially larger distributions should be employed to include also more distant nodes or higher orders of interpolation. For example with

$$R(x - x_j) = \begin{cases} (\Delta x)^{-1}\left(1 - |x| / (\Delta x)\right) & |x| \leq (\Delta x) \\ 0 & |x| > h \end{cases} \tag{3.5}$$

the force on the particle would be a quadratic interpolation of the three nearest neighbors, removing all jumps and edges and providing a smooth force evolution. This is the definition employed in all the simulations performed in this thesis.

Numerical dispersion Numerical dispersion is a term referring to an artificial dispersion of waves which is introduced in the simulation and not present in real systems. In the following this will be exemplified for two important cases.

First, the finite particle distribution function as it was introduced in the last two examples in the last paragraph leads to a dispersion of plasma waves. Physically, plasma waves in a perfectly conducting plasma are free of dispersion. Just as was done in Eqn. (3.2), one can redo most plasma physics for a finite particle size by replacing q with $qR(\boldsymbol{r})$. This results in a plasma frequency dispersion relation of

$$\omega^2 = |R(\boldsymbol{k})|^2 \, \omega_p^2 \tag{3.6}$$

with greater deviation of ω from ω_p for larger particle distribution functions [149].

Another source of numerical dispersion arises from the mesh discretization when solving the Maxwell equations. Fig. 3.1 shows the phase velocity of an electromagnetic wave when propagating in vacuum as a function of the cell size and wave vector $\boldsymbol{k}$ for the two Maxwell solving schemes FDTD and DS. As can be seen, the DS offers considerably less dispersion, and is even dispersionless for waves traveling along a mesh axis. This allows to significantly increase the mesh size and therefore decrease the computation need compared to FDTD.

Numerical heating All stochastic errors that arise due to the discretization, the use of macro particles, numerical dispersion, rounding errors and others lead to a stochastic error-field $\delta\boldsymbol{a}$ which acts on the particles in random direction. Limiting the discussion to non-relativistic particle motion, the error in the particle velocity reads

$$m\delta\boldsymbol{v} = q \cdot \delta\boldsymbol{a} \cdot \Delta t \tag{3.7}$$

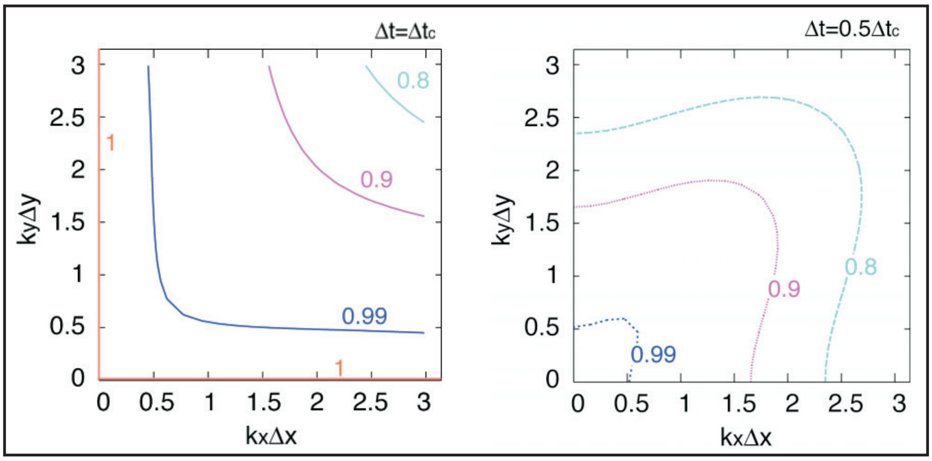

Figure 3.1: Numeric dispersion (a) for DS and FDTD (b), extracted from lecture by Y. Sentoku.

and while the average error of the velocities after n timesteps remains zero, $\langle \Delta \boldsymbol{v} \rangle = 0$, the error in the average energy increases to

$$\frac{m^2}{2} \langle \Delta \boldsymbol{v} \rangle^2 = nq^2 \Delta t^2 \left| \delta \boldsymbol{a} \right|^2 , \tag{3.8}$$

rising quadratically with time. This energy increase, usually called *numeric heating*, is in practice even worse due to a propagation of errors.

3.1.1 Collisions

While the PIC method correctly treats the forces on and between particles on a scale length larger than Δx, forces on small scales are underestimated [150]. As long as the physical range of particle-particle interactions is small compared to the average particle distance $\delta = \zeta n^{-1/3}$ (with $\zeta = 6.09 \times 10^{-3}$), this does not play a significant role. This is the case when the particle interaction potential at the average particle distance is weak compared to the average kinetic energy of particles,

$$\boxed{\Xi \equiv \frac{E_{pot}(r = \zeta n^{-1/3})}{T_e} \ll 1.} \tag{3.9}$$

Ξ is called the coupling parameter and can be used as a measure of energy exchange by binary interactions. In a plasma, the binary particle interactions are dominated by the

Coulomb force,

$$E_{pot}(r) = \xi \frac{q^2}{r}, \tag{3.10}$$

where q is the charge of the particle species, so that

$$\Xi = \frac{\xi}{\zeta} \left(n \lambda_D^3 \right)^{-2/3} \cong 2.9 \times 10^{-6}. \tag{3.11}$$

In the case of high intensity laser interactions with plasmas one usually has to deal with collisionless or weakly collisional systems. Typically, the energy of the laser accelerated hot electron current is in the range of $\mathrm{M}e\mathrm{V}$ for relativistic laser intensities with a density in the order of only a few times the critical density n_c, so that Ξ is in the order of 10^{-6} and collisions can be neglected. On the contrary, for the heating of the bulk of a target foil where the electron density usually is several hundred times the critical density and the cold bulk temperature is only in the $\mathrm{k}e\mathrm{V}$-range Ξ may be 10000 times higher and thus collisions have to be considered.

Collisions can be included into PIC simulations by noting that, as long as their role is weak, the dynamics of the system is still governed by the collisionless equations and collisions only lead to an exchange of energy and momentum between particles, which can be expressed by a collision operator. The only change to the PIC scheme then is to include another step in the PIC cycle implementing the collision operator. The full Boltzmann approach of calculating all binary interactions between particles within a cell would scale as N^2 and therefore is not feasible in high density plasmas. Another approach is to only define pairs of particles by a Monte Carlo algorithm and only calculate the Coulomb scattering between them, which scales more favorable as N [151]. In [150] it is described how this can be done relativistically correct between macro-particles with different α and conserving energy and momentum.

3.1.2 Directional splitting

The idea of the directional splitting as it was implemented by Sentoku et al. in the simulation software `iPICLS` relies on the specific properties of the Maxwell equations that their general solution can be expressed by a superposition of particular wave solutions that travel to the left, right, top, bottom, front or rear with phase velocity 1. Writing the Maxwell equations separately for terms including derivations for x, y,z, respectively, one obtains the twelve eigenvalues $a_x^{\pm}$, $a_y^{\pm}$, $a_z^{\pm}$ and $a'^{\pm}_x$, $a'^{\pm}_y$, $a'^{\pm}_z$ with [152]

$$\begin{aligned} a_x^{\pm} &= b_z \pm a_y & a'^{\pm}_x &= b_y \mp a_z \\ a_y^{\pm} &= b_x \pm a_z & a'^{\pm}_y &= b_z \mp a_x \\ a_z^{\pm} &= b_y \pm a_x & a'^{\pm}_z &= b_x \mp a_y. \end{aligned} \tag{3.12}$$

fulfilling the relations

$$\begin{aligned} (\partial_t \pm \partial_x)\, a_x^{\pm} \mp \partial_z b_x - \partial_y a_x &= \mp j_y & (\partial_t \pm \partial_x)\, a'^{\pm}_x \mp \partial_y b_x + \partial_z a_x &= \pm j_z \\ (\partial_t \pm \partial_y)\, a_y^{\pm} \mp \partial_x b_y - \partial_z a_y &= \mp j_z & (\partial_t \pm \partial_y)\, a'^{\pm}_y \mp \partial_z b_y + \partial_x a_y &= \pm j_x \\ (\partial_t \pm \partial_z)\, a_z^{\pm} \mp \partial_y b_z - \partial_x a_z &= \mp j_x & (\partial_t \pm \partial_z)\, a'^{\pm}_z \mp \partial_x b_z + \partial_y a_z &= \pm j_y. \end{aligned} \tag{3.13}$$

The validity of this set of equations can quickly be verified by explicitly writing out the eigenvalues and using Eqn. (2.30) and (2.31). The form of these equations is very similar to the standard advection equation

$$(\partial_t \pm \boldsymbol{\nabla})\, \boldsymbol{a}^{pm} = 0. \tag{3.14}$$

where the solutions are waves traveling to the positive or negative direction. The temporal evolution of such an equation would be extremely easy to solve numerically for $\Delta t = \Delta x$. To get the fields for the next time step one simply has to copy the transformed fields to the neighboring mesh node in the respective direction and transform backwards. The great advantage over the FDTD scheme is that this solution is exact for waves traveling along a coordinate axis. The cross terms in (3.13) are the result of the multidimensional coupling of non-planar waves or planar waves that are not aligned along one of the coordinate axis. One straight forward solution would be to extend the Leapfrog scheme and add the cell-centered current and the derivatives of the untransformed variables as finite centered differences to the particular solutions of (3.14) [152]. This however reintroduces dispersive terms. A different approach that is very easy to implement numerically and is used by the code employed in this thesis is to solve the equations (3.13) successively and calculate the new fields before doing the transformation of the next eigenvalue and solving the next equation. This way the cross terms cancel out in vacuum and can be written by currents in media. Consequently the field propagation in vacuum remains free of numerical dispersion for waves traveling along one of the coordinate axes

3.2 Simulation Simplifications

In the present work the code `iPICLS` [147] was used in its 2D3V version. Most important physics can be captured by only considering a 2D plane section (z-x) and extending to 3D by assuming invariance in the third dimension. This greatly reduces both the necessary particles and mesh nodes and therefore considerably speeds up the simulation and eases the memory requirements. Such a simulation is called 2D3V, since spatial coordinates are only considered as 2D but particle momenta are 3D. `iPICLS` is a very efficient powerful PIC code that allows to simulate large plasma volumes and particle numbers limited only by the computational resources available to the scientist. It can be run massively parallel on many CPU cores at once. The possibility to include collisional kinetic effects and collisional ionization as well as field ionization provides the ability to include all relevant physical effects. The EOM are integrated by a 4th order Runge-Kutta-scheme and the Maxwell equations are solved by the directional splitting method. The latter offers a field propagation virtually free of numeric dispersion in vacuum and therefore allows the use of comparably large mesh periods.

Yet, due to computational demands it is not feasible to run parameter scans using the full realistic solid plasma density. This is due to the fact the mesh period must be less than 1/4th of the shortest plasma wavelength and the time step must be less than 1/4th of the plasma frequency. Consequently, the simulated density has to be reduced which brings the solid plasma closer to transparency. This is of importance especially at ultra-high intensities where the relativistic mass increase of hot electrons leads to a reduction of the plasma frequency. It therefore has to be made ensured that at all times where the real solid would be opaque, the simulated model plasma is also opaque, i.e. $n_e > \gamma n_c$. If ionization effects are to be included in the simulation it has also to be considered that the reduced density model plasma requires less energy to reach a certain ionization state than the real solid plasma. The reduction of plasma density also brings the plasma closer to a collisionless plasma, which can be corrected by numerically increasing the collision frequency. The effect on radiation losses is negligible, since they account only for less than a permille of the total energy for the hot electrons during their passage through a micrometer scale thick foil.
Test simulations performed in the frame of this work have confirmed the above. Simulations with reduced model densities show the same hot electron dynamics and same qualitative ion dynamics with only slightly increased laser absorption and ion energies [116, 29] than simulations with higher, more realistic densities.

Experimentally, ultra-intense laser pulses are always preceded by prepulses or amplified

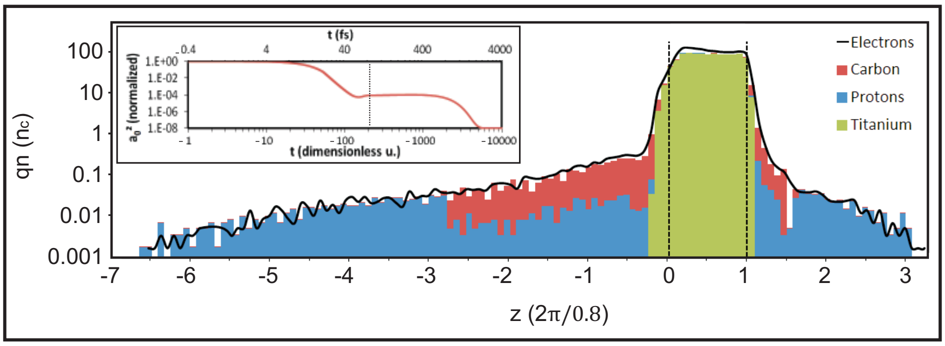

Figure 3.2: PIC simulation results for the plasma distribution after a realistic laser prepulse (DRACO) of approx 2 ps with $10^{-4}a_0^2$ where $a_0 = 21.6$, $w_0 = 2.1 \cdot 2\pi$, including ionization, collisions, $n_{e,0} = 120$ when fully ionized, laser incidence angle 35° with respect to target normal. Laser temporal profile shown in inset, time given relative to the time the maximum hits the target. Dotted line marks the time when preplasma distribution was measured. Plasma distribution for electrons (black line) and ions (color bars show charge distribution $q_i n_i$) along the laser axis. Given length scales correspond to µm for a laser with $\lambda = 0.8$ µm. The 1 µm thick target is located at z=0 and has a transverse width of 120 µm.

spontaneous emission (ASE). Their duration and intensity determine density and expansion of a preplasma developing in front of the target and at the rear side prior to the main pulse. However, prepulses and ASE occur on timescales of several picoseconds up to nanoseconds, which is many orders of magnitude more than typical timescales for solid density plasma oscillations. Consequently, it is not feasible to routinely simulate them in PIC simulations, other than in single large scale simulations. Hydrodynamic simulations are the method of choice for the long scale plasma evolution during the ps or ns pre-pulse plasma evolution.

Fig. 3.2 shows the simulated preplasma distribution after a realistic ps prepulse as it was measured for the DRACO laser system. This consisted of a long prepulse with intensity $10^{-8}a_0^2$ and a shorter prepulse of approx. 2 ps with intensity $10^{-4}a_0^2$ (see inset Fig. 3.2). Two preplasma scale lengths can be identified at the front surface of the foil: A short, few tenths of λ over-critical preplasma and a long few λ under-critical preplasma. In many cases it is therefore sufficient to simply add exponential preplasmas at the surfaces, mimicking the effect of pre-pulses and ASE. This was done in the present work, when such exponential preplasmas were added in front of a solid foil to study qualitatively the effects of prepulses and ASE. However, it is important to note that a more realistic treatment would require to also include a finite rear-side plasma gradient [115] and a gradient of temperatures and ionization levels, that however are not expected to significantly alter qualitatively the effects discussed in this thesis.

An exemplary input script, density profile definition file and description of the output files generated by PICLS can be found in Appendix A.

Chapter 4

Results

The results presented in this thesis focus on enhancing the ion maximum energy in the TNSA regime, namely by virtue of

- Increasing the laser intensity (Section 4.1)
- Ultrathin foils & stacks of ultra-thin foils (Section 4.2)
- Limiting the target foil transverse size (Section 4.3.1)
- Flat top cone targets (Section 4.3.2).

Within the framework of this dissertation those methods were studied both numerically and analytically with respect to their potential benefit in realistic experimental environments and to their potential scalings to higher laser intensities. All methods have in common that within the frame of this work the subsequent acceleration of ions still is governed by the well established TNSA mechanism, still exhibiting the beneficial properties ascribed to TNSA, including small source size, low emittance and high bunch density (see Section 2.3.1 for more details on TNSA). All methods influence more than one parameter at once with the aim of populating the hot electron ensemble more efficiently and to increase its average kinetic energy. It therefore is no simple task to find a global optimum for the laser target, optimizing intensity, thickness, shape, width and micro structure at the same time. Rather, in this work the individual fundamental mechanisms are studied with respect to their influence on electron density and temperature and the subsequent increase of proton energies. Before starting this discussion, a more detailed analysis of the ion acceleration from conventional flat foils and the importance of the electron temperature and density is given in the following section.

4.1 Ion Acceleration at a Flat Foil

Throughout this section it will be assumed that the target is a large flat solid foil with a thickness d sufficiently large so that the ion acceleration is dominated by the target normal sheath acceleration at the foil rear side. It is further assumed that the time the electrons need to fill the complete target volume is larger than the ion acceleration time. Those assumptions are valid for thick target foils, a small laser focus and a short laser pulse duration and ensure that the hot laser accelerated electrons interact only once with the ions at the rear side, so that the adiabatic phase can be neglected [112]. They may be violated for example in ultra-thin foils or mass limited targets, which will be dealt with later in Section 4.2 and 4.3.1.

The expansion of the rear side sheath can then be described by the isothermal self-similar expansion model introduced in Section 2.3.1.1 which predicts a maximum ion energy given by Eqn. (2.63). The hot electron temperature is a critical parameter together with the hot electron density, which are related to each other and to the laser strength parameter a_0 and laser absorption η by Eqn. (2.66). Hence, if the laser parameters are known it is sufficient to additionally know either n_e^{hot} or T_e^{hot} to solve Eqn. (2.63) for the maximum ion energy.

As a first approximation, Wilks et al. suggested to use the ponderomotive energy scaling (2.25) for an estimate of the electron temperature [49, 98]. Equation (2.66) then gives credit to the popular use of $n_e^{\mathrm{hot}} \approx \gamma n_c$. However, as was mentioned in Section 2.2.4, the ponderomotive scaling gives only good approximations for the electron temperature for small intensities, i.e. $a_0 \ll 1$ (Fig. 2.3). For larger values of a_0, the experimentally obtained temperatures are significantly below the ponderomotive energy. PIC simulations performed for and presented in this section also follow this trend.

It has been suggested that the deviations are a direct result of plasma heating by resonance absorption (Sec. 2.2.4.1). However, based on principal physics arguments the absorption is widely attributed to the $\boldsymbol{v} \times \boldsymbol{B}$ absorption mechanism as explained before, making a different explanation for the observations necessary. The explanation presented in [53], which circumvents the question of a specific absorption model by introducing a black box model and using general conservation laws, may not strictly hold true, as was discussed in the footnote on page 24. Hence, a new model for the temperature scaling with laser intensity must be developed in order to solve Eqn. (2.63).

In the following, a general argument based on a careful treatment of electron energy averaging will be developed. It will be applied for the two important exemplary cases of a

Reprinted with permission from T. Kluge, T. E. Cowan, A. Debus, U. Schramm, K. Zeil and M. Bussmann, Physical Review Letters, Vol. 107, page 205003 (2011). Copyright (2011), American Physical Society.

solid with step-like density gradient and considerably preplasma, respectively. The results will then be used in Sec. 4.1.3 together with Eqn. (2.63) to predict the maximum ion energies from flat foils. Those predictions will then be compared to available experimental data and the energies predicted by the alternative ion acceleration model of Schreiber et al. (see Section 2.3.1.2). Conclusions will then be drawn that allow the optimization of the ion acceleration process in the short and long pulse regime (Sec. 4.2 and 4.3).

4.1.1 Setup and simulations

The numerical simulations performed in this section were done using the two-dimensional, three velocity component fully relativistic electrodynamic PIC code `iPICLS`2D (Sec. 3), including ionizations and collisions. The model target is a flat foil with thickness 10π of copper ions, covered with a 4π thick proton layer mimicking the experimentally mostly present surface contamination layer. To reduce computational demands,the electron density when fully ionized was set to $10n_c$, $40n_c$ or $100n_c$ for intensities with $a_0 < 8.5$, $8.5 \leq a_0 \leq 20$ or $a_0 = 100$. Those choices ensure that the laser does not burn through the target and the

Parameter	Value
Geometry	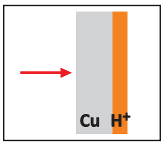
laser strength a_0	1-100
pulse shape	Gaussian[1]
laser waist w_0	4π
pulse duration	100
electron density $n_{e,0}$	10 ($a_0 < 8.5$), 40 ($8.5 \leq a_0 \leq 20$), 100 ($a_0 = 100$)
foil thickness d	$10\pi\ (Cu) + 4\pi\ (H^+)$
ions (electrons) per cell	4 (116)
cells (time steps) per laser wavelength	$25 \times \sqrt{n_{e,0}/10}$
box size ($x \times z$)	$120\lambda \times 240\lambda$ ($40\lambda \times 40\lambda$ for $n_{e,0} = 100$)
including collisions/ ionization	yes/yes

[1] A test simulation with a *plane wave* at $a_0 = 100$ yielded a similar temperature as the Gaussian profile at the pulse maximum.

Table 4.1: Parameters used for the simulations in this section.

foil behaves as a solid throughout the laser interaction. It will be discussed later in section 4.2 how a reduced thickness and/or density may influence the heating and acceleration processes. Table 4.1 summarizes the most important simulation parameters.

4.1.2 Exact electron temperature scaling

4.1.2.1 Temporal average of the electron quiver

In the following it will be shown that a careful ensemble average of the single electron energies can successfully explain the deviation seen between the ponderomotive scaling (Eqn. (2.25)) and experimental and simulated temperatures. The discussion is based on the single electron motion described in Sections 2.2.2 and 2.2.3 and the main ideas were first published by the author in [153]. It was discussed, that in the interaction with a solid the single electron energy is not given by the ponderomotive force since strictly speaking the pre-requisites for ponderomotive electron acceleration, i.e. a slowly varying envelope and the consideration of the slowly varying average force only, are not fulfilled at a steep density interface. However, neglecting any longitudinal forces – they can be assumed to be balanced by the plasma reaction in first approximation in the laser intensity – it was shown that the electrons undergo a transverse motion and the cycle averaged energy is given by Eqn. (2.50),

$$\langle\gamma(t)\rangle_t = \left\langle\sqrt{1+p_x(t)^2}\right\rangle_t, \tag{4.1}$$

which has similar structure as the ponderomotive energy given by Eqn. (2.25) and in fact coincides with it for low intensities. One has to keep in mind that for many cases, e.g. where $a_0 \geq n_e$ (relativistically induced transparency) or preplasma scale lengths greater than half a wave length (non-negligible skin-length), the prerequisite of vanishing longitudinal forces and an almost transverse electron motion ceases to be valid. However, assuming the prerequisites of Eqn. (4.1) to be fulfilled, the temporal average can be given in an explicit form with $p_\mathrm{x}(t) = -\mathrm{a}_0 \sin t$ from conservation of the transverse canonical momentum assuming electrons initially at rest[1] (Eqn. (2.10)). The temporal average then reads

$$\langle\gamma_\mathrm{quiver}\rangle_t = \frac{1}{2\pi}\int_0^{2\pi}\sqrt{1+a_0^2\sin^2 t}\mathrm{d}t \tag{4.2}$$

---

[1] Here and in the following the reflected wave is neglected, compare footnote on page 5.

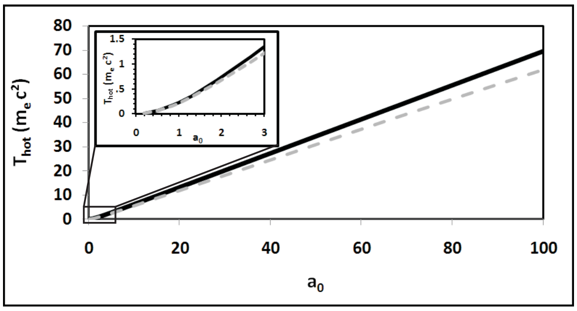

Figure 4.1: Comparison of ponderomotive scaling Eqn. (2.25) (solid black) with average transverse quiver energy averaged relativistically but ignoring longitudinal fields Eqn. (4.3) (dashed gray). The two coincide for $a_0 \ll 1$ while for $a_0 \gg 1$ the ponderomotive scaling overestimates the average quiver energy by $\approx 10\%$.

which can be rewritten using the complete elliptical integral of the second kind, [2] $F\left(-a_0^2\right)$,

$$\boxed{\langle \gamma_{\text{quiver}} \rangle_t = \frac{2F\left(-a_0^2\right)}{\pi}} \tag{4.3}$$

The energy given by this equation still agrees rather well with the ponderomotive energy even for large $a_0 \gg 1$ where it gives only a small correction by a factor of less than $2^{3/2}/\pi$ (see Fig 4.1). It can therefore not explain the large deviation seen between experiments and the ponderomotive scaling for $a_0 \gg 1$ (Fig. 2.3).

4.1.2.2 Ensemble average of laser accelerated electrons

The starting point of the following discussion is the fact that the electrons are generally not distributed uniformly in the time domain as implicitly assumed by averaging the single electron energy $\gamma(t)$ as done in Eqn. 4.1. To be more explicit, Eqn. (4.2) averages the motion of a *single* electron at the surface of a solid, but the temperature is determined by the average over *all* electrons of the ensemble at a given time,

$$\mathrm{T}_e^{\mathrm{hot}} = \frac{\int \gamma f_\gamma d\gamma}{\int f_\gamma d\gamma} - 1. \tag{4.4}$$

where

$$f_\gamma = \frac{dN}{d\gamma},$$

is the electron energy distribution function. When this simple time average coincides with the ensemble average, the system is called *ergodic*. In the present case of a laser driving

---

[2] There exist different definitions of the complete elliptical integral of the second kind. Here it is defined as $F(m) = \frac{\pi}{2}\left\{1 - \sum_{n=0}^{\infty}\left[\frac{(2n-1)!!}{2n}\right]^2 \frac{m^n}{2n-1}\right\}$.

the electrons and negligible stochastic electron motion, the system is both not closed and not chaotic. The electron trajectories are highly deterministic and hence the system is in fact not ergodic. This implies that generally f_γ cannot be assumed to be constant, so without implying a certain laser absorption mechanism, Eqn. (4.2) then also has to include a non-trivial distribution function f_t, so that

$$\mathrm{T}_e^{\mathrm{hot}} = \langle \gamma(t) f_t \rangle_t - 1 = \frac{\int_0^{t(\varphi=2\pi)} \gamma(t) f_t dt}{\int_0^{t(\varphi=2\pi)} f_t dt} - 1. \tag{4.5}$$

where $\gamma(t)$ is the temporal evolution of the single electron energy and the distribution function $f_t = dN/dt$ determines how many electrons there are in the specific phase of the single electron motion.

In the following, a general theoretical model for this distribution function is developed which does not rely on the specific laser absorption mechanism but takes into account the temporal dependence of the number of accelerated electrons. It therefore can be applied in a broad class of situations and for various absorption mechanisms and will be exemplified using the conventional $\boldsymbol{v} \times \boldsymbol{B}$ heating mechanism which is generally dominating for laser interaction at arbitrary a_0 (see Section 2.2.4) as long as the foil is opaque to the laser and the density gradient is small compared to a wavelength.

4.1.2.3 Lorentz invariant formulation of the electron distribution

Since the electron distribution f_t is difficult to derive ab initio, it is reasonable to first derive $f_\varphi = dN/d\varphi$ and then use the relation

$$f_t = \frac{dN}{d\varphi}\frac{d\varphi}{dt}. \tag{4.6}$$

This approach has the advantage that one can use the Lorentz scalar property of both the particle number N and the laser phase φ.

Before deriving f_φ for the general case, it is instructive to first consider the example of a plane wave with $a(\varphi) = b(\varphi) = a_0 \cos\varphi$ interacting with free electrons. From the conservation of energy flux density it follows

$$\frac{d(\Delta W_F)}{dt} + \frac{d(\Delta W_K)}{dt} = 0 \tag{4.7}$$

where

$$\Delta W_F = -\eta \frac{a_0^2}{2} \cos^2 \varphi \Delta\varphi \tag{4.8}$$

is the absorbed field energy density inside a box of width Δz at a given time t (note that then $\Delta z = -\Delta\varphi$), assuming a phase independent absorption fraction η, and

$$\Delta W_K = \sum_{i=1}^{\Delta N(\varphi)} \left(\gamma_i(\varphi_i) - 1\right) \tag{4.9}$$

is the sum of the kinetic energy of all the $\Delta N(\varphi)$ electrons with $\varphi_i \in [\varphi, \varphi + \Delta\varphi]$. The average electron energy of the electrons inside the length element can be defined as $\bar{\gamma}(\varphi) \equiv \sum_{i=1}^{\Delta N(\varphi)} \left[\gamma_i\left(\varphi_i\right)\right] / \Delta N(\varphi)$. Assuming the laser intensity has been ramped up adiabatically, it is simply $\gamma - 1 = a_0^2 \sin^2 \varphi / 2$ for a single free electron in a plane wave (Eqn. (2.21)). Setting the average electron kinetic energy $\bar{\gamma}(\varphi) - 1$ proportional to the single electron adiabatic energy, 4.9 can be written as

$$\Delta W_K = \left(\bar{\gamma}\left(\varphi\right) - 1\right) \frac{\Delta N}{\Delta\varphi} \Delta\varphi = \frac{a_0^2}{2} \sin^2\left(\varphi\right) \frac{\Delta N}{\Delta\varphi} \Delta\varphi. \tag{4.10}$$

Now putting (4.8) and (4.10) into Eqn. (4.7) it follows

$$\eta \frac{a_0^2}{2} \sin\left(2\varphi\right) \Delta\varphi = \frac{a_0^2}{2} \left(\sin\left(2\varphi\right) \frac{\Delta N}{\Delta\varphi} + \sin^2\left(\varphi\right) \frac{d}{dt} \frac{\Delta N}{\Delta\varphi} \right) \Delta\varphi \tag{4.11}$$

and hence it is

$$\frac{d}{dt} \frac{\Delta N}{\Delta\varphi} = \frac{\sin 2\varphi}{\sin^2 \varphi} \left(\eta - \frac{\Delta N}{\Delta\varphi} \right)$$

with the general solution

$$\frac{\Delta N}{\Delta\varphi} = \frac{1}{2} \left(\eta - \eta \cot^2 \varphi \right) + c_1 \csc^2 \varphi. \tag{4.12}$$

From the boundary condition of an adiabatic electron acceleration inside the pulse rising edge it follows that the electron energy flux density (RHS of (4.11)) must be vanishing at

$\varphi = 0$, so that $c_1 = 0.5\eta$.[3] It follows the trivial solution

$$\boxed{\frac{\Delta N}{\Delta\varphi} = const.} \tag{4.13}$$

This is an important result, since it conveys that the electrons are distributed homogeneously in the laser phase, while the naive approach of simply time averaging the single electron energy implicitly assumes $dN/dt = const.$ Rather, it is found that the single electron energy must be averaged with respect to the phase, so the electron ensemble average simply reads

$$\begin{aligned} T_e^{hot} = \bar{\gamma} - 1 &= \frac{1}{2\pi}\int_0^{2\pi} \gamma(\varphi) d\varphi \\ &= \frac{1}{2\pi}\int_0^{2\pi} \frac{a_0^2}{2}\sin^2\varphi d\varphi = \frac{a_0^2}{4}. \end{aligned} \tag{4.14}$$

One realization of this example of quasi-free electrons is the grazing laser incidence onto a target, as it occurs for example in the case of hollow cone targets with curved walls when the laser axis is aligned tangentially to an inner wall surface. The details of the dynamics and processes occurring in this interesting setup are discussed in Sec. 4.3.2. One interesting result is that PIC simulations of laser pulses with strength parameters a_0 between 1 and 20 support the electron temperature scaling (4.14), as shown in Fig. 4.40.

Using the Lorentz-invariance of dN and $d\varphi$, it is possible to derive the same result 4.13 for a more general case. Assuming only an electro-magnetic field where $\boldsymbol{a}\perp\boldsymbol{b}$, specifically dropping any further assumption on the laser field made before, e.g. the plane wave assumption, Lorentz invariance of $d\varphi$ can be easily derived by showing its equality with the Lorentz invariant proper time of the electron using Eqn. (2.13),

$$d\varphi = (1 - \beta_z)\, dt = \gamma^{-1} dt = d\tau.$$

Since dN is a Lorentz scalar, $dN/d\varphi$ must also be a Lorentz scalar. Consequently, assuming a uniform electron distribution at $\tau_0 = 0$ before the laser pulse has been switched on,

$$\left.\frac{dN}{d\varphi}\right|_{\tau=0} = const.,$$

---

[3] In the general case, c_1 can have arbitrary values, reflecting a non-vanishing energy flux at $\varphi = 0$, as for example in the case of an electron jet injected in an EM wave.

the distribution $dN/d\varphi$ will remain uniform for any given electron proper time $\tau_1 > 0$,

$$\left.\frac{dN}{d\varphi}\right|_{\tau=\tau_1} = const. \tag{4.15}$$

The requirement $\tau = \tau_1$ for all electrons is equivalent to the adiabatic ramp-up condition used before, because then the electron motion in the laser wave does not depend on its initial phase $\varphi_i(\tau_0)$.

Instead of assuming a uniform electron distribution in the laboratory time (as implicitly done in Eqn. (2.25) and (4.2), (4.3)) or postulating ad-hoc $\mathrm{n_{hot}} = \gamma \mathrm{n_c}$ (as done in [53][4]), the electrons are now found to be distributed uniformly with respect to the retarded wave coordinate φ, which is equal to the electron proper time. Hence, with (4.6) f_t is given by

$$\boxed{f_t \propto \frac{1}{\gamma}.} \tag{4.16}$$

Substituting this distribution function into Eqn. (4.5), the result reads

$$\boxed{\mathrm{T}_e^{\mathrm{hot}} = \frac{t\left(\varphi = 2\pi\right)}{\int_0^{t(\varphi=2\pi)} \frac{1}{\gamma} dt} - 1.} \tag{4.17}$$

This important relation states that the average kinetic energy of the accelerated electrons is equal to the inverse of the average of the inverse of the single electron kinetic energy $\gamma(t)$ with respect to laboratory time t, where $t\left(\varphi = 2\pi\right)$ is the time duration of the electron motion period. In other words, the electron temperature is obtained by averaging the single electron energy with respect to the phase φ or to the electron proper time. Consequently, the temperature of an electron ensemble cannot be derived simply by averaging the single electron energy over the laboratory time, so Eqn. (4.1, 4.3) can generally not be used to derive $\mathrm{T}_e^{\mathrm{hot}}$. Only for low intensities and hence small $|\boldsymbol{\beta}| \ll 1$ the temperature given by Eqn. (4.17) converges with the unweighted time averaged single electron energy $\langle\gamma\rangle_t$.[5]

---

[4] In [53] the symbol γ actually refers to the average Lorentz factor, averaging the single-electron temporal energy evolution over a laser period.

[5] This can be quickly seen as follows. First Taylor expanding $\gamma(t)$ and only considering terms in first order of a_0^2, $\gamma(t)^{-1} \cong 1 - a(t)^2/2$ and writing the integral in the denominator of Eqn. (4.17) as the sum $2\pi - \sum_{n=0}^{N-1} \frac{a(t_n)^2}{2} \Delta t$ (where $t_n = n\Delta t$ and $\Delta t = 2\pi/N$ and it was used that for $a_0 \ll 1$ it is $t(\varphi = 2\pi) = 2\pi$),

4.1.2.4 Ensemble average of the electrons at flat solids with negligible preplasma scale length

In the following the implications of (4.17) in the important case of laser normal incidence onto a solid are discussed. This case is especially interesting and resembles the general case for ultra-relativistic laser intensities, since then the acceleration of electrons is dominated by the relativistic Lorentz force and hence the laser incidence angle becomes less important. In the presence of a density gradient and/or high laser intensities most heating mechanisms that can play a role at oblique laser incidence are suppressed [70, 26] (see Sec. 2.2.4) and hence the electron temperature approaches that of normal incidence.

First the case of a very steep density gradient is treated, i.e. the situation where the penetration of the laser into the target can be neglected and longitudinal laser forces are balanced by the plasma reaction (cf. Sec. 2.2.3 and the discussion in Sec. 4.1.2.1). In the next section the more realistic case of the presence of a preplasma will be considered. There the laser pulse is reflected at the critical density surface ($n_e = \gamma$) and hence the penetration depth of the laser (local skin depth) can not be neglected anymore.
In the case of a very steep density gradient the electron dynamics can be approximated to be solely governed by the quiver motion (4.2) in the oscillating electric field of the laser. Eqn. (4.17) can then be evaluated explicitly, leading to the expression

$$\mathrm{T}_e^{\mathrm{hot}} = 2\pi \left[\int_0^{2\pi} \left(1 + a_0^2 \sin^2 t\right)^{-1/2} dt \right]^{-1} - 1 \tag{4.18}$$

which can be expressed using the complete elliptical integral of the first kind[6], $E\left(-a_0^2\right)$, by

$$\boxed{\mathrm{T}_e^{\mathrm{hot}} = \frac{\pi}{2E\left(-a_0^2\right)} - 1.} \tag{4.19}$$

Simple analytic expressions for $\mathrm{T}_e^{\mathrm{hot}}$ in units of $m_e c^2$ can be given for the extreme cases

---

the temperature Eqn. (4.17) from ensemble averaging can be Taylor expanded, reading

$$\mathrm{T}_e^{\mathrm{hot}} = \frac{1}{2\pi} \sum_{n=0}^{N-1} \frac{a(t_n)^2}{2} \Delta t + O(a_0^4) \cong \left\langle \frac{a^2}{2} \right\rangle_t .$$

This coincides with $\langle\gamma\rangle_t - 1 \cong \left\langle p_x^2 \right\rangle_t /2$ from Eqn. (2.51).

[6] There exist different definitions of the complete elliptical integral of the second kind. Here it is defined as $E(m) = \frac{\pi}{2} \sum_{n=0}^{\infty} \left[\frac{(2n-1)!!}{2n}\right]^2 m^n$.

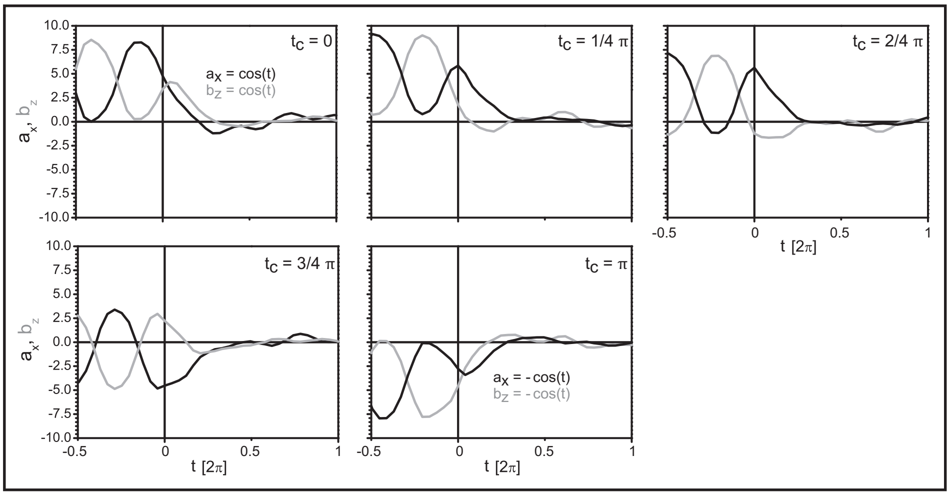

Figure 4.2: Temporal evolution of fields close to the critical density surface at the respective position of a test particle moving forward with c, varying the time t_c at which it crosses $z = 0$. Laser field strength was set to $a_0 = 5$, target density $n_{e,0} = 10$.

$a_0 \ll 1$ and $a_0 \gg 1$,

$$\boxed{\begin{aligned} \mathrm{T}_e^{\mathrm{hot}} &= \frac{a_0^2}{4} + O\left(a^4\right) && (a_0 \ll 1) \\ \mathrm{T}_e^{\mathrm{hot}} &= \frac{\pi a_0}{\ln 16 + 2\ln a_0} + O\left(a^{-1}\right) && (a_0 \gg 1) \end{aligned}}$$

For $a_0 \ll 1$, this is equal to the simple unweighted temporal average (4.3) and the ponderomotive energy, while for $a_0 \gg 1$ it predicts a considerably weaker scaling.

4.1.2.5 Ensemble average of the electrons at flat solids with long preplasma scale length

In the following a more realistic case is analyzed, including a certain amount of preplasma to be present in front of the foil, e.g. due to laser prepulses or ASE, which will give some correction to (4.19). It was mentioned before that the longitudinal motion may not be neglected for large values of a_0 or sufficient preplasma scale lengths. Therefore in this section, after shedding some light on the field structure at the plasma surface, the full electron motion in the fields will be considered.

The field structure at the surface of a solid consists of the incoming and partly reflected wave in front of the critical density surface and an evanescent wave behind. This results in a standing wave pattern for the electric and magnetic fields in front of the plasma, with

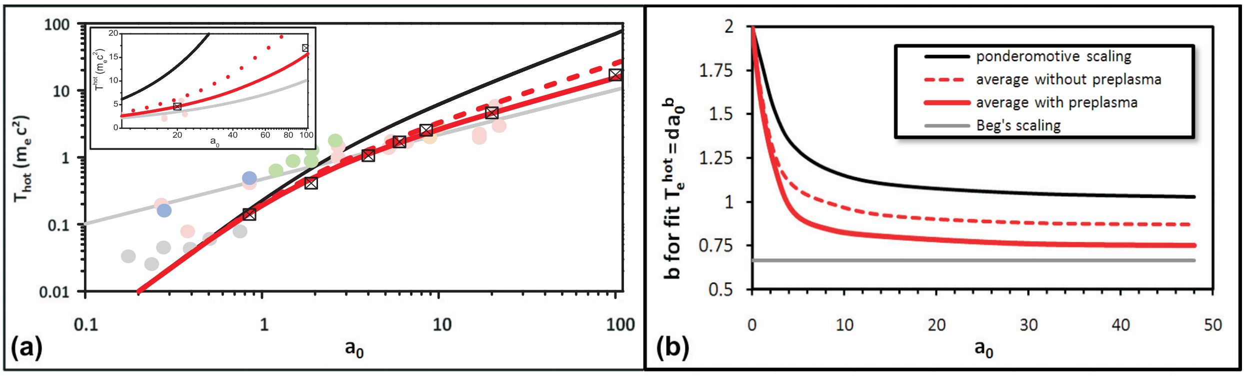

Figure 4.3: (a) Comparison of various temperature scalings (ponderomotive scaling (2.25): solid black; ensemble average for targets without (Eqn. (4.19), red dashed line) and with (Eqn. (4.24), red solid line) preplasma; Beg's empiric scaling (2.29): gray solid) with selected experimental values (circles, for data sources see Fig. 2.3 on page 18) and PIC simulations (squares). The exponent of a local power law fit to the respective scaling laws is plotted in (b).

maxima occurring every $\lambda_0/2$ and the electric field phase shifted in the direction towards the plasma by $\lambda_0/4$ with respect to the magnetic field. The temporal evolution of the electric and magnetic fields seen by a relativistic electron near the surface depends on the time when it starts its movement. To estimate the resulting temporal field evolution seen by the fast electrons, the temporal evolution of the fields on an imaginary test particle moving forward with $\beta_z \approx 1$ is plotted in Fig. 4.2 for the case that the laser can penetrate the overcritical region by more than half a laser wavelength. One is given by $a \approx \pm a_0 \cos t$, $b \approx \mp a_0 \cos t$, where t is measured relative to the time t_c when the test particle crosses $z = 0$. Here, the force on the electron is decelerating, so there is no energy transfer into the plasma in this phase. In the other limit ($t_c = 0$ or $t_c = \pi$) it is

$$\boldsymbol{a} = a_x \boldsymbol{e_x} \approx \pm a_0 \cos t \tag{4.20}$$

$$\boldsymbol{b} = b_y \boldsymbol{e_y} \approx \pm a_0 \cos t. \tag{4.21}$$

In that limit an electron will experience a large longitudinal field in forward direction and can thus detach from the surface, keeping its energy and being absorbed into the foil. The result are bunches emitted into and traveling through the foil at a frequency of $2\omega_0$ and a separation of $\lambda/2$ (Fig. 4.4). Consequently, the total average hot electron energy should be that of the electrons contained within a bunch, i.e. in cases where the local relativistic skin length is larger than half a laser wavelength, $\delta \geq \lambda_0$, one can assume an accelerating field (4.21) for the hot electrons.

(4.16) and therefore (2.14) and (4.17) are still valid. With the above fields and (2.13), (2.14)

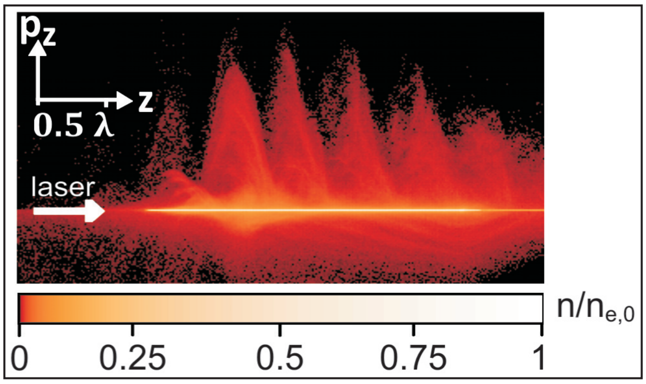

Figure 4.4: Electron phase space density in the z–p_z plane at the time the laser maximum reaches the foil front surface. Electrons are emitted into the target in bunches separated by $\lambda/2$. $a_0 = 5$.

the Lorentz equation for the transverse momentum component reads

$$\frac{dp_x}{dt} = -a_x(t) - \beta_z b_y(t) = -a_0 \left(1 - \frac{p_x^2}{2+p_x^2}\right)\cos t \tag{4.22}$$

This equation resembles a Riccati differential equation and can be solved analytically. The result reads

$$\boxed{\begin{aligned} p_x(t) &= \frac{2}{S(t)} - S(t) \\ S(t) &= \sqrt[3]{\sqrt{(3a_0 \sin t)^2 + 8} + 3a_0 \sin t} \end{aligned}} \tag{4.23}$$

Averaging the inverse $\gamma(t)^{-1}$ over time and taking its inverse according to (4.17), one finally finds an expression for the average electron kinetic energy

$$\boxed{T_e = \frac{2\pi}{\int_0^{2\pi} \left(\frac{S^2}{2} + \frac{2}{S^2} - 1\right)^{-1} dt} - 1} \tag{4.24}$$

which can only be integrated numerically.

Fig. 4.5 shows the spectrum obtained from simulations for a flat foil at $a_0 = 8.5$. The electron temperature is $T_e^{hot} \cong 2.4$ which is in remarkable agreement with the model described above which with (4.24) predicts $T_e^{hot} \cong 2.3$. In fact, the model is in remarkable agreement with the PIC results up to the highest simulated intensity with $a_0 = 100$ where the ponderomotive scaling (2.25) significantly overestimates the hot electron temperature. Figure 4.3 shows a comparison between the ponderomotive scaling (black line) and (4.24) (solid red line), together with selected experimental results extracted from literature and results from PIC simulations performed in the frame of this thesis. The deviation between the model and PIC is less than 5% for all a_0, while for example the scaling presented in [53]

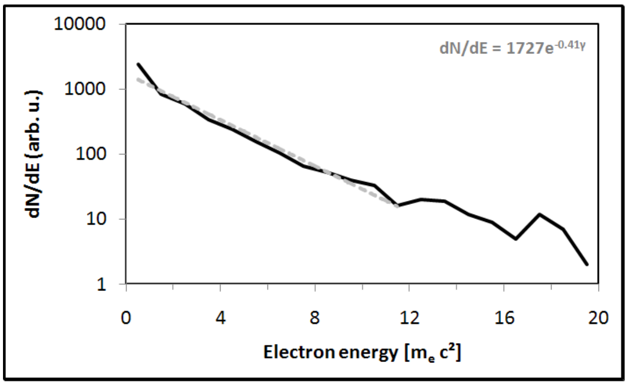

Figure 4.5: Electron spectrum of a flat foil with $a_0 = 8.5$. The gray dashed line shows an exponential fit with temperature $T = 1/0.41 = 2.4$, which is in agreement with the predicted temperature $T = 2.3$ from Eqn. (4.24).

for $a_0 = 100$ is off by more than 30% and the ponderomotive scaling is off by even more than an order of magnitude. Unlike the scaling from [53], the model presented here converges with the ponderomotive scaling for $a_0 \leq 1$ as expected.

Compared to scaling (4.19) (dashed red line), (4.24) yields moderately lower temperature values since in the first case the transverse canonical momentum was assumed to be conserved, which is not true in the latter case for the fields (4.21) assumed in the critical density region (Fig. 4.6). While the electron gains transverse velocity, its longitudinal momentum increases due to the $v_x \cdot B_y$ component of the Lorentz force which in turn reduces the transverse net force via the $v_z \cdot B_y$ component. In the case of a plane wave where the transverse canonical momentum is conserved, this latter reduction is exactly compensated by a slower phase-slippage in the traveling wave and hence a longer time of a high transverse electric field. This results in the same transverse momentum evolution as if the electron were fixed in z-direction (pure quiver motion, cp. $\boldsymbol{v} \times \boldsymbol{B}$ heating in Sec. 2.2.3). In the present case however the pure temporal dependence of the evanescent wave prohibits such a compensation and the transverse momentum reduces compared to an electron fixed in z-direction due to the reduced net force in transverse direction. This results in an overall reduction of the total energy as compared to the pure quiver motion.

4.1.3 Maximum ion energies

In this section the maximum proton energies from a flat foil are estimated based on the model of a plasma expanding into a vacuum (see Sec. 2.3.1.1). The maximum ion energies in this model are given by Eqn. (2.63), which requires the knowledge of the hot electron temperature and density. In the very basic case of normal laser incidence on a flat foil, the electron temperature is determined by Eqn. (4.19) or (4.24) which can lead to significant differences in the maximum ion energy compared to the use of the ponderomotive scaling

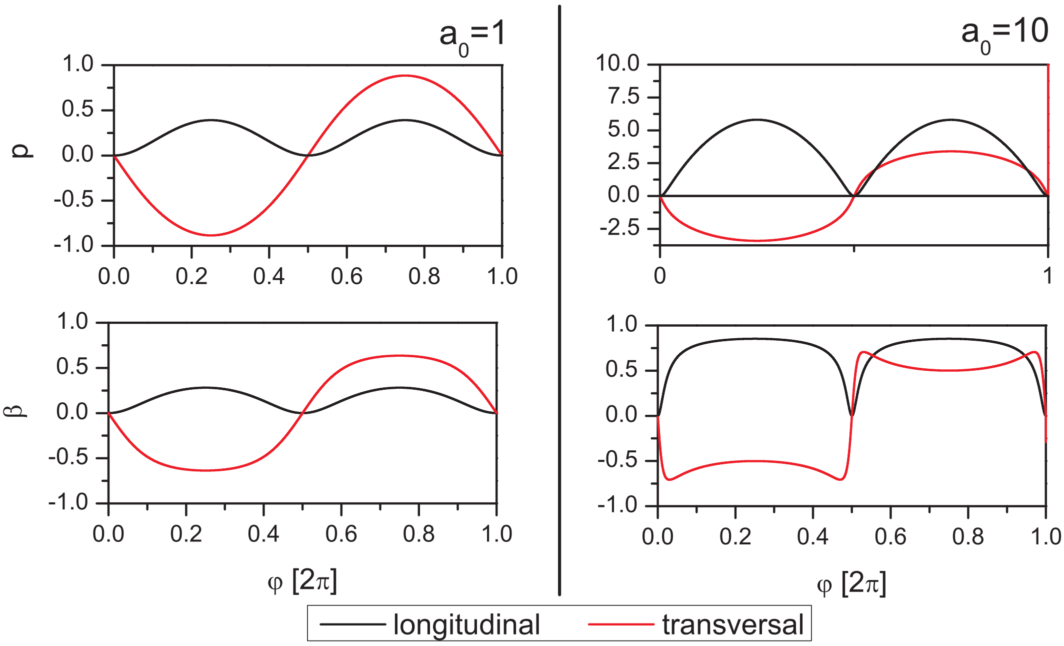

Figure 4.6: Trajectories of an electron in fields $a(t) = -b(t) = a_0 \cos(t)$ in momentum-phase space (top) and velocity-phase space (bottom) for the longitudinal (transverse) components p_z, β_z (p_x, β_x) given by the black (red) lines. The electron is assumed to be at rest at $\varphi_0 = 0$.

Eqn. (2.25). The two limits of short and long pulse duration will be discussed – the longer the pulse duration, the more does the temperature influence $\varepsilon_{\max}$ and the more important becomes the correct modeling of the electron temperature scaling (Fig. 4.10). This leads to conclusions which will be important for the optimization of the laser absorption and electron dynamics in the following sections.

The ion maximum energy formula (2.63), taking into account the laser absorption and temperature dependent hot electron density Eqn. (2.66) and the ion plasma frequency (2.58), can be rewritten as

$$\varepsilon_{max} = 2T_e^{hot}\left[\ln\left(a_0 t_p\sqrt{\frac{Z\eta g}{2em_iT_e^{hot}}} + \sqrt{(a_0t_p)^2\frac{Z\eta g}{2em_iT_e^{hot}}+1}\right)\right]^2 \tag{4.25}$$

where e is the Eulerian number, Z is the ion charge state, m_i is the ion mass, η is the laser absorption fraction and g is the geometric broadening of the electron bunch from the front surface to the rear surface of the foil with thickness d due to its divergence angle α,

$g = w_0^2/\left(w_0 + d\tan\alpha\right)^2$. Analogous to the discussion in Sec. 2.3.1.2, a reference time

$$t_{ref}^{PEM} = \frac{\sqrt{2e}}{\omega_{pi}} = \frac{1}{a_0}\sqrt{\frac{2em_i T_e^{hot}}{Z\eta g}} \tag{4.26}$$

can be defined, so that Eqn. (4.25) can be rewritten as

$$\varepsilon_{max} = 2T_e^{hot}\left[\ln\left(t_p/t_{ref}^{PEM} + \sqrt{\left(t_p/t_{ref}^{PEM}\right)^2 + 1}\right)\right]^2. \tag{4.27}$$

For the limits of $t_p \ll t_{ref}^{PEM}$ and $t_p \gg t_{ref}^{PEM}$ it then follows

$$\boxed{\begin{aligned} &\varepsilon_{max} = 2T_e^{hot}\frac{t_p^2}{\left(t_{ref}^{PEM}\right)^2} = \frac{Zg}{em_i}\eta a_0^2 t_p^2 && t_p \ll t_{ref}^{PEM} \qquad (4.28)\\ &\varepsilon_{max} = 2T_e^{hot}\ln^2\left(2\frac{t_p}{t_{ref}^{PEM}}\right) && t_p \gg t_{ref}^{PEM} \qquad (4.29)\end{aligned}}$$

These PEM predictions are in good agreement with the results obtained in the frame of the model by Schreiber [113, 24] for the two limits (see Sec. 2.3.1.2, Eqn. (2.70)). In the limit of short pulse durations one consistently finds that the ion maximum energy is proportional to the irradiation time t_p (proportional to the approximate ion acceleration duration) multiplied with the total absorbed energy density $\eta a_0^2 t_p/2$ (proportional to the approximate sheath field strength). Hence at fixed pulse duration the maximum ion energy is *proportional to the laser intensity* (assuming an intensity-independent laser absorption η) and *independent of the electron temperature.* For longer pulse durations the influence of laser absorption coefficient becomes smaller and the importance of the hot electron temperature rises. Then the correct modeling of the hot electron temperature becomes more important. This fact is illustrated in Fig. 4.7, which compares the proton maximum energy scalings expected from (4.25) for ponderomotive electron temperature scaling (2.25) and for scaling (4.24). For long pulse durations in the order of typically $t_p \approx 100 - 1000$ and considering that in most practical cases of currently available short pulse laser systems t_{ref}^{PEM} is in the order of $30 - 100$, the logarithm in Eqn. (4.29) becomes approximately proportional to $(t_p/t_{ref}^{PEM})^{1/5}$ and therefore

$$\varepsilon_{max} \propto T_e^{hot}\left(\frac{t_p}{t_{ref}^{PEM}}\right)^{2/5} \propto \left(T_e^{hot}\right)^{4/5}\left(t_p a_0\right)^{2/5}\left(Zg\eta\right)^{1/5}$$

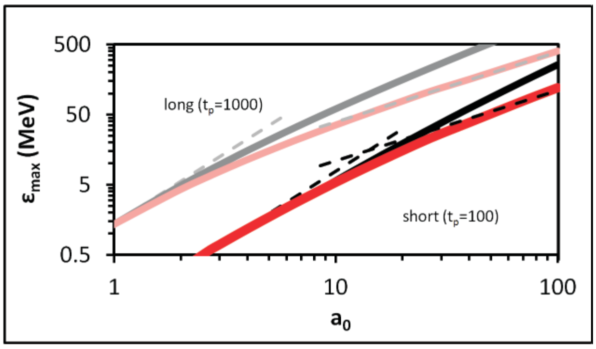

Figure 4.7: Comparison of proton maximum energy as a function of a_0 as predicted from the PEM model (Eqn. (4.25)) for short pulse ($t_p = 100$, dark) and long ($t_p = 1000$, light). The black/ gray curves are obtained assuming the ponderomotive temperature scaling (Eqn. (2.25)), the red lines assuming the temperature scaling (4.24). For comparison, the limits $\varepsilon_{max} \propto a_0^2$ (small a_0) and $\varepsilon_{max} \propto a_0$ (large a_0) are given by dashed lines.

and with $T_e^{hot} \propto a_0^{0.75}$ from Eqn. (4.19) (or $T_e^{hot} \propto a_0^{0.88}$ from Eqn. (4.24), see Fig. 4.3b) one derives the result

$$\boxed{\varepsilon_{max} \propto \eta^{1/5} t_p^{2/5} a_0^{\varsigma}} \tag{4.30}$$

with $\varsigma = 1.0$ ($\varsigma = 1.1$). This important scaling fits the available experimental data reasonably well, as can be verified by comparing it to Fig. 2.8 on page 37 which presents a compilation of all available data up to 2009. A power fit to the data yields a dependency of the proton maximum energy from the laser intensity of $\varepsilon_{max} \propto I^{0.68}$. In terms of the dimensionless laser strength parameter a_0 this corresponds to $\varsigma \approx 1.36$, which is surprisingly close to the result (4.30)[7]. This is especially surprising since the assumptions that had to be made in deriving (4.30) are rather crude, e.g. a one dimensional expansion, a limitation of the expansion time to the pulse duration and a constant absorption coefficient and geometric parameter g.

Yet, one has to be cautious in interpreting the pure fact that the model fits the experimental data as an evidence confirming Eqn. (4.27) and (4.24). Since there are many parameters entering the model equations which are experimentally unknown or error-prone, a model can be easily made to fit everything – a fact that was pointed out already by von Neumann[8] as reportedly quoted by Fermi [154].

Eqn. 4.27 predicts the existence of an optimum pulse duration for a given fixed laser pulse energy. This optimum pulse duration depends on the laser pulse energy, focal spot size, laser wavelength, target thickness and electron divergence. Fig. 4.8 shows the optimum pulse duration for a set of parameters as it could be expected for a short pulse laser system

---

[7] It is important to mention that Fig. 2.8 neglects all other dependencies than the laser intensity, the power fit effectively averaging over all other parameters. By comparing the resultant intensity power law to the laser strength parameter power law (4.30) it was used that the laser wavelength λ is with $(0.9 \pm 0.1)\,\mu\mathrm{m}$ the same for all laser systems

[8] Dyson actually reports in [154] about Fermi quoting von Neumann saying 'with four parameters I can fit an elephant, and with five I can make him wiggle his trunk,' a fact that was proven only recently in [155]

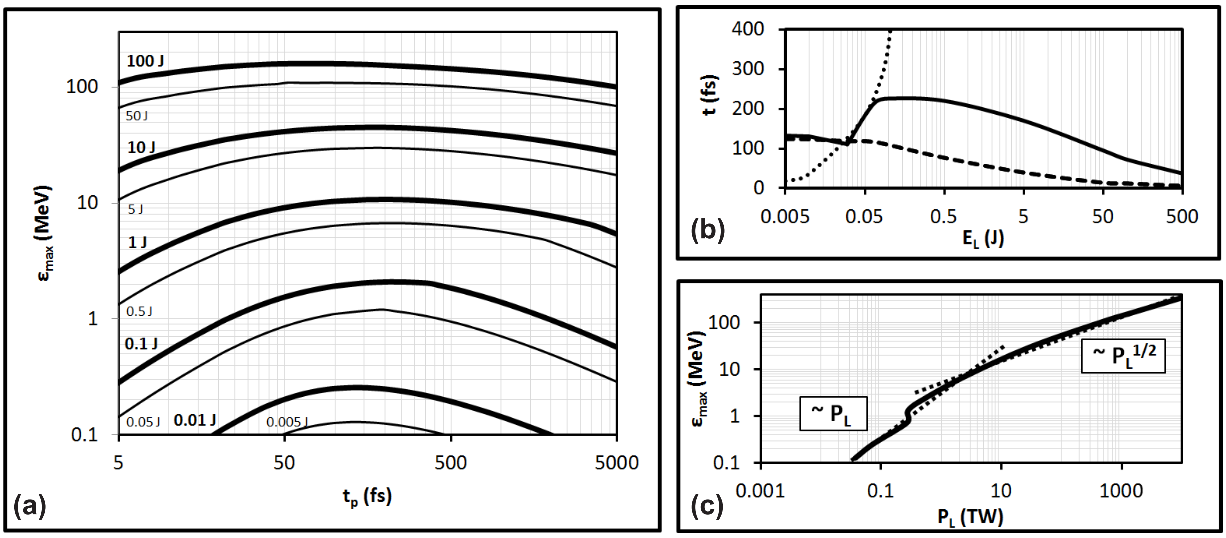

Figure 4.8: **(a)** Maximum proton energy as a function of the pulse duration from the PEM (Eqn. (4.24) and (4.27)) for laser parameters matching DRACO-like Ti:Sa laser systems ($\lambda = 0.8\,\mu\text{m}$, $w_0 = 2\,\mu\text{m}$) and thin foil targets (foil thickness $d = 2\,\mu\text{m}$, electron divergence 10° half opening cone). **(b)** Optimum pulse duration t_p^{opt} (solid), reference time $\pi \cdot t_{ref}^{PEM}$ at t_p^{opt} (dashed) and the time $t_p^{a_0=1}$ at which $a_0 = 1$ (dotted) as a function of the laser pulse energy $\mathrm{E_L}$. **(c)** Maximum proton energy ε_{max} as a function of the laser peak power $\mathrm{P_L}$ (assuming the pulse duration to be optimum). Dotted lines are the best fit with a power law, for small peak power (corresponding to $t_p^{opt} > t_p^{a_0=1}$) $\varepsilon_{max} \propto \mathrm{P_L}$, for larger peak power $\varepsilon_{max} \propto \mathrm{P_L^{1/2}}$.

like DRACO, laser wavelength of $0.8\,\mu\text{m}$, focal spot size $2\,\mu\text{m}$ and a target thickness of $2\,\mu\text{m}$ assuming an electron divergence of 10°. As can be seen, the optimum pulse duration t_p^{opt} increases sharply around a laser pulse energy of 0.1 J. For smaller pulse energies, it is $t_p^{opt} \approx t_{ref}^{PEM}$ and the maximum ion energy increases linearly with the laser power, for larger pulse energies it increases only with the square root of the power. These results are in qualitative agreement with the predictions presented in [113] based on a quasi-static acceleration model (Sec. 2.3.1.2). Quantitatively one finds that especially at higher pulse energies the maximum energy as function of the pulse duration shows a broader peak around the maximum in the PEM model and the maximum proton energies at the optimum pulse duration tend to be smaller.

4.1.4 Discussion

The temperature scalings (4.19) and (4.23) found using the Lorentz invariant electron distribution are significantly below the widely used ponderomotive scaling or the simple unweighted temporal average of the electron quiver motion at the front foil surface (4.3), but describe the available experimental data as well as the PIC results very accurately.

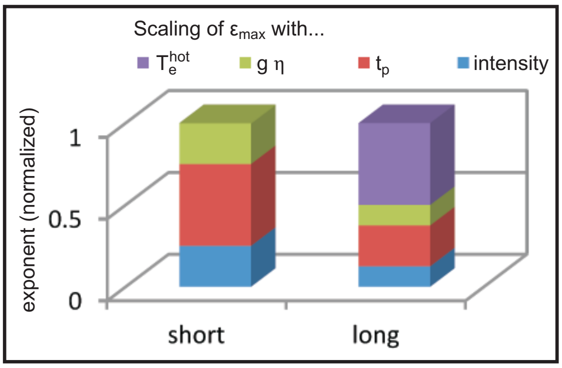

Figure 4.9: Relative importance of the laser and plasma parameters for the scaling of maximum ion energies for short ($t_p \ll t_{ref}^{PEM}$, left column) and long pulse durations ($t_p \gg t_{ref}^{PEM}$, right column). Shown are the exponents of the individual parameters in Eqn. (4.28) and (4.30), respectively, normalized to 1.

The model for the electron temperature scaling developed in 4.1.2 is chosen to resemble the situation of high-contrast high-intensity laser-matter interaction but ceases to be valid in the case of very long pulse duration or in the presence of intense prepulses or ASE pedestals, since the assumption of predominant laser absorption at the critical density surface interface may become invalid as the laser energy can be reduced in the interaction with the preplasma. Furthermore, it does not take into account the electron temperature increase due to longitudinal and transverse refluxing of electrons, though the findings can be easily adopted in models describing the electron energy enhancement, e.g. [29, 156].

In contrast to the standard ponderomotive scaling model, the approach presented here focuses on the ensemble dynamics at the critical density interface, taking into account the distribution of electrons with respect to the laser phase. A simple analysis of the interaction dynamics at the critical surface shows that the most energetic electrons detach from the interface when the longitudinal $v \times B$ force is maximum. With this assumption, validated by PIC simulations, this model can be naturally connected to transport models describing the energy and momentum transfer of these hot electrons into the target bulk and thus lead to a more complete understanding of the energy transfer in laser-matter interactions.

Both models yield different results, especially in the case of long pulse durations. There, the modified hot electron temperature scaling (4.23) discussed in the last section leads to significantly reduced energies compared to the ponderomotive temperature scaling and the Schreiber model. This result is in agreement with recent experimental data. It is a very important finding since now it becomes possible with that new electron temperature scaling to describe the experimental maximum proton energies, while the widely commonly used ponderomotive scaling leads to a significant overestimation of proton energies (see Fig. 4.10). The experimentally validated fact that the average electron energy is reduced compared to the ponderomotive energy is also very important for example for radiation protection calculations in the design of future laser accelerators, lowering substantially the expected

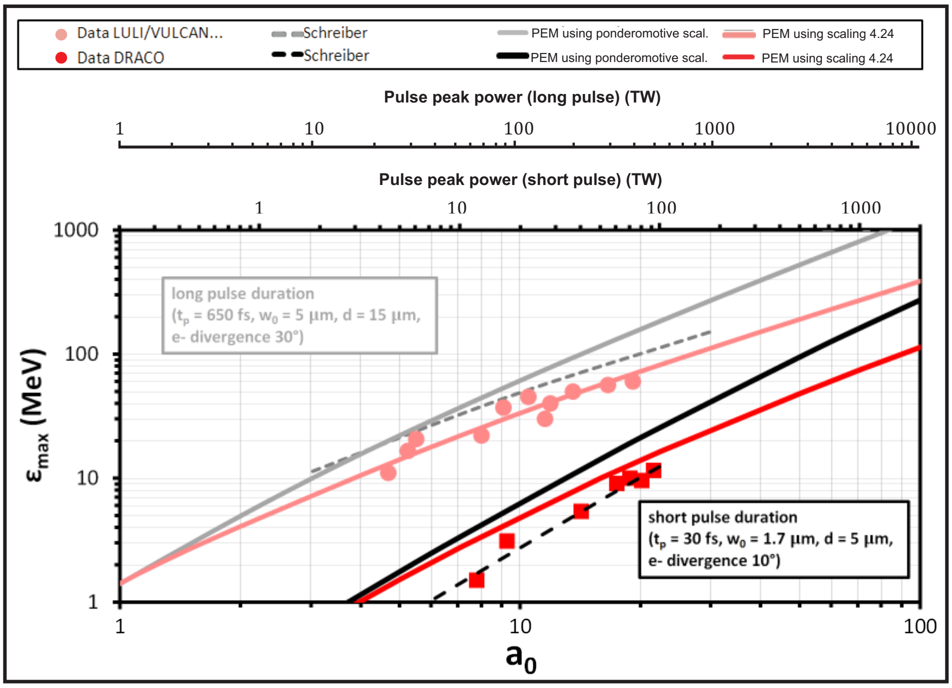

Figure 4.10: Comparison of proton maximum energy as a function of a_0 and the peak power for the Schreiber scaling (dashed lines) and the time limited fluid model discussed in this section for temperature scaling following the ponderomotive (black solid line) and the modified temperature scaling (4.23) (red solid line). Experimental data is from DRACO (red squares) and several glass laser facilities [24]. For the models, representative sets of parameters are chosen as in [24]: $[t_p, w_0, d, \alpha(°), \lambda(2\pi)] = [70, 3.4\pi, 10\pi, 10, 0.8]$ (red lines) and $[1226, 10\pi, 30\pi, 30, 1]$ (black and gray lines) and $\eta = 0.2$. As can be seen, for small a_0 it is $\varepsilon_{max} \propto a_0^2$, i.e. the absorbed laser energy while the temperature scaling becomes important only for large a_0. For long pulses, the modified temperature scaling can then explain the experimentally observed reduced ion energies compared to the Schreiber scaling or the fluid description with the temperature from the ponderomotive scaling (2.25).

radiation load and reducing the necessary shielding.

One important conclusion from the discussion of the ion acceleration in the frame of the PEM in the last subsection is the fact that for ultra-short pulse durations the exact scaling of the electron temperature is of minor relevance and the maximum ion energy is determined primarily by the absorbed laser energy, pulse duration and the foil thickness (via g) (see Fig. 4.9). Consequently, a model of the laser absorption efficiency alone is sufficient in this regime to predict the achievable ion energies. For long pulse durations or large a_0 the exact description of the electron temperature scaling becomes significantly more important while at the same time the importance of the absorption fraction reduces. The total absorbed energy then can actually even drop from η to η' as long as the electron temperature increases by just more than $(\eta/\eta')^{1/4}$. An experimental optimization in this case can hence focus on the temperature and even a reduction of η may be tolerated while for short pulse durations it must focus on the laser absorption fraction.

So far, only large flat foils have been considered. The aim of this thesis in the following is to determine conditions for the most efficient acceleration of ions from various target geometries with respect to their capability to increase the hot electron temperature and density and consequently the maximum achievable ion energy. For that, in the following three sections ultra-thin foils, foil stacks, mass limited foils and flat top cone targets will be analyzed by virtue of 2 dimensional PIC simulations. In the next section, first the case of a short laser pulse is considered. Following the above discussion, a target geometry is proposed that could increase the laser absorption and therefore the proton maximum energy. In the following two sections the case of a long laser pulse is discussed where the increase of the hot electron temperature becomes also important. In Sec. 4.3.1 the importance of an increase of the hot electron temperature for the ion acceleration will be shown on the example of mass limited targets while in Sec. 4.3.2 the temperature increase in flat top cone targets will be discussed.

4.2 Increase of Laser Absorption

It is a well-known fact that the reduction of the foil thickness from several microns down to the sub-micron level can considerably increase the proton energy [116, 110, 157] (see Sec. 2.3.2.1). In [116] the phenomenon was for the first time described theoretically based on PIC simulations. An optimum foil thickness d^{opt} can be determined experimentally and by means of simulations, below which a reduction in areal electron charge density prevents any further increase in ion energy. Typically, the experimentally observed optimum thicknesses are strongly influenced by laser prepulses and ASE levels, since those may heat and expand the foil prior to the main pulse. The laser absorption may then be reduced and the density gradient at the rear side also degrades the ion acceleration [115].

In PIC simulations, employing a perfect gaussian pulse without prepulses or ASE, it was observed that the optimum thickness coincides with the thickness where the laser absorption equals the laser transmission through the target. For very small thicknesses, the foil was found to explode quickly and the laser pulse is almost fully transmitted, while for thicker foils the electron density is reduced since the electrons spread over a larger volume as the absorption grows more slowly than the thickness. As discussed in the last section, the laser interaction can be thought of as happening only at the foil front surface up to a depth in the order of the relativistic skin depth $\delta = \left(\omega_p^2 - 1\right)^{-1/2}$ (2.41). While the electrons propagate through the foil, they diverge until they exit the rear side where they set up the quasi-static ion accelerating field (see Sec. 2.3.1). A reduction of the thickness hence will lead to a reduced spot size at the rear and hence an increased hot electron density and increased electric field strength. Only when the foil thickness becomes less than the relativistic skin depth (2.41), the hot electron density will again be reduced, now due to a lower number of accelerated electrons.

In the optimum case the electron heating is a volumetric heating of all electrons through the foil depth, as opposed to the surface-only heating in the case of thicker foils [116, 122]. The exact value of the optimum foil thickness has been found to be somewhat larger than the skin depth due to a more complex dynamics in a realistic case. Also, in real experiments the laser prepulses and ASE have to be considered which can lead to heating, expansion and target disintegration prior to the main pulse, especially ultra-thin foils can easily be destroyed. The laser then effectively does not interact with a solid anymore and in extreme cases can accelerate electrons by wakefields just as in underdense targets [50].

In the following, a different argument for the optimum foil thickness is given which imposes

Reprinted with permission from T. Kluge, W. Enghardt, S. D. Kraft, U. Schramm, Y. Sentoku, K. Zeil, T. E. Cowan, R. Sauerbrey and M. Bussmann, Physical Review E, Vol. 82, page 016405 (2010). Copyright (2010), American Physical Society.

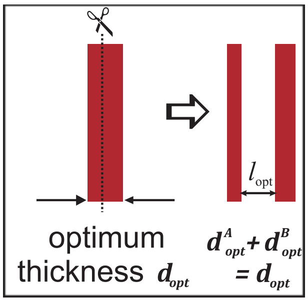

Figure 4.11: Setup of the foil stack: An ultra-thin foil at optimum thickness is slit into two halfs.

implications that will be studied in this section and can lead to an optimization of ultra-thin foils with regard to the ion maximum energy. The argument is based on the maximization of the laser absorption into hot electrons which means that the average electron temperature and the hot electron density should be maximized at the same time. Unfortunately, the parameters are connected with each other and show an opposite trend in ultra-thin flat foils. Compared to an extremely thin foil the average hot electron temperature at the foil rear side of a thicker foil is reduced since only electrons inside the skin-depth at the foil front surface are directly heated by the laser and deeper lying electrons experience only a reduced laser field shielded by the front electrons. The average kinetic energy of the electrons reduces the more the thicker the foil gets. To increase the temperature, one can decrease the thickness of the foil which however eventually will decrease the hot electron density when the number of electrons in side the focal spot becomes less than the number of electrons the laser *could* accelerate.

It may be assumed that the optimum transfer of laser energy to the plasma in terms of maximum kinetic energy to electrons happens when the force exerted on an individual electron by the laser fields equals the restoring force exerted on the electron by an inertially resting ion. In that case the energy stored in the plasma in the form of potential energy can be maximized. This argument and the quantitative implications on the optimum foil thickness will be studied in more detail in the following. As will be shown, the resulting optimum thickness for the energy transfer to electrons is usually less than the optimum thickness for ion acceleration, since the hot electron density then is far from optimum. To increase the average electron energy one would actually need to sacrifice electron density with the result of reduced ion energies.

A solution to this problem is a decoupling of the hot electron temperature increase from the electron density reduction. For this aim, in [158] a target design based on stacked foils was introduced by the author of this thesis and others. It was proposed to cut a foil of optimum thickness d^{opt} into slices of sub-skin-depth thickness and stack these slices (Fig. 4.11). While

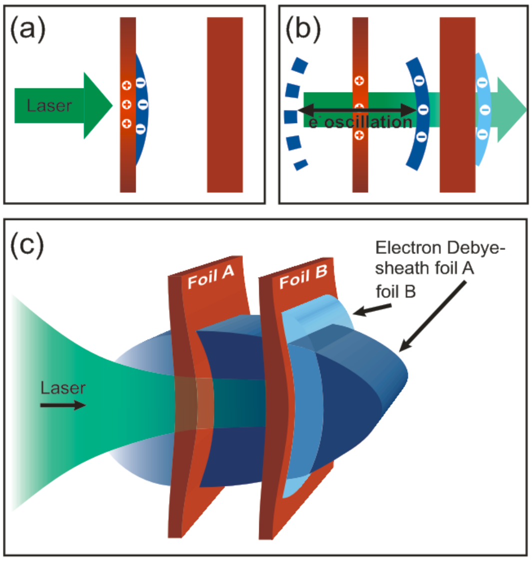

Figure 4.12: Basic principle of operation of the foil stack: The foil thickness is dimensioned so that the laser field strength is just sufficient to extract all electrons from the foil (a). Then the transfer of laser energy to electrons is immediate and optimum. The electrons move in an anharmonic oscillator set up by the resting ions, driven by the laser. For an optimum energy transfer the foils should be separated from each other by more than the amplitude (b). At later times, the electron cloud from the first foil will merge with the second one, setting up a high quasi-static electric ion accelerating field (c).

each foil can be chosen thin enough for an optimum electron heating therein and to become transparent at the onset of the interaction with the laser pulse, the laser energy is efficiently absorbed in the foil stack which provides the high number of electrons. Carefully choosing the distance between each pair of slices in the stack allows to precisely tailor the electron motion. Thus, for each slice in the stack the laser pulse interacts with all electrons in each foil almost instantaneously and in phase, while at optimum stacking the electrons emerging from each slice merge at the rear side of the last slice. The electron temperature can thus be increased without a reduction of the electron number, thereby overcoming the limitations observed for ultra-thin single-foil targets [159]. Theoretically a gain in proton energy of up to 30 % is predicted, for which in the single-foil case an increase in laser intensity of up to 70 % [113] would be required.

Other, experimentally-challenging schemes have been proposed to enhance ion energy. In contrast to complex schemes relying on the use of synchronized laser pulses [160], here, the time interval between the irradiation of the individual foils is simply determined by their spacing.

4.2.1 Setup and Simulations

At first the most simple case of a stack will be considered, that is a stack of two foils only. The front and rear foil will be called Foil 'A' and 'B' respectively. Sets of simulation show that for both foils optimum thicknesses d_A^{opt} and d_B^{opt} exist with respect to the proton maximum energy. The optimum values vary with the laser intensity and add up to the

Parameter	Value
Geometry	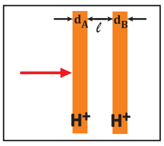
laser strength a_0	$8.5 - 26.9$
pulse shape	Gaussian
laser waist w_0	12π
pulse duration	60
electron density $n_{e,0}$	$5 - 50$
cells (time steps) per laser wavelength	80
box size ($x \times z$ cells)	7110×2550
including collisions/ ionization	no/no

Table 4.2: Parameters used for the simulations in this section. The standard laser strength parameter was 8.5, only for the parameter scan to higher laser strength this was increased up to 26.9, the standard electron density was 10 which again was varied only for the parameter scan.

optimum thickness of a single foil, $d_A^{opt} + d_B^{opt} = d^{opt}$, so the total amount of matter is the same for the optimum stack as it is for the optimum single foil. Hence, the target in the following can be treated as a *single optimum foil cut into multiple slices.* For the specific situation of $a_0 = 8.5$ and $n_{e,0} = n_{p,0} = 10$ the optimum thickness for a single foil found by simulations is $d_A^{opt} = 2.5 \cong 400\,\mathrm{nm}$. Also for the separation of both foils simulations predict an optimum region. Fig. 4.13 shows the evolution of the maximum proton energy observed in the simulation when increasing the space between the two foils, leaving their individual thicknesses untouched at their respective optimum value. At small separation distances, the maximum proton energy does not increase significantly. Rather, around 100 nm it falls somewhat short of the single foil energy. Further increasing the separation leads to a strong gain of the proton energy until a plateau is reached. As will be shown, the distance at which the energy reaches the plateau corresponds to the point when the electrons of the first foil, being driven out of the foil by the laser light pressure at $2\omega_0$, can oscillate freely without being pushed into the next foil. The proton energy gain can then be explained by an optimum transfer of laser energy to the electrons, which, at a larger timescale, transfer their energy TNSA-like to the protons after the electron sheaths from both foils have thermalized and merged.

In the following, first the electron dynamics during the laser interaction will be analyzed in detail. Based on this analysis, analytic expressions will be given for the optimum values of the foil thicknesses and separation as a function of laser strength and electron density.

4.2.2 Electron dynamics in a foil stack

The electron dynamics in a sub-skin-depth foil differs significantly from a thick foil. While at a thick foil as described in section 2.2.3 the longitudinal Lorentz forces can be balanced by the plasma and the electron motion is limited primarily to the surface of the foil, in sub-skin-depth foils the laser can actually act on all electrons at once and displace them as a unit and coherently. The electron sheath oscillates at $2\omega_0$ around the remanent ions. This can be seen in Fig. 4.14 and 4.15. Fig. 4.14 displays the electron density at three different time steps, demonstrating the dominating coherent electron reaction. The electrons of the first foil are driven out of the foil by the laser and start to oscillate around the ions, which remain virtually at rest during the laser pulse interaction. The electrons in this phase are coherently driven by the laser electric and magnetic fields. Their motion is governed by the laser light pressure and the restoring force set up by the remanent ions. This is an important statement, since a dominance of the laser light pressure over stochastic, thermal heating is usually only assumed in the case of CP (Sec. 2.3.2.2) or significantly higher laser strength [161]. However, obviously in the case of thin foils with thickness in the order of

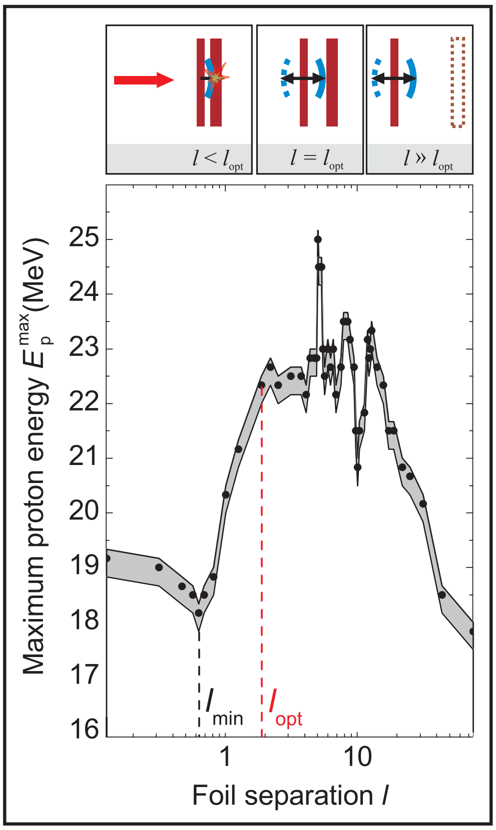

Figure 4.13: Maximum proton energy versus inter-foil distance l of a stacked target with $d_A = d_A^{opt} = 0.6 \hat{=} 100\,\mathrm{nm}$, $d = d^{opt} = 2.5 \hat{=} 400\,\mathrm{nm}$ as obtained from simulations. The gray area represents the systematic error. $a_0 = 8.5$, $n_{e,0} = 10$.

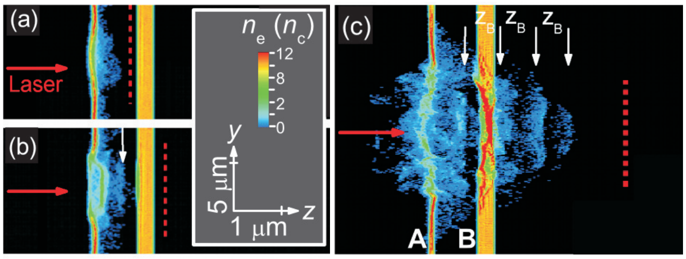

Figure 4.14: Electron density of an optimally stacked target (see main text for details) at times $0.8 \times 2\pi/\omega_0$ (a), $1.3 \times 2\pi/\omega_0$ (b), and $3.4 \times 2\pi/\omega_0$ (c) after the laser pulse maximum reaches the target. The dotted lines mark the position of the laser pulse front, arrows point to the emitted electron bunches with distances $z_B \equiv \pi c/\omega_0$.

the skin depth the laser light pressure is dominant at least for the first few laser cycles. The oscillation of the front foil electrons can also be seen in Fig. 4.15, where temporal evolution of the position of the center of mass of foil 'A' is shown. It follows nicely the longitudinal laser forces at $2\omega_0$ during the full laser pulse duration.

The advantages of the stack geometry now rely on the fact, that the energy gain of electrons within the first foil is larger than in a region of equal thickness in a thicker foil. For one, this means a higher absorbed energy fraction. Additionally, a higher electron energy means that the electron masses increase, decreasing the electron plasma frequency (2.28). Therefore the skin depth increases, causing a larger laser transmission to the rear foil than the laser transmission to electrons in the rear of a single thick foil would be, therefore increasing also the number of hot electrons.

The electron average kinetic energy of a single flat foil is contrasted with a stack of foils with optimum individual foil thicknesses at optimum spacing in Fig. 4.16(a). The maximum average energy is observed at the time when the laser maximum reaches the foil front surface and is about 25% higher for the stack than for a single foil. The fact of a faster transition to transparency can be seen in Fig. 4.16(b) which displays the temporal evolution of the maximum plasma frequency. It is due to the increased heating and therefore larger skin depth and laser transmission to the rear foil. In the case of the foil stack, ω_p decreases very early in the laser irradiation and drops faster below 1 than in the case of a single foil where it remains at its initial value for a longer time. Hence, the volumetric heating can set in earlier in the stack. Both effects, the increased heating in the first foil and the faster volumetric heating lead to an increased laser absorption (see inset of Fig. 4.16) and ion acceleration potential at the foil rear surface (Fig. 4.16(c)).

4.2.3 Optimum foil thicknesses

To derive analytical estimates for the optimum geometric foil parameters, first an analytic description of the electron motion is given. As explained above, the optimum will occur when the energy transfer to electrons in the front foil is maximum.

The incoming laser is described by a traveling plane wave with electric field strength $a_x(t,z) = a_0\cos(t-z)$, polarized in x-direction and propagating in z-direction. Assuming the amplitude of the electron sheet of foil A, $\hat{z}_A$, to be small compared to the laser wave length, the z dependency of the electric field can be neglected and it is $a_x \approx a_0\cos(t)$. The field is partially screened by the plasma, which can be taken into account by setting its average to

$$\langle a_0\rangle_{t,z} \equiv \frac{1}{d_\mathrm{A}}\int_0^{d_\mathrm{A}} \langle a_0\rangle_t\, e^{-z/\langle\delta\rangle_t}\mathrm{dz} \cong \langle a_0\rangle_t \frac{\langle\delta\rangle_t}{d_\mathrm{A}}\left[1-e^{-d_\mathrm{A}/\langle\delta\rangle_t}\right]. \tag{4.31}$$

Here and throughout this section mean values $\langle ...\rangle_t$ are used, averaging over the time the laser drives the collective electron motion, since the electron density decreases during the interaction as the laser constantly drives electrons out of the sheath. Obviously, this simplification is valid only for short laser pulses where the instantaneous values do not differ significantly from the average values. For long pulses a dynamic model including the temporally changing values would have to be employed.

The electric laser field causes each individual electron of the first foil to oscillate in x-direction, while the magnetic field accelerates the electrons along the z-axis. Then, the transverse momentum of each electron due to the electric laser field is approximately given by

$$p_x \cong -\int \sqrt{1+\eta}\,\langle a_0\rangle_{t,z}\cos(t)dt = \sqrt{1+\eta}\,\langle a_0\rangle_{t,z}\sin(t)$$

where $\eta = R - T$ (R (T): laser reflection (transmission). Here it is assumed that the electrons were at rest before the laser interaction and each individual particle experiences the same average electric field during one oscillation. This is equal to an adiabatic electron acceleration during the pulse up-ramp and to the condition that the oscillation amplitude is larger than the foil thickness, so that the oscillating electrons traverse the whole foil during each cycle. However, this is always true for foils close to the optimum thickness, which was defined before to be the thickness when the laser can push all electrons out of the foil. The motion in z-direction is governed by the $\boldsymbol{v}\times\boldsymbol{B}$ force

$$F_L = \dot{p}_z = \beta_x b_y \cong (1+\eta)\,\langle a_0\rangle_{t,z}^2\sin(t)\cos(t) = F_{\mathbf{L,0}}\sin(2t)\ , \tag{4.32}$$

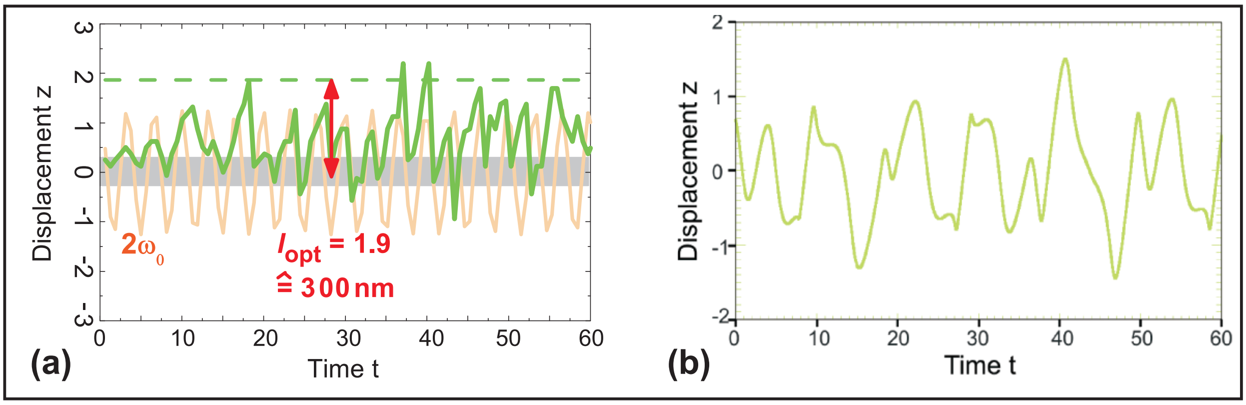

Figure 4.15: **(a)** Displacement of the first foil's electron center of mass over time (averaged over 1 µm around laser axis) if no second foil exists. The electrons are oscillating at roughly twice the laser frequency, their amplitude defining the optimum inter-foil distance l. The gray area indicates the initial foil position, the orange line a virtual oscillation at $2\omega_0$. **(b)** Displacement over time of an electron in a field superposition of the laser field and restoring field(4.33) as obtained from numerically solving the EOM assuming a plane wave. a_0=8.5, $n_{e,0} = 10$, $d = d_A^{opt} = 0.6$

where $F_{\mathbf{L,0}} \equiv \frac{P}{2}\left(1+\eta\right)\left\langle a_0\right\rangle_{t,z}^2$ is the maximum force in z-direction acting on a single electron and $P = 1$ for the LP laser.[9]

As was discussed above, the electrons oscillate coherently around the remanent ions (see Fig. 4.14(a-c) and 4.15), keeping their spatial coherence. Due to the charge separation an homogeneous electric restoring field a^R builds up. The attractive electrostatic force on a single electron in an infinitesimally thin sheath is then given by

$$F_{\mathrm{R}} = -\mathrm{sign}(z) d_{\mathrm{A}} n_{e,0}. \tag{4.33}$$

The equation of motion for a single electron resembles a driven oscillator and reads

$$F_z^{total} = F_{\mathrm{L}} + F_{\mathrm{R}}\ . \tag{4.34}$$

where F_{L} is the driving force and $\mathrm{sign}(z)F_{\mathrm{R}}$ the restoring force. For LP laser pulses considered here, the driving force F_{L} causes an oscillation at twice the laser frequency ω_0 as well as a constant drift while the restoring force accelerates the electron towards the center of the foil so that it remains trapped in the potential well. The resulting oscillation amplitudes of the electrons at foil A and B, denoted by $\hat{z}_A$ and $\hat{z}_B$, respectively, can easily be determined numerically (see next section).

---

[9] For CP laser pulses, the electron would also oscillate in the y-direction, adding another term in (4.32) which removes the temporal dependency and increases $F_{\mathbf{L,0}}$ by a factor of two, hence it then is $P = 2$.

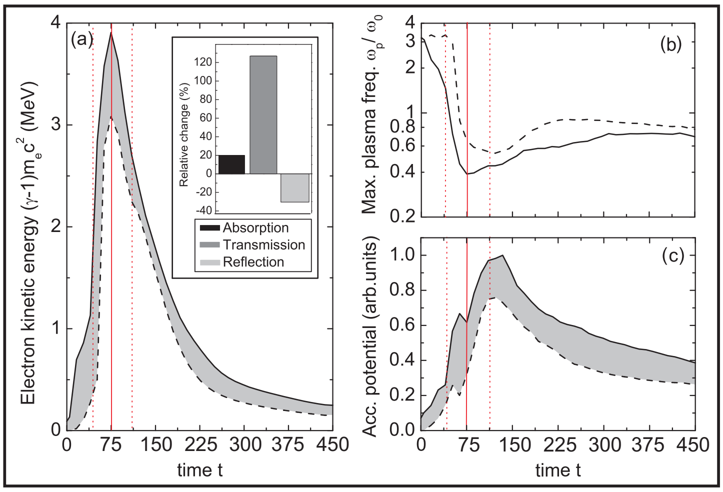

Figure 4.16: Temporal evolution of (a) average electron kinetic energy, (b) maximum electron plasma frequency on the laser axis and (c) acceleration potential at the rear side of the target for a single foil (dashed line) and a stack of two foils (black line) at optimum parameters each. Their difference is highlighted in light gray, the time the laser pulse maximum reaches the rear side of the foil stack is indicated by solid vertical lines (pulse FWHM by dashed lines). The inset in the upper right shows the difference in absorption, transmission and reflection.

Using the above, the optimum thickness d_A^{opt} of foil 'A' can be determined using the requirement $F_{\mathbf{L},\mathbf{0}} = F_\mathrm{R}$ introduced above. In that case, the transfer of energy to the electrons is maximized since smaller laser field strengths would not suffice to drive all electrons in the foil while any exceeding laser energy could not increase the charge separation and thus the electron potential energy but rather would decrease the electron density by driving out more electrons. This requirement was validated by simulations for various test cases. From Eqn. 4.32 and 4.33 it then follows with $\langle\delta\rangle_t^2 \approx 1/\langle n_\mathrm{e}\rangle_t$ from Eqn. (2.41) the relation

$$\boxed{d_\mathrm{A}^\mathrm{opt} \cong \frac{P\,(1+\eta)\,\langle a_0\rangle_t^2}{2n_{e,0}\,\langle n_e\rangle_t\,\left(d_\mathrm{A}^\mathrm{opt}\right)^2}\left[1-\exp\left(-d_\mathrm{A}^\mathrm{opt}\sqrt{\langle n_e\rangle_t}\right)\right]^2.} \tag{4.35}$$

Assuming $\langle n_e\rangle_t \cong n_{e,0}$ and $\langle a_0\rangle_t \cong a_0$ the predictions of this equation for the optimum thickness of foil A are found to be in very good agreement with the PIC simulation results for $\eta = 0$ as shown in Fig. 4.17. Interestingly, this condition is in agreement with $R = T$ discussed in Sec. 2.3.2.1, Fig. 2.9 for foils at the optimum thickness. It is important to note, that the linear scaling $\sqrt{\frac{P}{2}(1+\eta)}a_0 = n_{e,0}d_A^{opt}$ (Eqn. (2.75)) overestimates the optimum foil thickness.

Assuming $\Delta = \left(1-\exp(-d_\mathrm{A}^\mathrm{opt}/\langle\delta_0\rangle_t)\right) \approx 1$, Eqn. (4.35) reduces to the simple expression

$$\boxed{d_\mathrm{A}^\mathrm{opt} \cong \left(\frac{P\,(1+\eta)}{2}\right)^{1/3}\left(\frac{a_0}{n_{\mathrm{e},0}}\right)^{2/3}.} \tag{4.36}$$

If $\Delta \neq 1$, the above expression may still be helpful when replacing the equality with a proportionality, $d^{opt} \propto (a_0/n_{e,0})^{2/3}$, in cases when $\Delta \approx \mathit{const}$.

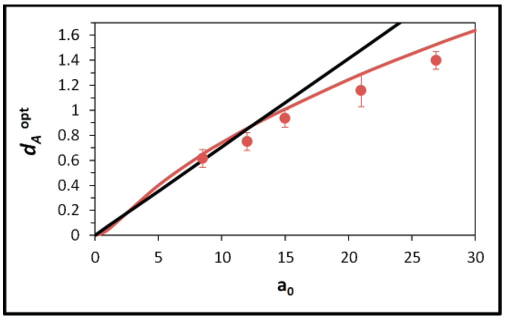

Figure 4.17: Optimum thickness of foil A versus laser intensity at $n_{e,0} = 10$. Red points represent simulation results, solid lines the model predictions (black: Eqn. (2.75), red: Eqn. (4.35) assuming $\eta = 0$, $\langle n_e \rangle_t \approx n_{e,0}$ and $\langle a_0 \rangle_t \cong a_0$. The thickness of foil B is set to its respective optimum value.

The above predictions of the scaling for the optimum thickness of a thin foil are of great importance not only in the case of a foil stack presented here but generally for systems dominated by the laser light pressure, especially including the Light Sail RPA regime for CP pulses, see Sec. 2.3.2.2. As was described there, one usually assumes the optimum energy transfer then to happen for the foil thickness d to be just large enough for the restoring force of the electrons to the ions to balance the laser light pressure. This leads to scalings similar to

$$d^{opt} = F \frac{{a_0}^B}{n_{e,0}} \tag{4.37}$$

where $F = \sqrt{\frac{P}{2}(1+\eta)}$ and $B = 1$ from analytic theory (see Eqn. (2.75)). For moderate a_0, simulations have shown empirically that the factor F is twice as large for flat top laser pulses as for Gaussian pulses, specifically in [135] it was given

$$F = \begin{cases} 1 & \text{Gaussian pulse} \\ 2 & \text{flat} - \text{top pulse} \end{cases} \tag{4.38}$$

However, as was discussed in Section 2.3.2.2, this scaling has not been proven by experiments yet and in simulations deviations occur from the simple proportionality for large a_0, the optimum thickness follows better $d^{opt} \propto a_0^{2/3}$ (Eqn. (2.77)).

This deviation can easily be understood in the frame of the above discussion. The empiric factor F can simply be identified in Eqn. (4.36) and (4.35) with $\left[\frac{P}{2}(1+\eta)\right]^{1/2}$ which then yields the scalings as shown in Fig. 4.18 for a flat top (solid blue line) and Gaussian laser pulse (solid red line), respectively, for

$$F = \begin{cases} 1/2 & \text{Gaussian pulse} \\ 1 & \text{flat} - \text{top pulse} \end{cases} \tag{4.39}$$

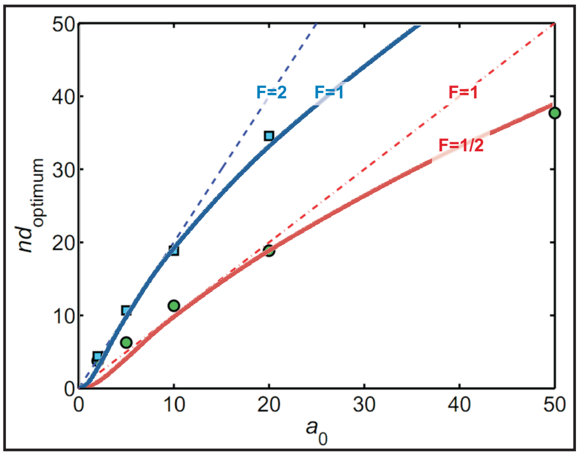

Figure 4.18: Optimum thickness of of a foil in a radiation pressure dominated regime with a CP laser as a function of a_0 for $n_{e,0} = 100$ (numerical values extracted from [135], compare with Fig. 2.12). The dashed lines follow the established linear RPA scaling (4.37) as derived in Sec. 2.3.2.2. The solid red (blue) line is the implicit result of Eqn. (4.35) for a CP laser pulse with gaussian (flat top) temporal profile with $F = 1/2$ ($F = 1$), respectively, as described in the main text.

that fit the simulation results very well even for the highest laser strength $a_0 = 50$. It is worth noting that now the empiric factors F are within the analytically possible bounds of $0 \leq F \leq \sqrt{2}$. The difference between the simple proportional scaling (4.37) and (4.35), (4.36) in this context would then be due the fact that here the finite reflectivity and the extinction of the laser electromagnetic wave inside the thin foil were considered by including a depth-dependency of a_0 via δ in the discussion presented above.

4.2.4 Optimum Foil Separation

The maximum proton energy is a strong function of the foil separation l as shown in Fig. 4.13. Starting at $l = 0$, equivalent to the single-foil case, the maximum proton energy ε_{max} decreases with increasing l until it reaches a minimum at l_{min}. At this point, the electrons are pushed into foil B and are no longer heated by the laser. Furthermore, the electron density at the front of foil B then increases, thereby decreasing the penetration depth of the laser field. For $l > l_{\text{min}}$ ε_{max} sharply increases until reaching an extended plateau whose left bound will be referred to as l^{opt} in the following. This optimum separation can be found analytically by taking into account that for the electron motion discussed above, the electrons of foil 'A' must move without interference of foil 'B'. The optimum distance therefore will be in the order of or larger than the amplitude of electrons from foil 'A' $\hat{z}_A$. This is shown by a test simulation consisting of foil 'A' only, from which the oscillation of the center of mass of the electron sheet can be inferred. Fig. 4.15 shows how the center of mass of the electrons oscillates in the laser field, exhibiting an amplitude of $\hat{z}_A \cong 1.9$ in the specific case of $a_0 = 8.5$, $n_{e,0} = 10$ and $d_A = d_A^{opt} = 0.6$. If the foils are spaced with a distance greater than this distance, the electrons of each foil can oscillate freely without much interference,

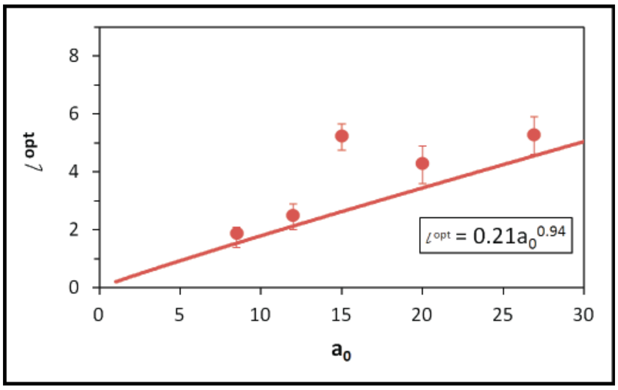

Figure 4.19: Optimum foil separation versus laser intensity at $n_{e,0} = 10$. Circles represent simulation results, solid line the oscillation amplitude $\hat{z}$ of electrons in foil A from numerically solving the EOM (4.34) with $\langle n_e \rangle_t \approx n_{e,0}$, $\eta = 0$ and $\langle \gamma \rangle_t$ given by Eqn. (4.3). The foil thicknesses are set to their respective optimum value.

hence the optimum transfer of laser energy to the electrons as described before is realized and ε_0 should increase up until this point. In deed, this is what is observed in Fig. 4.13 where it can be seen that $l_{opt} \approx 1.9$. Further increase of l hinders the electron ensembles to merge later in time, a scenario in which the acceleration dynamics in both foils are independent of each other. Fig. 4.19 shows the PIC simulation results for the optimum separation l^{opt} (circles) and the numerical results for $\hat{z}_A$ from solving the electron EOM (4.34) (solid red line). The two are in good agreement with each other except for one PIC simulation data point at $a_0 = 15$ where the optimum distance is larger than the oscillation amplitude of foil A. It may be speculated that this is due to an oscillation of the surface of foil B, so that in the worst scenario the two oscillation amplitudes of foil A and B should be added to ensure a free oscillation of electrons from foil A, hence $\hat{z}_A \leq l^{opt} \leq \hat{z}_A + \hat{z}_B$.

4.2.5 Discussion

The simulations have shown that in deed a stacked setup of individual foils can increase the observed proton energies. Compared to single flat foils, the electron temperature can be optimized in the first foils which in turn leads to a faster transition to transparency due to the larger relativistic electron mass (relativistically induced transparency, RIT) and hence greater laser absorption in the rear foils. This can be seen for the specific example of $a_0 = 8.5$, $n_{e,0} = 10$ in the inset of Fig. 4.16. The average electron energy is increased by about 30% compared to single foil and the relativistic plasma frequency drops faster below 1, indicating the RIT regime. The reason lies in the faster heating and expansion and hence transparency of the first foil that allows the laser to quickly penetrate it and consequently turn transparent the following foil and the whole target quicker [122]. Both, the optimum transfer of laser energy to electrons in the first foil and the accelerated transparency and hence longer interaction time with the bulk of the electrons, in combination with a yet high electron density lead to a higher total laser energy absorption.

The key of the stacked target hence lies in its decoupling of electron temperature and density optimization. The temperature can be optimized by optimizing the individual foil thicknesses, i.e. by adjusting the thickness so that the laser force equals the restoring force and the electrons gain the maximum possible energy. The density is optimized by the total amount of matter in the stack, i.e. the total thickness of the stack. Hence, the first foil mainly serves as a source for high energy electrons and to increase the total laser absorption in the target via faster RIT, while the rear foil ensures a high electron density in the accelerating sheath. By carefully choosing the separation distance, it must be ensured that the distance is large enough for the electrons of the individual foils to be able to oscillate without interference, yet small enough so that they can merge quickly after the laser interaction to form a dense hot quasi-static electron sheath accelerating the ions. The accelerating potential then is larger for the stack than for a single foil, which can be seen in Fig. 4.16(c).

The maximum gain in proton maximum energy for the two-foil setup compared to the equivalent single-foil setup is given in Table 4.3 for various laser intensities. For current high-intensity laser systems the predicted energy gain of about 25 % to 30 % is found to be independent of the laser intensity in the simulations. The total yield of forward accelerated protons is not altered considerably using two-foil targets compared to the single foil scenario, as their number is only about 5 % higher for the two-foil target.

a_0	ε_{max} (MeV)	gain
8.5	25	31% (40%)
12	37	28%
14.75	51	31%
27	115	25%

Table 4.3: Maximum proton energy and its gain for various laser intensities when using two (four) foils instead of a single foil, at their respective optimum parameters.

For completeness, test simulations of stacks of four foils were performed, their total thickness again adding up to d^{opt}. As the number of free parameters is significantly increased in this case, a parametric study to obtain optimum values would be rather time consuming. Nevertheless, in the best case a further increase in maximum energy compared to the two-foil scenario of up to 7 % was found.

It is interesting to consider the case of realistic electron densities of solid foils, typical values are $n_{e,0} = 500...1000$. Based on the simulations with $n_{e,0} = 10$ additional simulations

$I\lambda^2$ $[10^{18}\,\mathrm{W/cm^2}\lambda^2]$	a_0^{LP} (a_0^{CP})	$d^{opt}[\mathrm{nm}]$ LS-RPA Eqn. (2.75)	$d^{opt}[\mathrm{nm}]$ LS-RPA Eqn. (4.35)	$d_A^{opt}[\mathrm{nm}]$ Stack Eqn. (4.35)	$d^{opt}[\mathrm{nm}]$ eTNSA [116]
1	.85 (0.6)	0.14	0.022	0.086	5.3
10	2.7 (1.9)	0.46	0.21	0.77	5.6
35	5.0 (3.5)	0.86	0.68	1.9	6.4
100	8.5 (6.0)	1.4	1.7	4.4	8.3
350	16 (11)	2.7	4.1	8.1	16
1000	27 (19)	4.6	7.4	14	36

Table 4.4: Optimum foil thickness for the experimentally important target material diamond-like carbon ($n_{a,0} = 660$) predicted by Eqn. (2.75) (F=1) and Eqn. (4.35) (RPA: $F = 0.5$, stack: $F = \sqrt{0.5}$) for radiation pressure dominated regimes neglecting target heating, and for a single foil in enhanced TNSA by extrapolating [116] for gaussian pulses, $t_p = 60$.

were performed up to $n_{e,0} = 50$, verifying the analytic scaling behavior of Eqn. (4.35). Extrapolation these results for example to an initial density of $n_{e,0} = 660$ (diamond like carbon) and $a_0 = 8.5$, the optimum thicknesses is expected to be $d_A^{opt} \approx 0.028$ following Eqn. (4.35). Extrapolating results from [116] it is $d_B^{opt} \approx 0.024$, hence such a stack would still feasible to manufacture. Table 4.4 shows the optimum foil thicknesses for various laser intensities.

4.3 Increase of Electron Temperature

In this section, two examples will be given that specifically address the question of hot electron temperature increase at given laser parameters only by engineering the target geometry. Following the argument in Sec. 4.1.3 that for long pulse lasers the increase of the hot electron temperature is by far more efficient than an increase of laser absorption, the results here are crucial especially for such lasers, i.e. for pulse durations of several 100 fs. Nevertheless, also for short-pulse lasers an increase of temperature is beneficial when the electron density does not reduce, since this would mean an increase in laser absorption.

4.3.1 Limited Mass Targets

The idea of limiting the target transverse dimensions, i.e. its mass, is based on the idea to keep the hot electrons from dilution due to a transverse spread. Hot electrons reaching the lateral target edges can be reflected due to the charge separation field they create when leaving the target, if their energy does not exceed the surface potential. Both confinement [106] and recirculation [20] are discussed to lead to an increase in ion maximum energy [114, 162, 163, 164, 165, 166, 167]. Through a lateral confinement of electrons in a smaller volume than the ion source size in large foils, the density of the electrons at the foil rear surface will naturally be increased. Additionally the electrons that reach the lateral boundaries are reflected back into the target. This recirculation of hot electrons will maintain a higher electron average energy in the laser focal region than in a large foil. Moreover, this increases the effective ion acceleration time.

In principle, confinement and recirculation in mass limited foils are similar to ideas that triggered the research which has lead to ultra-thin foils, whose optimization was discussed in the previous section. For example, the optimization of foil thickness with respect to electron temperature by stacked foils in the previous section can be also seen as an optimization with respect to electron longitudinal reflux [103] down to the limiting case of such a thin first foil that the laser can act on all electrons at the same time, i.e. the electrons do not leave the laser interaction at all. It has long been discussed (e.g. [97, 103]), even for much thicker foils than considered in the previous section, that electrons exiting the foil rear side and pulled back into the target by the electrostatic fields can again interact with the laser, increasing their energy to a certain extend. This means, the electrons are not only refluxing but are also *reaccelerated*. To the author's knowledge, in [29] it was pointed out for the first time that a similarity of this transverse recirculation with the longitudinal recircula-

Reprinted with permission from T. Kluge, W. Enghardt, S. D. Kraft, U. Schramm, K. Zeil, T. E. Cowan and M. Bussmann, Physics of Plasmas, Vol. 17, page 123103 (2010). Copyright (2010), American Institute of Physics.

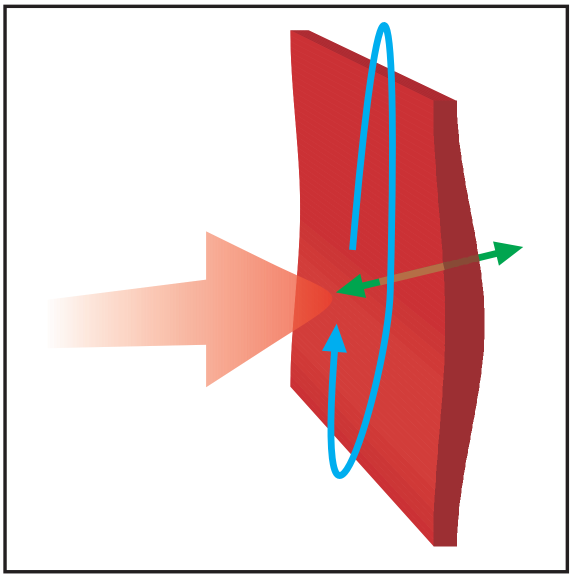

Figure 4.20: Electrons do not only oscillate along the target normal (green), but also drift laterally where they are also reflected back to the foil center. There they can repeatedly gain energy, increasing the average electron energy [29].

tion exists with respect to *repeated laser interaction and electron heating* (Fig. 4.20). It was proposed that transversely recirculating electrons can additionally be repeatedly accelerated when they cross the laser focal spot several times, leading to a yet increased electron average energy and even higher ion energies.

In the following a detailed analysis of mass limited targets (MLT) with respect to the electron dynamics and subsequent ion acceleration is presented. It will be analyzed with the help of PIC simulations what effects the transverse foil size and laser pulse duration have compared to the standard case of TNSA with large foils. The role of the three most important electron dynamic effects – including electron confinement, recirculation and reacceleration – will be illuminated, with the focus on their effect on the increase of the hot electron temperature (Sec. 4.3.1.2) and on the subsequent ion acceleration. All three effects alter the foil rear side sheath, maintaining a hotter and denser sheath, and lead to an increase of ion maximum energy.
In a recent experiment, an increase in proton maximum energy has been observed using foils with limited transverse size [109]. There, at the same time the electrons have been observed in accordance of the main results of the following theoretical analysis. Though the following analysis is focused on flat MLTs, the findings could well be extend to describe other target geometries with limited mass such as water droplets or conical targets.

Parameter	Value
Geometry	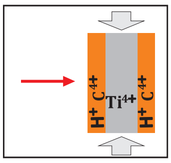
laser strength a_0	8.5
pulse shape	Gaussian
laser waist w_0	4π
pulse duration	610
electron density $n_{e,0}$	40
foil thickness d	4π (Ti)
	$+\ 0.2\pi$ contaminants at front- and rear surface
cells (time steps) per laser wavelength	50
box size ($x \times z$ cells)	$15,000 \times 15,000$
including collisions/ ionization	no/no

Table 4.5: Parameters used for the simulations in this section.

4.3.1.1 Setup and Simulations

The simulation geometry is shown in Tab. 4.5. The targets of thickness $d = 4\pi$ were positioned at 80π from the left border and centered laterally around the laser axis. In the simulations presented in this section the plasma electron density n_e was set to 40 times the non-relativistic critical density n_c. Additional simulations have shown that higher, more realistic electron densities show slightly reduced laser absorption and energy of accelerated ions but electron dynamics and qualitative results are similar. The initial electron temperature was set to 5 keV in order to avoid numerical heating.

Instead of self-consistently including the ionization of the foil by the laser field, only ions with fixed average charge states were considered, neglecting radiation losses and ionization effects connected with the temporal evolution of charge states. To study the effect of multiple ion species and to resemble a more realistic target setup, 4 different ion species with different charge-to-mass ratio q/A were included. The core consisted of ions with the lowest $q/A = 4/47.9$ which equals that of 4-fold ionized titanium and resembles the foil bulk material. This was covered with a layer of thickness 0.2π consisting of a mixture of ions with $q/A = 4/16$, $4/12$ and 1 (in ratio $8:5:2$), resembling 4-fold ionized oxygen, 4-fold ionized carbon, and 1-fold ionized hydrogen ions which usually are the main constituents of contaminations on the foils. The specific ionization state was chosen to be consistent with the average charge state during the ultra-short laser interaction that has been derived from

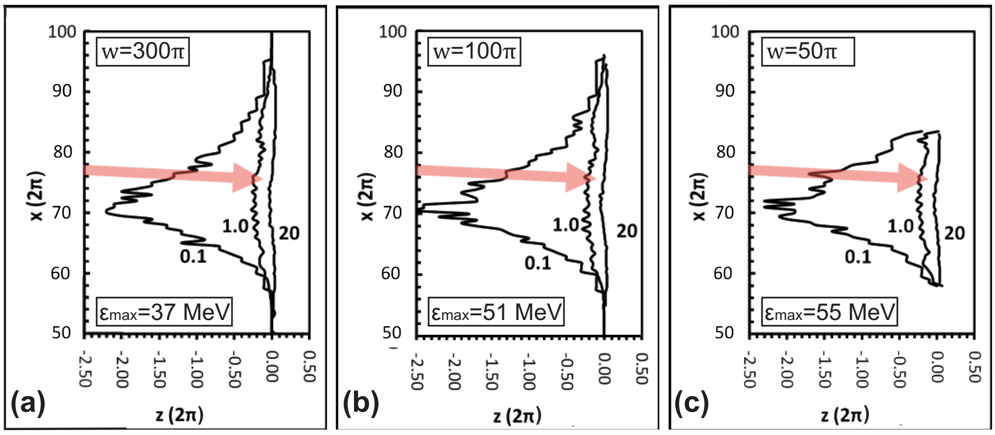

Figure 4.21: PIC simulation results for transverse preplasma electron density distribution. The 2.5π thick target is located at z=0 and has a width of $w = 300\pi$ (a), 100π (b), 50π (c). The preplasma development is seen to be independent of target transverse dimension, exhibiting two scale lengths of $\approx .5$ and ≈ 12 (see also Fig. 3.2). Final maximum energy of protons from rear is given in lower boxes and compare to 20 MeV ($w = 300\pi$), 26 MeV ($w = 100\pi$), 29 MeV ($w = 50\pi$) without ASE. $a_0 = 21.6$, $t_p = 70$, $w_0 = 2.1 \cdot 2\pi$, including ionization, collisions, $n_{e,0} = 120$ when fully ionized, laser incidence angle 35° with respect to target normal (red arrow). Laser temporal profile shown in inset of Fig. 3.2.

a preliminary simulation including ionization.

The effect of prepulses and ASE was studied by performing additional simulations with an exponential preplasma density gradient added at the foil front surface with two different scale lengths (π and 4π), thereby keeping the number of ions of each species and the number of electrons unchanged. Such scale lengths are expected for high-contrast laser systems (e.g. DRACO, see Fig. 3.2) or pulses cleaned by plasma mirrors [127, 168, 169]. It was checked for three different foil widths that the transverse dimension has no significant influence on the front-side preplasma (Fig. 4.21). Note, that a more realistic treatment would require to also include a finite rear-side plasma gradient [115] and a gradient of temperatures and ionization levels, that however are not expected to significantly alter the effects discussed in this section.

4.3.1.2 Dynamic Effects in MLT

Overview Electrons that are accelerated at the target front surface gain not only longitudinal velocity, but also acquire a transverse component. The result is an electron cloud that is expanding transversely. Consequently, the ion source size at the target rear surface is significantly larger than the focal spot (Section 2.3.2.1). A lateral reduction of the foil size consequently limits the lateral spread of the electrons. Several mechanisms influencing the ion acceleration can now become important. Table 4.6 gives a compact

	Condition	$w/2\pi$	Electron dynamics	Effect
I	$w > t_{\mathrm{acc}} v_{\mathrm{lat}}$	$> 100 \ldots 200$	electrons can drift laterally infinitely	flat foil
II	$t_p v_{\mathrm{lat}} < w < t_{\mathrm{acc}} v_{\mathrm{lat}}$	$70 - 100$	electrons can drift to edges and back to focus during ion acceleration	increased hot electron density and ion acceleration duration
III	$2w_0 < w < t_p v_{\mathrm{lat}}$	$10 - 70$	electrons can drift to edges and back to focus during laser interaction (re-acceleration)	increased hot electron temperature
IV	$w \leq 2w_0$	$\lesssim 10$	transverse $\approx$ longitudinal electrostatic fields	Coulomb expansion

Table 4.6: Definition of regions for MLT according to their diameter w corresponding to different effects of electron dynamics that become significant.

overview over those mechanisms how they can be observed in simulations.

Four distinct foil sizes can be differentiated with respect to the dominance of a respective mechanism. If the target diameter is greater than the transverse electron drift distance during the ion acceleration time (case I in the table), which is true for a conventional large flat foil, then the electrons can drift without bound. The result is, especially for long laser pulses, a diluted electron sheath at the target rear with a large ion source size (typically $\approx 2\pi \cdot 100$) and therefore reduced electron density compared to the original laser created electron bunch. If the target lateral dimension w is less then the electrons drift during the ion acceleration duration (case II), the transverse drift of hot electrons and hence the transverse spread of the accelerating electric field at the target rear during the ion acceleration time t_{acc} is limited. This decreases the effective ion source size while at the same time increasing the electron density. In the simulations a slight increase of the proton cutoff energy and a reduction in transverse spread of the protons can be observed for those foils. The ion acceleration becomes affected by the reduction of the target lateral dimension only when the laterally drifting electrons reach the margins of the foil during the acceleration time. To estimate the corresponding foil size, the time t_{acc} which the acceleration of ions lasts must be known as well as the electron lateral drift velocity v_{lat}. In the simulations it is found that the latter is in the order of $v_{\mathrm{lat}} \approx 0.7c$ and $t_{\mathrm{acc}} \approx 1.5t_p ... 3t_p$, which may vary with the pulse duration and laser focal spot size. The ion acceleration duration is longer than the pulse duration since the plasma continues to adiabatically expand after the laser pulse while energy is continuously transfered from the electrons to the massive ions [112, 170]. Consequently, the ion acceleration becomes affected by the reduction of the target lateral dimension for $w < v_{\mathrm{lat}} t_{\mathrm{acc}} \approx 2\pi \cdot 100 ... 2\pi \cdot 200$, but the effect in this region generally is little (in the range of up to 10% only).

When w is chosen smaller than $v_{\mathrm{lat}} t_p \approx 2\pi \cdot 70$ (case III), the recirculating hot electrons

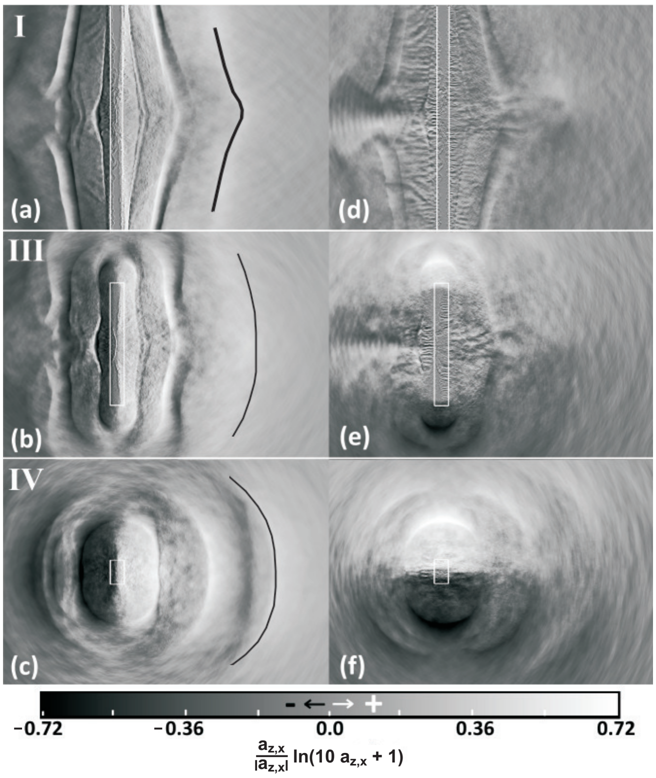

Figure 4.22: Map of the strength of the quasi-static electric field in longitudinal (a-c) and transverse (d-f) direction for foils with a transverse size of $w = 2\pi{\cdot}200$ (a,d), $2\pi{\cdot}20$ (b,e) and $2\pi 4$ (c,f) at $t = 570$ after the laser pulse maximum reaches the target, which is approximately the time when protons gain most of their energy. The position of the proton front is marked by black lines, the initial foil position is indicated by white boxes.

can reenter the laser interaction region while the laser pulse is still on and electrons can be re-accelerated. This increases the resulting hot electron temperature and hence the proton cutoff energy. Once the foil diameter is in the order of the laser focal spot size or smaller (case IV), the transverse electrostatic fields become as large as the longitudinal one and start to influence the high-energy proton sheath. Furthermore, the laser light can diffract around the foil, further accelerating electrons behind the foil, leading to still enhanced electron temperatures. As the laser now illuminates the whole target, a charge imbalance can be set up over the whole foil volume inducing Coulomb expansion of the bulk ions [171, 172, 173, 174]. The proton maximum energies continue to increase until saturation at $w \approx w_0$. It is worth noting that for short laser pulses (i.e. $t_p \lesssim 2\pi{\cdot}10$), the two latter cases III and IV degenerate.

Electron recirculation The transverse recirculation of hot electrons first becomes important when the lateral foil size is less than the electrons need to travel to the distant edges and return to the center of the foil, which is the case in regions II-IV. This influences the spatial shape of the acceleration sheath field (Fig. 4.22) and ion distribution (Fig. 4.23). It can be observed that upon reduction of the lateral foil size both the sheath fields and

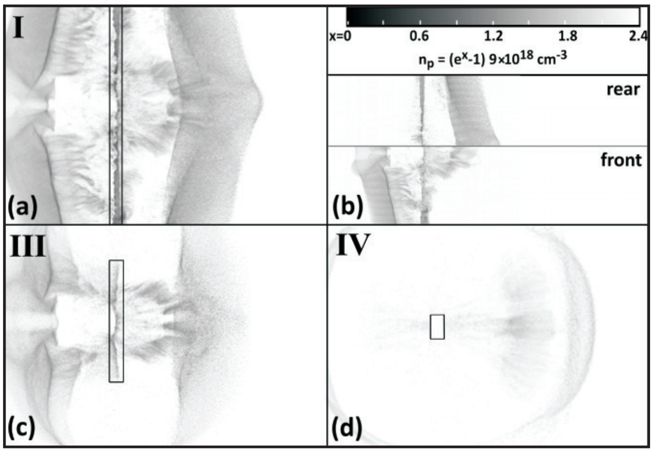

Figure 4.23: Proton density in the expanding sheath for foils with $w = 400\pi$ (a,b), 40π (c) and 8π (d). The initial target positions are marked by black boxes. In (b), the proton sheath density is shown independently for protons originating from the front and rear surface. The time of the snapshots is the same as in Fig. 4.22.

proton distribution first flatten before they become very divergent in region I again. Two effects counteract each other at the same time. First, the recirculating electrons lead to a flattening of the electrostatic rear surface fields due to the fact that the transverse dilution of electrons is inhibited. Another effect is the build-up of transverse quasi-static fields at the target edges. Their strengths can be in the same order of magnitude as the longitudinal fields. When the foil lateral size gets in the order of the ion source size, then these fields will significantly add to the divergence of the accelerated ion beam. This can be seen in Fig. 4.22(e,f) in the transition from region III to IV, when the transverse fields become equally large as the longitudinal fields depicted in panel (c).

A powerful indicator of the electron reacceleration is the electron energy density distribution and its flattening for small foil sizes in region III and strong curving for yet smaller foils. In Fig. 4.24a the transverse profiles of the electron energy density $\vartheta(x)$ is shown for various foil sizes. The flattening of the energy distribution due to a confinement and recirculation of hot electrons can be clearly seen in the intermediate regions II and III. A fit with a second order harmonic function $\vartheta(x) = -rx^2 + sx + t$ around the laser axis illustrates the above. While for intermediate foils in region II or III at first the curvature reduces with reduced foil size due to the electron recirculation (for $w/2\pi = (200, 40, 20)$ it is $r \times 10^4 = (2.3, 1.5, 0.15)$), for small foils the curvature increases significantly due to the transverse fields at the target edges (e.g. for $w/\pi = 8$ it is $r \times 10^4 = 590$).

The electron energy density spread and the curvature of the longitudinal electric field are imprinted on the proton sheath and its angular density distribution. As consequence of the flatter sheath field distribution in II, III, the proton acceleration is more laminar causing a smaller beam divergence (Fig. 4.24b). From a FWHM of 13° for the large foil, the angular spread of the most energetic protons is reduced to 11° and 8° for foil diameters

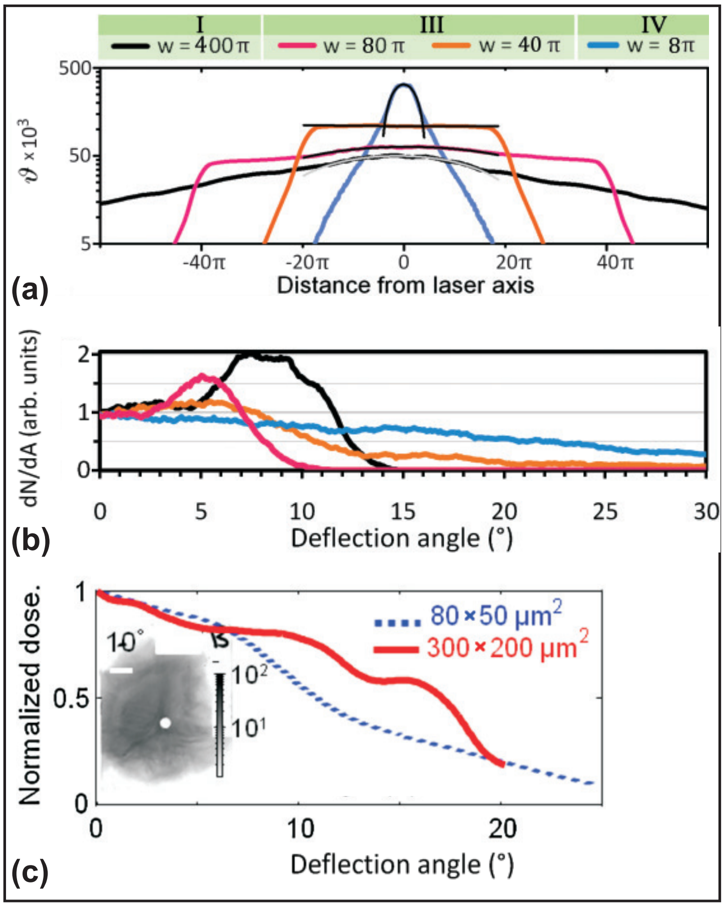

Figure 4.24: **(a)** 2D electron energy densities $\vartheta(y)$ for various foil diameters at the time the laser maximum reaches the target. Thin lines are the best fit with the function $\vartheta(y) = -ry^2 + sy + t$ around the laser axis, which is where the most energetic protons are accelerated. The time of the snapshots is the same as in Fig. 4.22. **(b)** Angular proton dose distribution for foils with different transverse size at $t = 1.2$ ps after the laser pulse maximum reaches the target. Only forward moving protons from the target rear side with $E_p > 0.75E_p^{\max}$ are considered. For statistical reasons, the data were smoothed by a 3 µm Savatzki-Golay filter. Each curve is normalized to its zero-deflection value. **(c)** Angular proton dose distribution for foils with different transverse size (extracted from [109]). Only forward moving protons from the target rear side with $E_p > 0.6E_p^{\max}$ are considered. Each curve is normalized to its zero-deflection value.

$w = 40\,\mu\text{m}, 20\,\mu\text{m}$, respectively. For the small foils in region IV, the proton divergence then significantly increases again as the lateral electric fields set up by the recirculating electrons at the target edges becomes comparable to the longitudinal field strength and shift close to the laser axis. This is adding a strong lateral force to the fast ions.

A first experimental evidence for the described geometric effects has been found experimentally in the angular proton dose distribution in a recent experiment performed at the Laboratoire pour l'Utilisation des Lasers Intenses (LULI) in France [109] (Fig. 4.24c). There, with a laser pulse with 7 J, focus $w_0 = 12\pi$ (FWHM), peak field strength $a_0 = 3$ and pulse duration $t_p = 755$ a target foil with transverse dimensions $160\pi \times 100\pi$ was compared to a large foil of $600\pi \times 400\pi$. The azimuthally averaged angular dose profiles show qualitatively the same features as revealed in the present PIC simulations when comparing the foil with $w = 2\pi \cdot 200\pi$ and $2\pi \cdot 20$: The FWHM of the distribution of the smaller foil is less than for the large foil (flattening by electron confinement and recirculation) with a low-dose tail extending to higher deflections angels (influence of transverse fields).

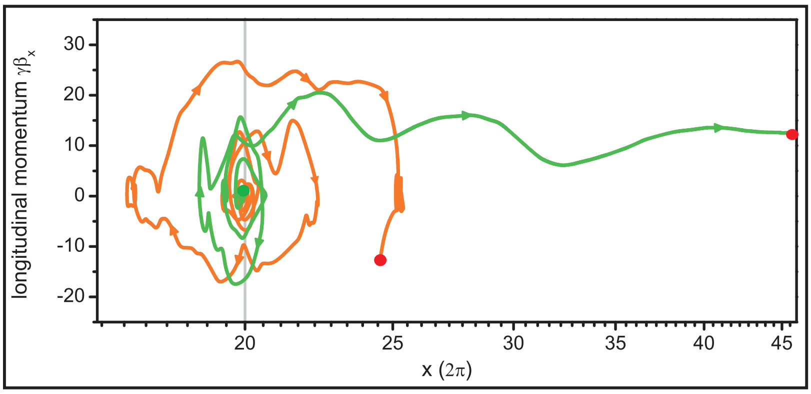

Figure 4.25: Trajectories in longitudinal phase-space of two representative longitudinally recirculating electrons in an ultrathin foil.

The electron recirculation additionally has an effect on the ion maximum energy. When the hot electrons are restricted in their transverse motion and reflected back into the foil center, the effective density during the ion acceleration becomes greater and following Eqn. 2.63 the maximum ion energy increases. However, the simulations exhibit only a small energy increase in region II. Fig. 4.29 shows the simulated hydrogen ion spectra and it can be seen that the hydrogen energy for the foil with $w = 200\pi$ the maximum energy is only slightly increased from 21.8 $\mathrm{M}e\mathrm{V}$ at large foil to 23.3 $\mathrm{M}e\mathrm{V}$.

Electron reacceleration It was first discussed in [29] that the repeated transit of the transversely recirculating electrons can increase the effective hot electron temperature since electrons have a chance of repeatedly gaining energy from the laser. The fact that an electron which repeatedly comes into the interaction region of the laser can repeatedly gain energy is confirmed in Fig. 4.25 which shows the trajectory of two sample energetic electrons in the longitudinal phase space of a thin foil (here the electrons are recirculating longitudinally). The electrons move back and forth, oscillating in the quasi-static fields set up by the initially almost resting ions and gain additional energy at each transit through the laser irradiated area at the foil front surface. The same does happen due to the transverse recirculation, only that the time needed to return to the laser interaction region now is determined by the lateral foil size rather than its thickness. In the following description one has to keep in mind that in the 2D case of the simulations performed here, each electron that returns from the lateral edges will eventually end up in the laser interaction region. This is not true in a realistic 3D case, where the electrons can spread over two lateral dimensions inside the foil, hence a non-normal reflection at the foil edges can cause the electron trajectory to not be closed, i.e. it does not necessarily return to the laser focal spot. This means that all estimates in the following are actually best suitable to a situation where at least one

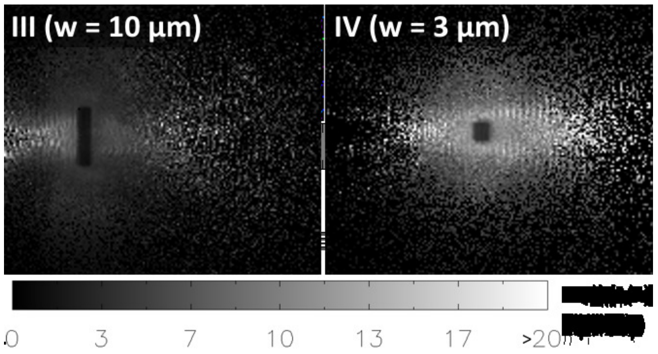

Figure 4.26: Average kinetic energy of plasma electrons for a foil with diameter $w = 10\,\mu\text{m}$ (left) and $w = 3\,\mu\text{m}$ (right) at the time the laser maximum reaches the target. In the latter case the average electron energy outside the foil is much larger than in the first one. At the small foil the laser can diffract around and accelerates electrons also behind the target.

dimension of the foil is comparable to the laser focal spot size, or a laser with a line focus.

The simulated dependence of the electron spectra on the transverse foil size is illustrated in Fig. 4.28. The electron spectra, summed up over the whole respective foil volume, are taken at the time when the laser maximum reaches the front foil surface. The spectra can be described by two temperature components. The lower temperature $T1$ is the temperature of a large flat foil as described in section 4.1.2. The hot electron density and temperature $T2$ are increasing with decreasing foil size for foils in region III and IV, the plot of $T2$ as a function of the inverse transverse foil size in Fig. 4.28 exhibits a proportionality of the hot electron temperature to the inverse transverse foil size. This increase is due to hot electron refluxing and reacceleration. Hot laser accelerated electrons circulating in the foil are drifting laterally towards the foil margins. There they exit the foil up to an average distance of the Debye length before they are pulled back by the restoring force set up by the remaining ions. When they reenter the laser focus while the laser is still on ($w/v_{\text{lat}} < t_p$), there is a chance that they are accelerated again. E.g. for the foil with $w = 2\pi \cdot 10$ the electron temperature $T2$ thus reaches $\approx 3\,\text{MeV}$, roughly $20\,\%$ higher than in the larger foils. The situation changes when the foil size is further decreased and gets comparable to the laser focal spot size (region IV). Now, the enhancement process is not limited to single recirculations anymore but rather the electrons are continuously heated by the laser as they are confined to the focal spot by the electrostatic attraction of the inert target ions (see Sec. 4.3.1.3). Additionally the peripheral regions of the laser beam can be diffracted around the target, so that the laser can effectively heat electrons behind the foil. This effect is illustrated in Fig. 4.26, where the electron temperature distribution of a foil of region III ($w = 20\pi$) is contrasted to one of region IV ($w = 6\pi$) at the time the laser intensity on target reaches its maximum. While for the 20π foil a high plasma electron temperature is observed only in front of the foil, for the small 6π foil the plasma temperature is high both in front and behind the target. Despite increasing geometrical losses, the conversion efficiency

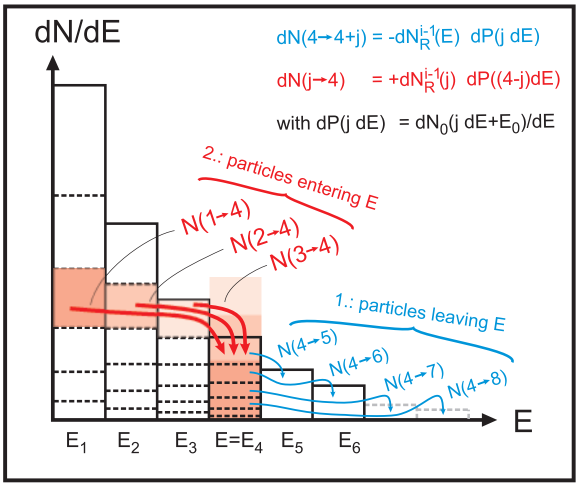

Figure 4.27: Reacceleration of electrons transversely refluxing from the lateral foil edges. Each time a hot electron with energy E traverses the laser focus, there is the probability $P(E')$ to gain an additional amount $E' = jdE$ of kinetic energy. The spectrum of recirculating electrons can thus be calculated iteratively by subtracting the electrons leaving an energy interval to higher energies and adding those entering it from lower energies. Here this is exemplary shown for the $k = 4th$ energy interval. Electrons leave to $k \geq 5$ (dashed lines indicate $dN(k \to k+j)$) and enter from $k < 4$ (indicated by red squares).

of the laser to kinetic particle energy is almost constant ($\approx 40\,\%$) throughout all simulated foil sizes (Fig. 4.30).

A model to analytically determine the temperatures and spectra of mass limited targets has been developed in [29]. It is based on the iterative increase in energy based on a probabilistic assumption for an electron to gain a certain amount of energy during each recirculation pass. Each time an electron coming from the lateral edges reenters the focal spot, there is a certain probability that it gains a certain amount additional energy from the laser. In the model it is assumed that the normalized electron energy distribution

$$f_0 = \frac{1}{N}\frac{dN_0}{dE}$$

seen in a large foil – where no recirculation occurs – resembles exactly this probability distribution (N is the total number of electrons initially inside the laser focus). I.e. the probability for an electron to gain an additional kinetic energy of more than E_1 and less than E_2 is derived from the large foil spectrum by

$$P(E_1, E_2) \equiv \int_{E_1}^{E_2} f_0(\tilde{E} + E_0)d\tilde{E} \tag{4.40}$$

where E_0 is the average kinetic energy of electrons not directly accelerated by the laser (bulk electrons). The number of transversely recirculating electrons in the following is assumed to be 1/2 of the total number of relativistic electrons (kinetic energy $E > 1$) which means that the electron velocities are distributed uniformly in the plane defined by the laser polarization and propagation vectors. This assumption is further motivated by the average

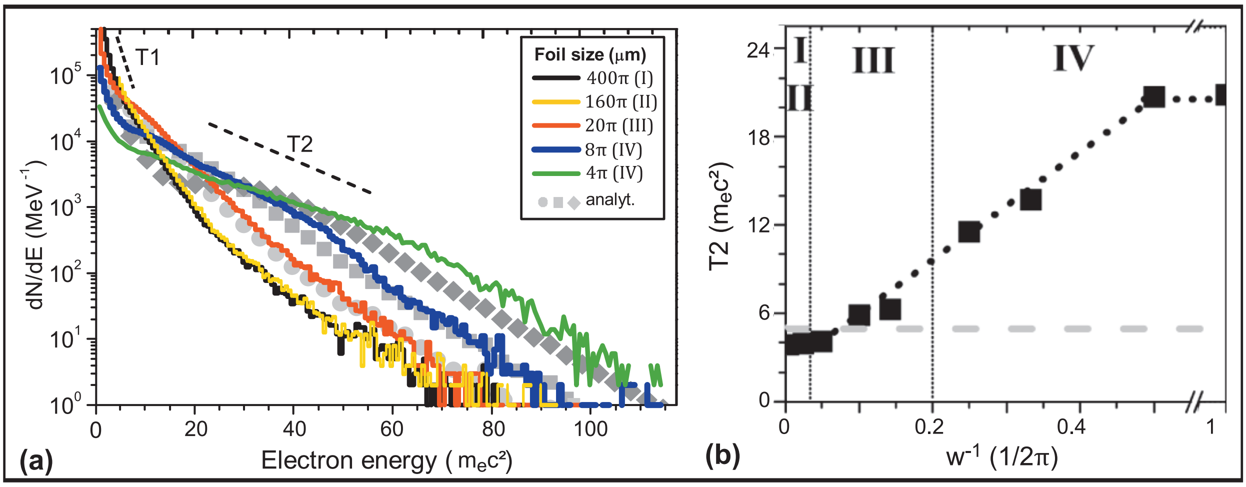

Figure 4.28: **(a)** Electron spectra of foils with varying transverse width at the time the laser maximum reaches the foil front surface. Gray circles, squares and diamonds mark the energy distribution for a foil with $w = 20\pi$, 8π, 4π, respectively, assuming the spectrum of the large foil being altered by multiple electron reflux and reacceleration. **(b)** Hot electron component temperature as a function of the inverse foil width.

transverse electron drift velocity $v_{trans} \cong 0.7$ extracted from the simulation run of the large foil ($w = 2\pi \cdot 200$). The spectrum $f_R^0 \equiv \frac{1}{N}\frac{dN_R^0}{dE}$ of the recirculating electrons before they are reaccelerated the first time then reads

$$f_R^0 = \frac{1}{2}\, f_0|_{E>E_0}\,. \tag{4.41}$$

Their spectrum after the i-th recirculation, $f_R^i = dN_{\mathrm{R}}^i(E)/dE$, will then be changed compared to the previous recirculation by subtracting at each energy interval $[E, E + dE]$ the number $dN_-(E)$ of electrons that are leaving the interval by being accelerated more than dE and by adding for all $\tilde{E} < E$ the number of electrons that are accelerated by more than $E - \tilde{E}$ and less than $E - \tilde{E} + dE$ and thus enter the energy interval (see Fig. 4.27)

$$dN_R^i = dN_R^{i-1}(E) - dN_-(E) + dN_+(E)$$

With the definition (4.40) for the probability P of an electron to gain a certain amount of energy when passing the laser focal spot, the number $dN_-(E)$ of electrons leaving the energy interval adds up to

$$\frac{dN_-(E)}{dE} = N f_R^{i-1}(E) P(0,\infty). \tag{4.42}$$

The number of electrons $dN_+(E)$ entering can be obtained by considering all electrons with energy $\tilde{E} < E$. The number of electrons with energy in the range $[\tilde{E}, \tilde{E} + d\tilde{E}]$ that are accelerated by an energy between $E - \tilde{E}$ and $E - \tilde{E} + dE$ and end up having an energy in the interval $[E, E + dE]$ is given by $dN_+(E)/dE = Nf_R^{i-1}(\tilde{E}) \cdot dP(E - \tilde{E})$ (where $dP(E - \tilde{E}) \equiv P(E - \tilde{E}, E - \tilde{E} + dE)$), hence the total number of electrons entering the interval $[E, E + dE]$ is given by

$$\frac{dN_+(E)}{dE} = N \int_0^E f_R^{i-1}(\tilde{E}) \frac{dP(E - \tilde{E})}{d\tilde{E}} d\tilde{E} \tag{4.43}$$

which is similar to the convolution $f_R^{i-1} * f_0$ but with limited bounds in the integral. The spectrum of the recirculating electrons after the i-th recirculation can then be calculated explicitly from the spectrum of the previous recirculation $i - 1$ by

$$\boxed{\begin{aligned} f_R^i = f_R^{i-1}(E) - f_R^{i-1}(E) \int_0^\infty f_0(\tilde{E} + E_0) d\tilde{E} \\ + \int_0^E f_R^{i-1}(\tilde{E}) f_0(E - \tilde{E} + E_0) d\tilde{E} \end{aligned}} \tag{4.44}$$

and the total electron spectrum reads

$$f = \frac{1}{2} f_0 + f_R^i. \tag{4.45}$$

Fig. 4.28(a) shows the electron spectra for various foil sizes at the time the laser maximum reaches the target. It can be seen that for the foils in region II the spectrum looks almost the same as in region I, since the laser pulse duration is shorter than the time needed to return even for the fastest electrons. On the contrary, for the small foils the spectra show an obvious and significant shift towards higher energies. Exemplary, for the three smallest foils the spectra predicted by the above model are given with $i = t_p/2w = (3, 8, 16)$ for the foils of diameter $w = 2\pi\,(10, 4, 2)$. They compare very well with the simulated spectra with respect to both the electron temperature $T2$ and hot electron density increase, validating the above model. The electron temperature $T2$ is found to increase linearly with decreasing foil size in regions III and IV as one could expect from an heuristic argument: Decreasing the foil transverse size by a factor a means that the electrons return to the focal spot a-times more often and hence the energy they acquire is a-times larger. This argument is in deed in agreement with both the model and the PIC results with respect to $T2$, but not with the total energy. Below $w = 4\pi$ the PIC simulations do not exhibit any further increase of the electron temperature and hence the applicability of the model ceases.

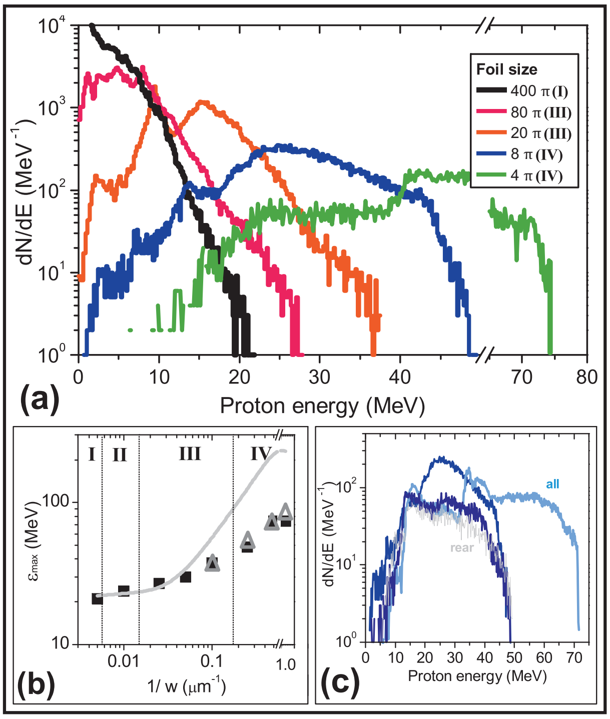

Figure 4.29: (a) Proton spectra for foils of varying transverse width. (b) Maximum energy ε_{max} as simulated by PIC (squares), as expected from PEM Eqn. 2.63 assuming a lateral sheath size of 80π or of the foil diameter if smaller (solid line) and as expected from Coulomb explosion Eqn. 4.46 (triangles). (c) Proton spectra for 8π foil for three preplasma scale lengths p (0: black line, π: dark line, 4π: light line). For $p = 4\pi$ the maximum energy is significantly enhanced due to front-side acceleration. The energy spectrum of rear side protons (small dots) remains virtually unaffected. For all spectra, only forward moving protons were considered.

At the same time as the electron energies and hot electron density increase, the proton maximum energies also increase as expected from Eqn. (2.63). Fig. 4.29 shows the proton spectra of several MLT, where an increase in maximum proton energy can be observed for decreasing foil size. After the increase is only little in region II from 21.8 $\mathrm{M}e\mathrm{V}$ at the large foil with $w = 400\pi$ up to 23.3 $\mathrm{M}e\mathrm{V}$ for the foil with $w = 160\pi$, the maximum energy rises considerably for yet smaller foils, for example exceeding 74.1 $\mathrm{M}e\mathrm{V}$ for the sub-focal-spot sized foil with $w = 4\pi$. For the foils below the laser focal spot size of 8π the proton cutoff energy is found to further increase significantly, in contrast to results obtained with short laser pulses [163], where the cutoff energy decreases for foils below the optimum foil size of the laser focal spot diameter. At the same time, the proton spectrum changes from a quasi-exponential distribution to a flatter distribution shifted to higher energy because the electric field can then be sufficiently large to accelerate all the light ions to MeV energies. This is very similar to the observations in the case of short, few fs pulse duration [175].
An exponential preplasma with scale length π and 4π at the front surface does not alter the energy of the rear side protons (Fig. 4.29c) which agrees with the fact that no increase in electron temperature can be observed when adding preplasma[10].

---

[10] This may not be the case for realistic preplasmas such as shown in Fig. 4.21. In these simulations, though with different laser parameters, ε_{max} for protons from the target rear in fact are more energetic compared to the case without preplasma.

4.3.1.3 Coulomb explosion

The observed proton cutoff energies in region IV fall short of the values predicted by the analytical plasma expansion model (Eqn. 2.63), as can be seen in Fig. 4.29(b). This is due to the fact that the model is only applicable assuming the target bulk sustains its charge neutrality and the hot electrons create a charge separation only at the foil surface (see Section 2.3.1.1). The foil expansion is then driven by the surface fields. In foils with diameter below the laser focal spot size the target is heated over the whole target surface, inducing an electron deficit. This is different to what is seen in the simulations for large foils where the charge neutrality is maintained by cold bulk electrons flowing into the focal region from the outer wings of the target. For example for the foils in region IV the electron deficit increases with decreasing foil diameter from 1.1% for $w = 8\pi$ to 6.5% for $w = 2\pi$. Hence, for foils with diameter in this region one can expect Coulomb expansion of the heavy bulk ions to dominate. In this case, the protons can be treated as test particles and their maximum energy $\varepsilon_{\mathrm{max}}$ is then determined by the electric field of the Coulomb exploding heavy ions. The proton maximum energy can be estimated analytically from an exploding sphere of radius $R \approx \sqrt{\mathrm{wd}/\pi}$ with [171]

$$\varepsilon_{\mathrm{max}} = \frac{2\eta n_{\mathrm{Ti}} e^2 Z_{\mathrm{Ti}} R^2}{3\varepsilon_0}. \tag{4.46}$$

in reasonable agreement with the PIC simulation results (see Fig. 4.29(b).

With reduced target diameter both the fraction of total energy transfered to heavy ions with low charge-to-mass-ratio Z/m (Fig. 4.30) and the fraction of the maximum energy per nucleon of heavy ions to light proton ions ($\varepsilon^{\mathrm{Ti}}_{\mathrm{max}}/\varepsilon^{p}_{\mathrm{max}}$) increases (e.g. from 0.014 to 0.077 for diameter $w = 400\pi$ and $w = 8\pi$). Fig. 4.30 shows that the simulations predict the laser energy converted into protons to decrease to ≈ 5 % for a 8π foil while for the large 400π foil the simulation yields a conversion efficiency into protons of ≈ 9 % (≈ 2.5 % for protons above 4 MeV). At the same time, the energy converted into the heavy titanium ions increases from ≈ 9 % to ≈ 30 %. Those numbers appear not be influenced much by the fact that the simulations were performed with a reduced electron density compared to solids, as for example in case of a large foil the conversion efficiency of laser energy into protons above 4 MeV is in reasonable agreement with experiments [170].

This shift of energy conversion into heavy ions for small foils is consistent with the dynamics being driven primarily by Coulomb explosion rather than the TNSA. Iteratively self consistently solving the Poisson equation and moving the ions in the field solution, the

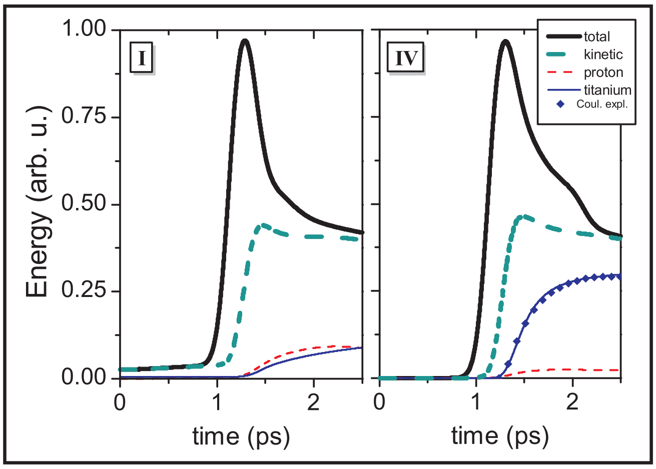

Figure 4.30: Energy conversion from laser energy to kinetic energy of particles (thick dashed). In the case of a 8π foil (right), the amount of energy transfered to ions with low Z/m (here Ti^{4+} ions) is substantially increased compared to the large 400π foil (left). This causes less energy to be converted to proton kinetic energy. The total conversion efficiency of laser light to kinetic energy is almost constant for all simulated foil sizes.

temporal evolution of the kinetic energy of the heavy ions for the target with diameter $w = 8\pi$ is in very good agreement with that seen in the PIC simulation (Fig. 4.30), using an initial electron deficit of 1.1 % and a linear neutralization over $t_{acc} \approx 2450\omega_0^{-1}$ taken from the PIC results. For large foils, heavy bulk ions are only accelerated by TNSA close to the surface. Since the lighter ions screen a significant portion of the field, the titanium ions then only gain comparatively little energy in total. In small foils, the electron deficit extends over the whole target bulk. Consequently a significant part of the Coulomb energy is transferred to the bulk ions instead of the light ions at the surface. The endpoint of total energy of the bulk ions only depends on the Coulomb energy available in the beginning, hence, under the assumption that this does not change significantly when including ionization, this effect can be expected to be qualitatively independent of the specific charge state distribution. That means, that even if there is a mixture of different charge states, the heaviest ions will always gain more total energy in small MLT than in large foils. In that case, assuming that there still is one dominant charge state Z_{Ti}, Eqn. 4.46 would still remain valid with $\varepsilon_{\max} \propto Z_{\mathrm{Ti}}$.

4.3.1.4 Discussion

The effect of target width on the target rear electric field and proton sheath angular divergence was studied. For medium sized targets ($40\pi \ldots 200\pi$) the divergence of energetic protons is significantly decreased compared to large foils. For smaller foils, large transverse fields at the target edges and Coulomb explosion leads to very broad proton distributions. The transfer of laser energy to electrons may be enhanced in the presence of a plasma gradient at the target front. While this enhanced electron temperature does not lead to an enhanced energy transfer into energetic protons of the rear surface, the protons from the front surface experience an enhanced acceleration within the target and for sufficiently large preplasma scale lengths can become more energetic than the rear side protons.

The possibility to control the electron temperature and subsequently the maximum proton energy of proton accelerated from mass limited foils following high intensity laser irradiation with comparatively long pulse duration of 330 fs has been demonstrated. An analytical model has been developed to predict the electron temperature and spectral shape which quantitatively explains the numerical observation of an increasing hot electron temperature with decreasing foil transverse size. The proton maximum energy at the same time is enhanced in agreement with the PEM predictions (4.25).
However, the most significant increase in proton maximum energy is observed for very small targets with diameter in the order of the laser focal spot size of only a few micron. Yet, it will be experimentally challenging to prepare this physical situation, as such an experiment would require excellent laser pointing accuracy within a few microns and any target holder would provide mass and prevent an efficient limitation of the target volume. Additionally, effects of the prepulse and 3D edge effects might also become important. Here, water droplets in a Paul trap, representing real isolated micro-targets, could provide an alternative to rigid foil targets in the future.

4.3.2 Flat Top Cone Targets

Curved-wall hollow micro-cone targets, with a flat-top at the tip, are of great interest for the acceleration of protons by laser pulses of high intensity and short pulse duration. Such micro-cones were recently shown to enhance the proton acceleration and the most energetic laser accelerated protons published to date were produced using this kind of targets [21]. In the following, this experiment will be described and a theoretical explanation of the most important observations will be given. The author has participated in this experiment and the basic ideas were developed during that campaign together with the principal investigators.

The important property of cone targets is the formation of surface currents along the cone wall when the laser is aligned tangentially to the inner cone wall, as identified for example in [30, 108, 176]. Reference [30] predicted a guiding of surface currents along the surface of cone-shaped targets by self-generated quasi-static magnetic and electric fields. Those currents can contain significantly more electrons than those accelerated at flat foils, improving the laser conversion efficiency to hot electrons and energetic ions. Several experiments have confirmed the existence of those currents by K_α emission [177, 108] and heating of a wire connected to the cone tip [178].

In addition, [30] predicted electron energies in the surface currents exceeding that of flat foils. The proposed mechanism is micro focusing, an optical geometric collection of laser light. This would result in a local increase of laser intensity, and therefore electron energies, with average hot electron energies predicted by particle-in-cell (PIC) simulations well exceeding the ponderomotive energy. This can in turn enhance the proton acceleration from the top as compared to regular flat foils [21] (see also Fig. 4.31c).

The best conditions to create such currents are a high laser contrast, high laser pulse intensity and the use of low density, small Z-targets [176]. However, the mechanism responsible for the energy increase has remained a subject of debate. The high proton energies in [21] were observed from cones with a large neck diameter of up to more than $10\,\mathrm{w}_0$. An enhancement of proton and electron energies was found by PIC simulations also for cones with a neck diameter much larger than the laser focal waist, and the energy exceeded that expected from micro-focusing alone. It therefore must be concluded, that the proposed micro focusing mechanism is only dominating in a certain class of experiments, i.e. inner cone neck diameter smaller than the focal spot size, straight walls and moderate laser intensity. In other cases, there must exist other mechanism responsible for the observed electron energy increase. For example, Nakamura et al. [31] found that a resonant acceleration of electrons oscillating in a self-created surface potential (very much similar to the direct laser acceleration mechanism

Reprinted with permission from T. Kluge, S. A. Gaillard, M. Bussmann, K. A. Flippo, T. Burris-Mog, B. Gall, M. Geissel, S. D. Kraft, T. Lockard, J. Metzkes, D. T. Offermann, J. Rassuchine, M. Schollmeier, U. Schramm, Y. Sentoku, K. Zeil and T. E. Cowan, AIP Conference Proceedings 1299, page 715 (2010). Copyright (2010), American Institute of Physics.
Reprinted with permission from T. Kluge, S. A. Gaillard, K. A. Flippo, T. Burris-Mog, W. Enghardt, B. Gall, M. Geissel, A. Helm, S. D. Kraft, T. Lockard, J. Metzkes, D. T. Offermann, M. Schollmeier, U. Schramm, K. Zeil, M. Bussmann and T. E. Cowan, New Journal of Physics, Vol. 14, page 023038 (2012). Copyright (2012), IOP Publishing Ltd. and Deutsche Physikalische Gesellschaft.

described in Sec. 2.2.4.6) can lead to higher electron energy in a long capillary with walls covered by preplasma when the laser is aligned at a resonant angle of ≈ 30° with respect to the walls.

In the following the electron dynamics in the case of cones with curved neck (see Tab. 4.7) and neck diameter well exceeding the laser focal waist is investigated with the aid of 2-dimensional PIC simulations. The main result is that both micro-focusing and resonant acceleration in this case are not efficient and cannot explain the simulated electron energies. Rather, a novel and previously unconsidered mechanism, the continuous, direct acceleration of electrons by the laser light [21] is found to be dominant. The interaction is analyzed in detail in order to optimize the cone geometry with respect to proton acceleration. Based on this analysis, analytical and empirical scaling laws for the electron energy can be given and the optimum geometric parameters for cone targets are inferred.

4.3.2.1 Setup and Simulations

Parameter	Value
Geometry	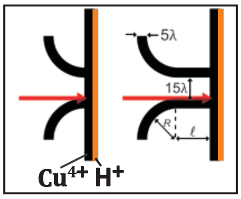
laser strength a_0	1-20
pulse shape	Gaussian/ flat top
laser waist w_0	4π
pulse duration	100
electron density $n_{e,0}$	$10 - 40$
foil thickness d	10π (Cu) + 4π (H^+)
ions (electrons) per cell	4 (116)
cells (time steps) per laser wavelength	$25 \times \sqrt{n_{e,0}/10}$
box size ($x \times z$)	$240\pi \times 480\pi$
including collisions/ ionization	yes/yes

Table 4.7: Parameters used for the simulations in this section. The cones are positioned 12.5λ from the left simulation box boundary and centered in the simulation box in the vertical direction. Its walls have a radius of curvature of $R = 20\pi$ with an inner neck diameter of 30π, the top has a diameter of 180π. The thickness of all copper walls is 10π, the top is additionally covered with 4π of hydrogen ions. The resulting position of the top front surface is 55π from the left box border. In some simulations the neck was extended, as shown in the right figure, and the wall curvature was varied. The influence of changing the geometric properties is discussed in Sec. 4.3.2.2.

The simulations in this section were performed with a typical laser duration $t_p = 100$ (FWHM) with a gaussian profile, if not stated otherwise. In cases where the electron dynamics and temperature scaling is analyzed, a temporal profile with a flat top and a gaussian rise and fall of $t = 16$ was used to provide a sufficient duration with constant intensity. The time t will always be given relative to the time when the laser maximum reaches the front inner surface of the flat top. The spatial profile was gaussian with a focal spot size of $w_0 = 4\pi$. The laser was linearly polarized with the electric field vector pointing in x-direction and the magnetic field vector pointing in y-direction, $\boldsymbol{E} = E\boldsymbol{e}_x$ and $\boldsymbol{B} = B\boldsymbol{e}_y$. Unless mentioned otherwise, the laser strength parameter was set to $a_0 = 8.5$, but other laser intensities were also used to study the scaling of the interaction processes with a_0.
The target geometry is shown in Tab. 4.7. It consists of a hollow cone[11], whose walls have a typical wall radius of curvature of 20π and a thickness of 10π. The separation distance between the walls is set to 30π, which is much larger than the laser focal spot size of 4π. At the tip of the cone a flat foil is mounted with a diameter of 180π and thickness 10π. The target is composed of copper, which was 4-fold pre-ionized in order to mimic the effect of prepulses and amplified spontaneous emission, and the flat top is additionally covered with a neutral proton-electron plasma layer of thickness 4π.

For most of the simulations the electron density was set to $\mathrm{n_{e,0}} = 10\,\mathrm{n_c}$ when fully ionized. For the simulations regarding the intensity scaling the density was set to $\mathrm{n_{e,0}} = 40\,\mathrm{n_c}$ for $a_0 > 8.5$ in order to prevent an artificial RIT that would occur for $\mathrm{n_{e,hot}}/\mathrm{n}_c > \gamma$. The number of macro-ions per cell was set to 4 which results in 116 macro-electrons when fully ionized. This choice ensures that the macro-particle dynamics still closely resembles the single particle dynamics. The simulation box volume of $\mathrm{z} \times \mathrm{x} = 481.6\pi \times 240.8\pi$ was divided into $6,000 \times 3,000$ cells, resulting in a cell size of $\Delta\mathrm{z} = \Delta\mathrm{x} = 0.08\pi = 0.125 \cdot 2\pi c/\omega_{\mathrm{p},0}$ ($\omega_{\mathrm{p},0}$ is the cold plasma angular frequency when the plasma is fully ionized). Correspondingly, the simulation time was discretized with steps of $\Delta\mathrm{t} = 0.08\pi = 0.125 \cdot 2\pi/\omega_{\mathrm{p},0}$.

4.3.2.2 Results

Compared to regular flat foils, flat top cone targets with circular walls have been shown experimentally to enhance the maximum energy of protons emitted behind the target [21] (Fig. 4.31a,b). This has been attributed to the laser interaction with electrons along the

---

[11] A cone is just one possible 3D realization of the 2D geometry used in the 2D3V PIC simulations. However, it is the geometry that was used in the experiments summarized in Fig. 4.31, while e.g. planar foils with a bent section at the front and an attached flat foil section at the rear show the same vertical 2D line-out and therefore also satisfy the simulation conditions and hence are also feasible.

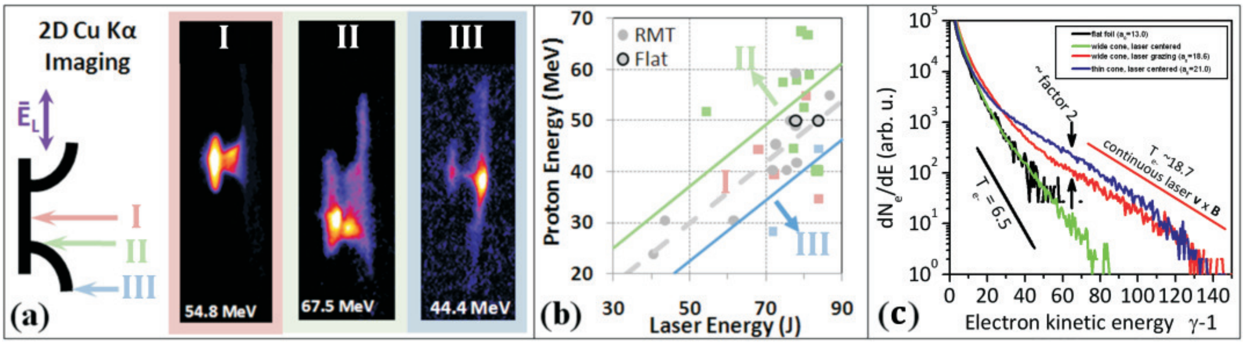

Figure 4.31: Experiments at the Trident laser at the Los Alamos National Laboratory have shown a significant increase in proton energy in 6 out of 8 shots that were performed grazing along a cone wall as confirmed by imaging the Kα radiation of hot electrons created by the laser pulse (green, 'II'), as compared to flat foils or coaxial alignment (gray, red, 'I'). (c) Simulations show that the electron temperature is greatly increased in the case of laser grazing incidence compared to flat foils, exceeding even the temperature expected from the intensity increase due to micro focusing. (extracted from [21])

inner cone wall [21]. A higher electron energy observed in PIC simulations is the key factor leading to higher proton energies, since the accelerated electrons can cross the cone top and contribute to the TNSA process at the rear surface. This process is equivalent to the regular TNSA process (Sec. 2.3.1) on flat foils but now with two electron ensembles: the ponderomotively heated electrons from the top front surface and the more energetic electrons from the cone walls which are responsible for the increase in maximum proton energy.

One simple scenario for the production of higher energy electrons could be the micro focusing as proposed by [30]. It was shown that when a laser pulse impinges on a solid surface at oblique incidence, the laser intensity simply increases by a geometric focusing. However, it can be shown numerically, that this intensity increase alone is not sufficient to explain the high energy of the electrons. Fig. 4.31c compares the spectra observed in simulations of a flat foil, a cone with wide neck (inner neck diameter $\gg w_0$, laser aligned grazingly) and a cone with thin neck (inner neck diameter $\ll w_0$, laser centered). The laser field strength was set to $a_0 = 13$ and consequently the expected hot electron temperature for the flat foil is $T_e^{hot,FF} \approx 6.7$ (Eqn. (4.24)) which is in good agreement with the observed temperature. As expected from micro focusing, the local field strength is increased in the case of grazing incidence on the cone. In the case of a wide neck the intensity is doubled with $a_0^{wide} = 18.6$ and at the thin neck cone it is $a_0^{wide} = 21.3$. From micro focusing alone one would expect an increase of the hot electron temperature to $T_e^{hot,wide} \approx 8.6$ for the wide neck

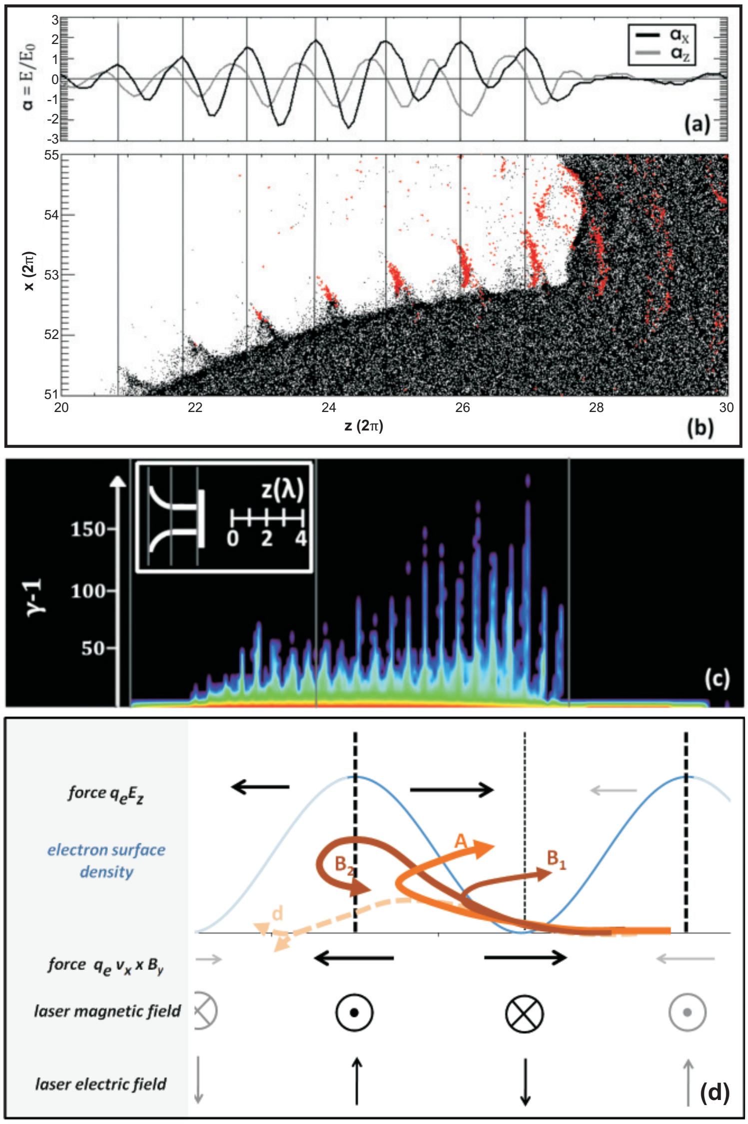

Figure 4.32: (a) Longitudinal (gray) and transverse (black) electric fields along the cone wall and (b) spatial distribution of electrons when the laser is aligned tangentially to the cone wall ($a_0 = 8.5$, FWHM $100/\omega_0$ (gaussian), $t = 0$). Hot electrons with energy exceeding 10 MeV are marked red. (c) Qualitative electron dynamics in the frame co-moving with the laser phase: The electron bunches (blue), extracted by the transverse laser field, are moving approximately in phase with the laser, the longitudinal forces on electrons are indicated by horizontal arrows (top: forces due to quasi-static longitudinal fields, middle: $\boldsymbol{v} \times \boldsymbol{B}$ forces (here: for electrons moving upward)). An electron extracted from the wall initially has a velocity in the laser direction of $\beta_z \ll 1$, so it will be overtaken by it (dashed line). If $\beta_z \approx 1$, it can be continuously accelerated by longitudinal fields (A) and via transverse fields ($\boldsymbol{v} \times \boldsymbol{B}$, ($B_1$, B_2)).

cone, but the observed temperature amounts to $T_e^{hot,wide} \approx 18.7$. In addition, the further increase in laser intensity at the thin necked cone does not lead to an observable increase in electron temperature as would be expected if micro focusing was the the mechanism for the high energy electron production. Rather, the temperature is found to remain constant and only the hot electron number is doubled, as now electrons from both the top and the bottom wall surface are accelerated. Those two observations demonstrate that the optical collection alone is not sufficient to explain the electron acceleration at cone targets.

Bunch formation Simulations show that the hottest electrons are localized in bunches moving forward along the inner wall surface (see Fig. 4.32b). Those bunches are created

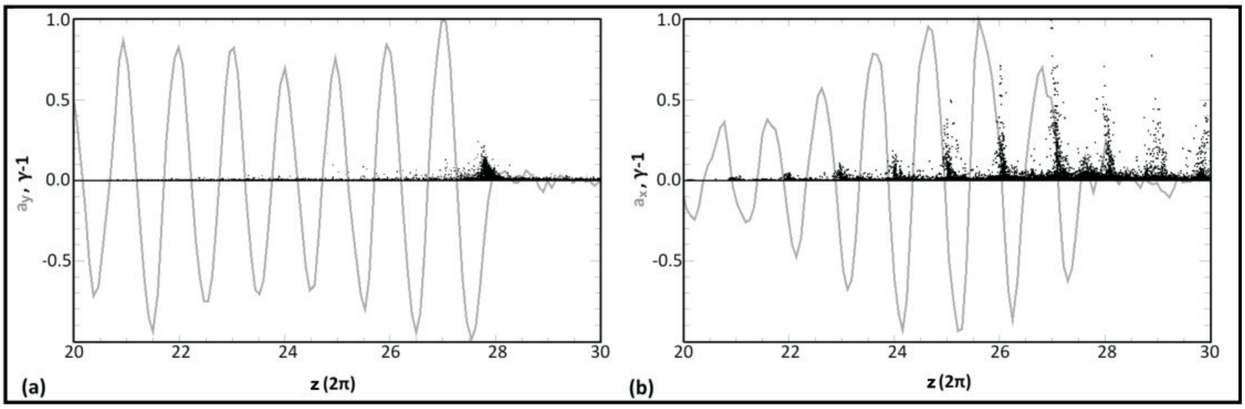

Figure 4.33: Electron kinetic energy $\pm 10\pi$ around the laser axis for grazing laser incidence and (a) s-polarized or (b) p-polarized light at the time when the laser maximum reaches the flat top front surface. In gray, the electric field of the laser in (a) y-direction or (b) x-direction is also shown for comparison. Energies are normalized to the maximum energy for p-polarization, fields are normalized to their respective maximum value. While for p-polarization the electrons are pulled out of the cone wall and form bunches which become accelerated towards the cone tip, in the case of s-polarization the interaction along the wall is negligible and most electron acceleration happens at the inner cone top surface, comparable to conventional flat foils.

by the laser electric field pulling out electrons from the cone wall into the vacuum. Since the transverse electric field is oriented negatively (corresponding to an upward force on the electron) once every laser cycle, the resulting electron density modulation is also periodic with a period length of 2π.

This is verified by Fig. 4.33 where the energy distribution is plotted over the longitudinal dimension summed over a region of $\pm 10\pi$ around the laser axis, which is aligned grazingly along the inner cone wall. In panel (a) the laser polarization is aligned parallel to the wall surface (s-polarization) while in (b) it is perpendicular (p-polarization). In the first case the laser electric field is aligned tangentially to the solid surface and therefore no electrons are extracted and no bunch formation can be seen. Electrons in this case acquire the most energy at the cone top inner surface comparable to the case of a flat foil. With p-polarization, the electric field can act to pull out electrons from the wall into the vacuum region forming bunches of hot electrons. As can be seen, the energy of the electrons increases continuously as they travel towards the tip.

In contrast to the well known $2\omega_0$ bunches created for example at oblique incidence on a plasma by the $\boldsymbol{v} \times \boldsymbol{B}$ force, the bunches here are separated by only 2π. Of course in the present case the Lorentz force still acts with 2ω, but only once every laser cycle the electric field is oriented in the negative x-direction there are electrons actually present outside the solid target. Pushed by the Lorentz force, the electrons can now move along the laser for a

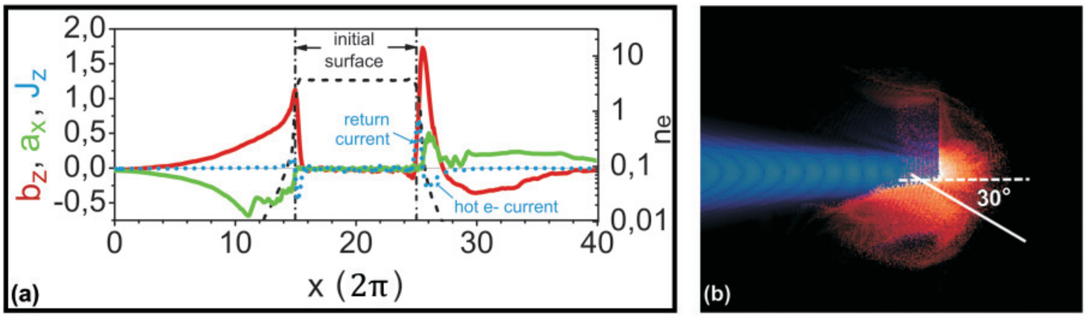

Figure 4.34: (a) Quasi-static electric field a_x and magnetic field b_y and charge current density j_z (here the charge of an electron is -1) averaged over a laser period. The laser is aligned tangentially to the inner cone wall (right side), where the quasi-static fields act to confine the hot electron current close to the surface. (b) The quasistatic magnetic field can confine even the most energetic electrons in the simulation for incidence angles of $\alpha < 30°$, creating a gap in the emission-angle distribution behind the target.

long distance along the cone target inner wall surface until they cross the cone top surface, thereby keeping the initial 2π modulation in density and forming bunches of energetic electrons. If the electrons remain in phase with the laser, they can gain much more energy than they could in a flat foil. In the simulations the maximum electron kinetic energy reaches up to $67 m_e c^2$ with an average of $12 m_e c^2$, which is more than three times that of a flat foil (see spectra in Fig. 4.38). The details of the acceleration mechanisms that are observed in the simulations in that case are analyzed below.

Surface confinement One important observation is that the electrons stay close to the surface on the laser axis once they are pulled out from the wall, so that they can continuously interact with it. This is ensured by quasi-static fields building up at the surface. Those fields are depicted in Fig. 4.34. The electrons are kept from exiting into the vacuum region by a quasi-electric field building up between the electrons outside the wall and the heavier ions inside. The electrons are kept from reentering the foil by a quasi-static magnetic field, self-created by the hot electron current and the cold return current inside the wall [30, 179] (Fig. 4.35), as long as the angle of incidence is small enough,

$$\alpha < \arccos\left(1 - \frac{\mathrm{w}}{\mathrm{R}_\beta}\right). \tag{4.47}$$

Here, w denotes the width of the magnetic field region and $\mathrm{R}_\beta = \frac{\sqrt{\gamma^2-1}}{\langle \mathrm{b} \rangle}$. In the specific case of the parameters used for the simulations here, the magnetic field is seen to extend inside the vacuum for about $\mathrm{w} \approx \pi$ with an average magnitude of $\langle b \rangle \approx 2$, preventing even the

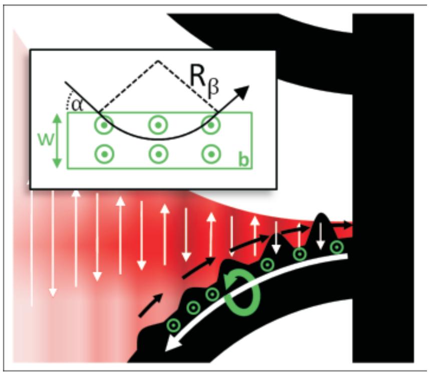

Figure 4.35: Schematics of electron confinement outside the solid wall. The black structure is a part of the cone target, irradiated by the laser (red, electric field direction indicated by up/down arrows). Laser electric field extracts electrons from cone wall, separated by 2π, which can then be forward accelerated (Sec. 4.3.2.2) (black arrows). This current is balanced by continuous return current inside the wall (white arrow), building up a quasi-static magnetic field at the surface. Inset illustrates trajectory of an electron (black) injected in a homogeneous quasi-static magnetic field at an angle α, following a circular path with cyclotron radius R_β.

most energetic electrons from reentering the foil for $\alpha < 30°$.

Electron acceleration mechanisms In the following the possible acceleration mechanisms for the surface-confined electron bunches are identified and their relevance in the grazing incidence setup will be analyzed. It is important to first study the field structure directly at the surface. Fig. 4.32a shows the longitudinal and transverse electric fields along the inner wall. The fields are the superposition of the original laser field (a_x), the laser fields diffracted from greater distance to the laser axis along the curved wall (adding both an a_x and a_z component) and the electrostatic fields originating from the space charge confined in the bunches. The longitudinal field follows the transverse field with a phase shift of $\pi/2$. There are now three possible mechanisms for electrons to become accelerated in such a configuration. First, electrons can oscillate in the potential well formed by the attractive electrostatic and repulsive magnetic fields (Fig. 4.34) and, in the case of an optimum phase match, be resonantly accelerated by the laser. The resonance occurs when the condition $\omega_e/\omega_0 = 1 - \beta_{z,drift} c_{ph} \cos\alpha$ is fulfilled [31] (ω_e: frequency of the electron oscillation, $\beta_{z,drift}$: forward velocity of electrons, c_{ph} = n: laser phase velocity, α: laser incidence angle). In the laser grazing setup, $\alpha = 0$ and the resonance condition effectively becomes a condition for the electro- and magnetostatic fields. One interesting limit occurs for high laser strength when the acceleration of electrons to velocities close to the laser phase velocity happens rapidly within a fraction of an electron oscillation. A prerequisite of course is the absence of preformed plasma outside the solid walls, so that the laser phase velocity is close to unity. In this case the resonance condition degenerates to $\omega_e = 0$ which means nothing more than that the electrons are accelerated continuously. As will be shown later, the electron acceleration in the present case is in deed not a resonant process but rather a continuous acceleration.
The possible acceleration scenarios for a continuous acceleration of surface electrons are sketched in Fig. 4.32c, which shows the qualitative electron dynamics in the co-moving

frame. An electron pulled out of the wall by the transverse electric laser field can gain forward momentum via the $\boldsymbol{v} \times \boldsymbol{B}$ force. It can then get caught in an accelerating $\boldsymbol{v} \times \boldsymbol{B}$ phase (moving upward (ia) or downward (ib)) or into the longitudinal electric field region (ii).

In order to quantify which of the three acceleration mechanisms (i,ii or resonant acceleration) are important, simple measures can be defined and calculated for each single electron. For this, the trajectories in the PIC simulation were followed for all electrons originating within a region where the most energetic electrons are expected to originate from, i.e. $\pm\pi$ around the laser axis.

The first two measures to be defined are the energy gain of an electron due to the transverse and longitudinal fields. The energy gain $d\gamma/dt$ of an electron due to the transverse laser fields is given by

$$\frac{d\gamma}{dt} = \frac{\boldsymbol{p}}{\gamma}\frac{d\boldsymbol{p}}{dt}.$$

Multiplying the Lorentz force equation with $\boldsymbol{p} = \gamma\boldsymbol{\beta}$,

$$\boldsymbol{p}\frac{d\boldsymbol{p}}{dt} = \boldsymbol{p}\left(\boldsymbol{a} + c\boldsymbol{\beta} \times \boldsymbol{b}\right) = -\boldsymbol{p}\boldsymbol{a}$$

and using $\boldsymbol{a} = a_x \boldsymbol{e_x}$ for the electric field of the laser wave, one obtains

$$\frac{d\gamma_{\mathrm{x}}}{dt} = -a_x\beta_x$$

for the energy gain of an electron due to the transverse laser field. For large $a_0 \gg 1$, this energy is predominantly converted into forward momentum via the $\boldsymbol{v} \times \boldsymbol{B}$ force. Similarly one can define

$$\frac{d\gamma_{\mathrm{z}}}{dt} = -a_z\beta_z$$

as the fraction of energy gained by longitudinal fields. One finally can define

$$\Gamma_z = -\int a_z\beta_z \mathrm{dt}$$
$$\Gamma_x = -\int a_x\beta_x \mathrm{dt}$$

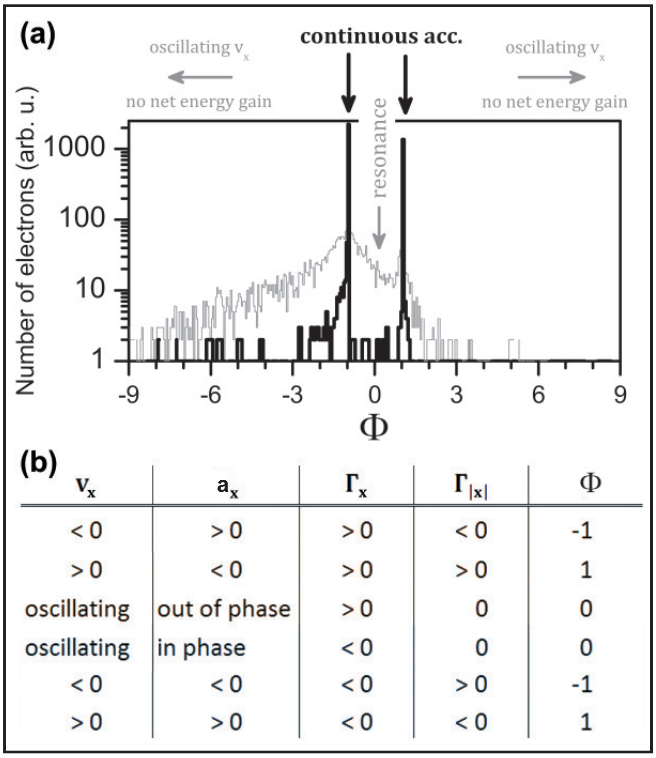

v_x	a_x	Γ_x	$\Gamma_{\vert x\vert}$	Φ
< 0	> 0	> 0	< 0	-1
> 0	< 0	> 0	> 0	1
oscillating	out of phase	> 0	0	0
oscillating	in phase	< 0	0	0
< 0	< 0	< 0	> 0	-1
> 0	> 0	< 0	< 0	1

Figure 4.36: (a) Histogram of Φ for electrons from group 'B' accelerated forward. Black line represents distribution when the lower limit of the integral is set to the time when the electron energy exceeds 4 MeV (see main text). For comparison, gray line shows distribution when the lower limit is set to the starting time of the simulation. Distribution of Φ exhibits distinct maxima at $\Phi = \pm 1$ which represent continuous acceleration, while there is no distinct peak at $\Phi = 0$ which would represent resonant energy absorption. (b) Γ_x, $\Gamma_{|x|}$ and Φ for different combinations of synchronization of electron transverse motion and laser electric field. First three rows represent forward acceleration (considered for the top figure), last three rows represent backward acceleration.

and calculate the corresponding values for each tracked electron. The first of the two integrals are a measure of the amount of energy gained by the electron due to longitudinal electric fields (trajectory ii in Fig. 4.32, in the following referred to as electron population 'A'). The second integral is a measure of the amount of energy gained due to transverse electric fields, which for ultra-relativistic intensities is converted into forward momentum via $\boldsymbol{v} \times \boldsymbol{B}$ (trajectories ia,b in Fig. 4.32, electron population 'B'). The most interesting part of the electron acceleration is the section of the energy gain beyond the energy seen in a flat foil, hence the lower limits of the integrals are chosen in the following to be the time when the respective electron has obtained a kinetic energy of more than $\gamma - 1 = 8$, an energy well exceeding the flat foil electron temperature. The upper limits of the integrals are given by the time the electron crosses the top inner surface and leaves the laser interaction region, which is at $z = 55\pi$.

The third measure to be defined is the ratio

$$\Phi \equiv \frac{\Gamma_{|x|}}{\Gamma_x}$$

where

$$\Gamma_{|x|} \equiv -\int |\beta_x| \, a_x \mathrm{dt}.$$

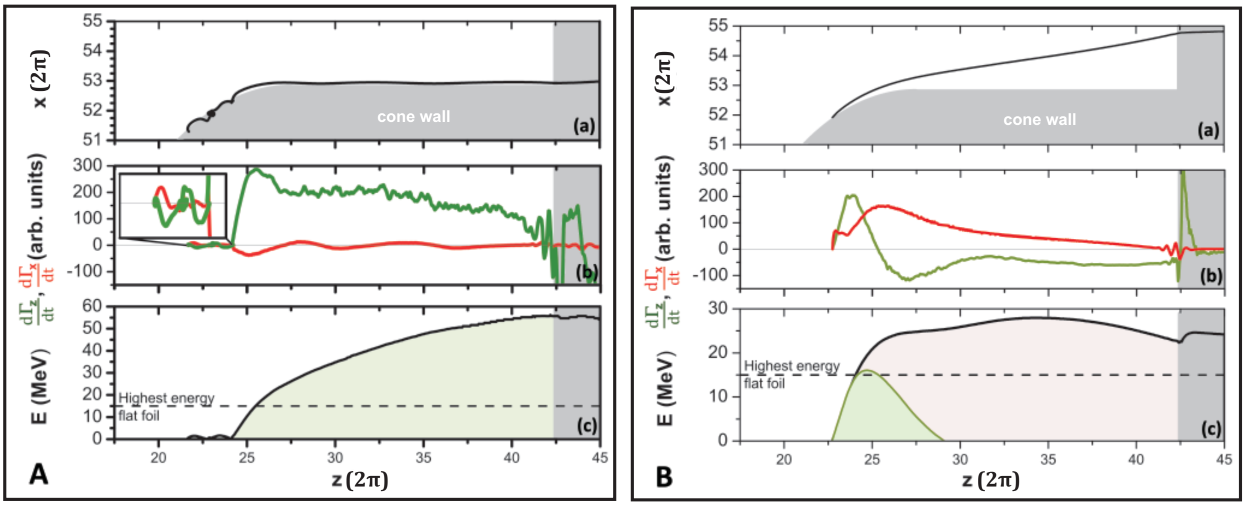

Figure 4.37: Trajectories of the most energetic electron of group ’A’ (top) and ’B’ (bottom) (a), its sources of energy gain (b) and the energy gain over its longitudinal propagation along the wall (c). The energy is continuously acquired mainly by longitudinal electrical fields (green). Laser and target parameters are described in the text, with the laser having a flat top temporal profile and $a_0 = 8.5$. The cone neck was elongated to $l = 30\pi$.

This quantity allows to distinguish between a resonant acceleration and continuous acceleration. The electric field strength of the laser $a_x(t)$ is a periodic function with $\langle a_x(t)\rangle = 0$. In the case of resonant absorption, $|\beta_x(t)|$ is also periodic and hence the integral $\Gamma_{|x|}$ and Φ vanish for integrating over many periods. In the case of an electron co-moving with the laser phase, $\beta_x(t)$ is increasing monotonically, hence the integral $\Gamma_{|x|}$ takes on a large value, and Φ becomes ± 1.

Fig. 4.36 shows the distribution of Φ for all forward accelerated electrons of group ’B’. It can be seen that there are only few electrons with $\Phi \approx 0$, but rather there are two distinct maxima around $\Phi = \pm 1$. This means that by far most electrons are accelerated *continuously* not by resonant energy transfer, but by co-moving with the laser field. This means that in the case of an intense laser with grazing incidence onto a solid curved wall the resonant absorption mechanism can be neglected and a continuous acceleration of electrons is the dominating source of electron energy beyond that seen at flat foils.

Continuous electron acceleration More insight into the continuous acceleration mechanism can be gained by studying the trajectories and forces of the most energetic electrons of each group. For the most energetic yet representative electron of group ’A’ Fig. 4.37(A) shows the trajectory (a), sources of energy gain (b) and the gain of energy over time (c).

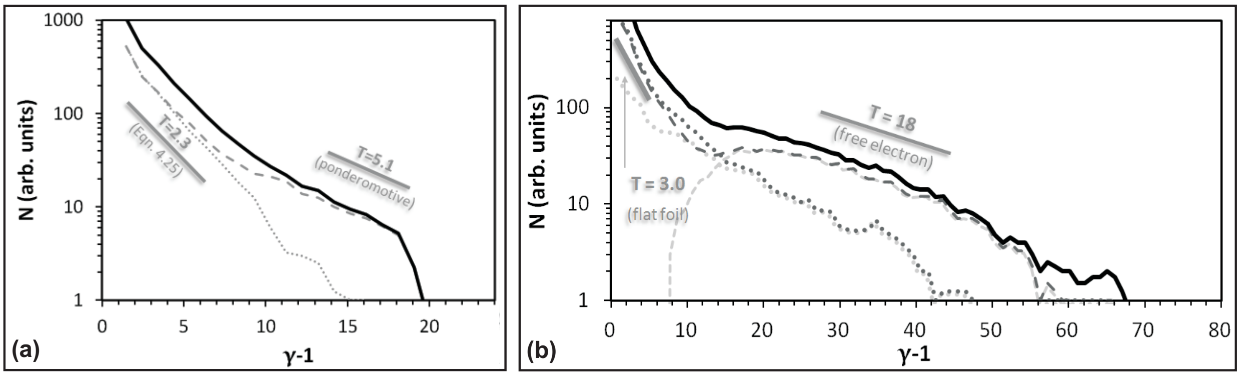

Figure 4.38: Electron spectrum after $t = 150$ of a flat foil (a) and a cone (b) at normal laser incidence (grazing incidence in (b)). The dashed (dotted) lines show the spectrum for electrons of group 'A' ('B') mainly accelerated via longitudinal (transverse) electric fields. Gray solid lines indicate the slope of an exponential distribution with the respective average energy. Laser parameters are the same as the ones used for Fig. 4.37.

It can be seen that the electron is caught in an accelerating phase of longitudinal electric fields after extraction and some oscillations where it is slower than the laser phase velocity, while the contribution of transverse fields remains very small. For the most energetic electron from group 'B' the same graphs are shown in Fig. 4.37(B). In this specific case, after being extracted at $z = 44.4\pi$, the particle at first experiences a strong acceleration due to longitudinal electric fields. Later, the electric field becomes decelerating and the $\boldsymbol{v} \times \boldsymbol{B}$ acceleration due to the transverse electron velocity becomes dominant. At the end of the acceleration process, the net energy gain due to longitudinal fields even becomes negative. The particle is *not* oscillating but it rather moves upwards monotonically and remains in phase with the laser.

Electron temperature The continuous acceleration of electrons leads to significant increase of the hot electron temperature compared to a conventional flat foil consisting of the cone top only. Figure 4.38 shows the spectra obtained from simulation with $a_0 = 8.5$ and $t_p = 100\omega_0^{-1}$ for a flat foil and a cone, respectively, when the laser is aligned tangentially to the inner cone wall. The graphs show the distribution of the energy of the individually tracked electrons at the respective time when they cross the flat top front surface and leave the interaction with the laser, up to the time when the laser maximum reaches the cone top front surface. The resulting energy distribution is a direct imprint of the laser-electron interaction. This would not be the case for spectra of the electron energy simply at a certain fixed point in time, since they would be biased by a transfer of energy to ions while they bounce back and forth across the flat top several times during the laser pulse due to the

electro-magnetic fields building up at the target surfaces.
The solid black line shows the spectrum including all electrons, while the thick dark gray lines show the spectra of electrons with $\Gamma_x > \Gamma_z$ (dotted) and $\Gamma_z > \Gamma_x$ (dashed). In the case of a flat foil, most of the electrons follow an exponential distribution with a scale length of $\gamma - 1 = 2.3$ in agreement with Eqn. 4.24. In the case of the cone, in the low energy region the spectra also follow an exponential curve. In that part, the spectrum is very similar to that of a flat foil with $a_0 = 12$ (which is higher than in the case of a flat foil due to micro focusing), from which it can be concluded that these are the electrons accelerated at the cone top front surface. For high energies $\gamma > 15$, the electrons follow a second exponential curve with a significantly larger scale length close to $\gamma - 1 = 18$. This part of the spectrum is dominated by the surface electrons accelerated via the two continuous acceleration mechanisms described before.

In order to estimate the relative relevance of the continuous acceleration by longitudinal and transverse fields, in the low temperature region the flat foil spectra must be subtracted from the individual spectra of electrons from group 'A' and 'B', respectively. This was done by subtracting an exponential distribution with scale length $\gamma - 1 = 3.0$, as obtained from Eqn. 4.24 for $a_0 = 12$, fitted to the respective distribution in the low energy energy region. The result are the spectra for surface electrons for both of the electron sub-ensembles, shown in Fig. 4.38 by gray lines. It turns out that the number of particles from group 'A' and 'B' is approximately the same while the energy contained in group 'A' is approximately twice that in 'B'.

The electron acceleration depends on the geometric parameters of the cone (e.g. wall radius of curvature, neck length) and in the above discussion a wall curvature and neck length optimized for proton acceleration ($\mathrm{R} = 20\pi$, $l = 2\pi$) was used. In that case it is found that the temperature of electrons from group 'B' saturates and coincides with the temperature of electrons from group 'A'. Then, the acceleration length l_{acc}, which can be defined as the length between the point where the curved cone wall approaches the laser axis by less than w_0 and the cone top, $l_{\mathrm{acc}} = \sqrt{\mathrm{R}^2 - (\mathrm{R} - w_0)^2} + l$, coincides with the dephasing length of a single electron in a plane wave

$$l_{\mathrm{deph}} = \frac{a_0^2}{4}\pi. \tag{4.48}$$

In Fig. 4.39 it can be seen that consequently an extension of the neck length does not change the temperature for electrons from group 'B' significantly. For electrons from group 'A' it

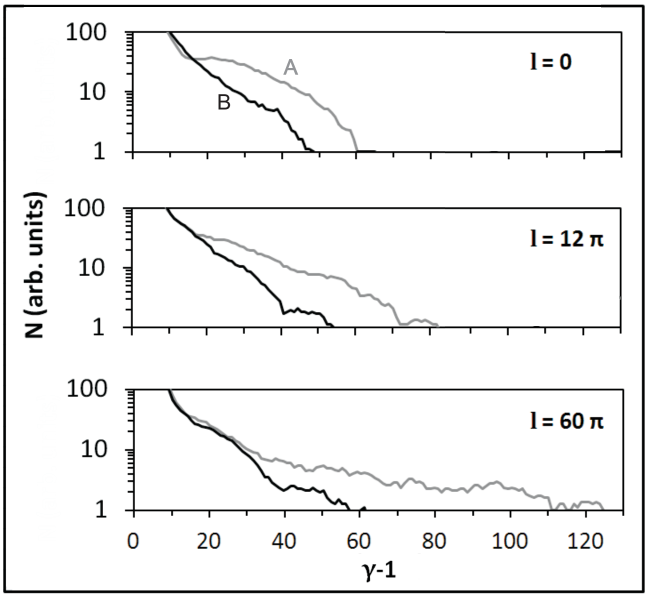

Figure 4.39: Electron spectra for cones with increasing neck length l. Black lines show spectra of group 'B', gray line show spectra for electrons from group 'A'. Laser parameters are the same as those used for Fig. 4.37.

leads to higher electron temperatures and higher maximum energy, but at the same time the number of hot electrons decreases, and hence an increased neck length is not beneficial for ion acceleration which depends on temperature *and* number of electrons (see Sec. 4.3.2.2). The temperature of electrons in the optimum case can be estimated by approximating the electron motion along the cone wall with the energy of a single initially resting electron in a plane electro-magnetic wave. This is given by Eqn. (2.21). In general, the energy of an electron is determined by the laser phase $\varphi = t - x$ in which it is born (i.e. extracted from the solid wall) and in which it leaves the laser (e.g. by going into an overcritical plasma region) and the average energy of all electrons is hence given by

$$\begin{aligned} \mathrm{T}_e^{\mathrm{hot}} &= \langle \gamma_{\mathrm{cone}} \rangle_\varphi - 1 = \frac{\int_0^{2\pi} \gamma d\varphi}{2\pi} - 1 \\ &= \frac{a_0^2}{4}. \end{aligned} \tag{4.49}$$

This estimate describes very well the average hot electron temperature seen in the simulations. In the case of the standard simulation parameters, Eqn. (4.49) predicts $\mathrm{T}_e^{\mathrm{hot}} \approx 18$ in agreement with the spectrum shown in Fig. 4.38(b). To verify this scaling over a broader range of laser intensities, additional simulations were performed with a_0 ranging from 1 to

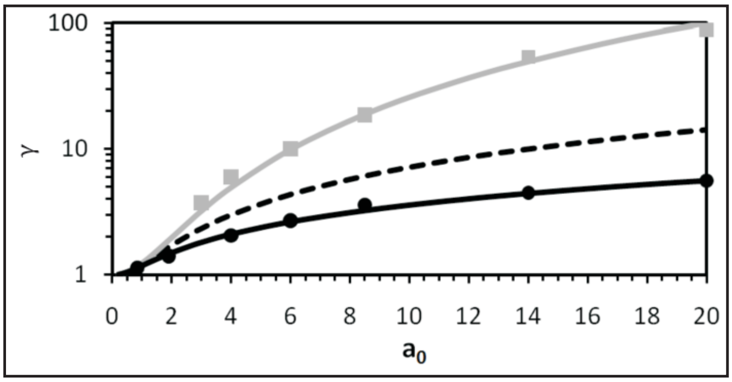

Figure 4.40: Scaling of electron temperature with laser strength. Circles and squares show the average kinetic energy $T_e + 1$ of hot electrons from a flat foil and a cone with grazing laser incidence, respectively, as obtained from simulations ran with $n_e = 10\ n_c$ ($40\ n_c$) for $a_0 < 8.5$ ($a_0 \geq 8.5$) and $w_0 = 4\pi$ (14π) for $a_0 \leq 8.5$ ($a_0 > 85$). The cone wall radius was varied to reach the maximum electron temperature to account for the intensity dependent dephasing length. Black dashed line for comparison shows the ponderomotive scaling Eqn. (2.25), gray line is the prediction acquired from Eqn. (4.49) and the black line is the prediction of Eqn. (4.24) for flat foils.

20. [12] In all cases with $a_0 < n_{e,0}$ Eqn. (4.49) is in very good agreement with the PIC results (see Fig. 4.40).

Ion acceleration The above results demonstrate the efficient generation of energetic electrons in the case of laser grazing incidence on a curved cone target along the inner wall. In this paragraph it is analyzed how the improved electron acceleration influences the acceleration of ions from the cone top based on geometric parameters (wall diameter, preplasma) and laser parameters (intensity, duration).

The ion acceleration process at the cone top is TNSA-like. Hot electrons that have been created both at the front surface and along the cone wall travel through the top and exit at the rear, building up a quasi-static electric field. The ions, which due to their larger mass remain initially at rest are then accelerated in this quasi-static field at the rear side of the cone top. The achievable maximum energies will be compared in the following to conventional flat foils of the same geometry as the cone top only, where the ion acceleration is also governed by TNSA, and to predicted maximum energies in the case of RPA, using

---

[12] It was taken into account that for greater a_0 the transverse elongation becomes larger. Since the transverse width of the laser pulse is limited, for high intensities the transverse electron elongation $\hat{x} \cong a_0$ will eventually exceed the laser waist and the electron will leave the laser focus before it reaches the energy given by Eqn. (4.49). With $w_0 = 4\pi$ this is the case for $a_0 > 4\pi$, which was taken into account by increasing the laser waist to 14π for $8.5 < a_0 \leq 20$.

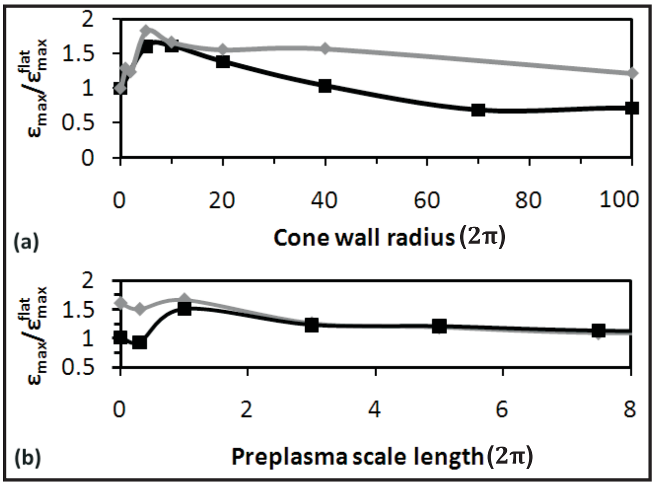

Figure 4.41: Proton maximum energy from cones with laser grazing incidence normalized to the maximum energy from flat foils, $a_0 = 8.5$, (a) as a function of cone wall radius without (black) and with preplasma (gray, scale length 1.1π) and (b) as a function of preplasma scale length for a radius of 20π (black) and 80π (gray).

the results from 2.3.2.2. RPA is highly promising for its predicted scaling of the maximum ion energy of up to $\varepsilon_{\max} \propto a_0^2$, even though the necessary experimental conditions are very difficult to realize (e.g. a flat top laser pulse with a very sharp rising edge, circular polarization, very little pre-pulses, ultra-thin foils) and an experimental validation has not yet been realized.

Fig. 4.41 shows the dependence of the maximum proton energy accelerated from a cone at grazing incidence as a function of the radius of the curvature of the walls. As was discussed before, the dephasing of electrons in the laser field prevents the electrons from gaining more energy when increasing the acceleration length l_{acc} beyond l_{deph}. For smaller wall radii the electron temperature and hence the proton energy is smaller, because the electron acceleration length is less than what is necessary to reach the maximum energy. For larger radii, electrons dephase with the laser and are decelerated again, the temperature remains constant. The density of electrons behind the top decreases due to the divergence of the electron beam, resulting in a reduced proton energy. Consequently, one expects an optimum radius of the cone walls where $l_{\text{acc}} = l_{\text{deph}}$,

$$\boxed{R_{\text{opt}}\,[\lambda] = \frac{a_0^4}{128 w_0\,[\lambda]} + \frac{w_0\,[\lambda]}{2}} \tag{4.50}$$

as long as $w_0 < \hat{x} \cong a_0$. Indeed a pronounced maximum near R_{opt} is observed, which however is shifted to smaller radii, e.g. for the laser strength $a_0 = 8.5$ and laser waist $w_0 = 4\pi$ used in the simulation the observed optimum radius is 20π which is somewhat less than that expected from Eqn. (4.50). To reach the maximum possible energy within 10%, it is found that the radius must be within ±8π around the optimum. The smaller optimum

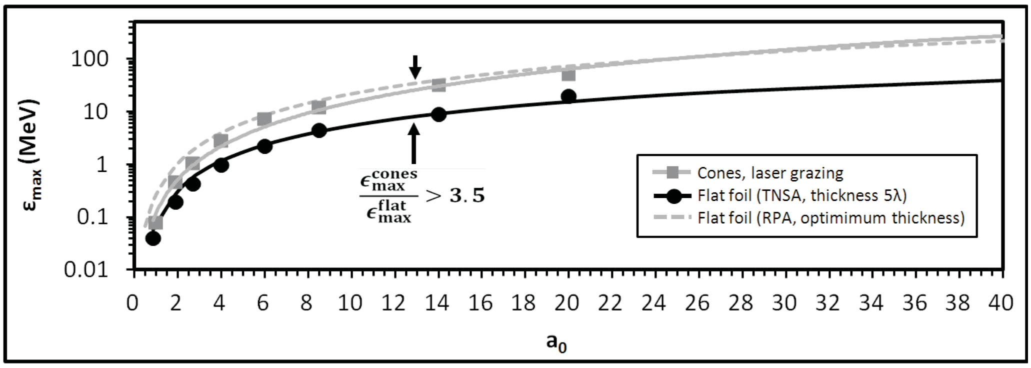

Figure 4.42: Scaling of proton maximum energy with laser strength. Squares and circles show the maximum energies from cones at grazing laser incidence and flat foils (same geometry as the cone top), respectively, as obtained from simulations. Laser parameters are the same as the ones used for Fig. 4.40. Solid lines are the predictions acquired from Eqn. (2.63) with T_e^{hot} from Fig. 4.40, $\eta_{cone} = .45$ and $\eta_{foil} = .25$, $\alpha = 40°$ from PIC simulations, $w_0 = 4\pi$ (14π) for $a_0 \leq 8.5$ $(a_0 > 85)$. The dashed line shows for comparison the maximum ion energies expected from radiation pressure acceleration (RPA) at optimum laser and foil parameters using the results of [137].

radius can be explained by pump depletion and laser reflection.

Next an exponentially decreasing preplasma density gradient is added at the surface of the inner cone walls and the inner cone top with a scale length of 1.2π. The gray line in Fig. 4.41 represents the maximum energies normalized to the maximum energy from a flat foil with the same preplasma at the front surface. The important finding is that now the condition for the radius in order to reach the maximum possible energy within 10% is fulfilled up to much greater values, i.e. to radii more than 80π. This means that at the same time the laser depletion connected with the propagation through the preplasma along the cone wall does not degrade the proton acceleration. This is especially important experimentally where the preplasma can be controlled by the laser prepulse contrast and ASE level, since it could allow to lower the restrictions on the cone geometry. Also, instabilities in laser pointing would be more tolerable when preplasma is added. The optimum value for the wall radius remains unchanged and the relative proton energy increase at the optimum wall radius is nearly the same as without any preplasma. The absolute energies are slightly increased as expected due to a more efficient laser absorption [104, 129]. Obviously there is an optimum preplasma scale length since for large scale lengths the laser depletion will be large and the laser eventually will not reach the cone top [180, 108, 181].

Fig. 4.42 presents simulation results for varying laser intensities at the respective optimum cone wall radius (and no preplasma). The black circles show PIC results for a flat foil, the gray squares give results for cone targets at grazing laser incidence. For intensities where

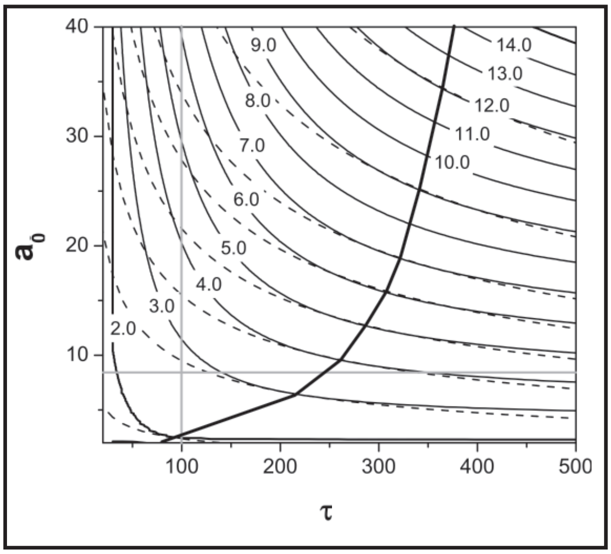

Figure 4.43: Enhancement factor of proton maximum energy from cones compared to flat foils as a function of pulse duration t_p and laser strength a_0, as obtained from Eqn. ((2.63)), assuming a temperature scaling as given by (4.24), a constant electron divergence and laser absorption as given in the main text. Dashed curves are iso-pulse-energy lines. For constant pulse energy, the enhancement peaks at a certain point, indicated by the strong black line (guide to the eye).

the plasma is opaque, $a_0 < n_e/n_c$, the cone targets show a significantly higher maximum proton energy of up to more than three times the energy seen for flat foils. Following the discussion of the previous paragraph, the proton energy enhancement can be estimated by Eqn. (4.25) with the temperature from Eqn. (4.49). In the case of cones with grazing laser incidence where γ scales proportional to a_0^2 as given by Eqn. (4.49) the hot electron density (2.66) behind the target is $n_{\mathrm{e,hot}} = \mathrm{const.}$, and its maximum value is $\mathrm{n_c}$. Based on the PIC simulation results, the laser absorption coefficient varies only little with the intensity in the range considered here, and is of the order of $\eta_{\mathrm{cone}} \approx \mathit{const.} \approx 0.45$. The average divergence is $\alpha \approx 40°$. Thus, t_{ref}^{PEM} is a constant. For a *fixed pulse duration* the maximum proton energy predicted by Eqn. (4.25) hence scales as

$$\boxed{\varepsilon_{\max} \propto a_0^2.} \tag{4.51}$$

as is indicated by the gray line in Fig. 4.42. The maximum energies observed in the PIC simulations agree very well with the analytical values, exceeding the proton energy from flat foils significantly.

For a *constant laser pulse energy* Eqn. (4.25) predicts a slight increase of the proton maximum energy with decreasing pulse duration, saturating at $\varepsilon_{\max} \approx 6$ for $t_p \ll \omega_0^{-1}$. Analytically, it can be easily found that for $t_p < 150\omega_0^{-1}$ the increase of proton energy with pulse duration is larger than proportional to the pulse duration while for larger pulse durations the proton energy increases more slowly. Combining the above, it follows that for a given laser pulse energy, in the first region it would be more beneficial to optimize for a longer pulse duration while in the latter region it would be better to optimize for a higher laser intensity.

The theoretical scaling of $\varepsilon_{max} \propto a_0^2$ is very promising. Compared to conventional flat foils, where the scaling usually is $\varepsilon_{max} \propto a_0^{1.0...1.1}$ only (Eqn. (4.30)), it is significantly better due to the better temperature scaling. Even for short laser pulses where the flat foil scaling approaches $\varepsilon_{max} \propto a_0^2$ the absolute energy of protons from flat top cone targets exceeds that of the flat foils by far, due to the increased laser absorption efficiency.

Interestingly, the factor of proton energy gain at constant pulse energy and laser strength $3 \leq a_0 \leq 30$ peaks at an optimum pulse duration of $100 < \omega_0 t_p <\approx 350$ which increases only little with increasing intensity (Fig. 4.43). Hence, at a given laser pulse energy there exists an optimum pulse duration and intensity for which the cone geometry gives the highest increase in proton energy compared to flat foils, and the cone geometry consequently should be especially beneficial for short pulse laser systems.

For the sake of completeness, the cones should also be compared to flat foils in the RPA regime. The expected scaling there is in between $\varepsilon_{max} \propto a_0^2$ for short pulse durations or small a_0 and $\varepsilon_{max} \propto a_0$ for long pulse durations or high a_0 (Eqn. (2.76)). In Fig. 4.42 the RPA predictions are plotted for the specific laser parameters used in the cone simulations. It can be seen that then for small a_0 RPA yields moderately higher proton energies while the scaling for high a_0 drops below that predicted for cones so that for $a_0 > 25$ the protons from cone targets become more energetic. It is important to point out that in the general case the laser field strength at which the scaling in the case of RPA changes from a quadratic to linear dependence from a_0 is proportional to the inverse of the laser pulse duration, so for longer pulse durations, cone targets should perform better than RPA for even lower a_0. Considering the experimental difficulties for the RPA regime as described in Sec. 2.3.2.2, the presented cone target geometry appears as a very promising alternative.

4.3.2.3 Conclusions

Hollow cone targets where the laser interacts with the inner walls have long been shown to produce high energy electrons. The high energy electrons are led towards the tip where a flat top can act to convert the electron energy into energetic protons. This is the proposed mechanism that has led to higher proton energies than in the case of flat foils [107] and even a new energy record for laser accelerated protons [21]. As shown in this section, the underlying process for the generation of energetic electron currents along the curved wall surface is primarily the continuous and direct acceleration of electrons by the laser.

When the laser spot size is smaller than the cone neck diameter, strong electron currents are created only when the laser is aligned grazing to the wall. Then, the laser electric field extracts electrons from the wall once every cycle. The Lorentz force and longitudinal electric fields accelerate the extracted electrons, forming energetic bunches directed along the wall towards the cone tip by self-generated fields, where they add to the electron sheath responsible to accelerate protons. The main mechanism of electron acceleration along the wall is this continuous acceleration of electrons. Other mechanisms such as micro focusing or resonant acceleration of surface electrons are found to be of minor importance and can be neglected.

The electron temperature scaling with intensity for the continuously accelerated electrons along the wall can be described by a simple model based on the vacuum energy gain of free electrons in a plane electro-magnetic wave. Using this temperature scaling, accurate analytic prediction for the proton maximum energy were possible with the help of Eqn. (4.25). From the electron dephasing length an optimum value for the cone wall curvature radius with respect to proton maximum energy can be derived. The increased electron density and temperature lead to a significant increase of the proton maximum energy especially for high laser intensities as compared conventional flat foils. Even for ultra-thin foils in the RPA regime, the predicted proton energy from cones is comparable or even larger, in particular for long laser pulse durations.

For a given laser pulse energy there exists an optimum pulse duration for which the cone geometry is expected to give the greatest proton energy increase compared to flat foils. For example, for a short pulse laser with 30 J pulse energy and wavelength $\lambda = 800\,\mathrm{nm}$, the expected optimum pulse duration would be 130 fs with a focal spot size of 3 µm resulting in an intensity of $7.9 \cdot 10^{20}\,\mathrm{W/cm^2}$. At this focal spot size the transverse electron excursion $\hat{x}$ equals the laser focal waist w_0. A smaller spot size would lead to higher laser intensity and hence larger $\hat{x}$ so that the electron would leave the laser beam waist transversely and stop being accelerated. Eqn. (4.50) predicts an optimum cone radius for such parameters of $R \cong 220\,\mu\mathrm{m}$. The maximum energy in such a case is expected to be more than 6 times higher than that of a regular thin foil, reaching up to 200 $\mathrm{M}e\mathrm{V}$ (assuming $\eta \cong 0.2$) or > 300 $\mathrm{M}e\mathrm{V}$ (assuming $\eta \cong 0.45$). Though speculative, such high energies would be sufficient for particle therapy, compensating the negative effect of the reduced electron temperature scaling described in Sec. 4.1.2.4 and 4.1.2.5 on the proton maximum energy when scaling TNSA to higher laser intensities.

Chapter 5

Conclusions and Future Perspectives

The results of this thesis demonstrate promising paths towards higher energies of laser accelerated ions and a higher degree of ion beam control which eventually might open up a broad range of applications such as fast ignition fusion [16], nuclear reactions and isotope production [17, 18], and tumor therapy [14, 13, 10].

A relativistic model for the temperature scaling of electrons accelerated at the front surface by a high-intensity laser pulse was derived in an analytical model taking into account the electron phase distribution. A Lorentz invariant expression for the electron distribution was obtained and applied to the two limiting cases of a step-like density gradient and a long preplasma at a solid. The model predictions are consistent with ad-hoc expectations in the low-intensity limit, numerical predictions for the ultra-relativistic intensity limit and experimental results. Since the latter show a large scatter and extend only to moderately high intensities, the model will play out its strengths especially at future laser systems with yet higher laser intensities, as deviations from previous models are predicted to be significant especially in the ultra-relativistic regime.

The expected advances in laser technology in the near future will create the necessity to apply the most accurate electron temperature scaling to PEM models in order to be able to predict, understand and enhance the ion acceleration especially with respect to its maximum energy. The novel electron scaling model was applied in this thesis to the plasma expansion model to derive the ion energies in the two limits of short and long laser pulses. It was demonstrated that especially in the ultra-relativistic case the ion maximum energies are expected to fall short of predictions based on previous electron scaling models, which has to be taken into consideration in the planning of future experiments. The same favorable asymptotic short pulse behavior of a proportionality between the laser intensity and maximum ion energy was shown for the isothermal PEM as was derived previously in the Schreiber model, which further motivates the research and development of short pulse laser systems.

Based on the PEM considerations, novel target types have been analyzed that make use of optimized electron dynamics during the laser irradiation. The ion acceleration mechanism itself still is the TNSA, taking advantage of over a decade of experience in that regime. This includes the knowledge and experimental validation of the exceptionally reliable and stable acceleration process [24] and assures the exceptional beam quality discussed above, making this acceleration regime promising for future applications. With the proposed novel target designs – stacked foils, mass limited foils and flat top cone targets – the hot electron density and energy were shown to be able to be engineered in such a way that the final ion maximum energy can be significantly increased compared to conventional flat foils.

Experiments employing novel flat top cones were conducted at the Trident laser system at LANL, yielding the present record in proton maximum energy produced by laser acceleration which exceeds the previous record set in 2000 at LLNL by more than 10%. Within the frame of this thesis it was shown that the observations of the present experiment cannot be explained by the theoretical models available. A new model was developed based on simulations suggesting a novel, previously unconsidered electron acceleration mechanism termed DLLPA, leading to higher hot electron temperatures and thus higher ion energies. Based on this new understanding, optimum target parameters were predicted and the feasibility of short pulse lasers was shown which hopefully will lead to yet higher proton energies in future campaigns.

It remains an open question how the optimum target geometry can be found for a specific application at a specific laser system. The optimum target design must account for energy deposited prior to the laser main pulse, allow for the optimum absorption of laser energy during the pulse, and tailor the subsequent ion acceleration to reach the maximum ion energy possible. At the same time the target should possibly optimize other beam parameters such as divergence, emittance, bunch charge and spatial distribution in order to minimize the need for a later beam correction.

For this complex task the current theoretical descriptions are not satisfying, as the following examples demonstrate:

- The self-consistent modeling of preplasmas and the temporal evolution of the ionization process, bulk electron temperatures and ion energies is a very important, yet largely unsolved issue – especially in the case of complex target geometries and the presence of laser prepulses and ASE .

- The question of optimizing the absorption of laser energy is still open. Much research is going on to influence the laser absorption by target design, e.g. by increasing the laser absorption by nano-structuring the front side, employing MLT, ultra-thin foils or optimize the preplasma generation. This thesis found a reference time for the pplasma expansion that can aid in the question of whether to optimize for higher electron temperature or for electron density. Yet, for example the question of which part of the electron spectrum in a non-thermal electron distribution gives the most contribution for a maximum final ion energy, or how the electron spectral shape alters the ion acceleration, need to be solved in a self-consistent model.

- Finally, the modeling of the energy transfer process of energy from the electrons to ions at the target rear surface remains a field of debate. Current PEM models have to adopt assumptions that do hold a deeper physical justification in order to produce predictions that match experiments. They rely on the assumption of thermalized electron distributions, estimations of the ion acceleration time and temporal evolutions that are not backed by simulations.

A possible solution to the sketched problems would be a fully consistent kinetic bottom-up theory that could become an alternative to current PEM models. The bottom-up approach means that the model is based on the basic binary relativistic electron-electron and electron-ion interactions and then expands by taking into account the specific target and laser parameters. This is in contrast to PEM models that assume a certain macroscopic plasma and describe its evolution based on macroscopic parameters, such as temperature and Debye length.

Simulations may assist in this task, since the direct experimental observation of the ultra-short scale physics is extremely difficult to realize. However, simulations can not replace the development of a self-consistent model, since they are extremely demanding in terms of computation needs – especially in realistic 3D, full density situations including the complete set of physical processes.

Appendix A

PICLS input and output

A.1 Input script

Main aspects of the simulation properties can be determined by an external input file that is handed over to PICLS upon startup. They include the definition of the simulation box size, plasma geometry and particle species, certain laser parameters and the use of the ionization and collision modules can be opted. The file format is the standard Fortran input file format. The first block of parameters is the option block with the following most important parameters

- `n_time`: the number of time steps for the simulation
- `nd_para`: the number of parallel tasks working on the simulation
- `rstrt`: switch to turn on the restart option, saving all necessary data to disk to be able to restart the simulation later
- `cpuhour`: set the time in hours after which the simulation terminates and the restart data is written to disk (when `rstrt=.t.`)

The `geometry` block defines the most important parameters of the simulation box size and plasma distribution:

- `c`: the velocity of light in dimensionless units
- `Nx, Ny`: the number of cells in x and y direction (The coordinate system used in PICLS and the one used throughout this thesis are rotated so that x(PICLS)=z(thesis) and y(PICLS)=x(thesis).)
- `system_lx, system_ly`: size of the system in units of the dimensionless plasma wavelength. The number N_λ of cells per laser wavelength can be defined by this parameter and is $2c\pi N_x/(ow \cdot system\_lx)$ where ow is the plasma frequency in dimensionless units.

- `NV`: number of cells without particles, counting from left boundary
- `NM`: number of cells with particles, counting from `NV`
- `igeom`: index of geometry definition used to distribute particles in density_profile.f
- `nops`: definition of particle shape function, 1: point-like, 2: quadratic like Eqn. (3.4) on page 49, 3: triangular like Eqn. (3.5)
- `period_bnd_y`: periodic boundaries in y-direction (otherwise absorbing)
- `refl_bnd_x`: reflecting boundaries in x-direction (otherwise absorbing)
- `wgmmax`: maximum weight of particles (weights are set in `density_profile.f`)
- `Ngeom`: number of supplementary geometric parameters required by the density profile chosen by igeom
- `pgeom(1), pgeom(2), ...`: first, second, ... supplementary parameter

The `diag` block defines parameters used for the output

- `Nx_d, Ny_d`: defines how many cells are skipped for the field and density outputs, e.g. `Nx_d = 3` writes only field data of every third cell to output file
- `N_dp`: defines how many particles are skipped for the single particle outputs, e.g. `N_dp = 3` writes only data of every third particle to output file
- `ndav`: time averaged field output is averaged over this number of timesteps
- `rst_f`: folder name where to save data necessary for restart (ignored if `rstrt=.f.`)
- `Nsnap`: number of output intervals
- `psnap(1), psnap(2), ...`: timesteps when outputs are written to disk first output is written after `psnap(1)` timesteps, next outputs are written in intervals of `psnap(1)` timesteps until reaching timestep `psnap(2)`, then next outputs are written in intervals of `psnap(2)` timesteps until reaching `psnap(3)` and so on

The `ions` block defines the ion species used in the simulations. Their distribution inside the simulation volume is defined in `density_profile.f`.

- `No-ions`: number of different ion species (two ion species can be the same physical ion type)
- `p_mass(1), p_mass(2), ...`: mass of ions of species 1, 2, ... in units of electron rest mass
- `q_i(1), q_i(2), ...`: maximum charge of ions of species 1, 2, ... When ionization is off (`ionize_opt=.t.`), this is the charge of ions.
- `Ti0(1), Ti0(2), ...`: initial temperature $T[keV]/511 \cdot c^2$ (where c is in code units) of ions of species 1, 2, ... (e.g. for 1 keV set $Ti0 = 0.196$)
- `Np_i(1), Np_i(2), ...`: number of ions per cell
- `track_i(1), track_i(2), ...`: Used to track ions. If set to > 0, it defines that there will be `track_i` untracked ions for every tracked ion (e.g. `track_i=0` to don't track ions of this species, `track_i=1` to track every ion, `track_i=2` to track every other ion, `track_i=3` to track every third ion)

The same parameters (exchanging `i` by `e`) can be set for the electrons in block `eons`, but only one electron species should be used. When the ionization option below is turned on, the parameter `Np_e` is ignored and the electrons are set according to the ions. The block `wave` defines the laser parameters:

- `spol_opt`: If set to false, only a limited set of directional splitting equations is used as this is sufficient for p-polarized light and only the E_x, E_y and B_z fields are written to disks when outputs are writtem, when true also E_z, B_x and B_y are written.
- `ow`: Laser frequency in units of the plasma frequency. When `ionize_opt=.f.`, the plasma frequency used here is the plasma frequency of a plasma where there are `Np_e` electrons per cell, otherwise $\sum_{j=1}^{No\_ion} Np\_i(j) \cdot q_i(j)$ electrons per cell.
- `Ey0`: maximum laser field strength in the simulation plane in dimensionless units
- `Ey0`: maximum laser field strength in z-direction in dimensionless units
- `w0`: laser waist
- `xf`: position of the laser focus in x-direction

- `yhlf`: position of the laser axis on the left boundary of the simulation box in y-direction, relative to simulation box height
- `angle`: angle of incidence measured between x-axis and laser in mathematic positive direction
- `ngaus`: transverse profile of the laser, 1: gaussian, 2: super-gaussian
- `nshp2`: temporal profile of the laser electric field, 1: gaussian, 2: linear rising and falling, 3: step-like rising to maximum and remaining constant, 9: sin profile
- `tau1`: width of the electric field profile rising or falling wing ($(2\ln 2)^{-0.5}t(FWHM)[periods]$, factor $\sqrt{2}$ larger when using FWHM of intensity profile)
- `tau2`: sum of the width of the electric field profile rising wing and the duration of a flat top (in units of laser periods)
- `tau3`: time before the laser pulse maximum enters the simulation box on the left simulation box boundary (in units of pulse periods)

In the block `coll` the collision module can be activated by `col_opt=.t.` The parameter `p1_opt` allows collisions between particles of the same species and `p2_opt` allows also collisions between particles of different species. `ncol` specifies every how many timesteps collisions shall be calculated. In the `ionize` block the ionization can be activated by `ionize_opt=.t.`, the ions are preionized to the charge state `zin0` and the lower local field threshold to consider ionization is `aip0` in dimensionless field units. Of course the complete behavior can be individually adjusted in the source code, e.g. to implement different values for `N_dp` for each particle species.

In the following the input file format is explained, an example of an input file for a simulation of ion acceleration from a flat foil as it was used for example in Sec. 4.1 is shown in listing A.1. Some parameters are only available in the version used at HZDR.

Listing A.1: input file

```
&option
 n_time=6800, n_time_max=700001, nd_para=192, iws=1, rstrt=.t.,
        cpuhour=500.0
&end
```

```
&geom
  c=10.d0,Nx=3141,Ny=3141,system_lx=25128.d0,system_ly=25128.d0,
  NM=1000,NV=1374,igeom=440,nops=3, period_bnd_y=.f.,
  ref_bnd_x=.f., wgmmax=1.,Ngeom=11,pgeom(1)=78.54,pgeom(2)=90,
  pgeom(3)=0,pgeom(4)=2.5,pgeom(5)=1,pgeom(6)=0,pgeom(7)=0,
  pgeom(8)=999999,pgeom(9)=0,pgeom(10)=0,pgeom(11)=0
&end
&diag
  Nx_d=5,Ny_d=5, N_dp=1,nd=500,ndth=5,ndav=78,nstp=1,nhalf=128,
  rst_f='rstrt ',Nsnap=3,psnap(1)=5390,
  psnap(2)=6173,psnap(3)=6762
&end
&ions
  No_ion=2,
  p_mass_i(1)=1836.0d0, q_i(1)=1.d0, M_i(1)=1, niy_func(1)=0,
  niy0(1)=0.5d0,Ti_func(1)=0,Ti0(1)=.20d0,Np_i(1)=4,track_i(1)=0,
  p_mass_i(2)=116.670d3, q_i(2)=29.d0, M_i(2)=1, niy_func(2)=0,
  niy0(2)=0.5d0,Ti_func(2)=0,Ti0(2)=.20d0,Np_i(2)=4,track_i(2)=0
&end
&eons
  p_mass_e=1.0d0, q_e=-1.d0,
  M_e=3, No_eon=1, ney_func=0,
  ney0=0.5d0,Te_func=0, Te0=.20d0, Np_e=29, track_e(1)=0
&end
&wave
  spol_opt=.f.,
  ow = 0.1d0, Ey0=100.0d0,Ez0=0.0d0, w0= 2.d0, xf=17.5d0,
  tau1=12.8, nshp1=1, tau2=12.8,tau3=38.3,nshp2=1,ngaus=1,
  angle=0.0d0, yhlf=0.5d0
&end
&coll
  col_opt=.f., ncol=1, p1_opt=.t., p2_opt=.t.
&end
&ionize
```

```
  ionize_opt=.t.,aip0=19.63,  zin0=4.0
 &end
 &brmm
  brm_opt=.f.,  nbrm=4,  nomeg=80,  ogmin=1.0  ,  ogmax=1.d4,
  nqh=20,  nph=40
 &end
 &ntron
  non_opt=.f.,  nnon=20,  enmax=8.0
 &end
# tracking
 &track
  Ntrack=1,  ptrack(1)=0
 &end
```

In the above example, the plasma frequency was defined by $\omega_p = 1/ow = 10$, so that the density is set to $\omega_p^2 = 100$. This is the density when all ion species defined in `ions` are actually present in one cell and have a weight of 1. Ion of species 1 are protons, ions of species 2 are defined as having a charge of 29 when fully ionized corresponding to copper. As will be defined later in `density_profile.f`, initially there will be either ions of species 1 or 2. The target bulk consists of copper ions and the electron density when fully ionized is $n_{e,0} = 100 \cdot \frac{Np_i(2)}{Np_i(1)+Np_i(2)} = 96.67$. The cell size is

$$\Delta x = \Delta y = \lambda \frac{\text{ow} \cdot \text{system\_lx}}{2\pi c_{code}\text{Nx}} \cong 0.0125\lambda \tag{A.1}$$

and the time step is

$$\Delta t = \frac{\lambda}{c} \frac{\text{ow} \cdot \text{system\_lx}}{2\pi c_{code}\text{Nx}} = 0.0125\lambda \tag{A.2}$$

The value of system_lx/Nx $= 1.6c_{code}$ was chosen such that Δx (Δt) ended up having exactly this value exactly matching 1/8th of a plasma wavelength (plasma oscillation period), independently of ow. Even though twice that size would be suffentialy small to describe a plasma wave at 100 n_c and for PICLS to run stable and accurate due to the very beneficial directional splitting Maxwell solver, it is a good idea to add some safety margin, e.g. to account for plasma compression and to reduce the numerical errors, i.e. numerical dispersion especially inside the plasma.

A.2 Density profile

Following these initial declarations, particles of all defined species are initialized with the temperature and number of particles per cell as defined in the input file. Then their initial charge, position and weight is defined in `density_profile.f`, in the following again exemplified for the case of a flat foil covered by a proton layer. The profile definition is the same as the one used for the flat top cone targets which is why it is more complex than necessary. For a flat top cone target with density $n_{e,0} = 10$ (ow=0.32713), the `geom` section in the input file reads as follows:

Listing A.2: geom section in input file for FTC target

```
# pgeom(1)  : amicron
# pgeom(2)  : diameter of pizzatop (PT)
# pgeom(3)  : thickness of walls
# pgeom(4)  : thickness of PT
# pgeom(5)  : thickness of proton-layer
# pgeom(6)  : thickness of preplasma layer
# pgeom(7)  : curvature of walls
# pgeom(8)  : smallest distance between walls
# pgeom(9)  : distance of PT from center of curvature of walls
# pgeom(10): diameter substrate (where curved walls are attached)
# pgeom(11): length of the neck extension
# pgeom(12): preplasma scale length in units of pgeom(6)
 &geom
  c=10.d0,Nx=6000,Ny=3000,system_lx=48000.d0,system_ly=24000.d0,
 NM=2850,NV=250,igeom=440,nops=3,period_bnd_y=.f.,ref_bnd_x=.f.,
        wgmmax=1,Ngeom=11,pgeom(1)=24.0,pgeom(2)=90,pgeom(3)=5,
  pgeom(4)=5,pgeom(5)=2,pgeom(6)=0,pgeom(7)=10,pgeom(8)=15,
  pgeom(9)=0,pgeom(10)=0,pgeom(11)=0, pgeom(12)=0
 &end
```

In the function `density_profile()` there are usually two interlaced loops, looping over all particles of all ion species (and if the ionization option is turned off also over the electrons). When the position is inside the desired plasma volume, their weight is set to a value greater than 0 and the ion charge is set to the preionization level. After setting all ions, the corresponding electrons are positioned and the particles for which a tracking output is wanted are specified by the `set_track()` function.

Listing A.3: density_profile.f for flat foils and FTC covered with proton contamination layer

```
      subroutine density_profile(x,y,wgm,P,qc,part_ind)
      include '../include/define.f'
      include '../include/input.f'
      include '../include/tracking.f'
      include '../include/prtcl.f'
      include '../include/prmter.f'
      include '../include/multi.f'
      include '../include/digav.f'
      include '../include/ionize.f'

      DOUBLE PRECISION mark
      dimension x(N_p_t_max),y(N_p_t_max),wgm(N_p_t_max)
     \        ,P(N_p_t_max,3),qc(N_p_t_max)
      integer(kind=8), dimension(N_p_t_max) :: part_ind
      integer(kind=8) :: part_c

c..   charge setting (default)
      do is=1, N_sp
         do j=l_st(is),l_ed(is)
            qc(j)=q(is)
         enddo
      enddo

      vln=NV*dlt_xg ! vacuum length
      vpl=NM*dlt_xg ! plasma length
      vpw=NY*dlt_xg ! plasma width

[...]

      if(igeom.eq.440) then
        amicron   =pgeom(1) *dlt_xg !number cells per wavelength
        dia_pt    =pgeom(2) *amicron!diameter of pizzatop
```

```
        thick     =pgeom(3) *amicron!thickness of walls
        thick_pt  =pgeom(4) *amicron!Thickness of Pizza-Top
        thick_H   =pgeom(5) *amicron!Thickness of Proton-Layer
        preplasm  =pgeom(6) *amicron!width of the preplasma
        r_walls   =pgeom(7) *amicron!curvature of walls
              dist_walls=pgeom(8)*amicron!smallest lateral distanc
                                         !between walls
        c_off     =pgeom(9)              !distance of PT from center
                                         !of curvature of walls
        dia_s     =pgeom(10)*amicron!diameter of substrate (where
                                         !the curved walls grow out)
        length    =pgeom(11)*amicron!length of the neck extension
        ppl       =1./pgeom(12)          !preplasma scale length

        vpw1= (vpw-dia_pt)*1./2
        vpw2= (vpw+dia_pt)*1./2

        r1= r_walls - thick/2
        r2= r_walls + thick/2
        r3= r2+preplasm
        xc1=vln+r2+thick
        yc1 = vpw/2-r2-dist_walls/2
        xc2=vln+r2+thick
        yc2 = vpw/2+r2+dist_walls/2
        x_pt = xc1 + c_off + length

        do is = 1, N_sp
          do j = l_st(is), l_ed(is)
            wgm(j)=0.
            rr1=(x(j)-xc1)**2+(y(j)-yc1)**2
            rr2=(x(j)-xc2)**2+(y(j)-yc2)**2

            if(x(j).ge.vln .and. x(j).le.x_pt-length.and.
     /        abs(y(j)-vpw/2).le.dist_walls/2+r2) then
```

```
c..           —— Everything before Pizzatop ——
              if(rr1 .ge.r1**2 .and. rr1.le.r2**2) then
c..           —— lower Cu half-circle ——
                if (is.eq.1) wgm(j)=0
                if (is.eq.2) wgm(j)=wgmmax
              else
                if(rr2 .ge.r1**2 .and. rr2.le.r2**2) then
c..             —— upper Cu circle ——
                  if (is.eq.1) wgm(j)=0
                        if (is.eq.2) wgm(j)=wgmmax
                else
c..               === not in one of two circles: ===
c..               ===          PREPLASMA         ===
                  if(rr1 .ge.r2**2 .and. rr1.le.r3**2) then
c..                 —— inside of cone between r2-r3, at lower
c..                                                        cone wall ——
                    if (is.eq.1) wgm(j)=0
                    if (is.eq.2) wgm(j)=wgmmax*exp(-(sqrt(rr1)-r2)
     /                 *ppl/preplasm)
                    if(wgm(j).gt.wgmmax) wgm(j)=wgmmax
                  else
                    if(rr2 .ge.r2**2 .and. rr2.le.r3**2) then
c..                   —— inside of cone between r2-r3, at upper
c..
cone wall ——
                      if (is.eq.1) wgm(j)=0
                      if (is.eq.2) wgm(j)=wgmmax*exp(-(sqrt(rr2)-
     /                   r2)*ppl/preplasm)
                      if(wgm(j).gt.wgmmax) wgm(j)=wgmmax
                   endif
                endif
                if(x(j).gt.x_pt-preplasm.and.x(j).le.x_pt
     /            .and.y(j).ge.vpw1.and.y(j).le.vpw2) then
c..               —— inside of cone, less then preplasma away
```

```
c..                                                         from top ---
                  if (is.eq.1) wgm(j)=0
                  if (is.eq.2) wgm(j)=wgm(j)+wgmmax*exp(-(x_pt-
     /               x(j))*ppl/preplasm)
                endif
              endif
            endif

c..         --- Pizzatop protons ---
            if(x(j).gt.x_pt+thick_pt.and.x(j).le.x_pt+thick_pt+
     /        thick_H.and.y(j).ge.vpw1.and.y(j).le.vpw2) then
              if (is.eq.1) wgm(j)=wgmmax
            endif

c..         --- Pizzatop Copper ---
            if(x(j).gt.x_pt.and.x(j).le.x_pt+thick_pt.and.
     /        y(j).ge.vpw1.and.y(j).le.vpw2) then
              if (is.eq.2) wgm(j)=wgmmax
            endif

c..         --- Neck extension ---
            if(x(j).gt.x_pt-length.and.x(j).le.x_pt.and.
     /        abs(y(j)-vpw/2).ge.dist_walls/2 .and.
     /        abs(y(j)-vpw/2).le.dist_walls/2+thick) then
              if (is.eq.2) wgm(j) = wgmmax
            endif

c..         --- Preplasma along neck extension ---
            if(x(j).gt.x_pt-length.and.x(j).le.x_pt.and.
     /        abs(y(j)-vpw/2).ge.dist_walls/2-preplasm .and.
     /        abs(y(j)-vpw/2).le.dist_walls/2) then
              dpw=abs(abs(y(j)-vpw/2)-dist_walls/2)
              if(wgmmax*exp(-dpw*ppl/preplasm).gt.wgm(j))
     /          if (is.eq.2) wgm(j) = wgmmax*exp(-dpw*ppl/preplasm)
```

```
            endif

c..         --- substrate ---
            if(x(j).gt.vln+thick.and.x(j).le.vln+2*thick) then
              if(abs(y(j)-vpw/2).le.dia_s/2.and.
     /          abs(y(j)-vpw/2).gt.yc2-vpw/2) then
                if (is.eq.2) wgm(j)=wgmmax
              endif
            endif

            if(x(j).le.vln+thick) wgm(j)=0.
          enddo
        enddo
      endif

[...]

c..   set initial ionization
      if(ionize_opt) then
c..   ion
         do is=1, N_sp-1
            do j=l_st(is),l_ed(is)
               if(zin0.le.q(is)) then
                  qc(j)=zin0
               else
                  qc(j)=q(is)
               endif
            enddo
         enddo
c..   eon
         is=N_sp
         do j=l_st(is),l_ed(is)
            qc(j)=0.d0
            wgm(j)=0.d0
```

```
         enddo
         je=l_st(N_sp)
         do is=1, N_sp-1
            do j=l_st(is),l_ed(is)
               iqion=int(qc(j))
               do k=1,iqion
                  qc(je) = q(N_sp)
c..   electron's initial position is the same with ion-->
c..   supposing electrons are randomized by collision
                  x(je)  = x(j)
                  y(je)  = y(j)
                  wgm(je)= wgm(j)
                  je=je+1
               enddo
            enddo
         enddo
         ndown=l_ed(N_sp)-(je-1)
         l_ed(N_sp)=je-1
         N_p_t = N_p_t - ndown
         N_p(N_sp) = N_p(N_sp) - ndown
      endif

      call set_track(x,y,wgm,part_ind,amicron)
      return
      end
```

After this function, the particles with a weight of 0 are removed from the simulation and the simulation is started.

A.3 Particle tracking

For certain tasks it may be necessary to follow a number of particles during the simulations. For this purpose, the possibility was implemented by the A. Helm and the author to attach a unique id-tag to some particles. Particles of which species should be tracked can be stated in the input file, as well as additional parameters – i.e. defining the volume in which particles should be tagged – can be given. The tagging of particles initially in the simulation then is realized after defining the density profile in the function `set_track()`. Electrons created during the simulation by ionization are tagged when necessary directly after their creation in `ionization.f`.

Listing A.4: tracking.f

```
      logical function track_in_volume(x,y)
        include '../include/define.f'
        include '../include/input.f'
        include '../include/tracking.f'
        include '../include/prtcl.f'
        include '../include/prmter.f'

        geom  = ptrack(1)
        lower = ptrack(2) * amicron
        upper = ptrack(3) * amicron
        track_in_volume = .false.
        if (geom.eq.1) then
c..       all particles between (lower < y < upper) are tracked
          if ((y.gt.lower).and.(y.lt.upper)) then
     &        track_in_volume = .true.
          endif
        end function track_in_volume


      logical function track_every_other(trk_tmp)
        call random_number(rdm)
        rdm_track = nint(2*trk_tmp*rdm)
        track_every_other = .false.
        if(rdm_track.eq.trk_tmp) track_every_other = .true.
        if(rdm_track-1.eq.trk_tmp) track_every_other = .true.
      end function track_every_other
```

```
    subroutine set_track(x,y,wgm,part_ind,amicron)
      include '../include/define.f'
      include '../include/input.f'
      include '../include/tracking.f'
      include '../include/prtcl.f'
      include '../include/prmter.f'
      include '../include/multi.f'
      include '../include/digav.f'
      include '../include/ionize.f'
      dimension x(N_p_t_max),y(N_p_t_max),wgm(N_p_t_max)
      integer(kind=8), dimension(N_p_t_max) :: part_ind
      integer(kind=8) mm_ind_num, step
      integer(kind=8) :: tracked

      mm_ind_num = huge(mm_ind_num) ! = 2**63-1
      step = mm_ind_num/(10**(ceiling(log10(real(nodes)))))
      ind_num_max = (iam+1)*step
      if ((iam+1).eq.nodes) ind_num_max = mm_ind_num
      do is = 1, N_sp
        tracked = 0
        ind_num = (iam)*step + 1
        counts = 0
        if(is.ne.N_sp) trk_tmp = track_i(is)
        if(is.eq.N_sp) trk_tmp = track_e(1)
        do j = l_st(is), l_ed(is)
          part_ind(j) = 0
          if ((track_in_volume(x(j),y(j)).eq..true.).and.
      \                 (track_every_other().eq..true.).and.
  \           (wgm(j).ne.0).and.(trk_tmp.gt.0)) then
            part_ind(j) = ind_num
            ind_num = ind_num + 1
            tracked = tracked + 1
          end if
        end do
```

```
   end do
 return
 end



 subroutine write_track(is,x,y,p,wgm,qc,ii,part_ind,
\                        oldfield)
   include '../include/define.f'
   include '../include/input.f'
   include '../include/tracking.f'
   include '../include/prtcl.f'
   include '../include/prmter.f'
   include '../include/multi.f'
   include '../include/digav.f'
   include '../include/ionize.f'
   include '../include/file.f'c
   integer(kind=8), dimension(N_p_t_max) :: part_ind
   dimension x(N_p_t_max),y(N_p_t_max),p(N_p_t_max,3),
\      wgm(N_p_t_max),qc(N_p_t_max),oldfield(N_p_t_max,7)
   character*2 label1
   character*5 label2,label3

   pai2=atan(1.0d0)*8.d0
   xone=pai2/ow*c
   call label_gen2(is,label1)
   call label_gen5(ii,label2)
   call label_gen5(iam,label3)
   do iam_i=0,nd_para
     if (iam.eq.iam_i) then
       if (iam.eq.0)
\       open(137,file=dir(1:idirln)//'/trk/trk'//label1//
\            '_'//label2)
       if (iam.gt.0)
\       open(137,file=dir(1:idirln)//'/trk/trk'//label1//
```

```
     \              '_'//label2,
     \         ACCESS='APPEND')
             do j = l_st(is), l_ed(is)
               if(part_ind(j).ne.0) then
                 write(137,500)
     \           int(part_ind(j),8),
     \           real(x(j))/xone,real(y(j))/xone,
     \           real(p(j,1)/p_mass(is)/c),
     \           real(p(j,2)/p_mass(is)/c),
     \           real(p(j,3)/p_mass(is)/c),real(wgm(j)),real(qc(j)),
     \           real(oldfield(j,1)),real(oldfield(j,2)),
     \           real(oldfield(j,3)),real(oldfield(j,4)),
     \           real(oldfield(j,5)),real(oldfield(j,6)),
     \           real(oldfield(j,7))
               endif
             enddo
             close(137)
           endif
           call MPI_Barrier(MPI_COMM_WORLD,mpierr)
         enddo
 500     format(I20,' ',F8.3,' ',F8.3,' ',2p,G10.3E1,' ',G10.3E1,' ',
     \     G10.3E1,' ',0p,F8.6,' ',F8.5,G10.3E1,G10.3E1,G10.3E1,
     \     G10.3E1,G10.3E1,G10.3E1,G10.3E1)
         return
       end
```

Listing A.5: ionization.f: tagging of electrons created by ionization

```
c      --- Track electron if requested ---
       if (track_e(1).gt.0) then
         if ((track_in_volume(x(je),y(je)).eq..true.)
     \      .and.(track_every_other(track_e(1)).eq..true.)
     \      .and.(wgm(je).ne.0)) then
           ind_num = ind_num + 1
           part_ind(je) = ind_num
```

```
                    endif
      endif
```

The id-tag, postion, momentum weight and charge of tracked particles as well as the value of the electric and magnetic fields at the respective particle position (saved in the global variable `oldfields` at the end of the function `p_push()`) are written into a separate file for each timestep and particle species after the particle push called in `e_magnetic`.

Listing A.6: call of write_track() in e_magnetic.f

```
            do is = 1, N_sp
              if (i_time.gt.0) then
          !here it can be defined, that not in every
          !timestep the tracking information is
          !written to disk (e.g. for ions this is not
          !necessary), e.g. to save memory
          if ((MOD(i_time,12).eq.0).or.((is.eq.N_sp).and.
     \      (i_time.lt.6125).and.(MOD(i_time,4).eq.0))) then
            if(track_SP(is))
     \        call write_track(is,x,y,P,wgm,qc,i_time,
     \        part_ind,oldfield)
                endif
        endif
      enddo
```

The tracking files are found in the working directory in the subdirectory `trk`. The files are named as `trk_[is]_[time]`. Here, `[is]` is the two-digit index of the ion species and `[time]` is the five-digit number of the timestep. In each file each line represents one tracked particle with the following information:

```
id-tag x y px py pz weight charge  Ex(time) Ey(time) Ez(time) Bz(time)
   0.5[Bx(time+Bx(time-1)] 0.5[By(time+By(time-1)] 0.5[Bz(time+Bz(time-1)]
```

A.4 Outputs

Regular outputs of the particle densities, energy densities, fields, current densities and the phase space are written to disk as defined in the input file. They are stored in the following subdirectories:

- dnss: particle density distribution (is1,is2,...,e), unit: normalized to maximum density 1/ow^2
- emes: field energy distribution
- empi/emps: field distribution E_x, E_y, B_z, unit: dimensionless field strength ($\approx$ 3.2 TV/m or 107 MG for $\lambda = 1\,\mu$m)
- emsi/emss: field distribution E_z, B_x, B_y, unit: dimensionless field strength
- gmns: energy density distribution (is1,is2,...,e), unit: normalized to $m_{is}c^2$/ow^2
- rjci/rjcs: current density distribution (is1,is2,...,e), unit: $en_c c$
- phs: phase space
- trk: tracking information (see last section)
- etc: total energies and misc

In the following the individual output files are described in detail.

A.4.1 Field data

All distribution outputs have a common format. Each individual process writes the field data of its volume into a separate file on disk. The filenames follow the scheme `[type]_[proc]_[output number]`. Here `[type] stands for one of the types stated above, e.g. \verbdnss`|, `[proc]` is the five-digit number of the process and `[output number]` is a five-digit number consecutively numbering the outputs at different timesteps. The field data in the files is stored such that each quantity (e.g. particle density of ion species 1 (is1)) is written in one column. The rows consecutively go through the x-values at y=0, followed by the x-values at y=1 and so on, skipping as many cells in x-direction as given in the input file by `Nx_d` and in the y-direction as given by `Ny_d`.

As an example, for a simulation using 48 parallel processes and 2 ion species with `Nx_d=3` and `Ny_d=4` and 1200 × 960 cells, there would be 48 files at each timestep when outputs are written to disk: E.g. for the first output (at timestep 0), there would be `dnss_00000_00000`, `dnss_00001_00000`, ..., `dnss_00047_00000`, for the second output – which possibly occurs several timesteps later, there would be `dnss_00000_00001`, `dnss_00001_00001`, ..., `dnss_00047_00001` and so on. In each file there would be three columns, one containing the density data for is1, one for is1 and one for electrons. Each column should have 2406 rows: `Ny=960` cells in y-direction are distributed over 48 processes, hence each process has `Ny_p=20` cells in y-direction and 1200 cells in x-direction. Since only every third cell is considered in x-direction and every fourth in y-direction, there are $(1200/3+1)\cdot(20/4+1) = 2005$ data point written to the file. In reality there are more rows, since at the process borders the two neighboring processes hold the same line in memory (they have to be averaged). The data in the rows then is the data of the cell with index (x,y) in the following order: (0,0), (`Nx_d`,0), (2 `Nx_d`, 0), (3 `Nx_d`,0), ..., (`Nx`,0), (0, `Ny_d`), (`Nx_d`, `Ny_d`), (2 `Nx_d`, `Ny_d`), ..., (`Nx`, `Ny_p`), where (0,0) is given relative to the origin of the process at (0,`Ny_p`·`[proc]`).

A.4.2 Phase space

The pahse space information is stored in the subfolder `phs`. Each individual process writes the particle data of particle in its volume into a separate file on disk. The filenames follow the scheme `phs[is]_[proc]_[output number]`. Here `[is]` stands for the five-digit index of the ion species as defined in the input file, electrons have the index is+1. Each particle's information is written into one line of the file, skipping as many particles as defined by `N_dp`. The information in one line is `x y px py pz weight charge`. x/y: x/y position of the particle in units of λ, given relative to the full simulation box, px/py/pz: particle momentum in units of $m_{is}c^2$, charge in units of e.

As an example, for a simulation using 48 parallel processes and 2 ion species, there would be 144 files at each timestep when outputs are written to disk (48 for each ion species and 48 for electrons): E.g. for the first output (at timestep 0), there would be `phs00001_00000_00000`, `phs00001_00001_00000`, ..., `phs00001_00047_00000`,`phs00002_00000_00000`, ..., `phs00003_00047_00000` for the second output – which possibly occurs several timesteps later, there would be `phs00001_00000_00001`, `phs00001_00001_00001`, ..., `phs00001_00047_00001`,`phs00002_00000_00001`, ..., `phs00003_00047_00001` and so on.

Bibliography

[1] A. Jemal, R. Siegel, E. Ward, Y. Hao, J. Xu, T. Murray, and M.J. Thun, "Cancer statistics, 2008," CA: a cancer journal for clinicians **58**, 71–96 (2008)

[2] Italy Istituto Superiore di Sanita, "Eurocare 4 survey database," (fetched Apr. 2012), `http://www.eurocare.it/Results/tabid/79/Default.aspx`

[3] H. Holthusen, "Erfahrungen über die verträglichkeitsgrenze für röntgenstrahlen und deren nutzanwendung zur verhütung von schäden," Strahlentherapie **57**, 254 (1936)

[4] H. Bethe, "Zur Theorie des Durchgangs schneller Korpuskularstrahlen durch Materie," Annalen der Physik **397**, 325 (1930)

[5] M. Baumann T. Herrmann, *Klinische Strahlenbiologie - kurz und bündig*, Vol. 3rd edition (Gustav Fischer Jena, 1997)

[6] G. Kraft, *Biologische Effekte schwerer Ionen. In: Wirkungssteigerung der Strahlentherapie maligner Tumoren* (Springer Berlin, 1987) p. 126

[7] Universitätsklinikum Heidelberg, "Zwei jahre heidelberger ionenstrahl-therapiezentrum: Universitätsklinikum heidelberg zieht eine positive bilanz," Press release, 169/2011, ID 5925(2011), `http://www.klinikum.uni-heidelberg.de/ShowSingleNews.176.0.html?&tx_ttnews[tt_news]=5925`

[8] T. E. Cowan, J. Fuchs, H. Ruhl, A. Kemp, P. Audebert, M. Roth, R. Stephens, I. Barton, A. Blazevic, E. Brambrink, *et al.*, "Ultralow emittance, multi-mev proton beams from a laser virtual-cathode plasma accelerator," Phys. Rev. Lett. **92**, 204801 (2004)

[9] M. Schollmeier, M. Roth, A. Blazevic, E. Brambrink, J.A. Cobble, J.C. Fernandez, K.A. Flippo, D.C. Gautier, D. Habs, K. Harres, B.M. Hegelich, T. Heßling, D.H.H. Hoffmann, S. Letzring, F. Nürnberg, G. Schaumann, J. Schreiber, and K. Witte, "Laser ion acceleration with micro-grooved targets," Nuclear Instruments and Methods A **577**, 186 (2007)

[10] J. Weichsel, T. Fuchs, E. Lefebvre, E. d'Humières, and U. Oelfke, "Spectral features of laser-accelerated protons for radiotherapy applications," Phys. Med. Biol. **53**, 4383 (2008)

[11] T. Burris-Mog, K. Harres, F. Nürnberg, S. Busold, M. Bussmann, O. Deppert, G. Hoffmeister, M. Joost, M. Sobiella, A. Tauschwitz, B. Zielbauer, V. Bagnoud, T. Herrmannsdoerfer, M. Roth, and T. E. Cowan, "Laser accelerated protons captured and transported by a pulse power solenoid," Phys. Rev. ST Accel. Beams **14**, 121301 (2011)

[12] Victor Malka, Sven Fritzler, Erik Lefebvre, Emmanuel d'Humières, Régis Ferrand, Georges Grillon, Claude Albaret, Samuel Meyroneinc, Jean-Paul Chambaret, Andre Antonetti, and Danièle Hulin, "Practicability of protontherapy using compact laser systems," Med. Phys. **31**, 1587–1592 (2004)

[13] U. Linz and J. Alonso, "What will it take for laser driven proton accelerators to be applied to tumor therapy?." Physical Review Special Topics-Accelerators and Beams **10**, 094801 (2007)

[14] K. W. D. Ledingham, W. Galster, and R. Sauerbrey, "Laser-driven proton oncology a unique new cancer therapy?." British Journal of Radiology **80**, 855 (2007)

[15] G. J. Caporaso, S. Sampayan, Y.-J. Chen, J. Harris, S. Hawkins, C. Holmes, M. Krogh, S. Nelson, W. Nunnally, A. Paul, B. Poole, M. Rhodes, D. Sanders, K. Selenes, J. Sullivan, L. Wang, and J. Watson, "Compact accelerator concept for proton therapy," Nuclear Instruments and Methods in Physics Research Section B: Beam Interactions with Materials and Atoms **261**, 777 (2007)

[16] M. Roth, T. E. Cowan, M. H. Key, S. P. Hatchett, C. Brown, W. Fountain, J. Johnson, D. M. Pennington, R. A. Snavely, S. C. Wilks, *et al.*, "Fast ignition by intense laser-accelerated proton beams," Phys. Rev. Lett. **86**, 436 (2001)

[17] K. W. D. Ledingham, P. McKenna, and R. P. Singhal, "Applications for nuclear phenomena generated by ultra-intense lasers," Science **300**, 1107 (2003)

[18] K. Nemoto, A. Maksimchuk, S. Banerjee, K. Flippo, G. Mourou, D. Umstadter, and V. Yu. Bychenkov, "Laser-triggered ion acceleration and table top isotope production," Appl. Phys. Lett. **78**, 595 (2001)

[19] D. Strickland and G. Mourou, “Compression of amplified chirped optical pulses,” Opt. Commun. **56**, 219 (1985)

[20] R. A. Snavely, M. H. Key, S. P. Hatchett, T. E. Cowan, M. Roth, T. W. Phillips, M. A. Stoyer, E. A. Henry, T. C. Sangster, M. S. Singh, S. C. Wilks, A. MacKinnon, A. Offenberger, D. M. Pennington, K. Yasuike, A. B. Langdon, B. F. Lasinski, J. Johnson, M. D. Perry, and E. M. Campbell, “Intense high-energy proton beams from petawatt-laser irradiation of solids,” Phys. Rev. Lett. **85**, 2945 (2000)

[21] S. A. Gaillard, T. Kluge, K. A. Flippo, M. Bussmann, B. Gall, T. Lockard, M. Geissel, D. T. Offermann, M. Schollmeier, Y. Sentoku, *et al.*, “Increased laser-accelerated proton energies via direct laser-light-pressure acceleration of electrons in microcone targets,” Phys. Plasmas **18**, 056710 (2011)

[22] F. Nürnberg, M. Schollmeier, E. Brambrink, A. Blažević, D. C. Carroll, K. Flippo, D. C. Gautier, M. Geiß el, K. Harres, B. M. Hegelich, O. Lundh, K. Markey, P. McKenna, D. Neely, J. Schreiber, and M. Roth, “Radiochromic film imaging spectroscopy of laser-accelerated proton beams,” Rev. Sci. Instrum. **80**, 033301 (2009)

[23] S D Kraft, C Richter, K Zeil, M Baumann, E Beyreuther, S Bock, M Bussmann, T E Cowan, Y Dammene, W Enghardt, U Helbig, L Karsch, T Kluge, L Laschinsky, E Lessmann, J Metzkes, D Naumburger, R Sauerbrey, M. Schürer, M Sobiella, J Woithe, U Schramm, and J Pawelke, “Dose-dependent biological damage of tumour cells by laser-accelerated proton beams,” New J. Phys. **12**, 085003 (2010), `http://stacks.iop.org/1367-2630/12/i=8/a=085003`

[24] K. Zeil, S. D. Kraft, S. Bock, M. Bussmann, T. E. Cowan, T. Kluge, J. Metzkes, T. Richter, R. Sauerbrey, and U. Schramm, “The scaling of proton energies in ultrashort pulse laser plasma acceleration,” New J. Phys. **12**, 045015 (2010)

[25] O. Klimo, J. Psikal, J. Limpouch, J. Proska, F. Novotny, T. Ceccotti, V. Floquet, and S. Kawata, “Short pulse laser interaction with micro-structured targets: simulations of laser absorption and ion acceleration,” New J. Phys. **13**, 053028 (2011)

[26] P. Gibbon, *Short pulse laser interactions with matter: An introduction*, ISBN 1-86094-135-4 (Imperial College Press London, 2005)

[27] P. Mulser and D. Bauer, *High power laser-matter interaction*, ISBN 978-3-540-50669-0 (Springer-Verlag Berlin Heidelberg, 2010)

[28] H. Schwoerer, J. Magill, and B. Beleites, *Lasers and nuclei: applications of ultrahigh intensity lasers in nuclear science*, ISBN 3-540-30271-9 (Springer Verlag Berlin Heidelberg New York, 2006)

[29] T. Kluge, W. Enghardt, S. D. Kraft, U. Schramm, K. Zeil, T. E. Cowan, and M. Bussmann, "Enhanced laser ion acceleration from mass-limited foils," Phys. Plasmas **17**, 123103 (2010), ISSN 1070664X

[30] Y. Sentoku, K. Mima, H. Ruhl, Y. Toyama, R. Kodama, and T. E. Cowan, "Laser light and hot electron micro focusing using a conical target," Phys. Plasmas **11**, 3083–3087 (2004), ISSN 1070664X

[31] T. Nakamura, K. Mima, H. Sakagami, and T. Johzaki, "Electron surface acceleration on a solid capillary target inner wall irradiated with ultraintense laser pulses," Physics of Plasmas **14**, 053112 (2007)

[32] T. Kluge, "High proton energies from cone targets: electron acceleration mechanisms," New J. Phys. **14**, 023038 (2012)

[33] W.L. Kruer, *The physics of laser plasma interactions*, Vol. 73 (Westview Pr, 2003)

[34] N. Bohr, "On the constitution of atoms and molecules, part i," Philos. Mag. **26**, 1.24 (1913)

[35] E. Mevel, P. Breger, R. Trainham, G. Petite, P. Agostini, A. Migus, J.-P. Chambaret, and A. Antonetti, "Atoms in strong optical fields: Evolution from multiphoton to tunnel ionization," Phys. Rev. Lett. **70**, 406 (Jan 1993), `http://link.aps.org/doi/10.1103/PhysRevLett.70.406`

[36] L. V. Keldysh, "Ionization in the field of a strong electromagnetic wave," Soviet Physics JETP **20**, 1307–1314 (1965)

[37] L.D. Landau and E.M. Lifshitz, *Quantum Mechanics*, Course of Theoretical Physics, Vol. 3 (Pergamon Press, New York, 1965) p. 276, `http://books.google.de/books?id=SOlgtwAACAAJ`

[38] X. M. Tong and C. D. Lin, "Empirical formula for static ?eld ionization rates of atoms and molecules by lasers in the barrier-suppression regime," J. Phys. B: At. Mol. Opt. Phys **38**, 2593 (2005)

[39] M. V. Ammosov, N. B. Delone, and V. P. Krainov, "Tunnel ionization of complex atoms and atomic ions by an alternating electromagnetic field," Sov. Phys. JETP **64**, 1191 (1986)

[40] J.D. Jackson and R.F. Fox, *Classical electrodynamics*, 3rd ed., ISBN 978-0471309321 (John Wiley & Sons, 1999) p. 841

[41] D. Bauer, P. Mulser, and W. H. Steeb, "Relativistic ponderomotive force, uphill acceleration, and transition to chaos," Phys. Rev. Lett. **75**, 4622 (1995)

[42] L.D. Landau and E.M. Lifshitz, *The classical theory of fields*, Vol. 2 (Addison-Wesley Press, 1951)

[43] E.M. McMillan, "The origin of cosmic rays," Phys. Rev. **79**, 498 (1950)

[44] W.L. Kruer, "Ponderomotive and thermal filamentation of laser light," Comm. Plasma Phys. Contr. F. **9**, 63 (1985)

[45] T.H. Stix, *Waves in plasmas* (Amer Inst of Physics, 1992)

[46] B. Bezzerides, S. J. Gitomer, and D. W. Forslund, "Randomness, maxwellian distributions, and resonance absorption," Phys. Rev. Lett. **44**, 651 (1980)

[47] G. Malka and J. L. Miquel, "Experimental confirmation of ponderomotive-force electrons produced by an ultrarelativistic laser pulse on a solid target," Phys. Rev. Lett. **77**, 75–78 (1996)

[48] A. Rousse, P. Audebert, J. P. Geindre, F. Falliès, J. C. Gauthier, A. Mysyrowicz, G. Grillon, and A. Antonetti, "Efficient $K\ \alpha$ x-ray source from femtosecond laser-produced plasmas," Phys. Rev. E **50**, 2200–2207 (1994)

[49] S.C. Wilks, W.L. Kruer, M. Tabak, and A.B. Langdon, "Absorption of ultra-intense laser pulses," Phys. Rev. Lett. **69**, 1383 (1992)

[50] T. Kluge, M. Bussmann, SA Gaillard, KA Flippo, DC Gautier, B. Gall, T. Lockard, ME Lowenstern, JE Mucino, Y. Sentoku, *et al.*, "Low-divergent, energetic electron beams from ultra-thin foils," in *AIP Conference Proceedings*, Vol. 1209 (2010) p. 51

[51] A. J. Kemp, Y. Sentoku, and M. Tabak, "Hot-electron energy coupling in ultraintense laser-matter interaction," Phys. Rev. Lett. **101**, 075004 (2008)

[52] D. Bauer P. Mulser and H. Ruhl, “Collisionless laser-energy conversion by anharmonic resonance,” Phys. Rev. Lett. **101**, 225002 (2008)

[53] M. G. Haines, M. S. Wei, F. N. Beg, and R. B. Stephens, “Hot-electron temperature and laser-light absorption in fast ignition,” Phys. Rev. Lett. **102**, 045008 (2009)

[54] J. Yu, Z. Jiang, J.C. Kieffer, and A. Krol, “Hard x-ray emission in high intensity femtosecond laser–target interaction,” Phys. Plasmas **6**, 1318 (1999)

[55] H. Chen, S. C. Wilks, W. L. Kruer, P. K. Patel, and R. Shepherd, “Hot electron energy distributions from ultraintense laser solid interactions,” Phys. Plasmas **16**, 020705 (2009)

[56] F. N. Beg, A. R. Bell, A. E. Dangor, C. N. Danson, A. P. Fews, M. E. Glinsky, B. A. Hammel, P. Lee, P. A. Norreys, and M. Tatarakis, “A study of picosecond laser–solid interactions up to 10^{19} w cm^{-2},” Physics of Plasmas **4**, 447 (1997)

[57] A. G. MacPhee, K. U. Akli, F. N. Beg, C. D. Chen, H. Chen, R. Clarke, D. S. Hey, R. R. Freeman, A. J. Kemp, M. H. Key, J. A. King, S. Le Pape, A. Link, T. Y. Ma, H. Nakamura, D. T. Offermann, V. M. Ovchinnikov, P. K. Patel, T. W. Phillips, R. B. Stephens, R. Town, Y. Y. Tsui, M. S. Wei, L. D. Van Woerkom, and A. J. Mackinnon, “Diagnostics for fast ignition science (invited),” Review of Scientific Instruments **79**, 10F302 (2008)

[58] J.C. Maxwell, “A dynamical theory of the electromagnetic field,” Philosophical Transactions of the Royal Society of London **155**, 459–512 (1865)

[59] R. B. White and F. F. Chen, “Amplification and absorption of electromagnetic waves in overdense plasmas,” Plasma Physics **16**, 565 (1974), `http://stacks.iop.org/0032-1028/16/i=7/a=002`

[60] T. Y. B. Yang, W. L. Kruer, R. M. More, and A. B. Langdon, “Absorption of laser light in overdense plasmas by sheath inverse bremsstrahlung,” Physics of Plasmas **2**, 3146 (1995)

[61] Y. Sentoku, V.Y. Bychenkov, K. Flippo, A. Maksimchuk, K. Mima, G. Mourou, ZM Sheng, and D. Umstadter, “High-energy ion generation in interaction. of short laser pulse with high-density plasma,” Applied Physics B: Lasers and Optics **74**, 207–215 (2002)

[62] D. F. Zaretsky, P. A. Korneev, S. V. Popruzhenko, and W. Becker, "Landau damping in thin films irradiated by a strong laser field," Journal of Physics B: Atomic, Molecular and Optical Physics **37**, 4817 (2004)

[63] V. L. Ginzburg, "The propagation of electromagnetic waves in plasmas (book on plasma behavior in electromagnetic field discussing radio and electromagnetic wave propagation in earth atmosphere, interplanetary space and laboratory generated plasmas)," (Pergammon Press Oxford and New York, 1964) p. 535

[64] W. Kruer, *The physics of laser plasma interactions*, Vol. 73 (Reading, MA, Addison-Wesley Publishing Co. (Frontiers in Physics.), 1988)

[65] N. G. Denisov, "On a singularity of the field of an electromagnetic wave propagated in an inhomogeneous plasma," Sov. Phys. JETP **4**, 544–553 (1957)

[66] D. E. Hinkel-Lipsker, Burton D. Fried, and G. J. Morales, "Analytic expression for mode conversion of langmuir and electromagnetic waves," Phys. Rev. Lett. **62**, 2680–2682 (1989)

[67] H. J. Kull, "Linear mode conversion in laser plasmas," Physics of Fluids **26**, 1881–1887 (1983)

[68] A. Bergmann, *Nonlinear Resonance Absorption and Wavebreaking*, Ph.D. thesis, Dissertation, TH Darmstadt (1990)

[69] D. W. Forslund, J. M. Kindel, and K. Lee, "Theory of hot-electron spectra at high laser intensity," Phys. Rev. Lett. **39**, 284–288 (1977)

[70] F. Brunel, "Anomalous absorption of high intensity subpicosecond laser pulses," Physics of Fluids **31**, 2714 (1988)

[71] S.C. Wilks and W.L. Kruer, "Absorption of ultrashort, ultra-intense laser light by solids and overdense plasmas," Quantum Electronics, IEEE Journal of **33**, 1954–1968 (1997)

[72] W. Yu, M. Y. Yu, Z. M. Sheng, and J. Zhang, "Model for fast electrons in ultrashort-pulse laser interaction with solid targets," Phys. Rev. E **58**, 2456 (1998)

[73] AA Andreev, IA Litvinenko, and K.Y. Platonov, "Escape into vacuum of fast electrons generated by oblique incidence of an ultrashort, high-power laser pulse on a solid target," Journal of Experimental and Theoretical Physics **89**, 632–639 (1999)

[74] H. Ruhl, Y. Sentoku, K. Mima, KA Tanaka, and R. Kodama, "Collimated electron jets by intense laser-beam–plasma surface interaction under oblique incidence," Physical review letters **82**, 743 (1999)

[75] Z.M. Sheng, Y. Sentoku, K. Mima, J. Zhang, W. Yu, and J. Meyer-ter Vehn, "Angular distributions of fast electrons, ions, and bremsstrahlung x/γ-rays in intense laser interaction with solid targets," Physical review letters **85**, 5340–5343 (2000)

[76] W. L. Kruer and K. Estabrook, "J × b heating by very intense laser light," Phys. Fluids **28**, 430 (1985)

[77] M. I. K. Santala, M. Zepf, I. Watts, F. N. Beg, E. Clark, M. Tatarakis, K. Krushelnick, A. E. Dangor, T. McCanny, I. Spencer, R. P. Singhal, K. W. D. Ledingham, S. C. Wilks, A. C. Machacek, J. S. Wark, R. Allott, R. J. Clarke, and P. A. Norreys, "Effect of the plasma density scale length on the direction of fast electrons in relativistic laser-solid interactions," Phys. Rev. Lett. **84**, 1459–1462 (2000), `http://link.aps.org/doi/10.1103/PhysRevLett.84.1459`

[78] H. Popescu, S. D. Baton, F. Amiranoff, C. Rousseaux, M. Rabec Le Gloahec, J. J. Santos, L. Gremillet, M. Koenig, E. Martinolli, T. Hall, J. C. Adam, A. Heron, and D. Batani, "Subfemtosecond, coherent, relativistic, and ballistic electron bunches generated at omega[sub 0] and 2 omega[sub 0] in high intensity laser-matter interaction," Physics of Plasmas **12**, 063106 (2005), `http://link.aip.org/link/?PHP/12/063106/1`

[79] D. Batani, *Atoms, solids, and plasmas in super-intense laser fields* (Plenum Pub Corp, ISBN 0-306-46615-5, 2001)

[80] P. Mulser, D. Bauer, and H. Ruhl, "Collisionless laser-energy conversion by anharmonic resonance," Phys. Rev. Lett. **101**, 225002 (2008)

[81] P. Mora, "Plasma expansion into a vacuum," Phys. Rev. Lett. **90**, 185002 (2003)

[82] D. Umstadter, J. K. Kim, and E. Dodd, "Laser injection of ultrashort electron pulses into wakefield plasma waves," Phys. Rev. Lett. **76**, 2073–2076 (1996)

[83] E. Esarey, R. F. Hubbard, W. P. Leemans, A. Ting, and P. Sprangle, "Electron injection into plasma wakefields by colliding laser pulses," Phys. Rev. Lett. **79**, 2682–2685 (1997)

[84] P. Sprangle, E. Esarey, J. Krall, and G. Joyce, "Propagation and guiding of intense laser pulses in plasmas," Phys. Rev. Lett. **69**, 2200–2203 (1992)

[85] T. M. Antonsen and P. Mora, "Self-focusing and raman scattering of laser pulses in tenuous plasmas," Phys. Rev. Lett. **69**, 2204–2207 (1992)

[86] NE Andreev, LM Gorbunov, VI Kirsanov, AA Pogosova, and RR Ramazashvili, "Resonant excitation of wakefields by a laser pulse in a plasma," JETP lett **55**, 571–576 (1992), `http://www.jetpletters.ac.ru/ps/1277/article_19308.pdf`

[87] P. Bertrand, A. Ghizzo, SJ Karttunen, TJH Pättikangas, RRE Salomaa, and M. Shoucri, "Generation of ultrafast electrons by simultaneous stimulated raman backward and forward scattering," Physical Review E **49**, 5656 (1994)

[88] D. Umstadter, S.Y. Chen, A. Maksimchuk, G. Mourou, and R. Wagner, "Nonlinear optics in relativistic plasmas and laser wake field acceleration of electrons," Science **273**, 472 (1996)

[89] C. I. Moore, A. Ting, K. Krushelnick, E. Esarey, R. F. Hubbard, B. Hafizi, H. R. Burris, C. Manka, and P. Sprangle, "Electron trapping in self-modulated laser wakefields by raman backscatter," Phys. Rev. Lett. **79**, 3909–3912 (1997)

[90] W. Lu, M. Tzoufras, C. Joshi, F. S. Tsung, W. B. Mori, J. Vieira, R. A. Fonseca, and L. O. Silva, "Generating multi-gev electron bunches using single stage laser wakefield acceleration in a 3d nonlinear regime," Phys. Rev. ST Accel. Beams **10**, 061301 (2007)

[91] K. Schmid, L. Veisz, F. Tavella, S. Benavides, R. Tautz, D. Herrmann, A. Buck, B. Hidding, A. Marcinkevicius, U. Schramm, M. Geissler, J. Meyer-ter Vehn, D. Habs, and F. Krausz, "Few-cycle laser-driven electron acceleration," Phys. Rev. Lett. **102**, 124801 (2009)

[92] A. Buck, M. Nicolai, K. Schmid, C.M.S. Sears, A. Sävert, J.M. Mikhailova, F. Krausz, M.C. Kaluza, and L. Veisz, "Real-time observation of laser-driven electron acceleration," Nature Physics **7**, 543 (2011)

[93] C. Gahn, G. D. Tsakiris, A. Pukhov, J. Meyer-ter Vehn, G. Pretzler, P. Thirolf, D. Habs, and K. J. Witte, “Multi-mev electron beam generation by direct laser acceleration in high-density plasma channels,” Phys. Rev. Lett. **83**, 4772–4775 (1999), `http://link.aps.org/doi/10.1103/PhysRevLett.83.4772`

[94] V. Malka, J. Faure, J. R. Marquès, F. Amiranoff, J. P. Rousseau, S. Ranc, J. P. Chambaret, Z. Najmudin, B. Walton, P. Mora, and A. Solodov, “Characterization of electron beams produced by ultrashort (30 fs) laser pulses,” Physics of Plasmas **8**, 2605–2608 (2001), `http://link.aip.org/link/?PHP/8/2605/1`

[95] A. Pukhov and J. Meyer-ter Vehn, “Relativistic magnetic self-channeling of light in near-critical plasma: Three-dimensional particle-in-cell simulation,” Phys. Rev. Lett. **76**, 3975–3978 (1996)

[96] A. Pukhov, Z.-M. Sheng, and J. Meyer ter Vehn, “Particle acceleration in relativistic laser channels,” Physics of Plasmas **6**, 2847–2854 (1999), `http://link.aip.org/link/?PHP/6/2847/1`

[97] Stephen P. Hatchett, Curtis G. Brown, Thomas E. Cowan, Eugene A. Henry, Joy S. Johnson, Michael H. Key, Jeffrey A. Koch, A. Bruce Langdon, Barbara F. Lasinski, Richard W. Lee, Andrew J. Mackinnon, Deanna M. Pennington, Michael D. Perry, Thomas W. Phillips, Markus Roth, T. Craig Sangster, Mike S. Singh, Richard A. Snavely, Mark A. Stoyer, Scott C. Wilks, and Kazuhito Yasuike, “Electron, photon, and ion beams from the relativistic interaction of petawatt laser pulses with solid targets,” Phys. Plasmas **7**, 2076–2082 (2000)

[98] S. C. Wilks, A. B. Langdon, T. E. Cowan, *et al.*, “Energetic proton generation in ultra-intense laser-solid interactions,” Phys. Plasmas **8**, 542 (2001)

[99] B. M. Hegelich, B. J. Albright, J. Cobble, K. Flippo, S. Letzring, M. Paffett, H. Ruhl, J. Schreiber, R. K. Schulze, and J. C. Fernaindez, “Laser acceleration of quasi-monoenergetic mev ion beams,” Nature **439**, 441–444 (2006), ISSN 0028-0836

[100] M. Hegelich, S. Karsch, G. Pretzler, D. Habs, K. Witte, W. Guenther, M. Allen, A. Blazevic, J. Fuchs, J. C. Gauthier, M. Geissel, P. Audebert, T. Cowan, and M. Roth, “Mev ion jets from short-pulse-laser interaction with thin foils,” Phys. Rev. Lett. **89**, 085002 (2002)

[101] H. Schwoerer, S. Pfotenhauer, O. Jackel, K.-U. Amthor, B. Liesfeld, W. Ziegler, R. Sauerbrey, K. W. D. Ledingham, and T. Esirkepov, "Laser-plasma acceleration of quasi-monoenergetic protons from microstructured targets," Nature **439**, 445–448 (2006), ISSN 0028-0836

[102] M. Borghesi, A. J. Mackinnon, D. H. Campbell, D. G. Hicks, S. Kar, P. K. Patel, D. Price, L. Romagnani, A. Schiavi, and O. Willi, "Multi-mev proton source investigations in ultraintense laser-foil interactions," Phys. Rev. Lett. **92**, 055003 (2004)

[103] A. J. Mackinnon, Y. Sentoku, P. K. Patel, D. W. Price, S. Hatchett, M. H. Key, C. Andersen, R. Snavely, and R. R. Freeman, "Enhancement of proton acceleration by hot-electron recirculation in thin foils irradiated by ultraintense laser pulses," Phys. Rev. Lett. **88**, 215006 (2002)

[104] M. Kaluza, J. Schreiber, MIK Santala, GD Tsakiris, K. Eidmann, J. Meyer-ter Vehn, and KJ Witte, "Influence of the laser prepulse on proton acceleration in thin-foil experiments," Phys. Rev. Lett. **93**, 045003 (2004)

[105] J. Schreiber, M. Kaluza, F. Grüner, U. Schramm, BM Hegelich, J. Cobble, M. Geissler, E. Brambrink, J. Fuchs, P. Audebert, *et al.*, "Source-size measurements and charge distributions of ions accelerated from thin foils irradiated by high-intensity laser pulses," Applied Physics B: Lasers and Optics **79**, 1041–1045 (2004)

[106] S. D. Baton, M. Koenig, P. Guillou, B. Loupias, A. Benuzzi-Mounaix, J. Fuchs, C. Rousseaux, L. Gremillet, D. Batani, A. Morace, M. Nakatsutsumi, R. Kodama, and Y. Aglitskiy, "Relativistic electron transport and confinement within charge-insulated, mass-limited targets," High Energy Density Physics **3**, 358 (2007), ISSN 1574-1818

[107] K. A. Flippo, E. d'Humières, S. A. Gaillard, J. Rassuchine, D. C. Gautier, M. Schollmeier, F. Nürnberg, J. L. Kline, J. Adams, B. Albright, M. Bakeman, K. Harres, R. P. Johnson, G. Korgan, S. Letzring, S. Malekos, N. Renard-LeGalloudec, Y. Sentoku, T. Shimada, M. Roth, T. E. Cowan, J. C. Fernández, and B. M. Hegelich, "Increased efficiency of short-pulse laser-generated proton beams from novel flat-top cone targets," Physics of Plasmas **15**, 056709 (2008)

[108] J. Rassuchine, SD Baton, P. Guillou, M. Koenig, M. Chahid, F. Perez, J. Fuchs, P. Audebert, R. Kodama, M. Nakatsutsumi, *et al.*, "Enhanced hot-electron localization and

heating in high-contrast ultraintense laser irradiation of microcone targets," Physical Review E **79**, 036408 (2009)

[109] S. Buffechoux, J. Psikal, M. Nakatsutsumi, L. Romagnani, A. Andreev, K. Zeil, M. Amin, P. Antici, T. Burris-Mog, A. Compant-La-Fontaine, *et al.*, "Hot electrons transverse refluxing in ultraintense laser-solid interactions," Phys. Rev. Lett. **105**, 15005 (2010)

[110] D. Neely, P. Foster, A. Robinson, F. Lindau, O. Lundh, A. Persson, C.-G. Wahlström, and P. McKenna, "Enhanced proton beams from ultrathin targets driven by high contrast laser pulses," Applied Physics Letters **89**, 021502 (2006)

[111] P. Antici, J. Fuchs, E. d'Humières, E. Lefebvre, M. Borghesi, E. Brambrink, C. A. Cecchetti, S. Gaillard, L. Romagnani, Y. Sentoku, T. Toncian, O. Willi, P. Audebert, and H. Pépin, "Energetic protons generated by ultrahigh contrast laser pulses interacting with ultrathin targets," Physics of Plasmas **14**, 030701 (2007)

[112] P. Mora, "Thin-foil expansion into a vacuum," Phys. Rev. E **72**, 056401 (2005)

[113] J. Schreiber, F. Bell, F. Grüner, U. Schramm, M. Geissler, M. Schnürer, S. Ter-Avetisyan, B. M. Hegelich, J. Cobble, E. Brambrink, J. Fuchs, P. Audebert, and D. Habs, "Analytical model for ion acceleration by high-intensity laser pulses," Phys. Rev. Lett. **97**, 045005 (2006)

[114] J. Pšikal, J. Limpouch, S. Kawata, and AA Andreev, "Pic simulations of femtosecond interactions with mass-limited targets," Czechoslovak Journal of Physics **56**, 515–521 (2006)

[115] T. Toncian, M. Swantusch, M. Toncian, O. Willi, A. A. Andreev, and K. Y. Platonov, "Optimal proton acceleration from lateral limited foil sections and different laser pulse durations at relativistic intensity," Phys. Plasmas **18**, 043105 (2011)

[116] E. d'Humières, E. Lefebvre, L. Gremillet, and V. Malka, "Proton acceleration mechanisms in high-intensity laser interaction with thin foils," Phys. Plasmas **12**, 062704 (2005), ISSN 1070664X

[117] AV Gurevich, LV PARIISKAIA, and LP Pitaevskii, "Self-similar motion of a rarefied plasma(nonlinear kinetic equation of self-similar motion of rarefied collisionless

electron-ion plasma)," ZHURNAL EKSPERIMENTAL'NOI I TEORETICHESKOI FIZIKI **49**, 647–654 (1965)

[118] JE Crow, PL Auer, and JE Allen, "The expansion of a plasma into a vacuum," Journal of Plasma Physics **14**, 65–76 (1975)

[119] Patrick Mora and R. Pellat, "Self-similar expansion of a plasma into a vacuum," Phys. Fluids **22**, 2300–2304 (1979), ISSN 00319171

[120] J. Denavit, "Collisionless plasma expansion into a vacuum," Phys. Fluids **22**, 1384–1392 (1979), ISSN 00319171

[121] S. J. Gitomer, R. D. Jones, F. Begay, A. W. Ehler, J. F. Kephart, and R. Kristal, "Fast ions and hot electrons in the laser?plasma interaction," Phys. Fluids **29**, 2679–2688 (1986), ISSN 00319171

[122] E. Lefebvre and G. Bonnaud, "Transparency/opacity of a solid target illuminated by an ultrahigh-intensity laser pulse," Phys. Rev. Lett. **74**, 2002–2005 (1995)

[123] M. Borghesi, A. J. Mackinnon, R. Gaillard, O. Willi, and A. A. Offenberger, "Guiding of a 10-tw picosecond laser pulse through hollow capillary tubes," Phys. Rev. E **57**, R4899–R4902 (1998)

[124] N. Renard-Le Galloudec, E. d'Humières, BI Cho, J. Osterholz, Y. Sentoku, and T. Ditmire, "Guiding, focusing, and collimated transport of hot electrons in a canal in the extended tip of cone targets," Phys. Rev. Lett. **102**, 205003 (2009)

[125] T. Kluge, SA Gaillard, M. Bussmann, KA Flippo, T. Burris-Mog, B. Gall, M. Geissel, SD Kraft, T. Lockard, J. Metzkes, *et al.*, "Theoretical understanding of enhanced proton energies from laser-cone interactions," in *AIP Conference Proceedings*, Vol. 1299 (2010) p. 715

[126] E. d'Humières, J. Rassuchine, S. Baton, J. Fuchs, P. Guillou, M. Koenig, L. Gremillet, C. Rousseaux, R. Kodama, M. Nakatsutsumi, T. Norimatsu, D. Batani, A. Morace, R. Redaelli, F. Dorchies, C. Fourment, J. J. Santos, J. Adams, G. Korgan, S. Malekos, Y. Sentoku, and T. E. Cowan, "Importance of magnetic resistive fields in the heating of a micro-cone target irradiated by a high intensity laser," Eur. Phys. J.-S. T. **175**, 89–95 (2009), ISSN 1951-6355, 10.1140/epjst/e2009-01123-6

[127] A. Andreev, N. Kumar, K. Platonov, and A. Pukhov, “Efficient generation of fast ions from surface modulated nanostructure targets irradiated by high intensity short-pulse lasers,” Physics of Plasmas **18**, 103103 (2011)

[128] Akifumi Yogo, Hiroyuki Daido, Atsushi Fukumi, Zhong Li, Koichi Ogura, Akito Sagisaka, Alexander S. Pirozhkov, Shu Nakamura, Yoshihisa Iwashita, Toshiyuki Shirai, Akira Noda, Yuji Oishi, Takuya Nayuki, Takashi Fujii, Koshichi Nemoto, Il Woo Choi, Jae Hee Sung, Do-Kyeong Ko, Jongmin Lee, Minoru Kaneda, and Akio Itoh, “Laser prepulse dependency of proton-energy distributions in ultraintense laser-foil interactions with an online time-of-flight technique,” Phys. Plasmas **14**, 043104 (2007)

[129] A. A. Andreev, R. Sonobe, S. Kawata, S. Miyazaki, K. Sakai, K. Miyauchi, T. Kikuchi, K. Platonov, and K. Nemoto, “Effect of a laser prepulse on fast ion generation in the interaction of ultra-short intense laser pulses with a limited-mass foil target,” Plasma physics and controlled fusion **48**, 1605 (2006)

[130] A. Pukhov, “Three-dimensional simulations of ion acceleration from a foil irradiated by a short-pulse laser,” Phys. Rev. Lett. **86**, 3562–3565 (2001)

[131] Y. Sentoku, T. E. Cowan, A. Kemp, and H. Ruhl, “High energy proton acceleration in interaction of short laser pulse with dense plasma target,” Phys. Plasmas **10**, 2009 (2003)

[132] J. Fuchs, Y. Sentoku, E. d’Humieres, T. E. Cowan, J. Cobble, P. Audebert, A. Kemp, A. Nikroo, P. Antici, E. Brambrink, A. Blazevic, E. M. Campbell, J. C. Fernandez, J.-C. Gauthier, M. Geissel, M. Hegelich, S. Karsch, H. Popescu, N. Renard-LeGalloudec, M. Roth, J. Schreiber, R. Stephens, and H. Pepin, “Comparative spectra and efficiencies of ions laser-accelerated forward from the front and rear surfaces of thin solid foils,” Phys. Plasmas **14**, 053105 (2007)

[133] J. Fuchs, Y. Sentoku, S. Karsch, J. Cobble, P. Audebert, A. Kemp, A. Nikroo, P. Antici, E. Brambrink, A. Blazevic, *et al.*, “Comparison of laser ion acceleration from the front and rear surfaces of thin foils,” Phys. Rev. Lett. **94**, 45004 (2005)

[134] A. P. L. Robinson, M. Zepf, S. Kar, R. G. Evans, and C. Bellei, “Radiation pressure acceleration of thin foils with circularly polarized laser pulses,” New J. Phys. **10**, 013021 (2008)

[135] S. G. Rykovanov, J. Schreiber, J. Meyer-ter Vehn, C. Bellei, A. Henig, H. C. Wu, and M. Geissler, “Ion acceleration with ultra-thin foils using elliptically polarized laser pulses,” New J. Phys. **10**, 113005 (2008)

[136] T. V. Liseykina, M. Borghesi, A. Macchi, and S. Tuveri, “Radiation pressure acceleration by ultraintense laser pulses,” Plasma Physics and Controlled Fusion **50**, 124033 (9pp) (2008)

[137] A. Macchi, S. Veghini, and F. Pegoraro, “"light sail" acceleration reexamined,” Physical Review Letters **103**, 85003 (2009)

[138] B. Qiao, M. Zepf, M. Borghesi, B. Dromey, M. Geissler, A. Karmakar, and P. Gibbon, “Radiation-pressure acceleration of ion beams from nanofoil targets: The leaky light-sail regime,” Physical review letters **105**, 155002 (2010)

[139] K. Tsander, “Light-pushed sails,” From A Scientific Heritage", NASATFF-541(1967)

[140] A. Macchi, S. Veghini, T.V. Liseykina, and F. Pegoraro, “Radiation pressure acceleration of ultrathin foils,” New J. Phys. **12**, 045013 (2010)

[141] A. Henig, S. Steinke, M. Schnürer, T. Sokollik, R. Hörlein, D. Kiefer, D. Jung, J. Schreiber, B. M. Hegelich, X. Q. Yan, J. Meyer-ter Vehn, T. Tajima, P. V. Nickles, W. Sandner, and D. Habs, “Radiation-pressure acceleration of ion beams driven by circularly polarized laser pulses,” Phys. Rev. Lett. **103**, 245003 (2009)

[142] F. Pegoraro and S. V. Bulanov, “Photon bubbles and ion acceleration in a plasma dominated by the radiation pressure of an electromagnetic pulse,” Physical Review Letters **99**, 065002 (2007)

[143] T.-P. Yu, A. Pukhov, and M. Chen, “Stable proton beam acceleration from a two-specie ultrathin foil target,” in *IPAC’10 ISBN 978-92-9083-352-9*, THPD034 (2010) p. 4352, `http://accelconf.web.cern.ch/accelconf/IPAC10/papers/thpd034.pdf`

[144] B. Qiao, M. Zepf, M. Borghesi, and M. Geissler, “Stable gev ion-beam acceleration from thin foils by circularly polarized laser pulses,” Phys. Rev. Lett. **102**, 145002 (2009)

[145] M. Chen, A. Pukhov, ZM Sheng, and XQ Yan, “Laser mode effects on the ion acceleration during circularly polarized laser pulse interaction with foil targets,” Physics of Plasmas **15**, 113103 (2008)

[146] W. P. Wang, B. F. Shen, X. M. Zhang, L. L. Ji, M. Wen, J. C. Xu, Y. H. Yu, Y. L. Li, and Z. Z. Xu, "Efficient acceleration of monoenergetic proton beam by sharp front laser pulse," Physics of Plasmas **18**, 013103 (2011)

[147] Y. Sentoku and A. J. Kemp, "Numerical methods for particle simulations at extreme densities and temperatures: Weighted particles, relativistic collisions and reduced currents," Journal of Computational Physics **227**, 6846 (2008), ISSN 0021-9991

[148] Hockney, R. W., and J. W. Eastwood, *Computer simulation using particles*, ISBN 0-85274-392-0 (Adam Hilger, Bristol (UK) IOP Publishing Ltd., 1988)

[149] C. K. Birdsall and A. B. Langdon, *Plasma Physics via computer simulation*, ISBN 0-7503-0117-1 (Adam Hilger Bristol (UK) IOP Publishing Ltd., 1995)

[150] Y. Sentoku and A.J. Kemp, "Numerical methods for particle simulations at extreme densities and temperatures: Weighted particles, relativistic collisions and reduced currents," Journal of Computational Physics **227**, 6846 – 6861 (2008), ISSN 0021-9991, `http://www.sciencedirect.com/science/article/pii/S0021999108001988`

[151] T. Takizuka and H. Abe, "A binary collision model for plasma simulation with a particle code," J. Comput. Phys. **25**, 205 (1977), `http://www.sciencedirect.com/science/article/pii/0021999177900997`

[152] B. T. Nguyen and S. A. Hutchinson, *The Implementation of the Upwind Leapfrog Scheme for 3D Electromagnetic Scattering on Massively Parallel Computers*, Tech. Rep. SAND95-1322 UC-705 (Sandia National Laboratories (USA), 1995) `osti.gov/bridge/servlets/purl/94009-7sTtJi/webviewable/94009.pdf`

[153] T. Kluge, T. Cowan, A. Debus, U. Schramm, K. Zeil, and M. Bussmann, "Electron temperature scaling in laser interaction with solids," Phys. Rev. Lett. **107**, 205003 (2011)

[154] F. Dyson, "A meeting with enrico fermi," Nature **427**, 297 (2004)

[155] Jürgen Mayer, Khaled Khairy, and Jonathon Howard, "Drawing an elephant with four complex parameters," American Journal of Physics **78**, 648–649 (2010), `http://link.aip.org/link/?AJP/78/648/1`

[156] M. Schnürer, A. A. Andreev, S. Steinke, T. Sokollik, T. Paasch-Colberg, P. V. Nickles, A. Henig, D. Jung, D. Kiefer, R. Hörlein, *et al.*, "Comparison of femtosecond laser-driven proton acceleration using nanometer and micrometer thick target foils," Laser and Particle Beams-Pulse Power and High Energy Densities **29**, 437 (2011)

[157] J. Fuchs, P. Antici, E. d´Humieres, E. Lefebvre, M. Boghesi, E. Brambrink, C. Cecchetti, T. Toncian, H. Pepin, and P. Audebert, "Ion acceleration using high-contrast ultra-intense lasers," J. Phys. IV **133**, 1151 (2006)

[158] T. Kluge, W. Enghardt, S. D. Kraft, U. Schramm, Y. Sentoku, K. Zeil, T. E. Cowan, R. Sauerbrey, and M. Bussmann, "Efficient laser-ion acceleration from closely stacked ultrathin foils," Phys. Rev. E **82**, 016405 (2010)

[159] T. Ceccotti, A. Lévy, H. Popescu, F. Réau, P. D'Oliveira, P. Monot, J. P. Geindre, E. Lefebvre, and Ph. Martin, "Proton acceleration with high-intensity ultrahigh-contrast laser pulses," Phys. Rev. Lett. **99**, 185002 (2007)

[160] I. Velchev, E. Fourkal, and C.-M. Ma, "Laser-induced coulomb mirror effect: Applications for proton acceleration," Phys. Plasmas **14**, 033106 (2007)

[161] T. Esirkepov, M. Borghesi, S. V. Bulanov, G. Mourou, and T. Tajima, "Highly efficient relativistic-ion generation in the laser-piston regime," Phys. Rev. Lett. **92**, 175003 (2004)

[162] J. Psikal, V. T. Tikhonchuk, J. Limpouch, A. A. Andreev, and A. V. Brantov, "Ion acceleration by femtosecond laser pulses in small multispecies targets," Physics of Plasmas **15**, 053102 (2008), ISSN 1070664X

[163] A. A. Andreev, J. Limpouch, J. Psikal, K. Yu. Platonov, and V. T. Tikhonchuk, "Laser ion acceleration in a mass limited targets," Eur. Phys. J.-S. T. **175**, 123 (2009), ISSN 1951-6355, 10.1140/epjst/e2009-01128-1

[164] A. Henig, D. Kiefer, M. Geissler, S. G. Rykovanov, R. Ramis, R. Hörlein, J. Osterhoff, Zs. Major, L. Veisz, S. Karsch, F. Krausz, D. Habs, and J. Schreiber, "Laser-driven shock acceleration of ion beams from spherical mass-limited targets," Phys. Rev. Lett. **102**, 095002 (2009)

[165] T. Sokollik, M. Schnürer, S. Steinke, P. V. Nickles, W. Sandner, M. Amin, T. Toncian, O. Willi, and A. A. Andreev, "Directional laser-driven ion acceleration from microspheres," Phys. Rev. Lett. **103**, 135003 (2009)

[166] A. V. Brantov and V. Y. Bychenkov, "Monoenergetic proton beams from mass-limited targets irradiated by ultrashort laser pulses," Plasma physics reports **36**, 256–262 (2010)

[167] J. Psikal, V. T. Tikhonchuk, E. d'Humieres, J. Limpouch, and O. Klimo, "Enhanced laser proton acceleration in mass-limited targets," ECA Vol.33E, 36th EPS Conference on Plasma Phys. Sofia, P–1.008(2009), `http://epsppd.epfl.ch/Sofia/pdf2/P1_008.pdf`

[168] C. Thaury, F. Quéré, J.-P. Geindre, A. Levy, T. Ceccotti, P. Monot, M. Bougeard, F. Réau, P. d'Oliveira, P. Audebert, R. Marjoribanks, and Ph. Martin, "Plasma mirrors for ultrahigh-intensity optics," Nature Physics **3**, 424 (2007)

[169] Paul Gibbon, "Plasma physics: Cleaner petawatts with plasma optics," Nature Physics **3**, 369 (2007)

[170] J. Fuchs, P. Antici, E. dȞumieres, E. Lefebvre, M. Borghesi, E. Brambrink, C. A. Cecchetti, M. Kaluza, V. Malka, M. Manclossi, S. Meyroneinc, P. Mora, J. Schreiber, T. Toncian, H. Pepin, and P. Audebert, "Laser-driven proton scaling laws and new paths towards energy increase," Nat Phys **2**, 48–54 (2006), ISSN 1745-2473

[171] E. Y. Echkina, S. V. Bulanov, T. Esirkepov, I. N. Inovenkov, K. Nishihara, T. Tajima, and V. V. Zhakhovskii, "Ion acceleration during the coulomb explosion of the multispecies clusters," ECA, P–2.032(2004), `http://crpppc42.epfl.ch/London/pdf2/P2_032.pdf`

[172] S. Sakabe, S. Shimizu, M. Hashida, F. Sato, T. Tsuyukushi, K. Nishihara, S. Okihara, T. Kagawa, Y. Izawa, K. Imasaki, *et al.*, "Generation of high-energy protons from the coulomb explosion of hydrogen clusters by intense femtosecond laser pulses," Physical Review A **69**, 023203 (2004)

[173] S. S. Bulanov, A. Brantov, V. Yu. Bychenkov, V. Chvykov, G. Kalinchenko, T. Matsuoka, P. Rousseau, S. Reed, V. Yanovsky, D. W. Litzenberg, K. Krushelnick, and A. Maksimchuk, "Accelerating monoenergetic protons from ultrathin foils by flat-top laser pulses in the directed-coulomb-explosion regime," Phys. Rev. E **78**, 026412 (2008)

[174] G. M. Petrov and J. Davis, "Laser acceleration of light ions from high-intensity laser-target interactions," Applied Physics B: Lasers and Optics **96**, 773–779 (2009)

[175] J. Limpouch, J. Psikal, V. T. Tikhonchuk, O. Klimo, A. V. Brantov, and A. A. Andreev, "Laser acceleration of ions in mass-limited multi-species targets," Journal of Physics: Conference Series **112**, 042033 (2008)

[176] S. Micheau, A. Debayle, E. d'Humières, JJ Honrubia, B. Qiao, M. Zepf, M. Borghesi, and M. Geissler, "Generation and optimization of electron currents along the walls of a conical target for fast ignition," Physics of Plasmas **17**, 122703 (2010)

[177] L. Van Woerkom, KU Akli, T. Bartal, FN Beg, S. Chawla, CD Chen, E. Chowdhury, RR Freeman, D. Hey, MH Key, *et al.*, "Fast electron generation in cones with ultraintense laser pulses," Physics of Plasmas **15**, 056304 (2008)

[178] JS Green, KL Lancaster, KU Akli, CD Gregory, FN Beg, SN Chen, D. Clark, RR Freeman, S. Hawkes, C. Hernandez-Gomez, *et al.*, "Surface heating of wire plasmas using laser-irradiated cone geometries," Nature Physics **3**, 853 (2007)

[179] APL Robinson and M. Sherlock, "Magnetic collimation of fast electrons produced by ultraintense laser irradiation by structuring the target composition," Physics of Plasmas **14**, 083105 (2007)

[180] S. A. Gaillard, K. A. Flippo, M. E. Lowenstern, J. E. Mucino, J. M. Rassuchine, D. C. Gautier, J. Workman, and T. E. Cowan, "Proton acceleration from ultrahigh-intensity short-pulse laser-matter interactions with cu micro-cone targets at an intrinsic 10^8 contrast," Journal of Physics: Conference Series **244**, 022034 (2010)

[181] S. D. Baton, M. Koenig, J. Fuchs, A. Benuzzi-Mounaix, P. Guillou, B. Loupias, T. Vinci, L. Gremillet, C. Rousseaux, M. Drouin, E. Lefebvre, F. Dorchies, C. Fourment, J. J. Santos, D. Batani, A. Morace, R. Redaelli, M. Nakatsutsumi, R. Kodama, A. Nishida, N. Ozaki, T. Norimatsu, Y. Aglitskiy, S. Atzeni, and A. Schiavi, "Inhibition of fast electron energy deposition due to preplasma filling of cone-attached targets," Physics of Plasmas **15**, 042706 (2008)

Publications by the author

T. Kluge, D. Möckel, J. Pawelke and W. Enghardt, First in-beam PET measurement of β^+ radioactivity induced by hard photon beams, Physics in Medicine and Biology 52(2007), N467-N473

J. Pawelke, T. Bortfeld, F. Fiedler, **T. Kluge**, D. Möckel, K. Parodi, F. Pönisch, G. Shakirin and W. Enghardt, Therapy monitoring with PET techniques, Proceedings of Ion Beams in Biology and Medicine (IBIBAM) (2007), 978-3-8249-1071-7, 97-105

D. Möckel, **T. Kluge**, J. Pawelke and W. Enghardt, Comparison of in-beam and off-beam PET experiments at hard photons, Proceedings of Nuclear Science Symposium and Medical Imaging Conference (2007), 1-4244-0923-3

T. Wurschig, **T. Kluge**, K. Heidel, M. Sobiella and W. Enghardt, An experimental positron emission tomograph for education, Zeitschrift für medizinische Physik **17**, 212 (2007)

T. Würschig, T. Kluge and W. Enghardt, Implementation of a High Level Hands-on-Training at an Experimental PET Scanner, Proceedings of IEEE NSS-MIC Nuclear Science Symposium Conference, M06-147(2008)

D. Kunath, **T. Kluge**, J. Pawelke, M. Priegnitz et al., In-Beam and Off-Beam PET Measurements of Target Activation by Megavolt X-Ray Beams, IEEE Transactions on Nuclear Science 56(2009)1, 57-65

D. Kunath, F. Fiedler, **T. Kluge**, T. Kormoll et al., The potential of in-beam positron emission tomography within image-guided radiation therapy, Radiotherapy & Oncology 90(2009)Suppl. 3, S77-S78

A. Debus, S. Bock, M. Bussmann, T.E. Cowan, A. Jochmann, **T. Kluge**, S.D. Kraft, R. Sauerbrey, K. Zeil, U. Schramm, Linear and Non-Linear Thomson-Scattering X-Ray Sources Driven by Conventionally and Laser Plasma Accelerated Electrons, Proc. of SPIE **7359**, 735908 (2009)

T. Kluge, W. Enghardt, S.D. Kraft, U. Schramm, Y. Sentoku, K. Zeil, T.E. Cowan, R. Sauerbrey and M. Bussmann, Efficient laser-ion acceleration from closely stacked ultrathin foils, Phys. Rev. E **82**, 016405 (2010)

K.A. Flippo, S.A. Gaillard, **T. Kluge**, M. Bussmann, D.T. Offermann, J.A. Cobble, M.J. Schmitt, T. Bartal, F.N. Beg, T.E. Cowan, B. Gall, D.C. Gautier, M. Geissel, T.J. Kwan, G. Korgan, S. Kovaleski, T. Lockard, S. Malekos, D.S. Montgomery, M. Schollmeier and Y. Sentoku, Advanced Laser Particle Accelerator Development at LANL, From Fast Ignition to Radiation Oncology, Proc. of AAC2010 AIP **1299(1)**, 693 (2010)

T.E. Cowan, U. Schramm, T. Burris-Mog, F. Fiedler, S.D. Kraft, K. Zeil, M. Baumann, M. Bussmann, W. Enghardt, K. Flippo, S.A. Gaillard, K. Harres, T. Herrmannsdoerfer, **T. Kluge**, F. Nürnberg, J. Pawelke, M. Roth, B. Schmidt, M. Sobiella and R. Sauerbrey, Prospects For and Progress Towards Laser-Driven Particle Therapy Accelerators, Proc. of AAC2010 AIP **1299(1)**, 721 (2010)

T. Kluge, M. Bussmann, S. A. Gaillard, K. A. Flippo, D. C. Gautier, B. Gall, T. Lockard, M. E. Lowenstern, J. E. Mucino, Y. Sentoku, K. Zeil, S. D. Kraft, U. Schramm, T. E. Cowan, R. Sauerbrey, Low-Divergent, Energetic Electron Beams from Ultra-Thin Foils, Proc. of AAC2010 AIP **1209(1)**, 51 (2010)

T. Kluge, S.A. Gaillard, M. Bussmann, K.A. Flippo, T. Burris-Mog, B. Gall, M. Geissel, S.D. Kraft, T. Lockard, J. Metzkes, D.T. Offermann, J. Rassuchine, M. Schollmeier, U. Schramm, Y. Sentoku, K. Zeil and T.E. Cowan, Theoretical Understanding of Enhanced Proton Energies from Laser-Cone Interactions, Proc. of AAC2010 AIP **1299(1)**, 715 (2010)

U. Schramm, K. Zeil, C. Richter, E. Beyreuther, M. Bussmann, T.E. Cowan, W. Enghardt, L. Karsch, **T. Kluge**, S. Kraft, L. Laschinsky, J. Metzkes, D. Naumburger, J. Pawelke and R. Sauerbrey, Ultrashort pulse laser accelerated proton beams for first radiobiological applications, Proc. of AAC2010 AIP **1299(1)**, 731, 2010

S.D. Kraft, C. Richter, K. Zeil, M. Baumann, E. Beyreuther, S. Bock, M. Bussmann, T.E. Cowan, Y. Dammene, W. Enghardt, U. Helbig, L. Karsch, **T. Kluge**, L. Laschinsky, E. Lessmann, J. Metzkes, D. Naumburger, R. Sauerbrey, M. Schürer, M. Sobiella, J. Woithe, U. Schramm and J. Pawelke, Dose dependent biological damage of tumour cells by laser-accelerated proton beams, New J. Phys. **12**, 085003 (2010)

K. Zeil, S.D. Kraft, S. Bock, M. Bussmann, T.E. Cowan, **T. Kluge**, J. Metzkes, T. Richter, R. Sauerbrey and U. Schramm, The scaling of proton energies in ultrashort

PULSE LASER PLASMA ACCELERATION, New J. Physics **12**, 045015 (2010)

T. Kluge, W. Enghardt, S.D. Kraft, K. Zeil, U. Schramm, T.E. Cowan and M. Bussmann, ENHANCED LASER ION ACCELERATION FROM MASS-LIMITED FOILS, Phys. Plasmas **17**, 123103 (2010)

S.A. Gaillard, **T. Kluge**, K.A. Flippo, M. Bussmann, B. Gall, T. Lockard, M. Geissel, D. T. Offermann, M. Schollmeier, Y. Sentoku, and T.E. Cowan, INCREASED LASER-ACCELERATED PROTON ENERGIES VIA DIRECT LASER-LIGHT-PRESSURE ACCELERATION OF ELECTRONS IN MICROCONE TARGETS, Phys. Plasmas **18**, 056710 (2011)

T. Kluge, T.E. Cowan, A. Debus, U. Schramm, K. Zeil and M. Bussmann, ELECTRON TEMPERATURE SCALING IN LASER INTERACTION WITH SOLIDS, Phys. Rev. Lett. **107**, 205003 (2011)

T. Kluge, A. Debus, W. Enghardt, S.A. Gaillard, S.D. Kraft, K. Zeil, U. Schramm, T.E. Cowan and M. Bussmann, HIGH PROTON ENERGIES FROM CONE TARGETS, ELECTRON ACCELERATION MECHANISMS, New J. Physics **14**, 023038 (2012)

Conference presentations by the author

T. Kluge, SIMULATIONS ON THIN FOILS, **talk** at ENLITE Forschungszentrum Dresden-Rossendorf (2009)

T. Kluge, M. Bussmann, K. Zeil, S. Kraft, U. Schramm, T. Cowan, HIGH-ENERGY PROTONS FROM ULTRA-THIN FOILS, **poster** at TR18-Meeting Frauenwörth (2009)

T. Kluge, Bussmann, M., Zeil, K., Kraft, S. D., Schramm, U., Cowan, T. E., HIGH-ENERGY PROTONS FROM CLOSELY STACKED, ULTRA-THIN FOILS, **poster** at ULIS Frascati, Italy (2009)

T. Kluge, Gaillard, S. A., Bussmann, M., Gall, B., Gautier, D. C., Geissel, M., Kraft, S. D., Lockard, T., Offermann, D., Schollmeier, M., Sentoku, Y., Schramm, U., Zeil, K., Cowan, T. E., Flippo, K., RECORD PROTON ENERGIES FROM LASER ACCELERATION WITH CONE TARGETS, poster at NIC-Symposium Jülich (2010)

T. Kluge, Gaillard, S., Gall, B., Lockard, T., Gautier, C., Geissel, M., Offermann, D., Kraft, Stephan D., Schollmeier, M., Schramm, U., Sentoku, Y., Zeil, K., Cowan, Thomas E., Flippo, Kirk A., Bussmann, M., PROTON, ELECTRON AND K-ALPHA EMISSION FROM MICRO-SCALE COPPER CONE TARGETS, **talk** at DPG Frühjahrstagung Hannover (2010)

T. Kluge, Bussmann, M., Gaillard, S. A., Flippo, K. A., C. Gautier, D., Gall, B., Lockard, T., Lowenstern, M. E., Mucino, J. E., Sentoku, Y., Zeil, K., Kraft, S. D., Schramm, U., Cowan, T. E., Sauerbrey, R., LOW-DIVERGENT, ENERGETIC ELECTRON BEAMS FROM ULTRA-THIN FOILS, **talk** at DPG Frühjahrstagung Hannover (2010)

T. Kluge, S. A. Gaillard, B. Gall, T. Lockard, D. C. Gautier, M. Geissel, J. Metzkes1, D. Offermann, S.D. Kraft, M.Schollmeier, U. Schramm, Y. Sentoku, K. Zeil, K. A. Flippo, M. Bussmann and T. E. Cowan, , **talk** at TR18-Meeting Frauenwörth (2010)

T. Kluge, S. A. Gaillard, K. A. Flippo, Bussmann, M., Burris, T., Gall, B., Geissel, M., Lockard, T., Metzkes, J., Offermann, D. T., Rassuchine, J., Schollmeier, M., Schramm, U., Sentoku, Y., Zeil, K., Cowan, T. E., THEORETICAL UNDERSTANDING OF RECORD PROTON ENERGIES FROM LASER ACCELERATION WITH CONE TARGETS AND FUTURE PROSPECTS, **invited talk** and **poster** at Ann. Meeting APS Plasma Phys. **52** (2010)

T. Kluge, S. A. Gaillard, K. A. Flippo, Gall, B., Lockard, T., Geissel, M., Offermann, D. T., Schollmeier, M., Kraft, S. D., Metzges, J., Zeil, K., Schramm, U., Sentoku, Y., Enghardt, W., Sauerbrey, R., Bussmann, M., Cowan, T. E., SCALING UP THE ENERGY OF LASER-ACCELERATED IONS USING NOVEL TARGET STRUCTURES, **poster** at 470. Heraeus Seminar on Part. Acc. and High Intens. Las. Bad Honnef (2010)

T. Kluge, W. Enghardt, S. D. Kraft, K. Zeil, U. Schramm, T. E. Cowan, M. Bussmann, ENHANCED LASER ION ACCELERATION FROM MASS-LIMITED FOILS, **talk** at DPG Frühjahrstagung Münster (2011)

T. Kluge, S. A. Gaillard, K. A. Flippo, B. Gall, T. Lockard, M. Geissel, D. T. Offermann, M. Schollmeier, S. D. Kraft, J. Metzkes, K. Zeil, U. Schramm, Y. Sentoku, W. Enghardt, R. Sauerbrey, M. Bussmann, T. E. Cowan, ELECTRON ACCELERATION MECHANISMS IN CONE TARGETS - SCALING UP THE ENERGY OF LASER ACCELERATED IONS, **talk** at DPG Frühjahrstagung Münster (2011)

T. Kluge, S. A. Gaillard, K. A. Flippo, B. Gall, T. Lockard, M. Geissel, D. Offermann, M. Schollmeier, S.D. Kraft, J. Metzkes, K. Zeil, U. Schramm, Y. Sentoku, W. Enghardt, R.

Sauerbrey, M. Bussmann, and T.E. Cowan, ELECTRON ACCELERATION MECHANISMS IN CONE TARGETS, SCALING UP THE ENERGY OF LASER ACCELERATED IONS, **talk** at SPIE Optics + Optoelectronics, Prague, Czech Republic (2011)

Acknowledgments

Writing a thesis is a tough enterprise, not just for the author but also for the people around him. First of all I want to thank Prof. Dr. R. Sauerbrey for giving me the opportunity to start working in his laser particle acceleration group. The dynamics of this young group gave a great freedom to pursue science and the necessary room to work on fundamental questions.

Ulrich Schramm has always been a very valuable person to talk to and gave support not only to me but the whole group. I want to thank him especially for introducing me to the field and numerical methods and establishing first contact with important people, as well as for enabling me to attend conferences and to present our science to the public.

A big thanks goes also to Thomas E. Cowan who pushed especially the cases of Mass Limited Targets and Cone Targets with great personal dedication and passion and enabled my attendance at the cone experiments at the TRIDENT facility. He is a real font of ideas and has always time to discuss ideas and results, almost always inevitably ending in a bet for a Dollar (or Yen).

I also want to thank Wolfgang Enghardt who continued his support from my Diploma work throughout the last five years and always was quick and accurate when correcting manuscripts.

Michael Bussmann has been the perfect post-doc who came to the group at the perfect time to guide me. His deep, never ending question sessions, his passionate fight for the perfect result, his dedication for all of his students are outstanding. He deserves great thanks for supporting me, without him this thesis would not be what it is.

I want to thank Karl Zeil and Josefine Metzkes for all the many discussions of experimental results, possible mechanisms and numerical results. Also, they deserve thanks for proofreading manuscripts and Karl for giving valuable suggestions on this thesis. They have been very valuable colleagues and friends. Thanks also to Axel, especially for giving me golf courses after lunch, Jurjen for kindly settling the candy war, Alexander for his support in derivations of equations and for enduring me in the office, and Markus (not only for giving valuable advice on strollers). Long barbecue evenings, hikes and ski holidays with them almost always ended up in fun physics discussions for us – which was most probable not so much fun for our spouses.

I also want to thank the students Anton, Klaus, Axel and Heiko who where always ready to listen to a physical problem and font to solve it. Special thanks to Anton for helping in the simulations and evaluation of numerical outputs.

Without the support of the HZDR IT-department this work would not have been possible. Henrik Schulz and Matthias Schlett were always promptly available when problems with the cluster occurred (rarely enough) and always quickly fixed them. I want to thank them for their effort and their help. I also thank Michael Geissler and Yasuhiko Sentoku for providing their PIC codes and thereby giving me the opportunity to do the science I did in the first place. Thanks also to Emmanuel d'Humieres who spent a whole lot of a time to introduce me to PICLS and explain many numerical details and tricks.

Very great and special and grateful thanks go to Sandrine Gaillard and Kirk Flippo. I will never forget the beam times at TRIDENT with them. Sandrines passion is legendary and the discussions, analysis and other work at LANL together with them as well as the rest of the TRIDENT team were among the most fruitful times during my graduation. I am very grateful that I was given the opportunities to work with them and every discussion was very insightful and worth it!

I thank my family for giving so much support. Visiting them has always been like diving into another world of freedom, happiness and security, especially since Arthur and Svea have stepped into the world.

But this thesis would never have been written without the great, selfless support of my wife. She stood by me in bad times and shares joy in good times. I thank her for waging the adventure of life together with me.

Eidesstattliche Erklärung

Hiermit versichere ich, Thomas Kluge, geboren am 21.5.1982 in Dresden, im Rahmen meines Promotionsverfahrens an der Fakultät Mathematik und Naturwissenschaften der Technischen Universität Dresden und an Eides statt, dass

1. ich die vorliegende Arbeit ohne unzulässige Hilfe Dritter und ohne Benutzung anderer als der angegebenen Hilfsmittel angefertigt habe; die aus fremden Quellen direkt oder indirekt übernommenen Gedanken sind als solche kenntlich gemacht. Die Arbeit wurde bisher weder im Inland noch im Ausland in gleicher oder ähnlicher Form einer anderen Prüfungsbehörde vorgelegt.

2. ich die vorliegende Arbeit am Helmholtz-Zentrum Dresden-Rossendorf am Institut für Strahlenphysik unter der wissenschaftlichen Betreuung von Prof. Roland Sauerbrey angefertigt habe.

3. mir die geltende Promotionsordnung (Stand 23.02.2011, Fakultät Mathematik und Naturwissenschaften der TU Dresden) bekannt ist und ich diese anerkenne.

Digital unterschrieben von Thomas
Kluge
DN: cn=Thomas Kluge, o, ou,
email=mail@t-kluge.de, c=DE
Datum: 2013.01.10 11:38:39 +01'00'

Dresden, 05.04.2012